



Detection and dynamics of satellite exospheres

Apurva Oza

► To cite this version:

Apurva Oza. Detection and dynamics of satellite exospheres. Planetology. Université Pierre et Marie Curie - Paris VI, 2017. English. NNT : 2017PA066224 . tel-01687043

HAL Id: tel-01687043

<https://theses.hal.science/tel-01687043>

Submitted on 18 Jan 2018

HAL is a multi-disciplinary open access archive for the deposit and dissemination of scientific research documents, whether they are published or not. The documents may come from teaching and research institutions in France or abroad, or from public or private research centers.

L'archive ouverte pluridisciplinaire **HAL**, est destinée au dépôt et à la diffusion de documents scientifiques de niveau recherche, publiés ou non, émanant des établissements d'enseignement et de recherche français ou étrangers, des laboratoires publics ou privés.



**THÈSE DE DOCTORAT DE
L'UNIVERSITÉ PIERRE ET MARIE CURIE**

Spécialité

Planétologie et Instrumentation Spatiale

École Doctorale Astronomie et Astrophysique Île de France (AAIF 127, Paris)

Présentée par

Apurva V. OZA

Pour obtenir le grade de

DOCTEUR de l'UNIVERSITÉ PIERRE ET MARIE CURIE

Sujet de la thèse :

Detection and Dynamics of Satellite Exospheres

Soutenue le 28 Septembre, 2017

Devant le jury composé de :

Dr. François LEBLANC	Directeur de thèse
Dr. Jean-Jacques BERTHELIER	Co-Directeur de thèse
Pr. Bruno SICARDY	Président de jury
Pr. Joachim SAUR	Rapporteur
Dr. Iannis DANDOURAS	Rapporteur
Dr. Olivier WITASSE	Examineur
Dr. Anna MILLILO	Examineur
Dr. Alain DORESSOUNDIRAM	Examineur

et

Pr. Robert E. JOHNSON

Invité

For Louis "Tony" Steiner (1990 - 2017), in
memoriam.

Laughed in victory

Laughed in defeat

Life presented a sword

Laughed along the blade.

-Shashin Natwarlal Oza (1923- 2011)

Abstract en Français

Astronomy & Astrophysics Ecole Doctorale 127
Institut Pierre Simon Laplace: LATMOS

Je présente une analyse multidisciplinaire du comportement d'une exosphère d'un satellite dont la limite inférieure est une surface solide. Une exosphère par définition n'a pas de limite supérieure, est constituée d'un gaz dont la dynamique n'est pas régie par des collisions et correspond à la région d'interaction entre un objet planétaire et sa planète mère ou étoile. Dans cette thèse, je montrerai qu'une population exosphérique d'un satellite qui serait volatile et dont la dynamique serait fortement dépendante de la température de surface, aura une évolution orbitale synchrone avec le cycle diurne. Par exemple, l'oxygène moléculaire autour d'Europa et de Ganymède, satellites de Jupiter, devrait suivre une telle évolution. Je m'attacherai donc à comparer les résultats d'un modèle 3D Monte Carlo reconstruisant l'évolution de cette exosphère et les observations d'émissions aurorales par le télescope Hubble pour souligner la persistance d'une asymétrie matin/soir caractéristique de ce cycle diurne. Par ailleurs, une analyse plus théorique de l'origine de cette asymétrie nous suggère qu'un réservoir d'O₂ sous forme gazeuse dans le régolite pourrait être à l'origine de la formation de cette exosphère. En plus de la description de l'O₂ exosphérique autour d'Europa, je soulignerai les différences notables avec l'H₂O et ses produits. Enfin, j'ai également travaillé à la caractérisation d'une nouvelle technologie pour une source d'ionisation basée sur l'utilisation de nano-tubes de carbone. Cet émetteur d'électron utilisé pour la spectrométrie de masse neutre s'avère nettement plus efficace que les émetteurs classiquement utilisés dans le spatial et devrait donc nous aider à explorer ces exosphères.

Abstract en Francais

Astronomy & Astrophysics Ecole Doctorale 127
Institut Pierre Simon Laplace: LATMOS

I present a multidisciplinary analysis on the behavior of a surface-bounded exosphere synchronously rotating about its primary. An exosphere is the boundless, external envelope of gas extending from a planetary surface or atmosphere. This collisionless gas represents the interface between planets and stars, as it directly interacts with the interplanetary medium. Should the exosphere possess a population of volatiles strongly coupled with the surface temperature, the exosphere will be capable of experiencing a diurnal cycle over an orbital period. I provide the first evidence of the existence of such a diurnal cycle in the molecular oxygen exospheres of two of Jupiter's icy moons: Europa and Ganymede. The evidence was surmounted by an in-depth comparison between the near-surface ultraviolet oxygen aurorae observations by the Hubble Space Telescope and 3-D Monte Carlo simulations of Europa's near-surface O₂ exosphere, where both aurorae and exospheres were found to be strongly peaking at dusk. The dusk-over-dawn asymmetry analysis also provides evidence that Europa may harbor a large O₂ reservoir embedded in its ice today. In addition to O₂, I present the first orbital simulations of all known water-products at Europa, and provide perspectives on discerning the effects of cryovolcanism on the exosphere. Lastly, at LATMOS, I characterized a novel ionization source: a carbon nanotube electron gun (CNTeg). This in-situ device used for neutral mass spectrometry, may prove to be a very efficient electron emitter ($P < 10$ milliWatts) and should aid future searches to detect trace gases in any exosphere.

Abstract en Francais

Astronomy & Astrophysics Ecole Doctorale 127
Institut Pierre Simon Laplace: LATMOS

આ મહાનિબંધમાં મેં હલકા વાતાવરણોનો અનેક વૈજ્ઞાનિક શાખાઓ દ્વારા વિશ્લેષણ કર્યું છે. ખાસ કરીને, આ હલકું વાતાવરણ જે ઉપગ્રહોની સપાટી ઉપરથી અવકાશમાં નિસરી જાય છે. આવાં જ વાતાવરણોનો અમે અભ્યાસ કર્યો છે.

આ વાતાવરણોનું માધ્યમ બધાં જ ઉપગ્રહો અને તારાઓ વચ્ચે હોય છે. જ્યારે આ વાતાવરણ ઉપગ્રહની સપાટીના તાપમાનના સંસર્ગમાં આવે છે, ત્યારે જ ક્રિયા-પ્રક્રિયા દ્વારા ઉપગ્રહના વાતાવરણમાં દૈનિક ચક્ર શરુ થાય છે. મેં આ દૈનિક ચક્ર, ગુરુના બે ઉપગ્રહો (યુરોપા અને ગેનીમીડ) ઉપર બતાવ્યું છે.

આ પુરાવો પ્રાણવાયુ ધ્રુવીય જ્યોતિ (હબલ ટેલિસ્કોપ દ્વારા) અને પ્રાણવાયુના હલકા વાતાવરણ (મોન્ટે કાર્લો સિમ્યુલેશન) -- આ બંનેની પુરાવેલ માહિતીની સરખામણીથી જોવા મળ્યો છે. યુરોપા અને ગેનીમીડના વાતાવરણોમાં પ્રાણવાયુનું પ્રમાણ સાંજના સમયે વધારે દેખાય છે. સવાર અને સાંજના અસમાન પ્રાણવાયુનું પ્રમાણ આપણું ધ્યાન એક મહત્વ ની બાબત તરફ દોરે છે કે યુરોપા ઉપરનો બરફ એ પ્રાણવાયુ નો મોટો સંગ્રહ હોવો જોઈએ.

આ ઉપરાંત, મેં યુરોપાની ગુરુ ફરતાની પ્રદક્ષિણા દરમિયાન પાણીના વાતાવરણનું શું થાય છે એ પ્રશ્ન ઉપર દ્રષ્ટિક્ષેપ કરી મારું મંતવ્ય રજુ કર્યું છે.

અંતમાં , કાર્બન નેનોટ્યૂબ ઇલેક્ટ્રોન ગન" એ 'ન્યુટ્રલ માસ સ્પેક્ટ્રોસ્કોપી' નામનું સાધન છે, જે આયનન માટે વપરાય છે. નેનોટેકનોલોજી આ વિદ્યુદળ બંધૂક ના ઉપયોગ થી હલકા વાતાવરણને બહુ જ સહજતાથી આયોનાઈઝ કરી શકે છે. ભવિષ્યમાં આ સાધન હલકા વાતાવરણની શોધ માટે ખૂબ જ ઉપયોગી નીવડશે.

Acknowledgements

*Gurus*¹ are far more than steady lamps of knowledge in the eyes of a Ph.D student in Astronomy & Astrophysics. Space *Gurus* are therefore those mentors that are able to train a student's mind to conquer the oblivions of the Universe, guiding a path to unlock nature's unknowns during *and after* a focused dissertation. Therefore, I begin by expressing my deepest gratitude to the three gurus who guided me throughout this thesis on satellite exospheres. I am first and foremost indebted to my versatile and ambitious PhD advisor and '*directeur de thèse*', Francois Leblanc. Sans Francois, the following pages would be the best demonstration of an island of disorder, floating in an ocean of entropy. The focus and dedication Francois holds on characterizing exospheres by employing multiple fields of study is exemplary, in that he has shown me that problems in Space Science are best solved when viewed from multiple angles. In this regard, Francois has taught me the true meaning of working efficiently as a scientist. The long discussions on the inner workings of Europa's exosphere, always filled with the utmost patience, has arguably given me my most profound understanding of physics today. Next, I thank our *maître*, my *co-directeur de thèse* Jean-Jacques Berthelier, for teaching me the fundamentals of space instrumentation. JJ taught me that if ever one wants an instrument to fly above the Earth's atmosphere, forget the old French proverb about nitpicking flies, rather it is absolutely essential to seamlessly tighten every bolt. My final Space Guru gratitude goes to Professor Bob Johnson for welcoming me with open arms into the field of planetary atmospheres. Never shall I forget the inspiring afternoon I met Bob, when one tantalizing discourse on Io's extreme volcanism led to a planetary impetus which I hope will last a lifetime. Bob's sagacious advices on approaching a problem with simplicity has taught me what the word elegance means in theoretical physics. After several years of learning under Bob, I still cannot express how impactful Bob's style of thinking is on my own, but can say with the utmost confidence how deeply appreciative I am for it.

I acknowledge also the Gurus from whom I gained several orders of magnitude of research knowledge, essential to my beginnings: Professor Dan Reichart, Professor Pascal Petit, Professor Phil Arras, and Professor Mike Skrutskie.

I also want to thank a series of extracurricular collaborations composed of the most dedicated and brilliant friends that have contributed enormously to any creativity that may exist in this dissertation. To Paris Panga for *la danse*, to La Resonance de Laplace for *la musique*. Shoutout to Haze Cube & Eccentric D, JEP de l'Observatoire, and ADS de Charlottesville for their astrophysical camaraderie. To PaanchCon for *la philosophie*, to CafeAstroParisien for *l'audace de penser au-delà*, to CDG-4 & 5Taara for *500,000,000*, and lastly to any Shadow Parchayis for their *esprit du corps*, *la gravité*, and *du chai*.

¹*Guru* is also the Vedic name for Jupiter, a significant driver of much of the satellite exosphere dynamics on Europa and Ganymede discussed in this thesis.

Above all, no thesis would have even started if it wasn't for my entire family's undying support. My mother's constant motivation— celestial even in her words, my brother's buoyancy—still floating and unparalleled. *Finalement*, I thank my father, Vikram Shashin Oza, for inspiring me to pursue astrophysics after years of describing phenomena to me by simply skipping stones in the waters of Carolina.

Contents

Abstract en Francais	4
Abstract in English	5
Abstract in Gujarati	6
Acknowledgements	7
List of Figures	12
List of Tables	19
Symbols	22
1 Introduction	24
I Dynamics of Satellite Exospheres.	31
2 Time-Dependent Atmospheric Bulges on Tidally-Locked Satellites	33
2.1 Introduction	33
2.2 Atmospheric Bulge Model	34
2.2.1 Stellar Radiation-Driven Source	39
2.2.2 Magnetospherically-Driven Source	40
2.2.3 Stellar Radiation & Magnetosphere-Driven Source	41
2.3 Orbital Evolution of Atmospheric Bulges	42
2.3.1 Europa's O ₂	42
2.3.2 Ganymede's O ₂	45
2.4 Conclusion & Summary	46
2.5 Dusk Over Dawn Molecular O ₂ Asymmetry in Europa's Exosphere.	48
2.6 Introduction	48
2.7 Europa Exosphere Global Model	51
2.7.1 Sputtering.	53
2.7.2 Surface Temperature	55
2.8 Results	56
2.8.1 Exospheric O ₂ Evolution	56

2.8.2	Atmospheric O ₂ Bulges	58
2.8.2.1	Stationary Case: Atmospheric O ₂ Bulge at Noon	58
2.8.2.2	Rotating Case: Atmospheric O ₂ Bulge at Dusk	60
2.8.2.3	Rotating Case: Surface-Exosphere Coupling of O ₂	62
2.9	Discussion	63
2.9.1	Orbital Evolution of Exospheric and Auroral Oxygen	64
2.9.2	O ₂ Adsorption on Grains in the Water Ice Regolith	66
2.9.3	Comparisons of Oxygen Aurorae and Oxygen Exosphere: A Stratified Exosphere.	67
2.9.3.1	Disk Emission: $r < 1.0r_{Eu}$	68
2.9.3.2	Limb Brightening: $0.8 < r < 1.2r_{Eu}$	68
2.9.4	Coronal Expansion: $r \gtrsim 1.25r_{Eu}$	74
2.9.4.1	Plasma-Driven Atmospheric Expansion	74
2.9.4.2	Water-Driven Expansion	75
2.10	Conclusion/Summary	77
2.11	Summary and Future Prospects of Chapter 2	79
II	Perspectives on Ocean World Exospheres	80
3	Exogenic & Endogenic Water-Product Exospheres: Examining Europa & Ganymede <i>Ensemble</i>	82
3.1	Introduction to Water-Product Exospheres	83
3.2	Water-Product Observations: Water Vapor and Atomic Hydrogen	84
3.2.1	Water Vapor Plumes	84
3.2.2	Europa Exospheric Hydrogen Observations	86
3.3	Orbital Evolution of Exospheric Water Products	86
3.3.1	H ₂ O Variability: Leading/Trailing Asymmetries	87
3.4	Perspective on Water Vapor Production Mechanisms	89
3.4.1	Surface Ice-Generated Exospheric H ₂ O	90
3.4.2	Subsurface: Ocean-Generated Exospheric H ₂ O	95
3.4.2.1	Tidal Heating	95
3.5	Final Perspectives	96
III	Detection of Exospheres	98
4	Astronomical Observations of Exospheres	100
4.1	Detecting Exospheres Remotely	101
4.1.1	Direct Imaging of Exospheres	101
4.1.2	Direct Spectroscopy of Exospheres	102
4.1.2.1	Infrared Spectroscopy of Exospheres	102
4.1.2.2	Sub-mm Spectroscopy of Exospheres	102
4.1.3	Transmission Photometry/Spectroscopy Observations	103
4.2	Searches for Volcanic Volatiles in Europa's Exosphere in the age of ALMA	104
4.2.1	NaCl Vapor at Europa	104
4.2.2	SO ₂ Vapor at Europa	108
4.2.2.1	Sputtered SO ₂ Exosphere	108

4.2.2.2	SO ₂ Venting	112
4.2.2.3	Description & Consequences of Possible SO ₂ Observa- tions	119
4.3	Detecting the Presence of a Toroidal Atmosphere	120
4.3.1	Escaping Exosphere Mechanisms to Populate a Toroidal Atmosphere	120
4.3.2	Detecting Neutral Tori	121
4.4	Conclusions on Ocean World Perspectives	122
5	In-Situ Observations & Technology	124
5.1	Mass Spectrometers	125
5.2	Introduction: A Carbon Nanotube Electron Gun.	127
5.3	CNTegs	128
5.3.1	Carbon Nanotube Field Emission	128
5.3.2	CNTeg emission runs	130
5.3.3	CNTeg energy characterization	131
5.4	Simulations of Primary Electron Emission Under Electric Fields	137
5.5	Secondary Electron Model	138
5.6	Results	140
5.6.1	Electron Energy Characterization	140
5.7	Conclusion	143

List of Figures

- 2.1 Satellite coordinate system for a planet and rotating satellite. The center body is the planet along with two orbital positions of the satellite depicted. Black vectors represent the fixed, observers frame, where y_{ϕ_s} in black indicates the incoming stellar radiation flux vector. ϕ_s is the anti-stellar insolation vector, defined as such in order to synchronize the two frames, where Dusk: $\phi_s = 3\pi/2$ and Dawn: $\phi_s = \pi/2$. Blue vectors represent the rotating, satellite frame where ϕ is the satellite longitude whose origin is the subplanetary point. We define the origin of the satellite system (blue circle) as $\phi_0 = \phi + \pi$ to effectively compare to observations such that the subobserver longitude is synchronized with the planetary longitude at midnight during satellite eclipse. As the satellite rotates over an arbitrary timescale Δt , the satellite will have rotated a $\Delta\phi_{obs} = \Omega\Delta t$ 35
- 2.2 A simple temperature-dependent source rate treated as a stellar radiation-driven exosphere source flux Φ_T in our model. Values are scaled to the most recent simulations for Europa's O_2 exosphere $\Phi_0 = 3 \cdot 10^8 O_2 \text{ cm}^{-2} \text{ s}^{-1}$, evaluated at the antijovian point, beginning at $\phi_{orb} = 0$, the origin of our planet-satellite system. Surface temperatures are results from the thermal model employed in Oza et al. [2017], where albedo and thermal inertia effects are included. 37
- 2.3 Dusk-over-dawn asymmetry ratio, R , versus $\beta = \Omega/\nu$. Ratios are determined by known orbital periods and estimated neutrals lifetimes. It is seen that if $\Omega \sim \nu$ the asymmetry is maximum. The dash-dotted blue line represents a possible upper limit to the radiation-driven dusk-over-dawn asymmetry, as it is computed at the terminator following Eqn. 2.7. The small circles represent various satellites in the solar system. Red, cyan, black, and gray are the Galilean satellites (Io, Europa, Ganymede, Callisto respectively). The magenta and green points are the Saturnian satellites Dione and Rhea respectively. The solid blue line is a hemispherical average of the radiation-driven dusk-over-dawn asymmetry; more representative of the observed asymmetry. 38
- 2.4 Average dusk-over-dawn asymmetry ratio, $\langle R \rangle$, versus ϕ_{orb} for the magnetospherically-driven and temperature-dependent magnetospherically driven sources as indicated by $\langle R \rangle_{mag}$ and $\langle R \rangle_{Tmag}$ respectively. The blue squares are Monte Carlo simulations from Oza et al. [2017] indicated a non-adsorbing O_2 population. The black squares are the dusk-over-dawn oxygen aurorae data by HST. The black dotted line represents a temperature-enhanced case where we triple the temperature enhancement factor $f(\phi_s)$ to confirm the increase in asymmetry *towards* dusk. 43

- 2.5 Top panel: Radiolytic O₂ production flux at Ganymede's poles at $\phi_{orb} = 90$. Bottom panel: Column density of O₂ demonstrating the *equatorial* atmospheric bulge at the same longitude implying downwards, equatorial diffusion as described in the text. 45
- 2.6 Top-down geometry of the simulation domain and associated physical processes at a sub-observer longitude of $\phi_{obs} = 90$ deg, corresponding to the sunlit leading hemisphere. The O₂ ejection flux due to sputtering, highlighted by the red vector Φ_0 , dominates ejection at the sub-plasma point against the ram direction of the plasma, following Equation 2.17. The ejected O₂ is assumed to be thermalized to the local surface temperature and is subject to dissociation and ionization. Adsorption, or sticking, is indicated in violet. 52
- 2.7 **a:** Equatorial subsolar surface temperature (K) as a function of sub-observer longitude, or Europa's orbital longitude, demonstrating the leading-trailing temperature profile asymmetry due to albedo. The darker, trailing hemisphere ($A_b = 0.45$) is seen to be ~ 18 K warmer than the brighter, leading hemisphere ($A_b = 0.65$). **b:** Surface temperature map of Europa's sunlit trailing hemisphere at $\phi_{obs} = 270^\circ$. The surface temperature rapidly increases from dawn, $\phi_{obs} = 90$ until the subsolar point at $\phi_{obs} = 0$. The surface then begins to cool slightly more slowly, passing through dusk at 18h Europa local time. The largest thermal gradients driving migration are therefore between 6h - 12h, and 12h-18h. Due to the thermal inertia of the ice, the dusk hemisphere is warmer than the dawn hemisphere. 57
- 2.8 Europa's static, O₂ exosphere for a simulation fixed at the sunlit trailing hemisphere with no rotation. Vectors are shown to demonstrate the day-night migration in the absence of rotation. An artificial day-side O₂ asymmetry is highlighted, due to preferential ion bombardment at the sunlit trailing hemisphere in the absence of rotation. The low albedo, sunlit trailing hemisphere has an equilibrium temperature of $T_d \sim 135K$, further exaggerating the effect of O₂ production on the exosphere due to the strong thermal dependence of the O₂ sputtering yield. 58
- 2.9 **a:** Monte Carlo simulation results for Europa while rotation about Jupiter is active. Orbital evolution of the surface-averaged O₂ column density (black) along with the surface-averaged O₂ production flux ($\langle f_{ej} \rangle$: blue) as well as the average O₂ loss flux ($\langle f_{loss} \rangle$: magenta) versus the sub-observer longitude. $\langle f_{loss} \rangle$ estimates the loss of the average O₂ content, throughout the exospheric lifetime of the O₂, at each sub-observer longitude: $\langle f_{loss} \rangle \sim \langle N \rangle \langle t_{exo} \rangle$. **b:** Illustration of the diurnal asymmetry with respect to the bulk O₂ source, which is on average sourced at plasma ram/trailing hemisphere. The day-night axis for plasma ram, is therefore rotated by 90° from the observer's reference frame. During 'Ram Day', the bulk exosphere grows. During 'Ram Night', the bulk O₂ exosphere slowly diminishes. 61

- 2.10 Formation map of Europa's O₂ exosphere, illustrating surface-exosphere coupling of the near-surface O₂. $\phi = 0$ degrees west longitude corresponds to the sub jovian point (SJ), where positive longitudes correspond to the trailing hemisphere (T) and negative longitudes, leading (L). At $\phi_{obs} = 180^\circ$ we provide a high-resolution map of Europa's surface, for comparison to the near-surface exosphere, taken by Voyager and Galileo as adopted in [Doggett et al., 2009]. On each simulation map, the sub-solar point is indicated by a white X, whereas the dawn and dusk terminators are indicated by the vertical dashed lines. **Inner circle surface maps:** Exospheric production as shown by the ejection rate of the O₂ sputtered from the surface with respect to latitude and west longitude at different orbital positions of Europa. The sputtering flux ranges from 2 (blue) - 12 (red) $\cdot 10^8$ O₂ cm⁻² s⁻¹ (right panel colorbar). Sub-observer longitudes(ϕ_{obs}), or phase angles are provided inside the orbit. **Outer circle exosphere maps:** Log₁₀ of the radially integrated column density of the O₂ exosphere with respect to latitude and west longitude at different orbital positions of Europa. The radial column density ranges from $\sim 1 - 30 \cdot 10^{13}$ O₂ cm⁻² (left panel colorbar). Whereas the average radially integrated column density of the O₂ exosphere ranges from $7.4 - 8.1 \cdot 10^{13}$ O₂ cm⁻². The reader is encouraged to refer to the web-version of this article for a more enhanced view of the smaller plots. . . . 70
- 2.11 Orbital evolution of the log of the dusk/dawn 1356 emission line versus the orbital longitude. The average auroral emission on the dusk-side of Europa is divided by the average emission on the dawn-side. Black points are HST observations. Black dashed lines represent the average error in HST observations. Solid black line is an arithmetic average of the HST data fitted to Figure 8A in R15. Squares represent the modeled auroral intensity ratios calculated from simulated LOS O₂ column densities assuming isotropic plasma conditions $n_e = 70$ cm⁻³ and $T_e = 20$ eV. The dark blue square is the nominal simulation in which the effective heat of adsorption is set to 0. The green square corresponds to the more extreme case in which the O₂ follows a a heat of adsorption of $E_{ads} = 3000$. The two cases indicate that a non-uniform heat of adsorption between the leading and trailing hemispheres, $E_{ads}(L) \neq E_{ads}(T)$, may be required to explain the exaggerated dusk enhancement at the leading hemisphere phases as simulated by the magenta square. 71
- 2.12 **Top panels:** LOS auroral intensities at $\lambda = 1356$ versus radial distance from Europa's center reconstructed by HST auroral images (black) along with corresponding EGM simulations (blue and red dashed lines). The spatial resolution is rings of $0.025 R_{Eu}$. Europa's limb is indicated with the dotted vertical line. The LOS O₂ column densities from the EGM simulation are symmetrically averaged in rings about Europa's center as in R15. The corresponding auroral intensities are then computed following Eqn. 2.24 employing modest plasma parameters with no asymmetries: isotropic electron density $n_e = 70$ cm⁻³ and $T_e = 20$ eV plasma temperature. **Bottom panels:** Simulated auroral images reconstructed directly from LOS O₂ and O column densities. The right-over-left ($< R/L >$), dusk-over-dawn, asymmetry is highlighted indicating the asymmetric nature of Europa's aurorae. 72

2.13	Auroral intensity, I , for the 1356 emission line at Europa's sunlit leading hemisphere as a function of the impact parameter (b) in units of European radii, r_{Eu} . The corresponding altitude, z , in km from the surface, is indicated on the top horizontal axis for reference. HST observations from R15 are shown by the black points. Two EGM simulations are presented for two different function distributions for the initial ejection of the O_2 molecule from the regolith: f_{MB} , in green and f_{U2} , in blue. The corresponding dotted lines represent the barometric scale heights assuming an isothermal atmosphere. In our EGM simulations the O_2 is perfectly thermally accommodated and thus the scale height reflects the average surface ice temperature $T \sim 110K$. The black dotted line fit to the HST data implies an atmospheric temperature of $T_x \sim 1500K$, or $E_x \sim 0.2$ eV roughly twice the energy of a sputtered O_2 molecule. The red dotted line is a fit to a power law distribution: $I = I_0 \left(\frac{r_{Eu}}{b}\right)^{a-1}$. b is the perpendicular scattering distance from the center of Europa's gravitational field. Both of these fits seem to suggest collisional processes occurring in Europa's corona, as described in the text.	73
2.14	Simulated LOS column densities with and without O_2+H_2O collisions, at subobserver longitude of 20 degrees. O_2 collisions are thought to occur with H_2O near sublimation + sputtering sites where the column is largest.	76
3.1	Simulated surface densities for the dominant species in Europa (solid) and Ganymede's (dashed) exospheres at the sunlit trailing hemisphere. The H_2O case represents a low-sublimation case[2].	87
3.2	Line-of-sight column density maps for atomic hydrogen on Europa and Ganymede. The right hand side is the sunlit trailing hemisphere (T), and the left hand side is the sunlit leading hemisphere (L). The average line-of-sight columns for our nominal assumptions for Europa are: $\langle N_H \rangle \sim 1.2 \cdot 10^{10}$	88
3.3	Line-of-sight column density maps for molecular hydrogen on Europa and Ganymede. The right hand side is the sunlit trailing hemisphere (T), and the left hand side is the sunlit leading hemisphere (L). The average line-of-sight columns for our nominal assumptions on Europa are: $\langle N_{H_2} \rangle 1.3 \cdot 10^{13}$	89
3.4	Line-of-sight column density maps for water vapor on Europa and Ganymede. The right hand side is the sunlit trailing hemisphere (T), and the left hand side is the sunlit leading hemisphere (L). First row: atomic hydrogen. Second row: molecular hydrogen. Third row: water vapor. The average line-of-sight columns for our nominal assumptions for Europa are: $\langle N_{H_2O} \rangle 2 \cdot 10^{13}$	90
3.5	Water Vapor sublimation flux as calculated in Leblanc et al. [2017a] and corresponding column density taken for an atmospheric lifetime equivalent to Ganymede's orbit. The derived column densities for the low sublimation case are not representative as they have not yet reached steady state.	92
3.6	H_2O High Sublimation. The color gradient for this simulation peaks at $n \sim 10^{6.5} cm^{-3}$	93
3.7	H_2O Low Sublimation; The color gradient for this simulation peaks at $n \sim 10^5 cm^{-3}$	94

4.1	Iogenic sodium stream arriving at Europa at $v_{stream} \sim 30-50\text{km/s}$. Impact parameter for collision at Europa's surface is $b_{90} < 1.1R_{EU}$. The derived Iogenic Na implantation rate from the observation is only 2% of the sputtered Europagenic Na loss rate Leblanc et al. [2002], indicating Europa is not strongly affected by Iogenic Na throughout its orbit. <i>Credit: Schmidt et al. 2015</i>	105
4.2	Europa's sublimated and sputtered water vapor, simulated at the sunlit leading hemisphere. The 3D Monte Carlo model was carried out with the LATMOS EGM (Exosphere General Model). Test particles are subject to gravitational fields, ionization, photolysis, as well as surface-interactions. The concentric pattern is due to peak columns at the center of the disk, due to solar insolation.	109
4.3	(Seasonal evolution of Europa's sodium. Europa's leading hemisphere as it arrives from eclipse shows the maximum sodium intensity. <i>Credit: F. Leblanc in Johnson et al. [2009]</i>	110
4.4	Possible cryovolcanically active region detected in 2014 and 2016 [6,13] near Pwyll crater (left panel), the mid-southern latitude region where our tidal stress estimates are carried out.	113
4.5	Results from a four-layer viscoelastic tidal stress model developed at JPL. Tidal stresses versus the true anomaly angle are plotted. 0 corresponds to perijove. Europa's average tidal stresses are roughly twice the crack initiation strength of 25kPa Hoppa et al. [1999] and furthermore, rival that of Enceladus ($\sim 14-85\text{kPa}$) whose four cracks are constantly venting. <i>Based on results from Johnston et al. [2016], and Patthoff and Davies [2017]</i>	114
4.6	Next three figures: 3-D Monte Carlo simulations of line-of-sight column densities of Europa's background atmosphere at the sunlit trailing hemisphere. $N \sim 10^{14}\text{H}_2\text{O}/\text{cm}^2$, $N \sim 3 \cdot 10^{14}\text{O}_2/\text{cm}^2$, and $N \sim 10^{13}\text{H}_2/\text{cm}^2$. Only O_2 has been confirmed indirectly through HST oxygen aurorae observations (Hall et al. [1995]). Roth et al. [2015] observation has also enabled us to understand the behavior of the near-surface O_2 throughout the European day, in that our recent 3D Monte Carlo simulations show that it builds preferentially at dusk local time (Figure based on Oza et al. 2017 in review).	115
4.7	See previous figure.	116
4.8	See previous figure.	117
4.9	118
4.10	118
4.11	A: Density versus altitude profile for a moderate venting source of SO_2 . B: Simulated non-LTE spectrum for the former altitude profile. We anticipate local Rayleigh-Jeans contrasts of 5 K in regions where SO_2 is present.	118
5.1	Schematic diagram of Ion Neutral Mass Spectrometer on board Cassini-Huygens. It shows the principle of the ion trap, where the neutral gas arrives along with the various electron guns. The closed ion source has a sensitivity to $n \gtrsim 10^4\text{cm}^{-3}$ and the open ion source has $n \gtrsim 10^5\text{cm}^{-3}$. From Waite et al. 2004.	126

5.2	Power characterization of our CNT setup, which also serves as demonstration of FN emission. As we increase the extraction voltage, more power is consumed. If the CNTs are emitting nominally, the extracted power should grow exponentially versus consumed power. The extracted power is calculated simply via Ohm's law : $P_{extracted} = I_{cnt}V$, where the consumption of the source is $P_{source} = I_{source}V$. The voltage source was a Stanford Research systems high-voltage power supply. We can see that we are only using on the order of tens of milliwatts of power, which is about 10x better than nominal cathode ray tubes (CRTs).	127
5.3	NAWA technologies CNT chip fabrication testbench, May 2017.	129
5.4	Birds eye view of the carbon nanotube chip through the lens of the G1 grill.	130
5.5	The CNTeg with the Anode facing up with a tungsten grill.	130
5.6	Schematic diagram of CNTeg. Electrodes and conductive elements are portrayed in gray tones, whereas insulators e.g. kaptons, coatings, are in pink. The two tungsten mesh-grills are in orange the Gate 1 electrode and the Anode electrode. The electric field which pushes the electrons upwards is between the CNT and G1, where the electric potential is applied at the CNT wafer. The two transparent green vectors emanating from G1 represent the secondary electrons we model.	131
5.7	Schematic diagram of CNTeg + Electrostatic Analyzer. Electrodes are boxed. In our electronic setup we regulate the voltage of T_{ext} , which is connected via a voltage divider to T_{b1}, T_{b2}, T_{int} as indicated explicitly in Figure 5.9, in order to guide the incoming electron beam to Collector 2 the final electrode.	132
5.8	Illustration depicting the operation of the electrostatic analyzer, as adopted from J. Becker 2013. The utility of the analyzer is to select only a specific set of ions corresponding to the energy band-pass (blue). The rest of the ions will not be deflected to the detector along with the neutrals. The electric field guiding the circular trajectory of the electrons is generated by the difference in voltages across the EA analyzer. A demonstration of how the beam is deflected by the variable electric fields in our simulations is provided here: http://oza.page.latmos.ipsl.fr/images/fast_e_mission.gif .	133
5.9	A simple electronic circuit diagram designed using the circuit simulator Partsim , which employs the engine SPICE . Only the principal electrodes are shown. The black arrow shows the direction of electron field emission. V_{CNT} is the negative cathode voltage of the CNT, V_{EXT} is the negative voltage of the external EA torus, and $V_{EXT}/2$ (via a voltage divider) is connected to T_{b1} and T_{b2} which are guiding electrodes places on the edge of the EA assembly. V_{C2} is a positive voltage applied to collector 2. Collector 1, Anode, and Gate 1 are all connected to ammeters for probing emission at each successive level above the CNT surface. Collector 2 is connected to a Keithley picoammeter in order to measure the electrons that reach the end of the analyzer. The anode and collector 1 are also connected to voltage sources.	134
5.10	Silicon CNTs from 2015-2017 with corresponding Fowler Nordheim curves fit to the extracted CNT current versus voltage. For discussion: A is the top left figure, B the top right, continuing with C in the next row left, and so forth.	135

5.11 CNTeg + EA assembly.	136
5.12 A zoom-in of the potential difference between the CNT cathode and the G1 electrode.	137
5.13 A simulation of the extraction device portraying how electrons are emitted in the presence of a sufficiently strong electric field.	137
5.14 Primary electrons arriving through the G1 grid (black). Secondary electrons (green) are shown in the beginning of the simulation.	141
5.15 Simulated secondary electrons emitted from G1 continuing upwards to the anode grid. Only a small fraction of the secondary electrons arrive inside the electrostatic analyzer.	141
5.16 secondary electrons in the electrostatic analyzer	142
5.17 Energy characterization of Collector 2. Here it can be seen that the energy peaks at $\sim 340V$. A small secondary electron peak near ~ 20 volts can be seen. The broader increase in energy beginning at ~ 290 volts could be due to the choice of initial kinetic energy. Here the electrons were given $E = 0.1$ eV.	142

List of Tables

1.1	Surface-bounded exospheres. Known species are listed, along with the average density of the exospheres. The maximum surface temperatures are provided along with the jeans escape parameter for a light species and a heavy species respectively. Jeans parameters for the icy Galilean satellites are evaluated for H ₂ -O ₂ ; KBOs CH ₄ -N ₂ ; Rhea & Dione for O ₂ - CO ₂ ; Moon: He-Ar; Mercury: He-Na. References for the various satellites are as follows. Europa: EGM; Callisto: Kliore et al. [2002]; Mercury: MESSENGER McClintock et al. [2008]; Enceladus (Tenishev et al. [2014]; Hansen et al. [2006]). ND signifies that the predicted exosphere is not yet detected.	28
1.2	Atmospheric-bounded exospheres in the solar system: terrestrial, KBOs, Io and Mars. Atmospheric parameters are largely unknown for Makemake & Quaoar, for the Jeans parameter at the exobase I provide a range depending on whether the exosphere is Pluto-like (colder) or Triton-like (warmer). [‡] Dandouras et al. 2008	28
2.1	Atmospheric parameters for all known surface-bounded satellite exospheres: Io (I), Europa (E), and Ganymede (G). The electron number density used for Europa and Ganymede's environments is 70 e ⁻ cm ⁻³ as in Marconi [2007]. Dione & Rhea loss rates are derived from Table 3 in Teolis and Waite [2016]. The loss rate at Callisto is assumed to be uniquely due to electron ionization [Vorbürger et al., 2015].	40
2.2	Magnitude of atmospheric O ₂ bulges on Europa, calculated as hemispherically averaged column-density ratios $\langle R \rangle \sim N_{Dusk}/N_{Dawn}$ over the four major orbital phases: sunlit trailing, eclipse, sunlit leading, and subsolar. The fixed sublimation source maintains a constant dusk-over-dawn asymmetry of: $R_T = 1.34$ for all orbital longitudes. The four R columns represent the latter two magnetospheric plasma cases in section §2.2, and 2.3. The first column is the EGM output of Oza et al. [2017] for a non-adsorbing, thermally-dependent O ₂ case. The final column is the average auroral intensity ratio, I_{Dusk}/I_{Dawn} , observed by HST at 1356 Å indicative of the exospheric asymmetry. The HST eclipse values are averaged around a $\sim 23^\circ$ interval in orbital longitude, whereas the subsolar values are averaged around a larger $\sim 100^\circ$ interval. For these latter two cases we provide pre and post transit values.	44

- 2.3 Exospheric timescales for Europa. Given $\tau_{orb} = 3 \cdot 10^5$ sec. The average hop time for an O_2 molecule is computed using an average surface temperature of $\langle T \rangle \sim 110K$, as $\sqrt{2 \frac{v_0}{g}}$. The ballistic hop, t_{hop} , assumes no interaction with the surface. The day-night migration time is estimated as a random-walk process across one Europa radius assuming no O_2 trapping or reactions with the surface ice. The average exospheric production time, $\langle t_{exo} \rangle$, for O_2 is the orbit-averaged radial column density over the orbit-averaged ejected O_2 flux, $\frac{\langle N \rangle}{\langle F \rangle}$, this timescale helps describe how long it takes to build the bulk O_2 column based on the production flux. The O_2 lifetime, τ_{O_2} , is limited by dissociation and ionization, computed by the product of the net reaction rate coefficient and the electron number density: $(\kappa \times n_e)^{-1}$, where $\kappa = 4.4 \cdot 10^{-8} \text{ cm}^3 \text{ s}^{-1}$ is the orbit-integrated reaction rate coefficient including e- impact as well as ionization, and $n_e = 70 \text{ cm}^{-3}$ the electron number density. 60
- 3.1 Sputtering & sublimation Fluxes for water volatiles with corresponding column densities. Values in parentheses are for a simulation with a high sublimation rate. The relative sputtering yields are 0.01, 0.3, 0.01, 0.01, 0.15 for H, H₂, O, OH, and O₂. The sputtering rate is computed by multiplying the sputtering flux Φ_{sputt} by the surface area of Europa, $4\pi r_{eu}^2$. Φ_{net} is computed using an incident ion flux of 1.6e8, and yields reported in Cassidy et al. [2013], at a longitude in between the trailing and leading hemispheres. Water vapor production is considered only at the sub-solar hemisphere. $\langle N \rangle$ are the average line of sight column densities computed for the trailing hemisphere $\Psi = 90$ and leading $\Psi = 270$. The exospheric residence time of the sputtered species can be computed if desired as in Smyth and Marconi [2006]: $t_{res} \approx \langle N \rangle / \Phi_{net}$ 91
- 3.2 Tidal stress parameters for Io (I), Europa (E), and Enceladus (E). The satellite's tidal energy dissipation, \dot{E} , is computed assuming a Tidal Q of 100. The energy dissipated in the satellite is equivalent to a 'tidal power'. At Io, the tidal power is of order one *sau-damini* an obsolete unit equivalent to 100 lightning bolts $\sim 10^{12}$ Watts Dvorak [2013]. Tidal pressures P_{tidal} are directly computed from SATstress, a viscoelastic model also described in the next section. Local temperatures, near the cm-wide cracks are computed assuming the an average plume radius as determined by Roth et al. [2014b] for Europa: $\Delta r = 550\text{km}$ (Eqn. 3.6. Furthermore the temperature assumes all of the dissipated energy arrives at the surface via the diurnal fractures which open and close over a demi-orbit. 96
- 4.1 Maximum radial and line-of-sight (LOS) column densities at the sunlit trailing hemisphere at a surface temperature of $T_0 = 136K$. Calculated column densities are the product of the source flux (sputtering in most cases) and the atmospheric residence time, or ballistic lifetime of the species scaled to Europa's orbital time where $\tau_{Eu} = 3.06 \cdot 10^5 \text{ s}$. Since H₂O and H₂ stick and escape we determine the atmospheric lifetimes via Monte Carlo simulations which treat these processes over the European orbit. For O_2 and SO_2 lifetimes we assume negligible interactions with the surface. The photodissociation lifetimes are found in Huebner et al. 1992, and the e- impact dissociation lifetimes for O_2 are given in Hall et al. [1995], whereas for SO_2 we use the values in Table 4.2. 111

4.2	SO ₂ electron impact dissociation reactions used for Io's interaction with the plasma torus in (Dols et al. [2012]) and personal communication with Don Shemansky. The last three O ₂ reactions are referenced: Marconi [2007] ; Ip [1996]; Smyth and Marconi [2006] respectively.	112
4.3	Atmospheric-bounded exoplanet exospheres Exoplanet Exospheres: The listed physical parameters are based on data compiled from HST and Spitzer observations (Sing et al. [2015]). ★ Recent asymmetric light curves also show evidence of potentially asymmetric exospheres in planets . † un-analyzed transmission spectroscopy data on this planet exists from 2014, in which a fast K I wind was already detected Colón et al. [2012]. ◇ Neutral atmospheric transport appears to generate photometri asymmetries in the light curve Turner et al. [2016].	121
5.1	A few classic, neutral mass spectrometers and their essential properties: mass resolution and power consumption.	125
5.2	Six CNT samples tested at LATMOS from 2015-2017. Samples E & F use a different workbench setup at NAWA technologies than at Ajou University (Samples A- D).	130
5.3	Simulated and measured (for an arbitrary CNT) current at each electrode. It can be seen in this example the anode and collector seem to have a large discrepancy from simulations, which secondary electrons are unable to account for. ΔI is the missing current comparing before and after emission.	140

Boltzmann's constant (CGS) $k_b = 1.38 \cdot 10^{-16} \text{ ergs } K^{-1}$

Boltzmann's constant (eV) $k_b = 8.6133 \cdot 10^{-5} \text{ eV } K^{-1}$

Gravitational constant $G = 6.67 \cdot 10^{-8} \text{ cm}^3 \text{ g}^{-1} \text{ s}^{-2}$

$m_e = 9.10938214 \cdot 10^{-28} \text{ g}$

$m_p = 1.672621637 \cdot 10^{-24} \text{ g}$

$m_{O2} = 32m_p \approx 5 \cdot 10^{-23} \text{ g}$

$m_{H2O} = 18m_p \approx 3 \cdot 10^{-23} \text{ g}$

$\sigma_T = 8\pi r_e^2/3 = 0.6652458558 \cdot 10^{-24} \text{ cm}^2$

Dynes $\text{cm}^{-2} = 1 \mu \text{ bar}$.

$1\text{eV} = 1.602176487 \cdot 10^{-12} \text{ erg}$ $1 \text{ ly} = 0.94606856 \cdot 10^{18} \text{ cm}$

$1 \text{ AU} = 1.49597870700 \cdot 10^{13} \text{ cm}$

$M_J = 1.89813 \cdot 10^{30} \text{ g}$

$R_J = 7.1492 \cdot 10^9 \text{ cm}$

Europa

$T_{Eu} \sim 85 - 135 K$

$a_{Eu} = 9.386 R_J = 6.71 \cdot 10^{10} \text{ cm}$

$\Omega_{Eu} = 2.048 \cdot 10^{-5} \text{ s}^{-1}$

$g_{Eu} = 132 \text{ cm/s}^2$

Ganymede

$T_G \sim 70 - 140 K$ $a_G = 14.97 R_J = 10.7 \cdot 10^{10} \text{ cm}$

$\Omega_G = 1.016 \cdot 10^{-5} \text{ s}^{-1}$

$g_{Eu} = 143 \text{ cm/s}^2$

Symbols

CNTeg	Carbon Nanotube Electron Gun
EGM	Exosphere General Model
NIMEIS	Neutral and Ion Mass and Energy Imaging Spectrometer
JUICE	Jupiter Icy Moon Explorer
TOF	Time Of Flight
ALMA	Atacama Large Millimeter/sub-mm Array
UV	Ultraviolet
IR	Infrared
NIR	Near-Infrared
MIR	Mid-Infrared
Cryovolcanism	Volcanism in which volatiles would nominally freeze at surface.

1

Introduction

An exosphere is the boundless, external envelope of gas tenuously extending from a planetary surface or atmosphere. This gas represents the interface between planets and stars as it directly transitions into the interplanetary medium. What is unique about this gas is: it is, by definition, essentially *collisionless* rendering it unlike any gas one experiences. This gas would be more similar to a near-vacuum than the air one breathes on Earth. Understanding the dynamics of such a system are hence quite complex, as the system can often behave far from the familiar thermodynamic equilibrium of a gas.

Therefore, our most accurate description of exospheres today relies on following the microscopic interactions of all gas particles. This is the foundation of kinetic theory, which is true even when the system is not in equilibrium (e.g. [Reif \[1965\]](#)). In 1963, [Chamberlain \[1963\]](#) set out to explain the state of Earth's hydrogen exosphere, $\sim 10,000\text{km}$ above the ground, a region in space also known as the geocorona. Chamberlain solved Liouville's equation by assuming energy and angular momentum was conserved for a system of particles above an altitude, r_x , defined as the exobase or critical altitude. The exobase is characterized by a density $n(r_x)$ and a temperature $T(r_x)$ above which collisions are trivial, as is the case for the Earth's hydrogen exosphere. The conservation laws helps one derive atmospheric density profiles with altitude. Overall, these solutions represent the foundation of exospheric theory, the so-called *Chamberlain exosphere*, demonstrating that this system of particles can be categorized into five groups:

1. Ballistic: Elliptic trajectories. Gravitationally bound to the body.
2. Satellite: Elliptic trajectories. Gravitationally-bound, but unlike ballistic particles do not go past the exobase altitude r_x .

3. Escaping: Hyperbolic trajectories. Velocities are greater than the escape velocity $(2G\frac{M_s}{r_s})^{1/2}$, where M_s and r_s are the satellite mass and radius respectively.
4. Captured: Hyperbolic trajectories. Exogenic particles enter the Hill sphere¹ of the body and cross the exobase.
5. Fly-by: Hyperbolic trajectories. Exogenic particles which enter the Hill sphere of the body, but do not cross the exobase.

The density then is derived considering the type of particle defined above and solving Liouville's equation for an imposed function distribution f for the particles at the exobase. Thus, [Chamberlain \[1963\]](#) introduced the following partition function valid only if the function distribution, f , is Maxwellian:

$$\zeta(\lambda) = \pi^{-3/2} \int \int \int e^{-\omega^2} \omega^2 \sin\theta d\omega d\theta d\psi \quad (1.1)$$

Where we must introduce the variables: ω , θ , and ψ , the coordinates in phase space over which the integrals are evaluated for each group of particles, as previously categorized. $\omega = \frac{v}{v_{th}}$ where $v_{th} = \left(\frac{2k_b T_x}{m}\right)^{1/2}$ and v is the particle velocity. The escape velocity v_{esc} is proportional in quadrature to another fundamental parameter, namely the Jeans parameter: $\lambda = \left(\frac{v_{esc}}{v_{th}}\right)^2$. The Jeans parameter then helps us determine the number density at a given altitude above the exobase r_x , for a given group of particles:

$$n(r) = n(r_x) e^{-\lambda_x - \lambda_0} \zeta(\lambda) \quad (1.2)$$

A full derivation of Chamberlain's theory can be found in Appendix A of [Leclercq \[2015\]](#).

Equations 1.1, 1.2 are valid only if the velocity distribution function of the particles at the exobase can be described as a Maxwell Boltzmann distribution, and if a clear exobase altitude can be defined. This is, for most known exospheres, a relatively improper assumption. Therefore, with advances in computation, numerical methods (often direct simulation Monte Carlo (DSMC), or test particle Monte Carlo) are used to evaluate the exospheric density. These methods are highly useful as they avoid the notion of the often unknown critical altitude, yet are still capable of describing any atomic or molecular species populating an exosphere. Given the large number of particles involved, this approach is often computationally expensive, yet the knowledge

¹The radius of this sphere is located when the primary's tidal force balances the satellite's own gravity:
 $r_H \simeq a_s \frac{M_p}{3m_s}^{1/3}$

gained from such a fundamental approach can be astoundingly powerful in that it permits one to calculate all of the macroscopic parameters along with average density $\langle n \rangle$, such as: energy dispersion (equivalent to a temperature) $\langle T \rangle$, and mean velocity $\langle \mathbf{v} \rangle$.

It is often said that the only light one will ever see from a star at night comes directly from its atmosphere since the mean free path of photons (Eqn. 1.3) in stellar interiors is quite small. Accordingly, the only light one generally sees from a planet is the reflection of star light off of the planetary surface or atmosphere. However, planets can radiate their own intrinsic light in a way, should there be magneto/radiative interactions occurring in the planetary atmosphere. Exospheres are often referred to by astronomers as 'coronas,' as they glow when the molecules present in the atmosphere are excited by photons, electrons, or other particle interactions. Tables 1.2 & 1.1 present a list of observed exospheres and their physical properties which have been distinguished over the decades. It can be seen that there is much to be explored for many of these bodies, as knowledge is lacking in the origin and evolution of these exospheres.

Two types of exospheres exist: (1) surface-boundary layer exospheres (SBE), and (2) atmosphere-boundary layer exospheres (c.f. Stern [1999]). The distinction depends on the very definition of an exosphere, when the atmosphere becomes so tenuous that the mean-free-path approaches the atmospheric scale height: $l_{mfp} \sim H$. Where the mean free path, of a particle of species i traversing through an atmosphere composed of species j with number density, n_i [cm^{-3}], the collisional cross-section σ_{ij} [cm^2], with species i is defined as:

$$l_{mfp} = \frac{1}{\sum_0^k n_i \sigma_{ij}} \quad (1.3)$$

The atmospheric scale height for a collisional atmosphere is: $H = \frac{k_b T}{mg}$, where T is the atmospheric temperature. The altitude at which the mean free path is equivalent to the atmospheric scale height, is defined as the exobase r_x . Above r_x , one is able to, in principle, fully neglect collisions. When $r_x = r_p$ or the exobase is at the surface, this constitutes a surface-bounded exosphere, often characterized by surface-exosphere interactions.

As different species have different scale heights, the dynamics of each species will eventually become collisionless above various altitudes. Therefore, the critical altitude r_x is species dependent. It should be noted that certain regions of an exosphere can be locally atmospheric-bounded or in certain cases only transiently. A transient

surface-bounded exosphere, experiences a collisional atmosphere solely over certain periods of time, otherwise collapsing to the surface. As an example, three particular Kuiper Belt Objects: Eris, 2007 OR 10, and Sedna experience transient SBEs of N_2 due to their large orbital eccentricities 0.434, 0.5, 0.86 respectively. As the bodies approach aphelion the atmosphere collapses for several years due to the low temperatures and low N_2 sublimation fluxes (Johnson et al. [2015]).

This thesis is dedicated to the investigation of *satellite* exospheres however, which can experience variability on much more rapid timescales. Ganymede's water-product exosphere for example will experience a moderately collisional atmosphere at noon (subsolar) due to the increased water sublimation fluxes. On the other hand, at midnight (antisolar) the atmosphere would be characterized as a strictly surface-bounded exosphere.

The exospheric transition Ganymede experiences, presents a vital, first question: what is the principal driver for exospheric variability on satellites? A satellite exosphere is of course fundamentally different than a planetary exosphere in that it is closely revolving around a planetary gravitational field. Coincidentally, all the known satellite exospheres in the solar system are also tidally-locked, and synchronized around its primary so that one rotation period is equivalent to one diurnal cycle. The diurnal period is thus equivalent to one satellite revolution about its primary, while the radiation source (the star) is fixed in space. This particular arrangement drives the exosphere to an asymmetric state in local time as we will explore for molecular oxygen on Europa and Ganymede.

The second question a satellite exosphere poses is, do the so-called inertial forces present in a rotating reference frame (centrifugal, Coriolis) influence the exospheric dynamics?

The above two questions address two phenomena I will refer to as *rotation-driven* in that it is the rotation of the exosphere coupled with the satellite surface, which is what drives inhomogeneities in the exosphere.

The final question is perhaps the most evident due to the observed fractures on several of the icy satellites: does the planet's gravitational field or tides [endogenically] influence the exosphere?

SBE	Species	n	T_x	λ	Sources
Europa	O ₂ , H ₂ O, H ₂ , O, H Na, K,	$2.5 \cdot 10^6$	135	4 - 59	Mag. Ion Sputtering, sublimation
Callisto	O ₂ , O, H ₂ O, H ₂	$1.2 \cdot 10^{10}$	165	4 - 69	Mag. Ion Sputtering
Mercury	H, He, Na, K, Ca, Mg	$4 \cdot 10^4$	617	7 - 41	Solar Wind Sputtering
Moon	H, He, Na, K, Ar, Ne	10^5	390	5-35	Solar Wind Sputtering
Rhea	O ₂ , CO ₂	10^4	99	8 - 11	Mag. Ion Sputtering, sublimation
Dione	O ₂ , CO ₂	10^4	95	5-7	Mag. Ion Sputtering, sublimation
Transiently SBE	Composition	n	T_x	λ	Sources
Ganymede	O ₂ , H ₂ O, H ₂ , O, H, Na, K,	10^8	152	7 - 107	Mag. Ion Sputtering; Sublimation
Eris	N ₂ , CH ₄	$< 1.7 \cdot 10^{11}$	42.5	43 - 76	Sublimation
2007 OR10	N ₂ , CH ₄	ND	31	13 - 22	Sublimation
Sedna	N ₂ , CH ₄	ND	30	8-14	Sublimation
Enceladus	H ₂ O	$3.3 \cdot 10^8$	74	0.83	Cryovolcanism , Sublimation

TABLE 1.1: **Surface-bounded exospheres.** Known species are listed, along with the average density of the exospheres. The maximum surface temperatures are provided along with the jeans escape parameter for a light species and a heavy species respectively. Jeans parameters for the icy Galilean satellites are evaluated for H₂-O₂; KBOs CH₄-N₂; Rhea & Dione for O₂ - CO₂; Moon: He-Ar; Mercury: He-Na. References for the various satellites are as follows. Europa: EGM; Callisto: [Kliore et al. \[2002\]](#); Mercury: MESSENGER [McClintock et al. \[2008\]](#); Enceladus ([Tenishev et al. \[2014\]](#); [Hansen et al. \[2006\]](#)). ND signifies that the predicted exosphere is not yet detected.

Exospheres	Species	r_p (r_\oplus)	r_x (r_p)	T_x [K]	λ_x
Io	SO ₂	0.29	1.27	2000	9.0
Mars	O	0.53	1.047	300	200
Venus	He	0.815	1.023	200	35
Earth	H, H ₂ , He, O , C, N	1.0	1.071	1000	130
Titan	H [‡] , H ₂ , N ₂ , CH ₄	0.404	1.58	160	45
Pluto	N ₂ , CH ₄ , HCN	0.186	1.44	70	34
Triton	N ₂ , CH ₄	0.21	1.69	100	23
MakeMake	N ₂ ? CH ₄ ?	0.11	—	—	9 - 13
Quaoar	CH ₄ , N ₂ ?	0.09	—	—	6 - 8

TABLE 1.2: **Atmospheric-bounded exospheres** in the solar system: terrestrial, KBOs, Io and Mars. Atmospheric parameters are largely unknown for Makemake & Quaoar, for the Jeans parameter at the exobase I provide a range depending on whether the exosphere is Pluto-like (colder) or Triton-like (warmer). [‡] Dandouras et al. 2008

By simulating the dynamics of planetary exospheres we can better probe the surface properties as well as unknown endogenic components without explicitly sampling the planetary body. With the limited data above we rely on Monte Carlo simulations (Chapter 2) accompanied with analytic models (Chapter 3 and 4) in the hope of providing predictions to future observers equipped with novel instrumentation capable of detecting tenuous species which have thus far evaded detection. I will provide a thorough analysis of one novel technology in the hope of advancing this overarching goal of understanding the global behavior of exospheres (Chapter 5).

I restrict our simulations and future instrumentation work in the interest of Gas-giant satellites, in the Solar System: Jupiter and its Galilean satellites. The Galilean satellites represent a unique planetary architecture, which should be abundant in the galaxy. With over 2000 + Extrasolar Giant Planets (EGPs) discovered it is certain that a portion of these exoplanets should have satellites. This dissertation therefore focuses on Jupiter and its Galilean satellite exospheres which can serve as an archetype of Gas-giant-satellite systems, and perhaps even a better analog to dwarf-star - planetary systems (e.g TRAPPIST-1). The dynamics discussed in chapters 2-4 may help observers seeking to detect the atmospheric signatures of extrasolar satellites.

I organize this dissertation by first answering the three questions posited above regarding the particular nature of a tidally-locked satellite exosphere. Answering these questions helps one understand the underlying global phenomena. In particular we examine these phenomena over an orbital time τ_{orb} , in the interest of highlighting observable atmospheric effects, which we demonstrate as being driven by the satellite's rotation in Chapter 2. This general phenomena generates strong atmospheric asymmetries for non-adsorbing, surface-bounded satellite exospheres (§2.1) where the exospheric lifetime approaches the orbital time $\tau_i \sim \tau_{orb}$. I validate this claim in both simulation and observation for Europa in Ch. 2.2.

Water, whether it is in the form of ice grains or vapor, may include trace constituents emanating (in the case of Europa) from the putative subsurface ocean. Therefore I seek to focus on water as well as its dissociative products H_2 and H , in the context of ocean world exospheres in Part II. Water in general, is a difficult species to observe. Ground-based observatories for example, suffer from the numerous telluric H_2O bands in the atmosphere making the often weak signals, extremely difficult to disentangle. Thus one must rely on new, more innovative observations and instrumentation to indicate its presence in satellite exospheres and resultingly advance our knowledge on these bodies. Part III then begins our discussion on how we can observe these exospheres via ground-based and in-situ instruments.

One set of species are of particular interest for Europa today, as there is increasing evidence of cryovolcanic activity. Interestingly, a few of these volcanic volatiles are

quite favorable to observations (e.g sodium due to its ability to fluoresce in the visible at 5990 and 5996 Å). I begin by reviewing the origin of sodium in Jupiter's magnetosphere as to set the stage for sodium production originated from Io's NaCl, as well as the potential for discerning the signatures of these *volcanic volatiles* in the sub-mm with the aid of ALMA. I discuss the origin of the volcanic volatiles due to the Laplace resonance around Jupiter, maintaining orbital eccentricity and therefore significant tidal heating capable of melting the satellite's interiors. This melting leads to volcanism which can populate Jupiter's magnetosphere and generate observable emission (Mendillo et al. [1990] ; Schneider and Trauger [1995]). Therefore, I also predict that even at enormous stellar distances, it should be possible to probe the presence of these volatiles in exoplanetary transmission spectra (Chapter 4.2). Ultimately a satellite exosphere, if escaping, will source the Hill sphere of the planet it orbits, and contribute to its atmosphere. This interplay between satellite and planet often results in a toroidal atmosphere which I believe provides the highest probability for extrasolar satellite detection today.

Lastly I focus on the future of in-situ technology and space exploration. At LATMOS I have been leading the development of a novel technology: a carbon nanotube electron gun (CNTeg), a cold cathode. I describe its utility in future space missions in the context of detecting tenuous exospheres in the Solar System where power efficiency is a critical issue. The detection methods discussed in Ch.4 and 5 are at the limits of current instrumentation and thus I hope the work presented in this dissertation will help in satellite exosphere detection in the coming decades.

Part I

Dynamics of Satellite Exospheres.

In this chapter, we seek to understand the critical role of rotation on tidally-locked satellite exospheres. We begin with an analytical approach to examine the problem more generally by solving a 1-D mass flux-conservation equation for the column density at each planetary longitude, over an orbital time. Upon integrating the column density over a half-hemisphere one can discern the magnitude of an 'atmospheric bulge' in local time when comparing day, night, dusk, or dawn hemispheres. We note that this investigation is considerably simplified when one works with a molecule which is generally non-escaping, non-adsorbing, and heavy as is the case for molecular oxygen. These conditions allow for the O_2 to rotate *with* the surface similar to a thin isothermal gas coupled to the surface temperature. We discuss the physical implication here.

2

Time-Dependent Atmospheric Bulges on Tidally-Locked Satellites

This section was submitted as an Icarus Note 2017

We demonstrate that solar heating of a rotating surface, coupled to a volatile, surface-bounded atmosphere, results in a permanent atmospheric bulge throughout the satellite's orbit. These types of atmospheric bulges have recently been observed via asymmetries in ultraviolet auroral emissions in the exospheres of the icy satellites Europa and Ganymede. The Hubble Space Telescope observations indicate that these satellites host unique, surface-bounded O₂ exospheres which bulge at dusk. We present an analytic model which solves 1-D mass conservation balancing a strongly thermally-dependent source with atmospheric loss, for a tidally-locked satellite on which the ballistic hop distance is much smaller than the satellite radius. We find that the key condition for a longitudinal atmospheric bulge shifted towards dusk is for the satellite to be rotating at a similar rate to the atmospheric loss rate.

2.1 Introduction

Recently, evidence has indicated that the near-surface, far-ultraviolet oxygen aurorae observed for decades at Europa and Ganymede (Hall et al. [1995]; Hall et al. [1998]) by the Hubble Space Telescope are indicative of neutral O₂ bulges which peak near dusk (Oza et al. [2017]; Leblanc et al. [2017a]; Roth et al. [2015]; McGrath et al. [2013]). These exospheres with atmospheric bulges, host *surface-bounded* molecular gases, often beneath $z < 1.25r_p$, where volatiles undergo frequent interactions with the surface such

that the hop distances are much less than the planetary radius, and the ballistic hop time is also much smaller than the lifetime of the volatile species $\tau_i \gg t_{hop}$. This permits the volatile to respond to the surface properties over a rotational period. A condition for the solar insolation to play an observable role in the exosphere is that the volatile thermally accommodates to the surface temperature. In this way, diurnal changes in the surface temperature, will not only result in a diurnal change in the production flux, but also in the *re-emission* flux.

O₂ on these bodies have a far different origin than on Earth. These satellites are covered in water ice and are embedded in gas giant magnetospheres. The magnetic fields accelerate charged particles to high energies bombarding and subsequently ejecting observable gas columns of O₂, H₂, H₂O, as well as other trace species depending on their concentrations in the ice. This process is often referred to as magnetospheric ion sputtering [Johnson et al. \[1982\]](#), and in the case of O₂ and H₂, the volatiles undergo a series of chemical reactions before they are emitted near thermal velocities, a process known as radiolysis ([Johnson 1990](#); Teolis et al. 2017B submitted). Thus, the products of radiolysis are expected to have a strong thermal dependence when initially ejected from the ice as well as on their absorption and reemission. In this way, radiolytically produced O₂ behaves similarly to a sublimation source. Sublimation-driven exospheres, such as that ion neighboring satellite Io, are of course strongly dependent on the surface temperature.

To better understand the mechanisms behind how the atmospheric bulge is consistently held in local time, we consider a general, sublimation-driven case where the random-walk diffusion length scale is negligible. The problem is further simplified by considering satellites tidally-locked to their planet, where the surface heating source is fixed in space and time, and the orbital frequency is equivalent to the rotation rate.

2.2 Atmospheric Bulge Model

Here we describe the atmospheric evolution of a tidally-locked satellite over position ϕ and time t , in terms of its gas column density, N .

In this analysis, we seek to understand the effect of satellite rotation rate Ω on generating an atmospheric bulge, sourced by a source. Therefore we start by presenting the case in which the diffusion time across the surface is much longer than the atmospheric lifetime and the ballistic hop time, such that the average thermal hop distance of the molecules is much less than the planetary radius.

Consider the reference frame of a synchronously rotating or tidally-locked satellite of mass m_s , radius r_s , about a planet of mass M_p , a distance a_s away, both orbiting a

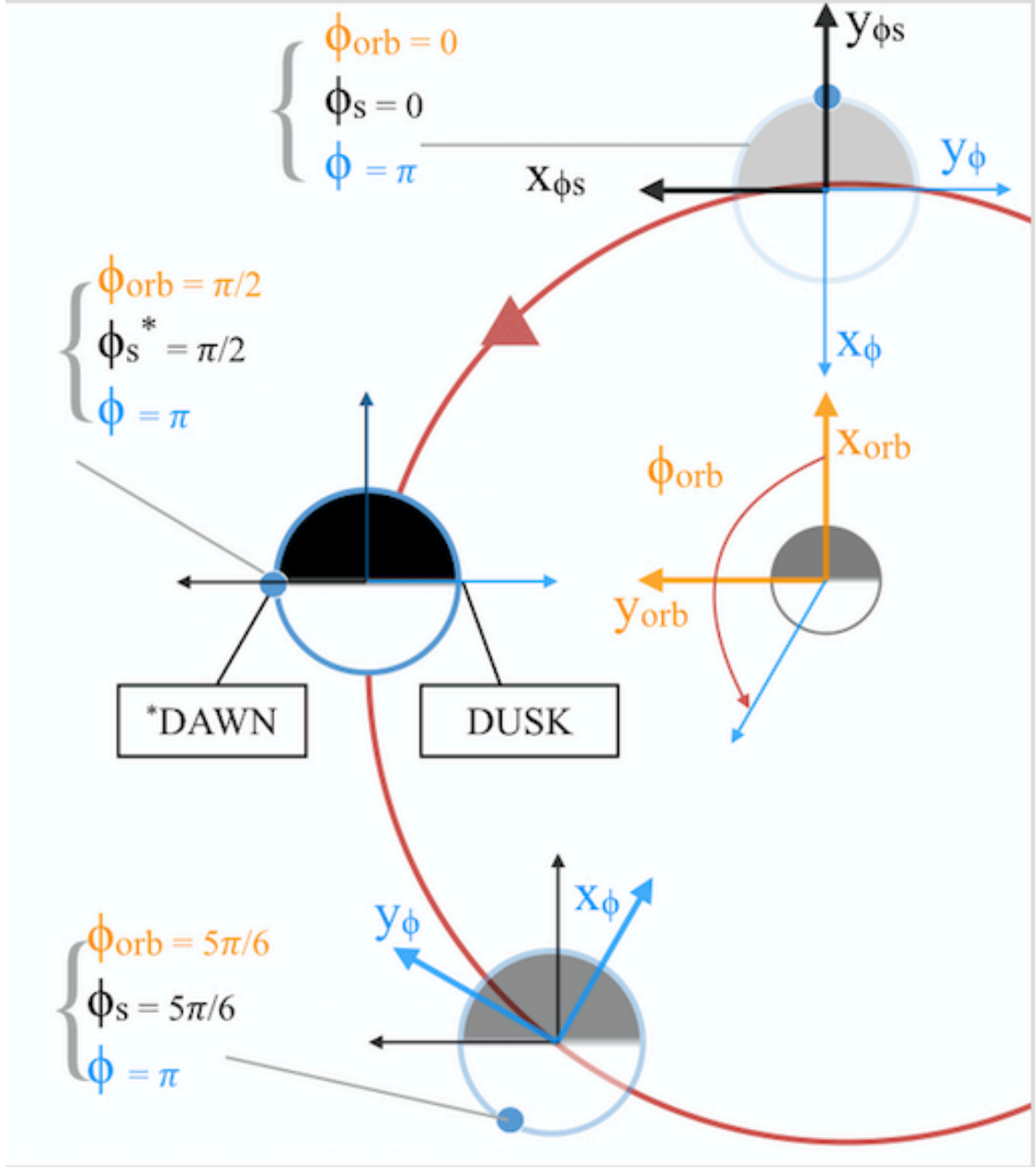


FIGURE 2.1: Satellite coordinate system for a planet and rotating satellite. The center body is the planet along with two orbital positions of the satellite depicted. Black vectors represent the fixed, observers frame, where y_{ϕ_s} in black indicates the incoming stellar radiation flux vector. ϕ_s is the anti-stellar insolation vector, defined as such in order to synchronize the two frames, where Dusk: $\phi_s = 3\pi/2$ and Dawn: $\phi_s = \pi/2$. Blue vectors represent the rotating, satellite frame where ϕ is the satellite longitude whose origin is the subplanetary point. We define the origin of the satellite system (blue circle) as $\phi_0 = \phi + \pi$ to effectively compare to observations such that the subobserver longitude is synchronized with the planetary longitude at midnight during satellite eclipse. As the satellite rotates over an arbitrary timescale Δt , the satellite will have rotated a $\Delta\phi_{obs} = \Omega\Delta t$.

non-variable distance a from the stellar primary. For a tidally-locked body the rotation rate or spin, is equivalent to the mean motion, such that $\Omega = n_s = (\frac{GM_p}{a_s^3})^{1/2}$, where the orbital period is $\tau_{orb} = \frac{\Omega}{2\pi}$. Figure 2.1 illustrates our equatorial coordinate system, where the stellar radiation flux is fixed and arrives from the bottom of the page, along

the black y_{ϕ_s} -axis. The inertial reference frame is therefore represented by the black vectors, dictating local time for the planet-satellite system which we define as an anti-stellar insolation vector ϕ_s where midnight corresponds to 0, and the subsolar point is at $\phi_s = \pi$. The sub-observer longitude ϕ_{orb} (orange axes) is the star-planet-satellite angle and keeps track of the satellite's rotation around the planet. It is also the longitude on the body with respect to the plasma ram along the corotation axis ϕ' (red). The satellite's rotational reference frame (blue axes) on the other hand, is defined as a planetocentric longitude measured counter-clockwise from its origin at the subplanetary point where $\phi = \phi' + \frac{\pi}{2}$. As our calculations will be integrated over time, we will find it useful to consider an origin synchronizing our reference frames. For example, if we begin by evaluating the anti-planetary point, $\phi = \pi$, represented by the blue dot at satellite eclipse: $\phi_{orb} = 0$, $\phi_s = 0$. In this way, the observer's clock at eclipse is synchronized with the satellite's clock at midnight local time. Therefore, in a time interval t , the satellite rotates Ωt about its own axis such that $\phi_{orb} = \Omega t$. The translation between inertial and non-inertial reference frames is then: $\phi_s = \phi_{orb} + \phi - \pi = \Omega t + \phi - \pi$. After a time $\frac{\tau_{orb}}{4}$, the satellite arrives at the *sunlit* leading hemisphere corresponding to $\phi_{orb} = \pi/2$ for the observer, and $\phi_s = \pi/2$ corresponding to dawn local time as indicated in Figure 2.1. If we consider rotating an additional $\tau_{orb}/6$, the fixed blue points on the satellite rotate towards subsolar. Here as in Figure 2.1: $\phi_s = 5\pi/6$. Lastly, not shown in the figure is the blue point reaching the *sunlit* trailing hemisphere orbital longitude where $\phi_{orb} = 3\pi/2$ and $\phi_s = 3\pi/2$ corresponding to dusk local time.

After a number of orbits, the atmosphere is assumed to reach approximate steady-state such that the atmospheric source flux, Φ , balances the atmospheric loss flux νN , where ν is the loss rate in s^{-1} , which in principle can depend on the longitudes ϕ and ϕ_s . We write the rate of change of the latitudinally-averaged atmospheric column as a simple balance between a temperature-dependent source rate and atmospheric loss, which permit us to follow the orbital evolution, using:

$$\frac{dN(\phi, t)}{dt} = \Phi(\phi, \phi_s) - \nu(\phi, \phi_s)N(\phi, t) \quad (2.1)$$

In principle the source rate and the loss rate can depend on the local properties of the plasma and the solar flux. For a satellite embedded in a planetary magnetosphere, like the Galilean satellites, ν is assumed to be constant. The expression is equivalent to expressions of latitudinally averaged transport written in terms of the atmospheric number density n and scale height H : $\frac{\partial N(\phi, t)}{\partial t} = -\Omega \frac{\partial}{\partial \phi} (nH)$ as described in earlier works by Hodges and Johnson [1968] valid for Jeans parameters $\lambda \gtrsim 15$, or as we state, $r_s \gg x_{hop}$. Equation 2.1, can be solved analytically, yielding a solution of the form:

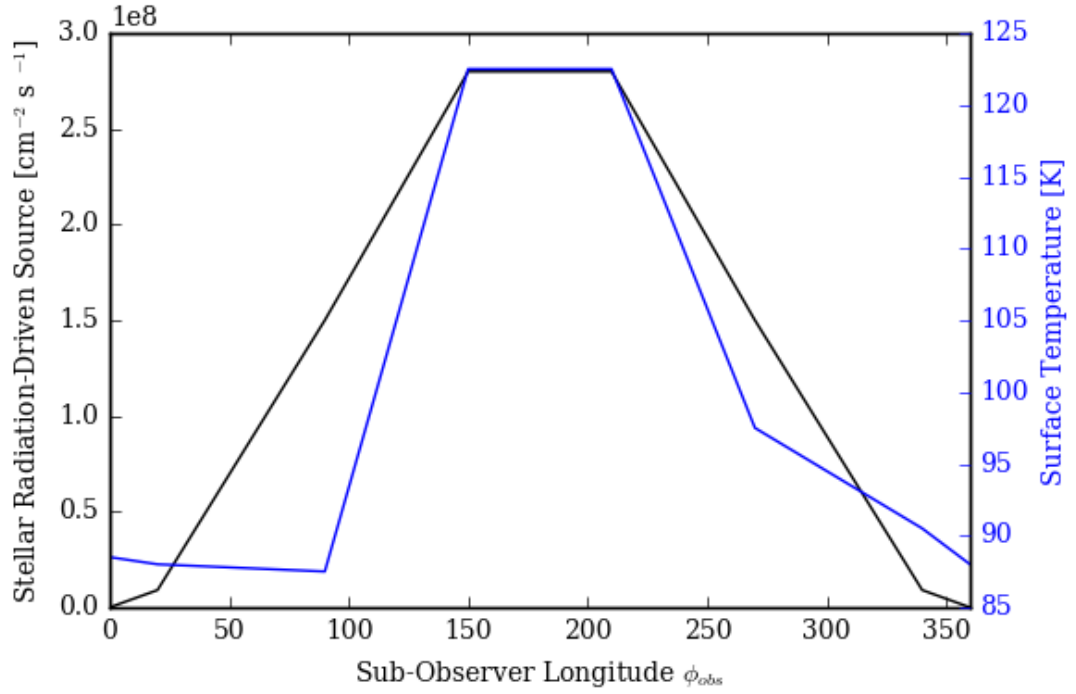


FIGURE 2.2: A simple temperature-dependent source rate treated as a stellar radiation-driven exosphere source flux Φ_T in our model. Values are scaled to the most recent simulations for Europa's O_2 exosphere $\Phi_0 = 3 \cdot 10^8 \text{ O}_2 \text{ cm}^{-2} \text{ s}^{-1}$, evaluated at the antijovian point, beginning at $\phi_{orb} = 0$, the origin of our planet-satellite system. Surface temperatures are results from the thermal model employed in [Oza et al. \[2017\]](#), where albedo and thermal inertia effects are included.

$$N(\phi, t) = \exp(-\nu t) \left(\int_0^t \exp(\nu t') \Phi(\phi, \phi_s) dt' + N(\phi)_0 \right) \quad (2.2)$$

Therefore, the radial column density over position and time is determined by the functional form of the source, Φ . The presence of an atmospheric bulge is indicated by evaluating N at the dusk and dawn terminators ($\phi_s = 3\pi/2; \pi/2$ respectively), and computing the ratio of column densities: R . This ratio gives the latitudinally averaged asymmetry expected for a near-surface atmosphere coupled to a rotating surface subject to time-dependent solar insolation over its orbit. $R > 1$ corresponds to a bulge at dusk assumed in these thin atmospheres. It is directly related to the ratio of the dusk-over-dawn *auroral* emissions, as confirmed by Monte Carlo simulations at Europa & Ganymede as discussed. In principle, a near-surface atmospheric bulge for any species then, can be discerned by near-surface auroral asymmetries at a given wavelength λ . For a thin atmosphere, e^- -impacted auroral intensity for instance, depends on the electron density n_e , the emission rate coefficient $\langle \sigma_\lambda v \rangle$, and of course the neutral column N being impacted (Eqn. 2.2), so that: $I_\lambda \sim n_e \langle \sigma_\lambda v \rangle N$. As the remotely observed line-of-sight (LOS) emissions uniquely probe the sunlit

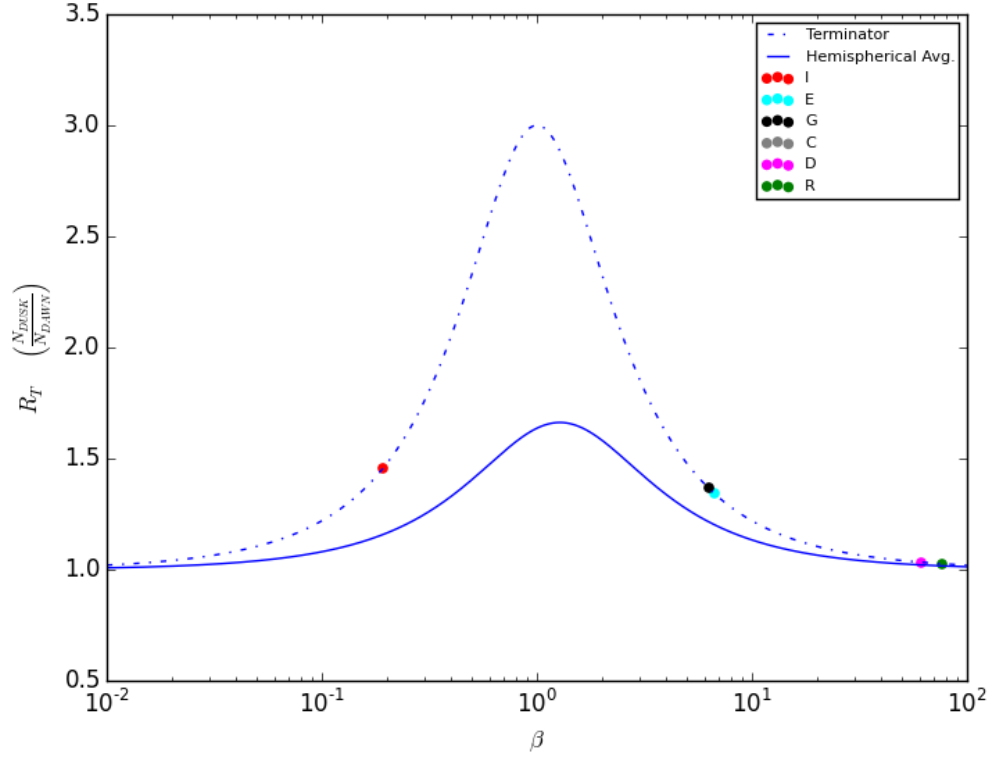


FIGURE 2.3: Dusk-over-dawn asymmetry ratio, R , versus $\beta = \Omega/\nu$. Ratios are determined by known orbital periods and estimated neutrals lifetimes. It is seen that if $\Omega \sim \nu$ the asymmetry is maximum. The dash-dotted blue line represents a possible upper limit to the radiation-driven dusk-over-dawn asymmetry, as it is computed at the terminator following Eqn. 2.7. The small circles represent various satellites in the solar system. Red, cyan, black, and gray are the Galilean satellites (Io, Europa, Ganymede, Callisto respectively). The magenta and green points are the Saturnian satellites Dione and Rhea respectively. The solid blue line is a hemispherical average of the radiation-driven dusk-over-dawn asymmetry; more representative of the observed asymmetry.

hemispheres, the direct near-surface aurorae-exosphere comparison requires an average over the hemispheres. We therefore compute the hemispherically averaged ratio, $\langle R \rangle$, in which the net emission from the dusk hemisphere is divided by the net emission from the dawn hemisphere. The average ratio is calculated by integrating N from Eqn. 2.2 over a range of longitudes $d\phi_s$, effectively averaging the columns across a *solar* longitudinal region of $\phi_s \sim \pi/2$ across each hemisphere. Integrating over the solar dusk hemisphere: $\phi_s = \pi \rightarrow 3\pi/2$, yields $\langle N_{DUSK} \rangle$, solar dawn hemisphere: $\phi_s = \pi \rightarrow \pi/2$ yields $\langle N_{DAWN} \rangle$.

$$\langle R_{Aur} \rangle \sim \frac{\langle I_{DUSK} \rangle}{\langle I_{DAWN} \rangle} \sim \frac{\langle N_{DUSK} \rangle}{\langle N_{DAWN} \rangle} \quad (2.3)$$

Apart from *in-situ* observations e.g Rhea and Dione's O_2 exospheres by Cassini's

INMS [Teolis and Waite \[2016\]](#), the aurorae-exosphere linkd is the only way to probe asymmetries in satellite exospheres. Below we present three source functions corresponding to three simple scenarios that might produce a satellite atmosphere. For each source function we derive the column density as a function of ϕ and t , computing R , the dusk-over-dawn, column density ratio, and lastly the hemispherically averaged ratio $\langle R \rangle = \frac{\langle N_{DUSK} \rangle}{\langle N_{DAWN} \rangle}$. Comparing $\langle R \rangle$ with the auroral observations, helps in gaining insight on how the atmospheric bulge may evolve over the satellite's orbit.

2.2.1 Stellar Radiation-Driven Source

We first describe a source solely dependent on the solar insolation, such as sublimation. We assume the loss rate is constant to 1st order. As an example, we consider a simple sublimation-like source that depends solely on ϕ_s , and peaks at noon as can be seen in [Figure 2.2](#):

$$\Phi_T(\phi_s) = \frac{\Phi_0}{2} (1 - \cos(\phi_s)) \quad (2.4)$$

Substituting and integrating defining by defining the variables $\beta = \Omega/\nu$ and $\alpha = \phi - \pi$, the solution is then:

$$N_T(\phi, t) = \frac{\Phi_0}{2\nu} ([1 - \exp(-\nu t)] - N_{rot}(\phi_s, t)) \quad (2.5)$$

where $N_{rot}(\phi_s, t)$ is equal to: $(1 + \beta^2)^{-1} ([\cos(\phi_s) + \beta \sin(\phi_s)] - [\cos(\alpha) + \beta \sin(\alpha)] \exp(-\nu t))$. It is seen that as $t \rightarrow \infty$, when steady-state is reached, the column density depends solely on the solar insolation angle ϕ_s . The steady state solution is then:

$$N_T(\phi) = \frac{\Phi_0}{2\nu} (1 - (1 + \beta^2)^{-1} [\cos(\phi_s) + \beta \sin(\phi_s)]) \quad (2.6)$$

In this approximation the maximum column density, the atmospheric bulge, occurs past noon. This is simply due to the rotation of the source peak towards dusk. The ratio R_T , of the latitudinally averaged, dusk-over-dawn sublimation column densities evaluated at the terminator is:

$$R_T \sim \frac{1 + \beta + \beta^2}{1 - \beta + \beta^2}. \quad (2.7)$$

corresponding to the dashed blue curve as shown in [Figure 2.3](#). Therefore it is seen that for such a source with constant loss rate, R_T depends only on the ratio β and is

always greater than unity, indicating a column density enhancement at the dusk terminator over the dawn terminator.

R_T when averaged over a half-hemisphere gives dusk-over-dawn LOS column densities, via the following relation:

$$\langle R_T \rangle = \frac{1 + \frac{2}{\pi}(\beta + 1) + \beta^2}{1 - \frac{2}{\pi}(x\beta - 1) + \beta^2} \quad (2.8)$$

The solid blue curve in Figure 2.3, plots the β dependence on $\langle R_T \rangle$ with values in Table 2.1.

On each of these curves we indicate as colored dots the value of β for a number of planetary satellites using the data in Table 2.1. It can be seen that since $0.1 < \beta < 10$, for Io, Europa, and Ganymede, these surface-bounded atmospheres should possess atmospheric bulges which are at least 50 % thicker at dusk than at dawn. At Saturn, the loss rates are roughly a factor of 10 smaller (Table 3; [Teolis and Waite \[2016\]](#)) therefore a tidally-locked satellite with a similar orbital period will have a much larger β . This eliminates the dusk-over-dawn asymmetry, but a subsolar atmospheric bulge is observed. Dione, with a 66 hour orbital period has $\beta \sim 61$ similar to Rhea, where $\beta \sim 77$ and only a noon bulge is present.

S	τ_{orb} [hrs]	τ_i [hrs] (τ_{orb})	β	R_i
I	42.5	13.0 (0.031)	0.193	1.4559
E	85	90 (1.06)	6.78	1.337
G	172	170 (1.0)	6.28	1.367
C	408	681 (1.67)	4357	1.00
D	66	604 (9.2)	61	1.03
R	108	1262 (12)	77	1.02

TABLE 2.1: **Atmospheric parameters for all known surface-bounded satellite exospheres: Io (I), Europa (E), and Ganymede (G).** The electron number density used for Europa and Ganymede’s environments is $70 \text{ e}^- \text{ cm}^{-3}$ as in [Marconi \[2007\]](#). Dione & Rhea loss rates are derived from Table 3 in [Teolis and Waite \[2016\]](#). The loss rate at Callisto is assumed to be uniquely due to electron ionization [[Vorbuerger et al., 2015](#)].

2.2.2 Magnetospherically-Driven Source

Satellite exospheres embedded in large planetary magnetospheres are often generated by plasma flow along the satellite’s orbit. The exosphere source in this case, is depends on the satellite corotation direction and the flow speed depends on the rotation rate of the planetary magnetosphere. Since the plasma has a thermal component and the

particles have gyromotion determined by their energy and the local fields, it is difficult to determine whether the exosphere source peaks at plasma ram or if it is more symmetric.

The plasma source is a function of the angle from the corotation direction at $\phi = \pi/2$ (corresponding also to the origin of standard Cartesian coordinate systems for satellites i.e. Xphi0), assumed for simplicity as:

$$\Phi(\phi)_{mag} = \frac{\Phi_0}{2} (1 + \sin(\phi)) \quad (2.9)$$

As the planetary longitude is independent of time, the integration yields an expression with no rotational term:

$$N_{mag}(\phi) = \frac{\Phi(\phi)_{mag}}{\nu} ([1 - \exp(-\nu t)]) \quad (2.10)$$

When we evaluate at dusk and dawn over the orbit $\phi_s = 3\pi/2, \pi/2$, we find the dusk-over-dawn ratio oscillates over the orbit as $R_{mag} = \frac{1+\sin(\phi_{s,dusk})}{1+\sin(\phi_{s,dawn})}$, from a dawn enhancement $R_{mag} \sim 0.2$ to a dusk enhancement $R_{mag} \sim 4.5$. When latitudinally averaging over the orbit, $\langle R_{mag} \rangle \sim 1$. Thus a trailing hemisphere plasma source is not responsible for generating the observed exospheric asymmetries.

2.2.3 Stellar Radiation & Magnetosphere-Driven Source

What is most representative of Europa and Ganymede's O₂ is the above trailing hemisphere source $\Phi(\phi)_{mag}$ coupled with a thermal dependence included as a temperature-enhancement factor: $f(\phi_s) = 1 + [1 + \cos(\phi_s - \pi)]/2 = 1 + \frac{\Phi_T}{\Phi_0}$, following the dependence from Eqn. 2.4. The enhancement can be included in the source rate as: $\Phi(\phi, \phi_s)_{Tmag} = \Phi(\phi)_{mag} * f(\phi_s)$, approximated here as:

$$\Phi(\phi, \phi_s)_{Tmag} = \frac{\Phi_0}{2} (1 + \sin(\phi)) * [3 - \cos(\phi_s)]/2 \quad (2.11)$$

The resulting steady-state column employing the same substitutions as earlier is :

$$N_{Tmag}(\phi) = \frac{\Phi(\phi)_{mag}}{2\nu} \left(3 - \frac{1}{1 + \beta^2} (\cos(\phi_s) + \beta \sin(\phi_s)) \right) \quad (2.12)$$

when differentiating the above expression 2.12 one finds that the maximum and minimum column are offset from noon local time, by $\tan^{-1}(\beta)$. For Europa and

Ganymede, with β values near 2π , this shift corresponds to $\sim 81^\circ$. In satellite local time, the column increases from its minimum near dawn, $\sim 6\text{h}30$, to its maximum column near dusk, $\sim 17\text{h}30$. One can estimate the magnitude of this dusk-over-dawn asymmetry as with the other cases at the terminator and as a hemispherical average:

$$R_{Tmag} \frac{1 + \beta/3 + \beta^2}{1 - \beta/3 + \beta^2} \quad (2.13)$$

Here, like in the previous magnetospherically-driven case, R varies over the orbit from the sunlit leading hemisphere to the sunlit trailing hemisphere.

2.3 Orbital Evolution of Atmospheric Bulges

Now that we derived analytical expressions for the expected column densities due to the two principal energy sources of stellar radiation and magnetospheric ions in isolation, as well as their combined effect, we can evaluate how the column varies over the orbit for each case.

Thus, to better understand the orbital evolution we tabulate R for four orbital positions with respect to the observer: eclipse, sunlit leading, subsolar, and sunlit trailing. Table 2.2 shows these diurnal variations for the above three cases: R_T , R_{mag} , and R_{TMag} , starting first with Europa.

2.3.1 Europa's O_2

To date, observations of Europa's near-surface oxygen aurorae have provided the most complete orbital observations of any satellite exosphere. Furthermore, Europa fortuitously hosts a molecular oxygen exosphere which has a lifetime approximately equal to the diurnal period, a timescale which greatly helps identify new phenomena at Europa.

Figure 2.4 therefore plots the values in Table 2.2, to illustrate the orbital evolution observed and simulated for Europa. We plot our three cases, along with an additional 'T-enhanced' case (blue dotted line where $f(\phi_s) \times 3$) to further emphasize the role of the temperature dependence in boosting the dusk-over-dawn asymmetries as was already demonstrated by the first case.

Thus it is seen, that a fixed, energy source in space, driving temperature-dependent exospheric production over an orbital period, is the principal driver for the dusk-over-dawn asymmetry and atmospheric bulge at dusk. Table 2.2 and Figure 2.4

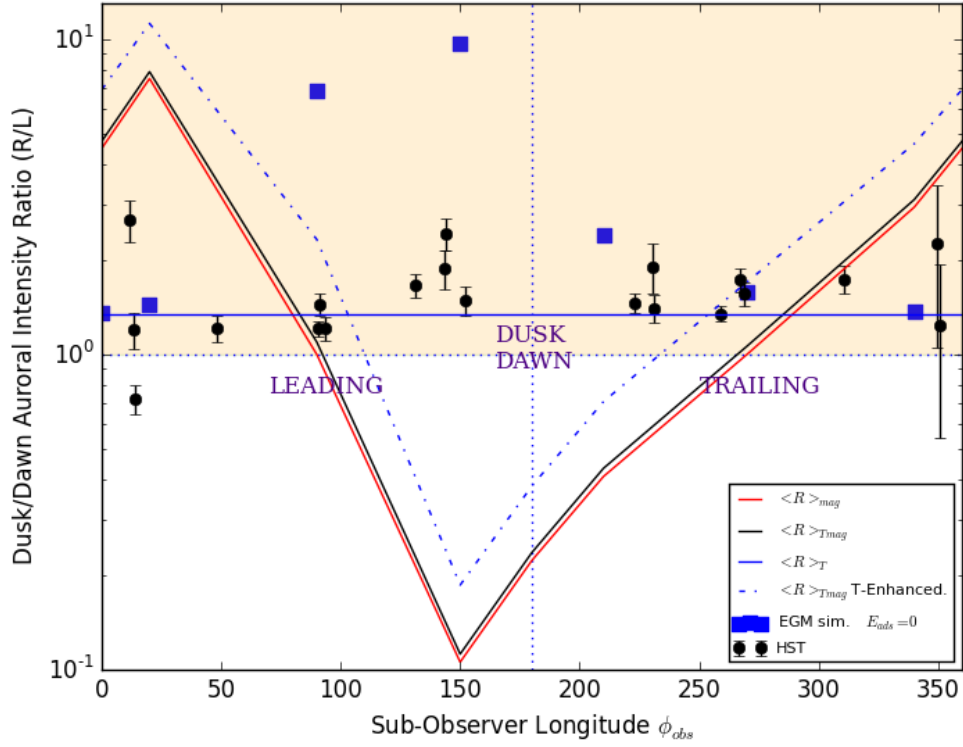


FIGURE 2.4: Average dusk-over-dawn asymmetry ratio, $\langle R \rangle$, versus ϕ_{orb} for the magnetospherically-driven and temperature-dependent magnetospherically driven sources as indicated by $\langle R \rangle_{mag}$ and $\langle R \rangle_{Tmag}$ respectively. The blue squares are Monte Carlo simulations from Oza et al. [2017] indicated a non-adsorbing O₂ population. The black squares are the dusk-over-dawn oxygen aurorae data by HST. The black dotted line represents a temperature-enhanced case where we triple the temperature enhancement factor $f(\phi_s)$ to confirm the increase in asymmetry towards dusk.

emphasize how the orbital behavior over Europa's orbit is not easily understood. When examining the observed near-surface oxygen aurorae (black points) it would appear that most simple explanation of its orbital variability is one that does not vary. In our model, this would be an O₂ sublimation source (blue line) with a very little leading-trailing plasma asymmetry, which is difficult to argue for based on magnetospheric ion bombardment arguments (Cooper et al. [2001], Cassidy et al. [2013]). This hypothesis also requires an immediate temperature response on the radiolytic O₂ yield, which was observed to have a time-delay in the laboratory Teolis et al. [2005].

On the other hand, the Monte Carlo simulations may suggest an incomplete description of the source flux which may include a combination of second order effects. When examining the HST near-surface oxygen auroral data, accurate to $\sim 10\%$, the dusk-over-dawn asymmetry experiences a *minimum* at the sunlit leading hemisphere although the ratio rises by $\gtrsim 30\%$ just before the subsolar point. The EGM model

produces large values at the leading hemisphere partly due to the strong thermal dependence of the O_2 yield ($Y_T(T = 135K)/Y_L(T = 85K) = 5.3$), in that the large flux at the trailing hemisphere longitudes accumulates at the leading hemisphere longitudes, half an orbit later. As the large ratio is not observed it may be that the O_2 which accumulates near the sunlit leading hemisphere phases is strongly adsorbed on to regolith grains (described in detail in Section 4.2 Oza et al. [2017]). Another possible contributor to the mismatch in observations is O_2 migration as we discuss below.

PHASE	ϕ_{orb}	$R(T)_{EGM}$	$\langle R \rangle_{mag}$	$\langle R(T) \rangle_{Tmag}$	R_{HST}
TR	270	1.58	1.0	1.06	1.64 ± 0.14
ECL	0	1.35	4.5	4.8	$1.73 \pm 0.7 ; 1.53 \pm 0.2$
L	90	6.87	1.0	1.09	1.29 ± 0.1
S	180	6.06	0.22	0.24	$1.92 \rightarrow 1.57 \pm 0.2$

TABLE 2.2: Magnitude of atmospheric O_2 bulges on Europa, calculated as hemispherically averaged column-density ratios $\langle R \rangle \sim N_{Dusk}/N_{Dawn}$ over the four major orbital phases: sunlit trailing, eclipse, sunlit leading, and subsolar. The fixed sublimation source maintains a constant dusk-over-dawn asymmetry of: $R_T = 1.34$ for all orbital longitudes. The four R columns represent the latter two magnetospheric plasma cases in section §2.2, and 2,3. The first column is the EGM output of Oza et al. [2017] for a non-adsorbing, thermally-dependent O_2 case. The final column is the average auroral intensity ratio, I_{Dusk}/I_{Dawn} , observed by HST at 1356 Å indicative of the exospheric asymmetry. The HST eclipse values are averaged around a $\sim 23^\circ$ interval in orbital longitude, whereas the subsolar values are averaged around a larger $\sim 100^\circ$ interval.

For these latter two cases we provide pre and post transit values.

2.3.2 Ganymede's O₂

The picture presented is of course over simplified, as it does not count for O₂ motion relative to the surface. Evidence of O₂ motion has been simulated, and is strongly supported in the case of Ganymede, where O₂ is produced at the poles, yet half of an orbit later, the O₂ is found to have apparently migrated towards the equator (Fig. 2.5 also see Leblanc et al. [2017a]).

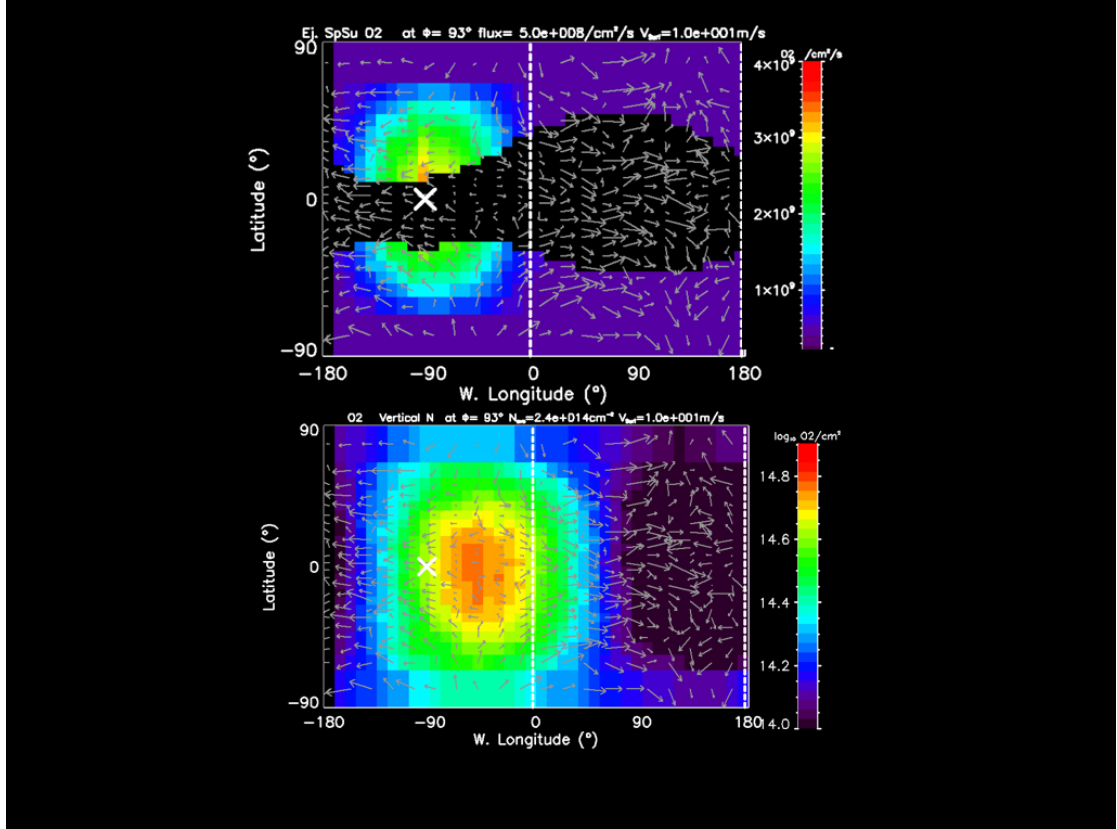


FIGURE 2.5: Top panel: Radiolytic O₂ production flux at Ganymede's poles at $\phi_{orb} = 90$. Bottom panel: Column density of O₂ demonstrating the *equatorial* atmospheric bulge at the same longitude implying downwards, equatorial diffusion as described in the text.

This latitudinal motion is due to the centrifugal force. If we first assume the O₂ is stationary with respect to Europa's surface, so that it has an orbital velocity equivalent to Europa's $v_{orb} \sim 32 \text{ m/s}$, we can compare this velocity to the O₂ ejection velocity $v_{O_2} \sim 100 \text{ m/s}$ to get an idea of the magnitude of the downwards, latitudinal centrifugal force. If we consider the forces on an O₂ particle (gravity and centrifugal), we have:

$$m\Omega^2 r \sin\theta = -mg \frac{1}{r} \frac{dr}{d\theta} \quad (2.14)$$

where $m\Omega^2 r$ is the latitudinal component of the centrifugal force, and $\frac{1}{r} \frac{dr}{d\theta}$ gives the gravitational gradient across the latitude θ in question.

Solving then, for the effective latitudinal velocity $v_\theta = \frac{dr}{d\theta}$, we find:

$$\frac{dr}{d\theta} = \frac{\Omega^2 r^2 \sin\theta}{g} \sim \frac{v_{orb}^2}{g} \quad (2.15)$$

It can be seen that comparing the orbital and ejection velocities scales to this downwards, 'flattening' component as the thermal ejection velocity is $v_{ej} = (\frac{2k_b T}{m})^{1/2}$. If we take the ram day temperature of 135 K and the ram night temperature of 85K, we find that the ratio between v_{orb}/v_{ej} increases by 20% during the leading hemisphere phases, suggesting a stronger latitudinal centrifugal force, as our simulation maps demonstrate for Europa and Ganymede. The implication of this is an equatorial atmosphere, or an atmospheric ring as was observed at Io ([Roth et al. \[2011\]](#)). This phenomena is most apparent at Io since its SO₂ exosphere is sublimation-driven [Tsang et al. \[2016\]](#), in that the warmer equatorial regions should result in a thicker column as inferred from the aurorae. Based on Io experiencing twice the centrifugal acceleration than Europa, its equatorial column density should be even higher than that predicted by equator-pole temperature differences alone. While the centrifugal acceleration does not yet explain the Hubble data at Europa, it provides a concrete explanation for the leading/trailing exospheric asymmetry over Europa and Ganymede's orbit. Moreover, the atmospheric bulges we have discussed in this work not only peak near dusk, but also near the equator as was also confirmed in our 3D Monte Carlo simulations.

2.4 Conclusion & Summary

We have provided a simple analytic model to consider the effect of time-dependent solar heating on a tidally locked satellite exosphere in which the exospheric species is non-adsorbing, non-escaping, and closely follow the rotation of the satellite surface. Our results demonstrate that, to first order in the most simple scenario, a satellite naturally generates a dusk over dawn asymmetry, or atmospheric bulge, if the exospheric source has a thermal dependence. The magnitude and extent of the bulge will depend on the thermal source and how much faster or slower the satellite is rotating with respect to the exospheric lifetime. If the satellite is rotating at the same rate as it is losing its exosphere, the dusk over dawn asymmetry is a maximum. In the formalism presented above, this occurs when $\beta = \Omega/\nu$ is at unity.

In this work we ignored lateral transport for simplicity, and assumed the column is synchronized with the surface, this proves to be useful for demonstrating that these types of exospheres are to first order, longitudinally static. When comparing to recent, detailed Monte Carlo exosphere simulations of Europa and Ganymede's exospheres we

find that rotationally-driven mechanisms significantly influence the magnitude and positions of their atmospheric bulges. There is strong evidence of these additional effects occurring on the exosphere Io, where sub-mm observations indicate prograde SO₂ winds moving near 100m/s (Mouillet et al. [2008]), on the order of thermal migration velocities for O₂ at Europa and Ganymede. Leblanc et al. [2017a] showed that an atmospheric O₂ bulge at Ganymede requires latitudinal O₂ transport, most likely due to the horizontal centrifugal force. These considerations are of interest as there is also evidence of trapped O₂ in the ice (Spencer et al. [1995] ; Spencer and Calvin [2002]) and future missions would like to characterize the oxidation rates into the ocean (Hand et al. [2006]; Vance et al. [2016]). Adsorption on to regolith grains is critical in assessing the location of the atmospheric bulge for strongly adsorbing species such as Lunar Ar or sodium at Mercury and Europa (Cassidy et al. [2016]; Leblanc et al. [2005]). For instance, Argon is destroyed during the day by photoionization, and is adsorbed at night building a reservoir which is ejected as soon as it rotates into sunlight again. Thus there is a *dawn-over-dusk* enhancement as observed (Hodges 1974).

O₂ interactions with water ice at $T \sim 100K$ are difficult to measure in the laboratory, however comparing HST observations, 3D Monte Carlo simulations, and simple analytic models, may help illuminate the dominant mechanisms underlying satellite exosphere transport. For instance, mitigating the steep thermal dependence of O₂ in our 3D Monte Carlo simulations, actually reduced R . The analytical model presented in this work also confirms that reducing the thermal, stellar radiation-driven source, reduces the dusk-over-dawn asymmetry suggesting it as the principal driver. This also implies that at least at Europa, prompt chemistry may dominate over late chemistry effects, contrary to what has been suggested by the O₂ laboratory data as reported in Teolis et al. 2017B (submitted).

While the mechanism that generates the dusk-over-dawn asymmetry has been identified, namely radiation-driven production, a good match between the *orbital* observations and simulations has still not be found. Mitigating the thermal dependence and possible O₂ adsorption in the surface ice ameliorates the orbital asymmetry only slightly. While our analytic model is far from comprehensive, the goal is to highlight and isolate the influence of time-dependent surface heating for satellite exospheres. Thus, it appears that the assumptions on the magnetospherically-driven source may need to be reexamined. Lastly, O₂ migration may play a larger role than previously thought, affecting the precise location of these atmospheric bulges modeled in this work.

2.5 Dusk Over Dawn Molecular O₂ Asymmetry in Europa's Exosphere.

This section was submitted to the journal Icarus 2017

Europa's icy surface is constantly bombarded by ions trapped in the Jovian magnetosphere which sputter the surface, populating a water-product exosphere. Here we simulate Europa's exosphere using a ballistic 3-D Monte Carlo routine and find that the O₂ component, while global, is not homogeneous in Europa local time. The O₂ exosphere, formed primarily by Jovian magnetospheric ions ejecting ~ 5 kg/s of neutrals from the water ice regolith, generating an orbit-averaged column density of $\sim 10^{14}$ O₂ cm⁻², preferentially accumulates towards Europa's dusk. This inhomogeneity persists and evolves throughout the satellite's orbit, implying a diurnal cycle of the exosphere, recently observed during a Hubble Space Telescope (HST) oxygen aurorae campaign [Roth et al., 2015]. We conclude that the consistently observed 50% dusk-over-dawn increase in far ultraviolet (FUV) auroral emission is principally driven by Europa's O₂ production, subject to rotation. Including the effect of rotation on Europa's collisionless O₂ exosphere results in a near-surface O₂ atmospheric bulge consistently maintained at dusk throughout Europa's orbit. This diurnal, exospheric O₂ cycle builds the O₂ column from transit to eclipse, while the trailing hemisphere source is illuminated. From eclipse to transit, the e⁻-impact loss rate slightly overwhelms the quiesced O₂ production rate. Since Europa's diurnal timescale is fortuitously comparable to the O₂ lifetime, the dusk bulge is maintained throughout Europa's orbit. When comparing HST observations to simulations, we find the tightly coupled O₂ is likely influenced by Europa's non-uniform surface composition. Lastly, the extended nature of the observed aurorae is indicative of ongoing plasma-driven expansion of the near-surface O₂. Remarkably, the behavior of the near-surface O₂ exosphere, as suggested by the observations of the FUV oxygen aurorae, acts as a tracer for the physical processes occurring in Europa's icy regolith as well as its interaction with ions or other exospheric species.

2.6 Introduction

Europa's molecular oxygen exosphere is of keen interest as it has been suggested to be a possible source of ~ 0.1 - 100 kg/s of O₂ (Johnson et al., 2003 ; Hand et al., 2007; Greenberg, 2010) to Europa's putative saltwater ocean, thought to have a chemistry analogous to Earth's oceans [Vance et al., 2016]. This range of oceanic source rates can in principle be connected to the production and dynamics of the oxygen exosphere,

which we seek to understand in this work. The presence of such a molecular oxygen exosphere has long been predicted based on laboratory experiments (Brown et al., 1982; Johnson et al., 1982) since the Voyager spacecraft confirmed the presence of energetic ions trapped in the Jovian magnetosphere, with the dominant sulfur and oxygen ions sourced from Io's extreme volcanism [Peale et al., 1979a]. These energetic ions both electronically excite and impart significant momentum to the water molecules in Europa's surface triggering dissociation and chemistry [Johnson et al., 2013]. The energy released by these processes leads to ejection (sputtering) of water-products: primarily H_2O , H_2 , O_2 , and presumably also OH , H , and O . The first indirect observational evidence of the oxygen component of Europa's water exosphere was provided by Hubble Space Telescope (HST) spectral observations of far-ultraviolet (FUV) airglow radiation, hereafter aurorae, of excited atomic oxygen (O I) lines: $\lambda = 1356 \text{ \AA}$ and $\lambda = 1304 \text{ \AA}$, (Hall et al., 1995; Hall et al., 1998) during the Galileo spacecraft epoch. The FUV auroral intensity ratio, $i = \frac{I_{1356}}{I_{1304}} \sim 2$, suggested the presence of O_2 in accordance with the expected emission ratios due to e^- impact dissociation of O_2 .

The former HST observations and O_2 presence have been debated (e.g. Shemansky et al., 2014), however recent observations performed with the upgraded Space Telescope Imaging Spectrograph (STIS) with a spatial resolution between 71-95 km have since resolved the debate, Roth et al., 2015 hereafter R15, discerned that the ratio is variable in altitude and orbital longitude, due to a two-component oxygen O_2 & O exosphere:

(1) Near-surface O_2 exosphere below $\sim 1.25r_{Eu}$ (altitude, $z \lesssim 390\text{km}$), with an orbit-averaged auroral intensity ratio $\frac{I_{1356}}{I_{1304}}$ of $\langle i \rangle \sim 2$. It is unknown whether this near-surface component is collisional, and therefore an atmosphere, but for this work we will refer to the ensemble as an exosphere. R15 deduced the ratio $\langle i \rangle$, decreased by $\sim 10\%$ near the sunlit trailing hemisphere at phase angles near 270° , and increased by $\sim 15\%$ near the sunlit leading hemisphere at phase angles near 90° . While the 1356 \AA emission line is primarily excited by electron impact on O_2 and O , the emission at 1304 \AA additionally includes solar photons resonant scattering on O . Therefore, any variation of $\langle i \rangle$ can be interpreted as a variation between these two mechanisms: either due to a change in the electron impact rate or to a change in the O/O_2 mixing ratio. Disentangling these two emission processes is tough, as one requires a better knowledge of the plasma environment at Europa.

(2) Upper exosphere, or extended corona, beyond $\sim 1.25r_{Eu}$ with a more variable ratio of $\langle i \rangle \sim 0.5 - 1.0$. Table 2 in R15 shows the increasing presence of atomic oxygen with increasing altitude, where plasma-exosphere interactions appear to be far more significant than at the near-surface component.

The plasma behavior, governed by Jupiter’s magnetosphere, has been shown since the Voyager era to have local time asymmetries. At Io’s orbit ~ 5.9 Jovian radii, R_J , [Barbosa and Kivelson \[1983\]](#) deduced a dawn-to-dusk electric field in Jupiter’s magnetosphere, globally pushing charged particles and electrons in the Io-plasma torus towards dawn by $0.25R_J$. This explained the local time-variability in extreme ultraviolet (EUV) intensity observed by Voyager. While the plasma is highly variable at Europa’s orbit $\sim 9.4R_J$, this variability is independent of local time [Bagenal et al. \[2016\]](#). Moreover, various plasma models at Europa have indicated the O_2 production rate (and in turn the auroral emission) can vary by an order of magnitude based on the atmospheric source. While most numerical and laboratory analyses of the O_2 source have included the energetic ion component discussed above ([Shi et al., 1995](#); [Ip et al., 1998](#); [Cooper et al., 2001](#); [Plainaki et al., 2012](#); [Cassidy et al., 2013](#); [Milillo et al., 2016](#)) it was shown that the plasma could influence the neutrals via locally produced O_2^+ pick-up ions which impact the surface enhancing the sputtering and the O_2 production rate. MHD simulations by [Ip \[1996\]](#) ; [Ip et al. \[1998\]](#) suggested that pick-up O_2^+ ions could increase the O_2 production rate by a factor of 10, which was in disagreement with [Saur et al. \[1998\]](#) who found thermal ions ($\sim 100eV$) to dominate production as did [Eviatar et al. \[1985\]](#) and [Cassidy et al. \[2013\]](#). Agreement on the O_2 production rate has not yet been reached, due to the lack of information on Europa’s near-surface plasma conditions. For instance, the incident ion flux and its exospheric interaction, as recently modeled by [Lipatov et al. \[2010\]](#) and [Rubin et al. \[2015\]](#), has not been well constrained to date. In addition, charge-exchange reactions were shown to affect the neutral escape rate of O_2 ([Dols et al., 2016](#); [Lucchetti et al., 2016](#)). Based on a re-analysis of Voyager, Galileo, and Cassini data [Bagenal et al. \[2015\]](#) one can expect the radiolytically produced O_2 to vary by a factor of two.

We focus here on the near-surface molecular oxygen component to better understand the origin of the non-uniform neutral exosphere. We employ a ballistic, 3-D Monte Carlo Exosphere Global Model (EGM: §2.7). The EGM simulates Europa’s neutral exosphere as it orbits Jupiter in Europa’s rotating frame (EphiO). The neutral O_2 exosphere is governed by various physical processes illustrated in Fig. 2.6, driven principally by three external influences :

- §2.7.1 *Sputtering*: The bulk O_2 production is dependent on the surface temperature and occurs on Europa’s trailing hemisphere in a direction *against* the incident plasma ram, with flow direction denoted as $\hat{\mathbf{x}}$ in the rotational frame. Here we will assume that it is the primary source for all of the water-products ejected into Europa’s exosphere. The sink for the sputtered O_2 is assumed here to be primarily electron impact dissociation by Jupiter’s magnetospheric plasma.

- §2.7.2 *Surface Temperature*: The O_2 molecules are assumed to have a thermal dependence upon ejection from the surface. Therefore, the O_2 is coupled to the surface ice temperature so that thermal gradients across Europa's surface ice control the migration of the surface-bounded O_2 .
- §2.8.2.2 *Rotation*: Europa's 85-hour orbit requires a treatment of the inertial forces acting on the exosphere. Thus, our simulations are carried out in Europa's rotating reference frame where the Coriolis and centripetal forces act on the exospheric molecules under a gravitational potential dictated by both Europa and Jupiter's gravitational fields.

The importance of including rotation was partly motivated by the thorough orbital observations by R15, in which a dusk-over-dawn oxygen auroral asymmetry was noticed, that was not readily explained by any plasma or understood atmospheric asymmetry. Here, we show that the near-surface O_2 component of the exosphere, governs the observed FUV oxygen aurorae dusk-over-dawn asymmetry. The neutral dynamics which drive this asymmetry are described in section 2.8.1 and can be thought of as an orbital evolution of the O_2 exosphere driven by Europa's rotation (§2.8.2.2). We compare this orbital evolution of the simulated neutral component with the observed auroral components in section 2.9. Lastly, we comment on the possible expansion of the coronal component of the exosphere due to a combination of physical processes in section 2.9.4 .

2.7 Europa Exosphere Global Model

Europa's exosphere is simulated here by tracking representative particles in a rotating, non-inertial reference frame, in spherical coordinates (r, θ, ϕ) , centered on Europa and extending up to $\sim 15R_{Eu}$. We employ a parallelized Monte Carlo routine which is the core of the Exosphere Global Model (EGM). The numerical routines are similar to those described in detail in Turc et al. [2014] where the collisionless Boltzmann equation is solved for an imposed function distribution at the surface f_i , for a species i , a velocity v , and the acceleration due to gravity $\mathbf{g} = \frac{GM_{Eu}}{r^3}\mathbf{r}$, where $\mathbf{r} = \sqrt{x^2 + y^2 + z^2} \mathbf{e}_r$ following Marconi [2007]:

$$\frac{\partial f_i}{\partial t} + v \cdot \nabla f_i + g \nabla_v f_i = 0 \quad (2.16)$$

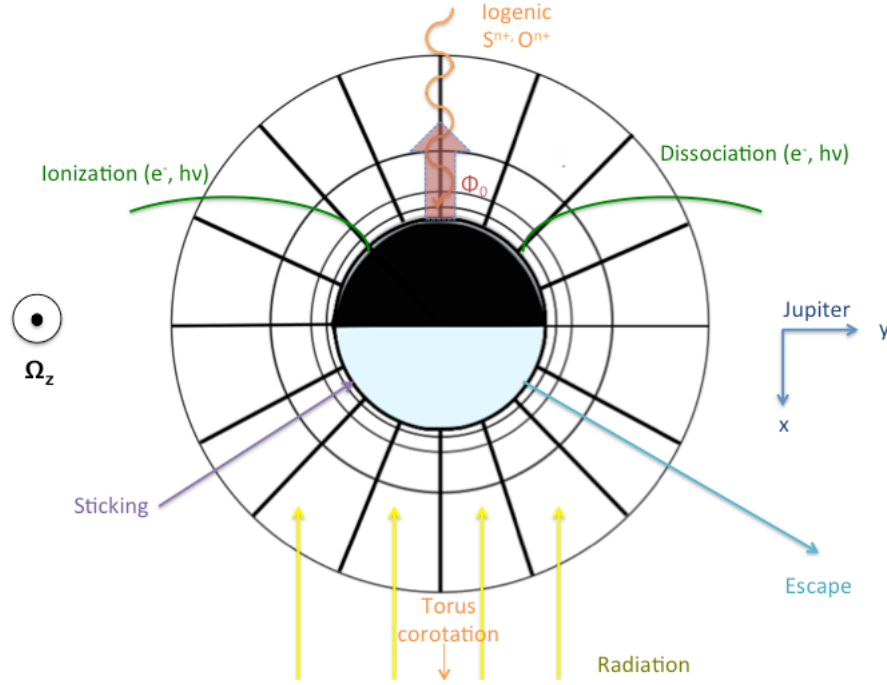


FIGURE 2.6: Top-down geometry of the simulation domain and associated physical processes at a sub-observer longitude of $\phi_{obs} = 90$ deg, corresponding to the sunlit leading hemisphere. The O_2 ejection flux due to sputtering, highlighted by the red vector Φ_0 , dominates ejection at the sub-plasma point against the ram direction of the plasma, following Equation 2.17. The ejected O_2 is assumed to be thermalized to the local surface temperature and is subject to dissociation and ionization. Adsorption, or sticking, is indicated in violet.

For a more detailed description of the EGM we refer the readers to Turc et al. [2014] and Section 2.2 of Leclercq [2015]. In the EGM we eject $\sim 10^7$ test particles from Europa's surface following known energy and angle distributions, $f(E, \theta)$ as described later (§2.7.1). These test particles are on ballistic (collisionless) trajectories, and can escape, stick, and be re-emitted from the surface depending on their properties as indicated in Fig. 2.6. The fate of ions is not considered although we discuss their influence on escape in section 2.9.4. In the case of O_2 , we track its interaction with the surface and account for electron and photon induced dissociation as well as ionization. Following dissociation, we also track the O formed. This procedure is carried out for approximately 5-6 orbits until a steady state exosphere of O_2 and O is achieved. Exospheric thermodynamic quantities are then computed based on the statistical weights of each test particle: $W_i = \Phi_i A_{cell} N_i dt$. Here Φ_i is the flux of ejected test particles, A_{cell} the area of the grid-cell, N_i is the number of time steps between each test particle ejection, and dt is the time step between two successive positions of the test-particles, chosen so that these two positions are within one cell or two nearby cells. After a sufficient number of time-steps to achieve approximate steady state, the average number density $\langle n \rangle$, temperature $\langle T \rangle$, and velocity $\langle v \rangle$ are calculated in each

cell on a spherical grid, and at seven orbital positions, ϕ_{obs} the sub-observer longitude of the satellite defined as $\phi_{obs} = 0^\circ$ when Europa is in eclipse behind Jupiter. In our analysis, we display the calculated densities at seven sub-observer longitudes: $\phi_{obs} = 0^\circ$, $\phi_{obs} = 20^\circ$, $\phi_{obs} = 90^\circ$ (sunlit leading), $\phi_{obs} = 150^\circ$, $\phi_{obs} = 210^\circ$, $\phi_{obs} = 270^\circ$ (sunlit trailing), and $\phi_{obs} = 340^\circ$. To improve statistics, these quantities are reconstructed on intervals spanning six degrees in orbital longitude, around each orbital position, corresponding to a total of 1.4 hours. Lastly, in section 2.9.1 we discuss the possibility of $O_2 + H_2O$ collisions in the near-surface atmosphere of Europa. When testing the importance of collisions we employ the same collisional scheme described for Ganymede's locally collisional atmosphere in [Leblanc et al. \[2017a\]](#) where a test particle, collision-pair approach was employed following [Bird \[1998\]](#), and cross-sections from [Lewkow and Kharchenko \[2014\]](#) were used.

2.7.1 Sputtering.

The O_2 exosphere is produced primarily by ions originating in the Io-plasma torus. The torus, composed predominantly of sulfur and oxygen ions trapped in Jupiter's magnetic field rotates, on average, seven times as fast as Europa, with the plasma primarily impacting Europa's trailing hemisphere in the corotation direction ($+\mathbf{x}$). Evidence for preferential bombardment of the trailing hemisphere by heavy ions has been observed by the Galileo Near-Infrared Mapping Spectrometer (NIMS) [[Carlson et al., 1999](#)]. We model the effective ion flux, Φ_{eff} , onto Europa's trailing hemisphere as diminishing with the corotation longitude, ϕ' , which is 90° out of phase with planetary West Longitude $\phi = 0$ at the subjovian point, such that $\phi' = \phi - \pi/2$ in Europa's reference frame. Following [[Leblanc et al., 2002](#)], $\phi' = 0$ is at the leading hemisphere in the direction of corotation :

$$\Phi_{eff}(\phi') = \frac{\Phi_i}{4\pi} \cos\left(\frac{1}{2}(\phi' - \pi)\right) \quad (2.17)$$

Molecules are ejected from the trailing surface by the energy and momentum deposited by the incident ion flux Φ_i in the grains of the water ice regolith. Here we use sputtering rates summarized in [Cassidy et al. \[2013\]](#) to discuss the fate of the oxygen component. In [Cassidy et al. \[2013\]](#) both the hot and thermal components of the incident plasma are accounted for as well as the regolith porosity, assuming the surface is primarily pure water ice. [Cassidy et al. \[2013\]](#) construct a spatially-dependent yield as the number of molecules ejected per incident ion based on [Fama et al. \[2008\]](#) and

Johnson et al. [2008]:

$$Y(T_0)_i = Y_0(1 + q_i e^{\frac{-0.06\text{eV}}{kT_0}}) \quad (2.18)$$

In Equation 2.18, T_0 is the local surface temperature, Y_0 the yield at low temperature, and q_i scales the temperature dependence of the yield for a species i . For the total yield given, in terms of equivalent water molecules, $q_{H_2O} = 200$. The globally averaged O_2 ejection rate also depends on the surface temperature of the ice, with $q_{O_2} = 1000$, empirically derived from extensive laboratory data described in (Teolis et al. [2010]; Teolis et al. [2017a]), is $10^{26} O_2 s^{-1}$, with an H_2 yield that is twice this rate. [Cassidy et al., 2013] then estimates a globally averaged sputtering rate: $2 \cdot 10^{27} H_2O s^{-1}$, of which the primary ejecta are H_2O , H_2 , O_2 with trace amounts of O , H , OH .

The energy distribution, $f(E)$, of the ejected particles is modeled according to the species in question. The H_2O , OH , O , and H are assumed to follow a water-ice sputtering distribution, based on the heavy ion ($E \sim keV$) sputtering of H_2O ice [Johnson, 1990]:

$$f(E)_{Sputt} \sim \frac{EU^x}{(E + U)^{2+x}} \quad (2.19)$$

where $x = 0.7$, and the effective surface binding energy $U = 0.052$ eV. The highly volatile molecular species O_2 and H_2 are produced by radiolysis. As the energetic ions penetrate the ice, they break bonds leading to chemistry and the temperature dependent formation of H_2 and O_2 . The initial ejection energy of O_2 (and H_2) can also be described by Equation 2.19 using $x = 0$ and $U = 0.015$ eV [Johnson, 1990]. We refer to this distribution as $f(E)_{U2}$ in this work. After the first ejection, those molecules returning to the surface can either react or are subsequently thermally desorbed so that their ejection speeds are roughly determined by a Maxwell Boltzmann (MB) distribution at the surface. The Maxwell Boltzmann speed distribution, accurate for a localized point is given by:

$$f_{MB}(v)dv = 4\pi \left(\frac{m}{2\pi k_b T_0} \right)^{3/2} v^2 \exp \left(\frac{-mv^2}{2k_b T_0} \right) dv \quad (2.20)$$

This distribution applies since the desorbed molecules undergo multiple interactions with the surface, which we model to be fast relative to the production of a new O_2 , and are thus in local thermodynamic equilibrium with the surface ice, with an average energy, $\frac{3}{2}k_b T_0$.

2.7.2 Surface Temperature

The effective temperature of the surface ice, T_0 is defined by radiative equilibrium. In our model, we consider a slab of ice with conductivity $\kappa_T = 2.52 \times 10^2 \text{ erg cm}^{-1} \text{ K}^{-1} \text{ s}^{-1}$ [Abramov and Spencer, 2008], and calculate the equilibrium temperature across the surface, over latitude θ and planetary longitude ϕ :

$$\frac{F_{\odot,1AU} (1 - A)}{R^2} \cos\theta \cos\phi = \varepsilon \sigma T_0^4 - \kappa_T \frac{\partial T}{\partial r} \quad (2.21)$$

$F_{\odot,1AU}$ is the total solar irradiance in $\text{erg s}^{-1} \text{ cm}^{-2}$ at 1 AU, R the orbital distance in AU, and σ the Stefan-Boltzmann constant. The albedo, A , is assumed to vary linearly with ϕ between 0.65 on the leading hemisphere and 0.45 on the trailing, approximating the most recent interpretation of Galileo PPR results [Rathbun et al., 2014]. The emissivity of the ice, ε , is set at 0.96. A small correction for the latent heat of sublimation is included [Abramov and Spencer, 2008]. Endogenic heatflow, as estimated by Spencer et al. [1999] with an upper limit of $5 \times 10^8 \text{ erg s}^{-1} \text{ cm}^{-2}$, is neglected in this work.

The temperature gradient at the surface, $\frac{\partial T}{\partial r}$ in the last term of Eqn. 2.21 is given by the one dimensional equation for heat conduction along a direction r that is *normal* to the surface:

$$\rho C_P \frac{\partial T}{\partial t} = \frac{\partial}{\partial r} \left(\kappa_T \frac{\partial T}{\partial r} \right) \quad (2.22)$$

where ρ is the mass density, taken as 0.92 g cm^{-3} , and the specific heat at constant pressure, C_p , is $1.96 \times 10^7 \text{ erg g}^{-1} \text{ K}^{-1}$ [Vance and Goodman, 2009]. Eq. 2.22 is solved with the aid of a [thermal routine](#) using the slab boundary method (Spencer et al. [1989]; Young [2017]). Forcing of solar insolation over a synodic day in late Feb. 2015 is determined in 2° increments of θ and ϕ using the `309.bsp kernel` provided by JPL. While this approach simplifies the variation of thermophysical parameters over the surface [Rathbun et al., 2010], it provides a basis for longitudinal asymmetries about the subsolar axis that result from the thermal inertia of the ice.

In Figure 2.7(a) we show the evolution of Europa's equatorial surface ice temperature along its orbit in panel A. The Figure 2.7(a) inlet is a zoom of the eclipse region where Europa's temperature drops by $\sim 30 \text{ K}$ before rising to $\sim 110 \text{ K}$ at the brighter, leading hemisphere. Figure 2.7(b) is the corresponding temperature map of the darker, trailing hemisphere mapped in west longitude. As is true for most planetary bodies, on

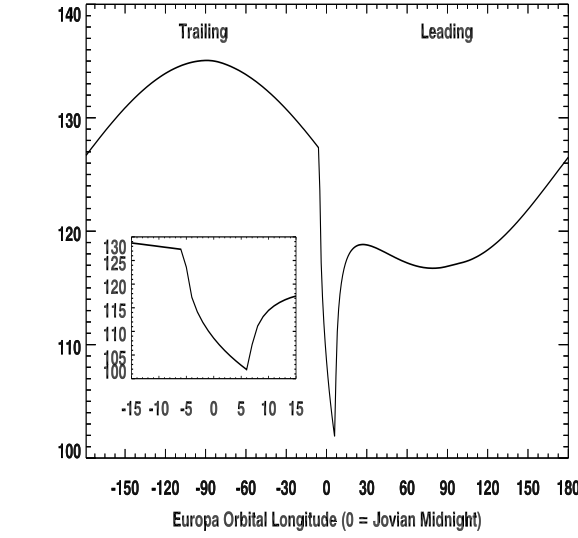
average, the largest thermal gradient is between noon and midnight, or day and night, as indicated in Fig. 2.7(b) with a slight increase in surface temperature, $\Delta T \sim 10$ K, at dusk over dawn due to the thermal inertia of the ice. The surface temperature inhomogeneities due to thermal inertia, as we will explore below, is *not* the principal driver for the observed dusk-over-dawn asymmetry.

2.8 Results

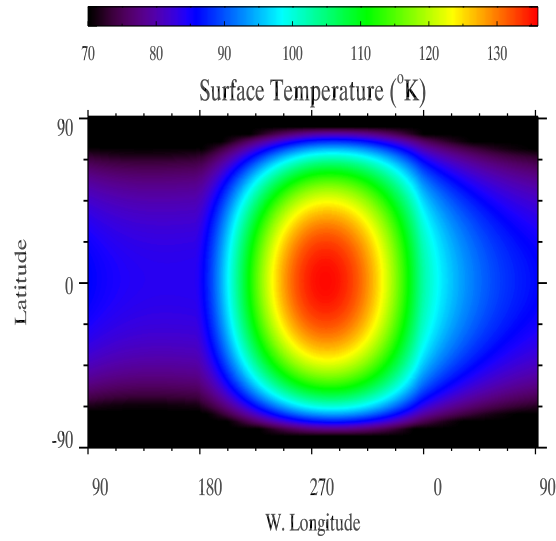
Implementing the physical processes described above, we have simulated the approximate steady state morphology of the O₂ and water-product exospheres, for a number of orbital positions around Europa. Steady-state is achieved when the change in number densities between orbits is insignificant for the various species modeled. Our principal result, as described in more detail below, is that the dynamics of Europa's near-surface O₂ exosphere is responsible for the observed dusk-over-dawn line-of sight (LOS) auroral asymmetry observed by the HST. For the assumptions described, our simulations yield a near-surface O₂ enhancement towards dusk driven by the steady production and destruction of the O₂ exosphere throughout the European day. This diurnal cycle of O₂, peaking in density at dusk (§2.8), is strongly dependent on two factors: (1) Europa's rotation rate and (2) Europa's O₂ production & loss rates. The larger O₂ column near dusk, persists throughout the entire orbit along with its dissociation products (O* & O) leading to consistently brighter oxygen aurorae at dusk. Below, we describe the dynamics essential to this diurnal O₂ cycle of molecular oxygen.

2.8.1 Exospheric O₂ Evolution

Europa's O₂ exosphere has been shown to be asymmetric over its orbit, as it experiences various solar insolation angles while co-rotating along with the plasma (Cassidy et al. 2007; Plainaki et al. 2013). Previous HST observations also provided evidence of O₂ evolution with excess emission at the trailing hemisphere near antijove, $\phi = 200 - 250^\circ$ McGrath et al. [2004, 2009], and the leading hemisphere near subjove $\phi \sim 90^\circ$ [Saur et al., 2011]. These sets of HST observations are consistent with R15, and are more readily evaluated in Europa local time, as the excess emission at both sunlit trailing and sunlit leading hemispheres corresponds to dusk. The diurnal dependence is due to the varying exospheric production of the 'bulk O₂ source', assumed to be maximum at the plasma ram/trailing hemisphere (Eqn. 2.17), being

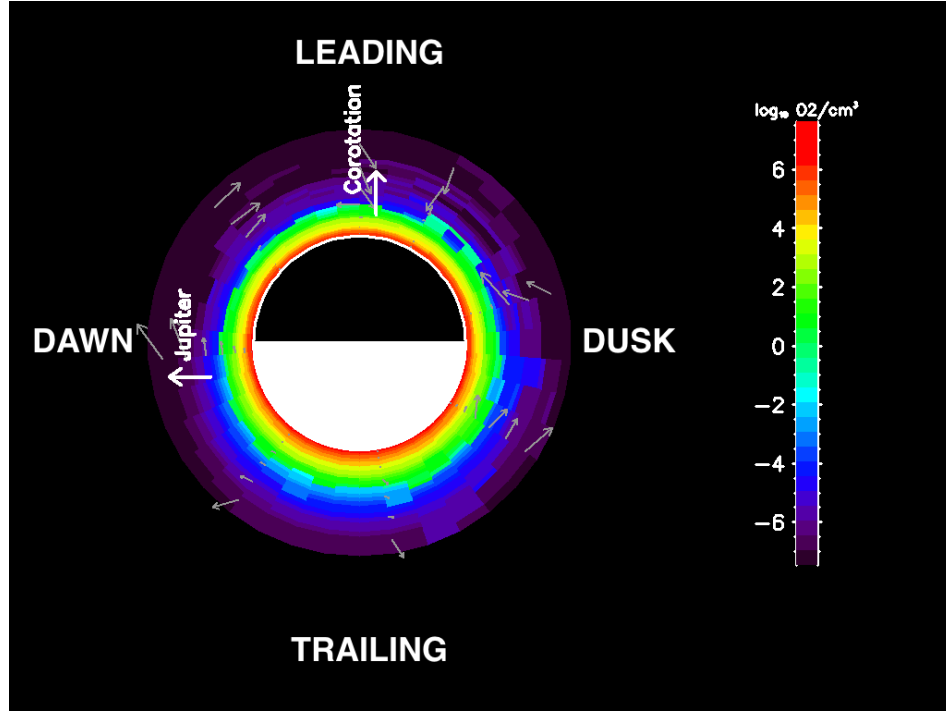


(a) a



(b) b

FIGURE 2.7: **a**: Equatorial subsolar surface temperature (K) as a function of sub-observer longitude, or Europa's orbital longitude, demonstrating the leading-trailing temperature profile asymmetry due to albedo. The darker, trailing hemisphere ($A_b = 0.45$) is seen to be ~ 18 K warmer than the brighter, leading hemisphere ($A_b = 0.65$). **b**: Surface temperature map of Europa's sunlit trailing hemisphere at $\phi_{obs} = 270^\circ$. The surface temperature rapidly increases from dawn, $\phi_{obs} = 90$ until the subsolar point at $\phi_{obs} = 0$. The surface then begins to cool slightly more slowly, passing through dusk at 18h Europa local time. The largest thermal gradients driving migration are therefore between 6h - 12h, and 12h-18h. Due to the thermal inertia of the ice, the dusk hemisphere is warmer than the dawn hemisphere.



(a)

FIGURE 2.8: Europa's static, O_2 exosphere for a simulation fixed at the sunlit trailing hemisphere with no rotation. Vectors are shown to demonstrate the day-night migration in the absence of rotation. An artificial day-side O_2 asymmetry is highlighted, due to preferential ion bombardment at the sunlit trailing hemisphere in the absence of rotation. The low albedo, sunlit trailing hemisphere has an equilibrium temperature of $T_d \sim 135K$, further exaggerating the effect of O_2 production on the exosphere due to the strong thermal dependence of the O_2 sputtering yield.

linked to the solar heating of the surface ice throughout the European day or orbit (Eqn. 2.18). The source rate is balanced by a loss rate which in this work, is initially assumed to be *constant* over the orbit. Our simulations reproduce the overall dusk-over-dawn asymmetry with a symmetric leading-trailing plasma, requiring neither exogenic nor endogenic sources. These simulations indicate that Europa's O_2 requires an orbital time to evolve and cannot be evaluated in the absence of rotation. We demonstrate two cases of an atmospheric bulge representative of excess UV emission, with and without rotation below.

2.8.2 Atmospheric O_2 Bulges

2.8.2.1 Stationary Case: Atmospheric O_2 Bulge at Noon

If Europa is held static, and evaluated at the darker, sunlit trailing hemisphere: $\phi_{obs} = 270^\circ$, then the O_2 production flux is maximal due to the solar insolation angle

being aligned with the anti-corotation vector, resulting in maximum heating and maximum sputtering generating a subsolar atmospheric bulge at noon for the bulk O₂ source. This atmospheric O₂ bulge is strongly dependent on the local temperature as the radiolytically produced O₂ on returning to the surface desorbs at the surface ice temperature, T_0 . Furthermore, while Europa is held static, the O₂ is still dynamic, and it is useful to evaluate its motion in the absence of Europa's rotation. Consider an inertial, non-rotating, reference frame as simulated in Figure 2.8. Solar radiation heats the subsolar hemisphere to $T_d \sim 135K$ decreasing to $T_n \sim 85K$ at the antisolar hemisphere as illustrated in Fig. 2.7(a). As shown in Figure 2.8, the peak in O₂ production due to sputtering is on the day side resulting in stochastic day-to-night migration, similar to a fountain-like phenomenon from the ejection region, as indicated by the gray vectors. In a collisionless exosphere, ejected molecules return to the surface where they stick or are re-emitted with an energy determined by the local, surface ice temperature. On interacting with the surface, the fate of a molecule is sensitive to the surface residence time: $\tau_{res} = \tau_0 \exp(\frac{E_{ads}}{k_b T_0})$ where E_{ads} is the effective heat of adsorption, indicating the energy needed for an atom to be released from the molecular bond. Initially for molecular oxygen, we assume the heat of adsorption is negligible and the surface residence time is extremely short, on the order of the vibration time for a Van der Waals potential ($\tau_0 \sim 10^{-13}s$) so that O₂ has a negligible sticking coefficient. The effect of O₂ sticking due to a longer residence time will be examined in section 2.9. Thus one can treat O₂ motion as a series of random walks. Hunten et al. [1988] for example, defines $\lambda_0 = \frac{U_0}{k_b T_0}$, the ratio of gravitational binding energy, $U_0 = \frac{GM_p m_i}{r_p}$ to the thermal energy $k_b T_0$ at the surface, approximately equal to the ratio of planetary radius r_p to the scale height, $H(T_0)$, so that $\lambda_0 \sim \frac{r_p}{H}$. λ_0 , is roughly equivalent to the number of ballistic hops a molecule experiences in traveling an average distance r_p yielding a diffusion timescale: $t_d \sim r_p^2/D$, where D is the effective diffusion coefficient. As approximated in Hunten et al. [1988], $D \sim \frac{H^2}{t_{hop}}$, so that the migration time for traveling a distance r_p at the surface is:

$$t_d \sim \lambda^2 t_{hop} \quad (2.23)$$

In Table 5.1, we estimate several timescales critical to the evolution of Europa's near-surface O₂, scaled to Europa's orbital period, τ_{orb} . Under a uniform gravitational potential, the ballistic hop time for an O₂ molecule is on the order of a few minutes. Since $t_{hop} \ll \tau_{orb}$, it is readily seen that the near-surface O₂ can be expected to follow the diurnal temperature variations in Fig. 2.7(b). Table 5.1 also indicates that the production and net loss timescales are comparable to the orbital period, yielding an average exospheric column of $\langle N \rangle_{O_2} \sim 8 \cdot 10^{13} \text{O}_2 \text{ cm}^{-2}$. Thus, the exosphere is

	Timescale (τ_{orb})	
Orbital Period	τ_{orb}	1.0
Ballistic O_2 hop	t_{hop}	$8 \cdot 10^{-4}$
Day-night migration	t_d	4.2
O_2 average exospheric production	$\langle t_{exo} \rangle$	0.98
O_2 lifetime*	τ_{O_2}	1.08

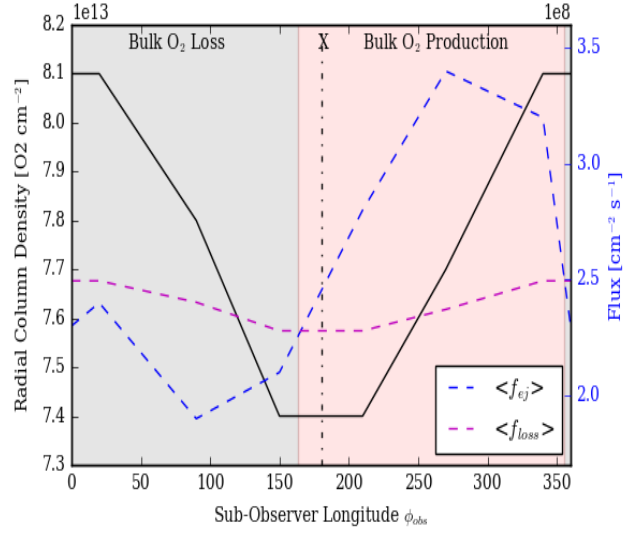
TABLE 2.3: Exospheric timescales for Europa. Given $\tau_{orb} = 3 \cdot 10^5$ sec. The average hop time for an O_2 molecule is computed using an average surface temperature of $\langle T \rangle \sim 110K$, as $\sqrt{2 \frac{u_0}{g}}$. The ballistic hop t_{hop} , assumes no interaction with the surface. The day-night migration time is estimated as a random-walk process across one Europa radius assuming no O_2 trapping or reactions with the surface ice. The average exospheric production time, $\langle t_{exo} \rangle$, for O_2 is the orbit-averaged radial column density over the orbit-averaged ejected O_2 flux, $\frac{\langle N \rangle}{\langle F \rangle}$, this timescale helps describe how long it takes to build the bulk O_2 column based on the production flux. The O_2 lifetime, τ_{O_2} , is limited by dissociation and ionization, computed by the product of the net reaction rate coefficient and the electron number density: $(\kappa \times n_e)^{-1}$, where $\kappa = 4.4 \cdot 10^{-8} \text{ cm}^3 \text{ s}^{-1}$ is the orbit-integrated reaction rate coefficient including e- impact as well as ionization, and $n_e = 70 \text{ cm}^{-3}$ the electron number density.

actively built and destroyed throughout an orbit. It is seen that the timescale for the day-to-night flow on a non-rotating body, t_d , is not only about four times longer than both the average production, $\langle t_{exo} \rangle$, and lifetime of the O_2 , τ_{O_2} , but also four times as long as Europa's rotation. Therefore, as the net spreading of the O_2 source is on average *slower* than Europa's orbital speed we can, to first order, consider the exospheric O_2 as coupled to the rotating surface. We find that this will easily identify the principal mechanisms for the apparition of an atmospheric O_2 bulge at dusk.

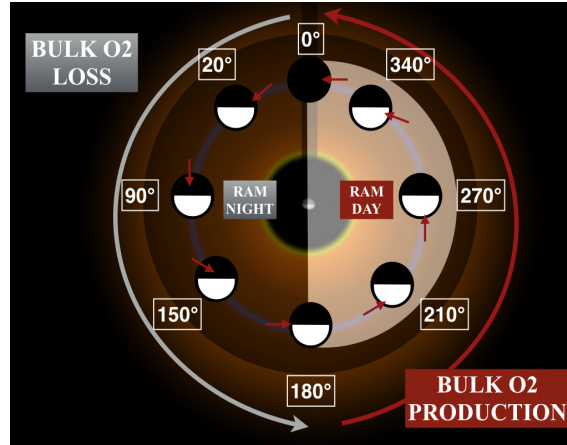
2.8.2.2 Rotating Case: Atmospheric O_2 Bulge at Dusk

Once rotation is activated, and the O_2 column density is tracked throughout the orbit, an asymmetry is generated about the Jupiter-system, roughly along Europa's orbital longitudes $\phi_{obs} = 180^\circ$ and $\phi_{obs} = 0^\circ$, due to the diurnal cycle of the thermally-dependent, bulk O_2 production flux maximum at plasma ram/trailing hemisphere. As indicated in Figure 2.9(a) (dashed blue line), the maximum O_2 production is between orbital longitudes $180^\circ \rightarrow 0^\circ$ (sunlit trailing hemisphere: *Ram Day*) and minimum O_2 production between $0^\circ \rightarrow 180^\circ$ (sunlit leading hemisphere: *Ram Night*). Figure 2.9(b) illustrates the bulk O_2 production over the sunlit trailing hemisphere phases (red arrow) and the bulk O_2 loss over the sunlit leading hemisphere phases (gray arrow). The day-night terminator for the rotating plasma ram source, is overlayed in Fig. 2.9(b) illustrating the two regimes of Europa's diurnal O_2 cycle.

The production of an atmospheric O_2 bulge at a given point in the orbit therefore, is a natural consequence of the diurnal asymmetries, as was simulated by previous works.



(a)



(b)

FIGURE 2.9: **a:** Monte Carlo simulation results for Europa while rotation about Jupiter is active. Orbital evolution of the surface-averaged O_2 column density (black) along with the surface-averaged O_2 production flux ($\langle f_{ej} \rangle$: blue) as well as the average O_2 loss flux ($\langle f_{loss} \rangle$: magenta) versus the sub-observer longitude. $\langle f_{loss} \rangle$ estimates the loss of the average O_2 content, throughout the exospheric lifetime of the O_2 , at each sub-observer longitude: $\langle f_{loss} \rangle \sim \langle N \rangle \langle t_{exo} \rangle$. **b:** Illustration of the diurnal asymmetry with respect to the bulk O_2 source, which is on average sourced at plasma ram/trailing hemisphere. The day-night axis for plasma ram, is therefore rotated by 90° from the observer's reference frame. During 'Ram Day', the bulk exosphere grows. During 'Ram Night', the bulk O_2 exosphere slowly diminishes.

What is unexpected however, is a consistent atmospheric bulge with local time. We find that for an atmospheric O₂ bulge to be maintained at dusk local time, even when the exospheric loss rate exceeds the exospheric production rate is entirely fortuitous, in that Europa's average O₂ lifetime is approximately equal to Europa's orbital period or $\tau_{O_2} \sim \tau_{orb}$ (Table 5.1). Since Europa's O₂ exosphere, to 1st order, is directly coupled to the surface, $\tau_{O_2} \sim \tau_{orb}$, the O₂ exosphere is directly influenced by the diurnal changes in the surface temperature. In this way, an atmospheric bulge at dusk can only be sustained if, as in our simulations, the thermally-desorbed O₂ is allowed to rotate with the surface, capable of replenishing the bulge even when bulk production is minimal (Ram Night). The decrease in production results in a bulk O₂ loss phase decreasing the total content by $\sim 10\%$ over half an orbit (gray: Fig. 2.9(a)). This relatively small variation in column density, is sufficiently large to dominate the spatial morphology and evolution of the atmospheric bulges throughout the orbit. The magnitude of the atmospheric bulge, and hence the dusk-over-dawn asymmetry (in the absence of adsorption or other loss processes) is therefore set by these ongoing equilibrium processes throughout the orbit.

2.8.2.3 Rotating Case: Surface-Exosphere Coupling of O₂

The constant equilibrium between time-dependent O₂ production and isotropic O₂ loss results in a certain surface-exosphere coupling or synergy throughout the orbit which we describe here. In the 1-D O₂ evolution figures 2.9(a), 2.9(b) described above, we notice that the maximum O₂ column, on average, accumulates $\sim 90^\circ$ after the maximum O₂ production flux. Again, as these rotational effects are more readily evaluated in Europa local time, the max production roughly corresponds to noon for the bulk O₂ source ($\phi_{obs} = 270^\circ$), and the max column naturally accumulating what has been built by the end of the day, arrives at dusk for the bulk O₂ source ($\phi_{obs} = 0^\circ$).

A second effect of building the O₂ exosphere at Ram Day and isotropically dissipating the O₂ exosphere at Ram Night is seen in the simulated spatial morphology of the bulge ejecta and the bulge columns as illustrated in real time as maps in Fig. 2.10. The center circle indicates the orbital longitudes of the seven simulated orbital positions. The inner and outer circles represent the critical synergy between the O₂ production and O₂ columns varying with rotation. The inner circle, maps the radiolytically sputtered ejecta in O₂ cm⁻² s⁻¹, and the outer circle, maps the radial column density in O₂ cm⁻². On the outer maps, consistent with the inner maps, we have indicated dusk, dawn, and the subsolar position (X), where an exospheric bulge can be seen to consistently appear at the dusk terminator. The apparent rotational behavior

occurring between half-orbit intervals is due to the production and destruction at the sunlit trailing and sunlit leading hemispheres respectively, as discussed. The ejecta bulge at $\phi_{obs} = 270^\circ$ (inner circle) accumulates into an exospheric bulge at $\phi_{obs} = 90^\circ$ (outer circle). The exospheric bulges near the sunlit leading hemisphere longitudes are vastly more apparent due to the bulk O₂ column slowly dissipating as described in the 1-D O₂ evolution figures. In particular, at phase angles 90° and 150° , the O₂ exosphere at dawn almost completely vanishes. These are also the orbital locations where we predict a maximum dusk-over-dawn asymmetry. Overall, the 2-D maps of Fig. 2.10 reveal that the *local* exospheric column densities vary substantially, by more than an order of magnitude: $\sim 90\%$ and are responsible for the shape of the exospheric dusk bulges. These maps provide the first detailed picture of how Europa's *rotating* O₂ exosphere evolves throughout its orbit due to the diurnal O₂ production ultimately responsible for the observed dusk-over-dawn auroral oxygen asymmetries.

2.9 Discussion

While our simulations appear to reasonably explain the dusk-over-dawn oxygen auroral asymmetries, the precise magnitude and position of these bulges is dependent on our assumptions as stated above as well as our limited knowledge of the near-surface plasma interaction with Europa. Below we examine our assumptions. The effective radiolytic yield (Eqn. 2.18) might be much less sensitive to the local trailing hemisphere temperature. As was shown by Teolis et al. [2005], the O₂ sputtering yield derived from laboratory experiments of crystalline water ice requires a flux of $\sim 10^{15}$ ions cm⁻² ($\tau > 15\tau_{orb}$) before the O₂ responds to the temperature change. This suggests that late-chemistry and prompt-chemistry effects occurring in the water ice regolith could play a role at Europa. In this section we discuss how comparisons with HST data can potentially help in disentangling such uncertainties. We emphasize however, that certain direct comparisons between the near-surface oxygen auroral profiles and near-surface O₂ exospheric profiles may be limited due to the unknown nature of the plasma at Europa's surface (e.g. Fig. 2.12). These comparisons are still useful in assessing the overall state of Europa's exosphere. Re-analysis of spacecraft data Bagenal et al. [2015] and sophisticated modeling of the plasma interaction Rubin et al. [2015] would help improve our understanding before *in-situ* observations by Europa Clipper and JUICE. For instance, the electron temperatures calculated by Rubin et al. [2015] imply a cold electron population at the near-surface altitudes, effectively reducing the auroral brightness.

At present, the only observational evidence of Europa's oxygen exosphere rests in FUV auroral emission occurring at two particular atomic oxygen transitions: $\lambda = 1356$, $\lambda = 1304$. Should the ratio of these two wavelengths $\langle i \rangle = \frac{I_{1356}}{I_{1304}}$ be close to 2, it is indicative of e^- impact dissociation of O_2 . The novel data the HST imaging spectrograph has acquired are full orbital information (spectral and spatial) for these two auroral emission lines, not only confirming $\langle i \rangle \sim 2$ throughout the orbit, but also demonstrating the orbital evolution of the oxygen aurorae. We find the new observations, when compared with our EGM simulations, are reflective of the *behavior* of the rotation-driven near-surface O_2 exosphere as Europa orbits in Jupiter's dynamic magnetosphere. We will first directly compare the orbital evolution of auroral and exospheric oxygen in section 2.9.1. Finally, we will discuss the radial evolution of auroral and exospheric oxygen in the context of the oxygen corona (2.9.3, 2.9.4). The two sets of comparisons demonstrate Europa's oxygen exosphere is neither static in Europa local time nor in radial extent.

2.9.1 Orbital Evolution of Exospheric and Auroral Oxygen

Our simulations (Figure 2.10) indicate an O_2 column consistently accumulating near dusk at each orbital longitude generating an exospheric asymmetry. We find that to first order, the diurnal production of the near-surface O_2 balanced with e^- impact loss, appears to dictate the global behavior of the FUV oxygen aurorae over time.

Photodissociation is also treated in our model and is a negligible contributor to FUV auroral intensity for oxygen, as was also shown in previous models with and without photodissociation [Shematovich et al., 2005]. The main source of the auroral emission observed by HST are electron-impact dissociated O_2 molecules:

$O_2 + e^- \rightarrow O^* + O + e^- + \Delta E$. Where a fraction of these excited oxygen atoms O^* will undergo one of two FUV transitions occurring at: 1304 , or at the forbidden line at 1356 Å. The 1304 line can additionally resonantly scatter photons due to the presence of atomic oxygen. The emission intensity I occurring at a given wavelength λ , can then be estimated by summing each reaction which generates excited atomic oxygen, O^* .

$$I_\lambda = (n_e \kappa_{O_2+e^-}) N_{O_2} + (n_e \kappa_{O+e^-}) N_O \quad (2.24)$$

I_{1304} also includes the photo-excitation term for $O + h\nu$: $g_{exc} N_O$, where g_{exc} is the excitation frequency in s^{-1} for atomic oxygen.

The electron-impact dissociation reaction rates κ [cm^3/s] are identical to those used by [Turc et al. \[2014\]](#) for e- impact dissociation as well as photoexcitation. Here N_{O_2} is the line-of-sight column density of O_2 , and N_{O} is the line-of-sight column density of the neutral O, where λ corresponds to wavelengths 1304 & 1356 Å. Of course, the plasma torus is tilted in accordance to the tilt of Jupiter’s magnetic dipole with respect to the orbital plane, and thus the auroral emission can be enhanced at the poles as was observed by R15 for various magnetic longitudes. Furthermore, recent simulations of Europa’s ionosphere [Rubin et al. \[2015\]](#) indicate the electron density and electron temperature distributions vary along the plasma co-rotation direction and can in principle contribute to upstream/downstream auroral asymmetries. However, as stated by R15, the observed dusk-over-dawn asymmetries cannot be explained by plasma asymmetries alone. In Figure 2.11 we compare the hemispherically averaged, dusk-over-dawn auroral intensity ratio for HST observations (black circles, fitted in R15 by the black line) and our EGM simulations assuming isotropic plasma conditions (squares). All points in the orange region correspond to a dusk-over-dawn asymmetry, whereas points in the light blue region represent a dawn enhancement. It can be seen in our nominal O_2 case (no surface interactions, blue squares) that the dusk hemisphere is brighter than the dawn hemisphere throughout the *entire* orbit, which is globally consistent with HST observations. This nominal case using only meager plasma assumptions, demonstrates that the exospheric oxygen dynamics describing the formation of an O_2 bulge is the principal driver in generating Europa’s bright aurorae at dusk.

To recapitulate, the O_2 molecules are preferentially ejected from the surface on the day side because the surface temperature regulates the sputtering efficiency as well as the adsorption probability. On the other hand, the probability of electron impact, and resulting O_2 loss, is uniform in local time with no diurnal dependence (at least as treated in the EGM). Furthermore, as indicated in Table 5.1 due to the short hop times, the O_2 migrates only $\sim r_p \frac{\tau_{\text{orb}}}{t_d} \sim r_p/4$ over a diurnal timescale. Hence, one can consider the O_2 exosphere to essentially be at rest in Europa’s rotating reference frame, or equivalently, in the observer’s frame the bulk O_2 is simply orbiting at $v_{\text{orb}} \sim 32\text{m/s}$. Therefore, a steady state O_2 exosphere tends, on average, to be built on the dayside and to be destroyed on the nightside, resulting in an atmospheric bulge at dusk (§2.8.2.2) corresponding to the observed auroral patches used to derive the dusk-over-dawn auroral asymmetry in Figure 8 of R15. As Europa orbits Jupiter, the nominal EGM simulations suggest that the dusk-over-dawn asymmetry should peak when Europa approaches its leading hemisphere phases. The HST observations also show brightening of the dusk aurorae over the orbit, but never as conspicuous as the

leading hemisphere anomalies we simulate. These highly asymmetric aurorae simulated at $90^\circ < \phi_{obs} < 150^\circ$ provide insight into the actual exospheric O_2 behavior at Europa. We question first the diurnal O_2 production, the principal dusk-dawn driver, by reexamining the prompt-thermal response of the radiolytic O_2 yield in Eqn. 2.18. We simulate a far weaker thermal dependence of O_2 ($q'_{O_2} = 100$ instead of $q_{O_2} = 1000$) and find it reduces the dusk-over-dawn asymmetry (indicated in cyan). Furthermore, this particular choice of q_{O_2} , brightens the dawn aurorae to an even higher intensity than the dusk aurorae during the trailing hemisphere phases which was never observed. Although as we will discuss below, there are various other ways to mitigate the dusk-over-dawn asymmetry at the leading hemisphere, this simulation result implies the thermal dependence on the O_2 yield may be necessary for an exospheric bulge consistently maintained at dusk. Next, we consider surface-exosphere interactions, notably the possibility of O_2 adsorbing on to the water ice regolith.

2.9.2 O_2 Adsorption on Grains in the Water Ice Regolith

As discussed in Section 2.8.2.1, exospheric O_2 on Europa's $\sim 100K$ surface is thought to undergo a series of unimpeded ballistic hops due to its low sublimation temperature of $\sim 54K$. Recently, on the far colder Rhea and Dione, evidence of exospheric evolution due to O_2 adsorption was discussed by [Teolis and Waite \[2016\]](#). To deduce the influence of O_2 adsorption on Europa's exospheric evolution we also show two other simulations in which we uniformly change the surface heat of adsorption (in Kelvins or equivalently in eV once multiplied by k_b) for the returning O_2 :

$E_{ads} = 3000k_b$ (green), $E_{ads}(L) \neq E_{ads}(T)$ (magenta). $E_{ads} = 0$ (blue) is the nominal case discussed above in which the exospheric O_2 does not react with the surface.

The larger heats of adsorptions (green) imply stronger O_2 interactions with the regolith, and thus longer residence times in the regolith and in effect, longer migration times. Non-uniform heats of adsorption from leading to trailing are considered (magenta) as the large discrepancy occurs uniquely when observing one region (sunlit leading hemisphere region, where dusk is near Europa's subjovian hemisphere: $90^\circ < \phi_{obs} < 150^\circ$). To test this effect globally we model the heat of adsorption with a simple \cos^2 function with latitude (θ) and planetary longitude (ϕ'):

$$E_{ads}(\phi', \theta) = E_1 \cos^2 \left(\frac{(\phi' - \phi'_0)}{2} \right) \cos^2(\theta - \pi/2) + E_0 \quad (2.25)$$

Equation 2.25 is a simple surface adsorption relation modeled in the EphIO frame where $\phi'_0 = 0$ treats E_{ads} as preferential adsorption on the leading hemisphere and

$\phi'_0 = \pi$ as preferential adsorption on the trailing hemisphere. In Fig. 2.11 the magenta points present one particular case of a simulation where $E_1 = 500k_b$, $E_0 = 2300k_b$, and $\phi'_0 = 0$. It can be seen that the higher effective heats of adsorption significantly reduce the dusk-over-dawn asymmetry. The adsorption increases the surface residence time, reducing the exospheric lifetime like H_2O molecules freezing to the surface, and therefore the effects of diurnal O_2 production are largely erased and an O_2 bulge at dusk is not maintained. The higher dusk emission occurs at the leading hemisphere phases $\phi_{obs} \sim 90 - 150^\circ$, potentially indicating that this region possesses stronger surface- O_2 interactions. Equivalently, the trailing hemisphere could also adsorb more efficiently since the column of O_2 driven towards $90-150^\circ$ is due to the ejection roughly half of a rotation earlier. While we are currently unable to deduce whether the O_2 is adsorbing more at the leading or trailing surfaces, we note that unlike at Ganymede there is not a strong asymmetry at Europa in the trapped O_2 observed in absorption bands at $\lambda = 5771$ [Spencer and Calvin \[2002\]](#), [Spencer et al. \[1995\]](#). This O_2 however is likely trapped before it is radiolytically ejected, as described by [\[Johnson and Jesser, 1997\]](#). O_2 can be trapped as bubbles in the H_2O regoliths of the Galilean satellites should the temperature be sufficiently high to allow for vacancies produced by diffusion of the incoming ion. It is conceivable that the observed sulfate impurities on Europa's trailing hemisphere, suggest the adsorbed O_2 is permanently removed by reactions as analyzed by [Cassidy et al. \[2007\]](#). In addition, there are rather different thermal anomalies on the two hemispheres, uncorrelated with geologic or albedo features at Europa's equator at the leading antiojovian quadrant [Rathbun et al. \[2010\]](#), [Spencer et al. \[1999\]](#).

2.9.3 Comparisons of Oxygen Aurorae and Oxygen Exosphere: A Stratified Exosphere.

A comparison between the FUV oxygen aurorae observed by R15 and the simulated neutral exosphere can be made assuming isotropic plasma conditions as described in Figure 2.12. This comparison enables one to discern the behavior of the neutral O_2 in the exosphere, which appears to be split into two populations. The first population is the largely thermally accommodated, near-surface O_2 , the principal focus of this work. This is the component of the exosphere most strongly subject to the rotation-driven dusk-dawn asymmetry. The second population, which we will refer to as the corona, appears to be vastly more energetic extending well beyond 400 km in altitude or $\sim 1.25 r_{Eu}$ from disk center as illustrated in Fig. 2.12 & Fig. 2.13. Here, we will compare the HST auroral emissions averaged over all phase angles by R15 to our EGM

molecular oxygen simulations symmetrically-averaged from Europa's disk center. Europa's exosphere is not spherically-symmetric as shown in section 2.8.1, and thus the radial profiles may average out structures in the aurora over time despite an orbital average over various system III longitudes. Furthermore, Jupiter's rapidly rotating magnetosphere governs auroral emission, unlike at Ganymede whose intrinsic magnetic field is able to regulate the flux of precipitating ions. At Europa in particular, the north-south auroral patches are due to the tilting of the Io-Europa plasma torus (R15) with Jupiter's magnetosphere. The average profile of the auroral emissions as derived by R15 are therefore constructed from highly variable, patchy observations, in latitude and longitude. Hence it is difficult to compare to our simulations, in particular near Europa's disk which is partially blocking the emissions of Europa's exosphere. Despite these variabilities this spherically-symmetric comparison helps us understand the global nature of Europa's exosphere and its interaction with the Jovian magnetosphere.

2.9.3.1 Disk Emission: $r < 1.0r_{Eu}$

We find that simulated on-disk auroral intensities even under simple, isotropic assumptions are consistent with the average on-disk intensities observed by HST: ~ 45 Rayleighs at leading hemisphere and ~ 60 Rayleighs at the trailing hemisphere. Here we present only the 1356 emission line as to focus on O_2 , although the ratio of the two lines can indicate the abundance of atomic oxygen. The increase in the observed auroral intensity ratio $\frac{I_{1356}}{I_{1304}}$ from 1.6 to 2.3, indicated $\sim 80\%$ less O at leading ($\chi_{O/O_2} = 1\%$) versus trailing ($\chi_{O/O_2} = 5\%$) which we also confirm to be consistent when comparing our derived LOS column densities for both O_2 ($\langle N_{O_2} \rangle \sim 10^{14} O_2 \text{ cm}^{-2}$) and O ($\langle N_O \rangle \sim 10^{11} O \text{ cm}^{-2}$). Our model predicts a slightly smaller decrease $\sim 25\%$ in O from sunlit trailing (270°) to sunlit leading (90°). The overall LOS column density however, is still slightly greater at noon at trailing than at leading, $\Delta N \sim 7 \cdot 10^{13} O_2 \text{ cm}^{-2}$, due to the subsolar axis being aligned with the sputtering axis/plasma ram (modeled to be maximum at the trailing hemisphere following Eqn. 2.17.) The auroral observations confirm the brighter trailing hemisphere by ~ 15 Rayleighs for the on-disk, near-surface O_2 emission.

2.9.3.2 Limb Brightening: $0.8 < r < 1.2r_{Eu}$

On Europa's disk, the average auroral emission profiles reconstructed by the auroral image observations by R15 display a brightening inside the limb. This is contrary to expectations as one should expect limb brightening due to the larger path lengths off

of the disk as we simulate in Fig. 2.12. The lack of limb brightening may imply an exosphere peaking in density near the subsolar region or an incident plasma interacting with Europa in a much more complex way than assumed in our simulations. Profiles off of the limb and into the corona however offer a more direct comparison between the observed auroral emission and the exospheric neutrals as illustrated in the atmospheric profiles of Figure 2.13. We fit a scale height of $H_{O_2} \sim 140km$ (blue and green dashed lines) up to an altitude of ~ 400 km. These scale heights are consistent with a thermally accommodated near-surface O_2 exosphere as evidenced by the on-disk profile fit to $H_{O_2} \sim 300km$ by R15 (Figure 11c). However it is clear that the neutral exosphere (colored lines blue and green) cannot explain the brightness of the observed aurorae (black line) past $\sim 280km$ in altitude. Further into the exosphere, past $\sim 390km$ ($r \gtrsim 1.25r_{Eu}$) even for a more energetic sputtering distribution, sub-Rayleigh emission is predicted. This discrepancy can be interpreted in a variety of ways which we describe below.

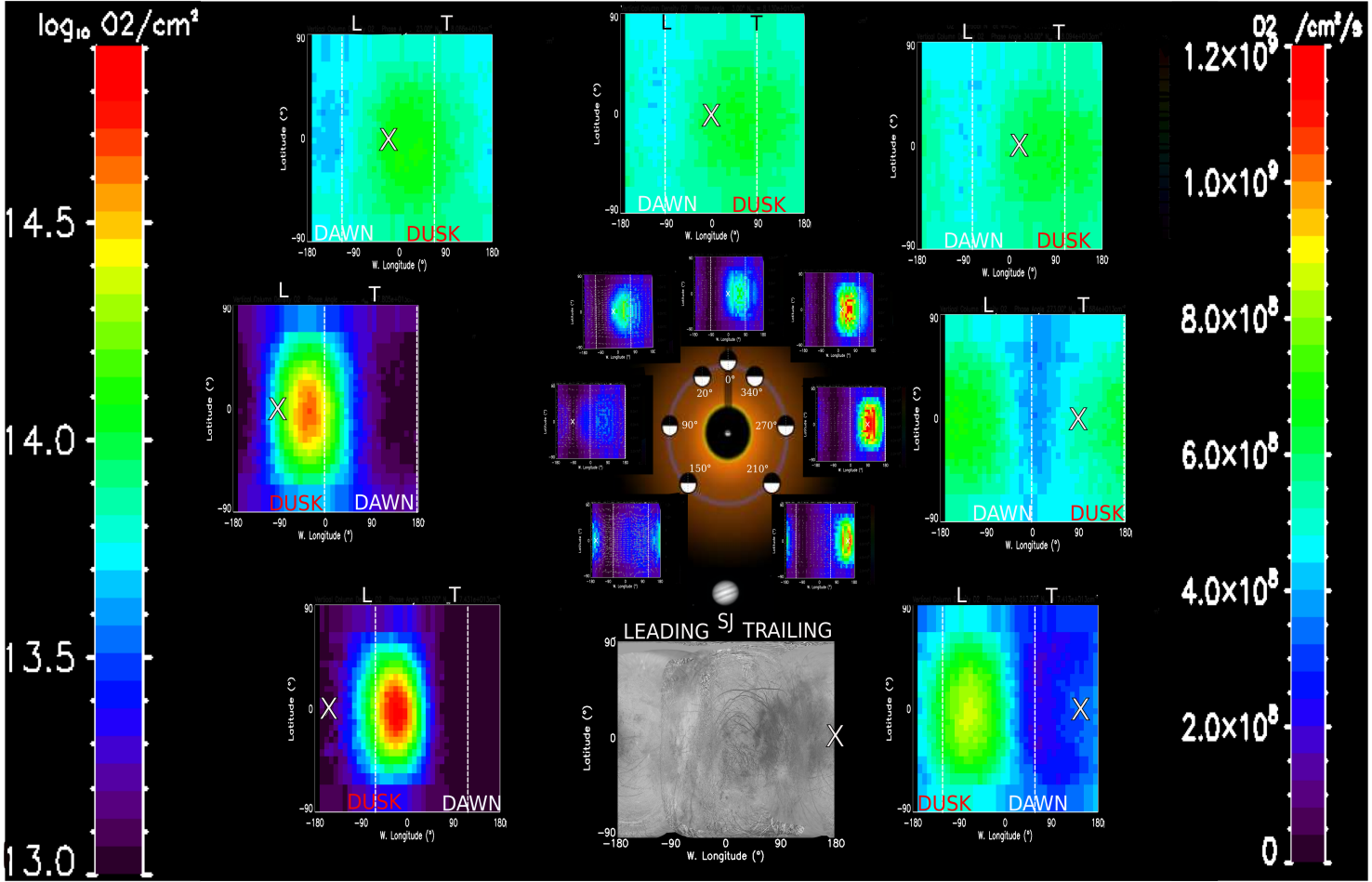


FIGURE 2.10: Formation map of Europa's O_2 exosphere, illustrating surface-exosphere coupling of the near-surface O_2 . $\phi = 0$ degrees west longitude corresponds to the subjovian point (SJ), where positive longitudes correspond to the trailing hemisphere (T) and negative longitudes, leading (L). At $\phi_{\text{obs}} = 180^\circ$ we provide a high-resolution map of Europa's surface, for comparison to the near-surface exosphere, taken by Voyager and Galileo as adopted in [Doggett et al., 2009]. On each simulation map, the subsolar point is indicated by a white X, whereas the dawn and dusk terminators are indicated by the vertical dashed lines. **Inner circle surface maps:** Exospheric production as shown by the ejection rate of the O_2 sputtered from the surface with respect to latitude and west longitude at different orbital positions of Europa. The sputtering flux ranges from 2 (blue) - 12 (red) $\cdot 10^8 \text{ O}_2 \text{ cm}^{-2} \text{ s}^{-1}$ (right panel colorbar). Sub-observer longitudes(ϕ_{obs}), or phase angles are provided inside the orbit. **Outer circle exosphere maps:** \log_{10} of the radially integrated column density of the O_2 exosphere with respect to latitude and west longitude at different orbital positions of Europa. The radial column density ranges from $\sim 1 - 30 \cdot 10^{13} \text{ O}_2 \text{ cm}^{-2}$ (left panel colorbar). Whereas the average radially integrated column density of the O_2 exosphere ranges from $7.4 - 8.1 \cdot 10^{13} \text{ O}_2 \text{ cm}^{-2}$. The reader is encouraged to refer to the web-version of this article for a more enhanced view of the smaller plots.

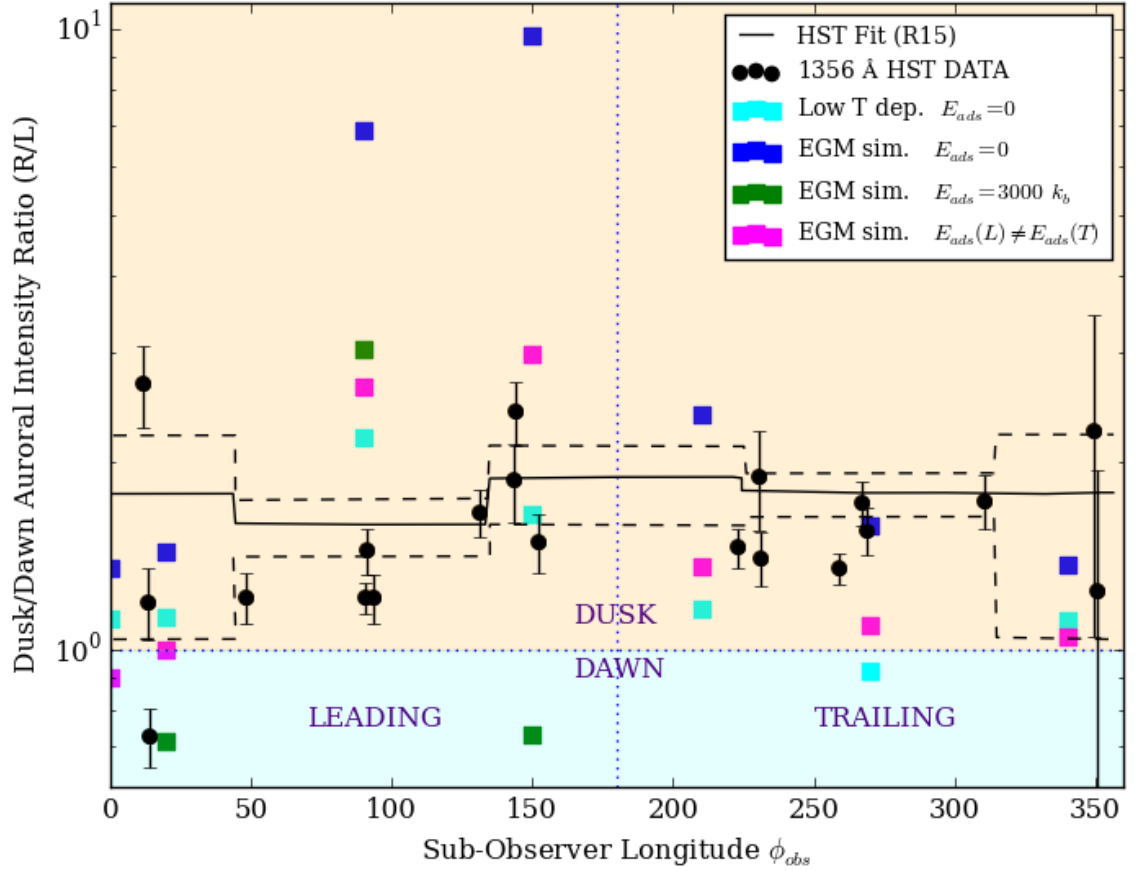
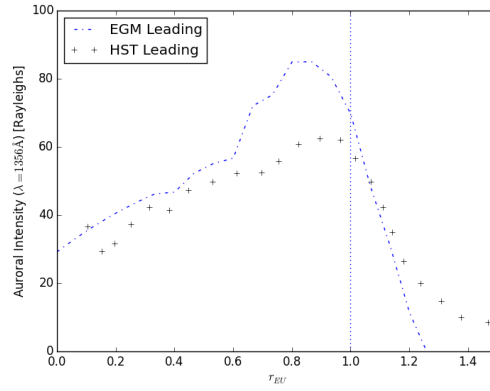
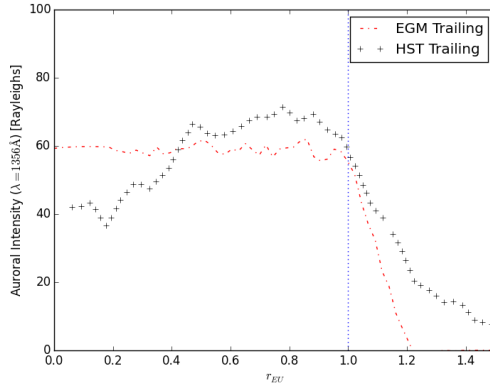


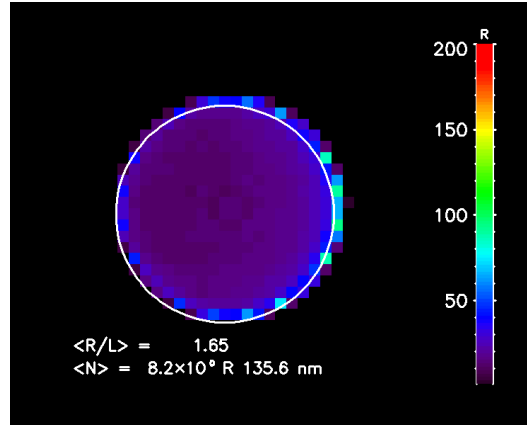
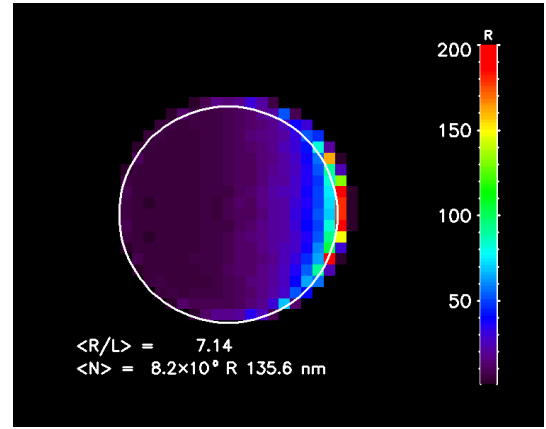
FIGURE 2.11: Orbital evolution of the log of the dusk/dawn 1356 Å emission line versus the orbital longitude. The average auroral emission on the dusk-side of Europa is divided by the average emission on the dawn-side. Black points are HST observations. Black dashed lines represent the average error in HST observations. Solid black line is an arithmetic average of the HST data fitted to Figure 8A in R15. Squares represent the modeled auroral intensity ratios calculated from simulated LOS O_2 column densities assuming isotropic plasma conditions $n_e = 70 \text{ cm}^{-3}$ and $T_e = 20 \text{ eV}$. The dark blue square is the nominal simulation in which the effective heat of adsorption is set to 0. The green square corresponds to the more extreme case in which the O_2 follows a heat of adsorption of $E_{ads} = 3000$. The two cases indicate that a non-uniform heat of adsorption between the leading and trailing hemispheres, $E_{ads}(L) \neq E_{ads}(T)$, may be required to explain the exaggerated dusk enhancement at the leading hemisphere phases as simulated by the magenta square.



(a) Sunlit Leading Hemisphere EGM (dash-dot) & HST(+).



(b) Sunlit Trailing Hemisphere EGM (dash-dot) & (c) Simulated auroral emission viewing the Sunlit Leading Hemisphere.



(d) Simulated auroral emission viewing the Sunlit Trailing Hemisphere.

FIGURE 2.12: **Top panels:** LOS auroral intensities at $\lambda = 1356$ versus radial distance from Europa's center reconstructed by HST auroral images (black) along with corresponding EGM simulations (blue and red dashed lines). The spatial resolution is rings of $0.025 R_{Eu}$. Europa's limb is indicated with the dotted vertical line. The LOS O_2 column densities from the EGM simulation are symmetrically averaged in rings about Europa's center as in R15. The corresponding auroral intensities are then computed following Eqn. 2.24 employing modest plasma parameters with no asymmetries: isotropic electron density $n_e = 70 \text{ cm}^{-3}$ and $T_e = 20 \text{ eV}$ plasma temperature. **Bottom panels:** Simulated auroral images reconstructed directly from LOS O_2 and O column densities. The right-over-left ($\langle R/L \rangle$), dusk-over-dawn, asymmetry is highlighted indicating the asymmetric nature of Europa's aurorae.

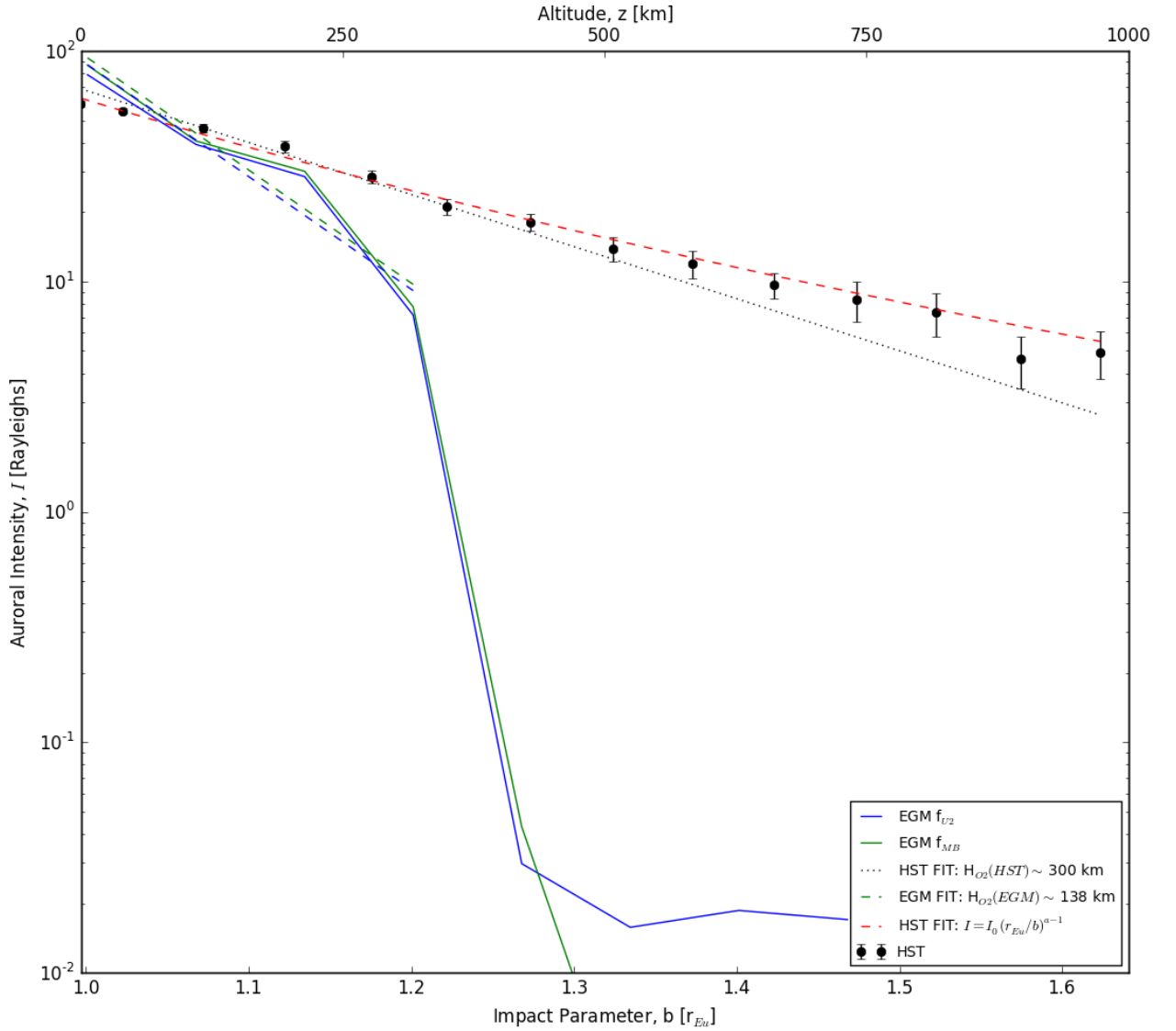


FIGURE 2.13: Auroral intensity, I , for the 1356 emission line at Europa's sunlit leading hemisphere as a function of the impact parameter (b) in units of European radii, r_{Eu} . The corresponding altitude, z , in km from the surface, is indicated on the top horizontal axis for reference. HST observations from R15 are shown by the black points. Two EGM simulations are presented for two different function distributions for the initial ejection of the O_2 molecule from the regolith: f_{MB} , in green and f_{U2} , in blue. The corresponding dotted lines represent the barometric scale heights assuming an isothermal atmosphere. In our EGM simulations the O_2 is perfectly thermally accommodated and thus the scale height reflects the average surface ice temperature $T \sim 110K$. The black dotted line fit to the HST data implies an atmospheric temperature of $T_x \sim 1500K$, or $E_x \sim 0.2$ eV roughly twice the energy of a sputtered O_2 molecule. The red dotted line is a fit to a power law distribution: $I = I_0 (r_{Eu}/b)^{a-1}$. b is the perpendicular scattering distance from the center of Europa's gravitational field. Both of these fits seem to suggest collisional processes occurring in Europa's corona, as described in the text.

2.9.4 Coronal Expansion: $r \gtrsim 1.25r_{Eu}$

The O_2 above the near-surface, hereafter coronal O_2 , appears to behave far more energetically according to the HST auroral profiles as can be seen by the solid black points in Figure 2.13. For both e- impact dissociation lines, the simulated emission is too faint in the corona. Scale heights of $H \sim 150 - 300km$ were fit by R15 Figure 11b & 11c. The black dotted line in Figure 2.13 shows a scale height of $\sim 300km$ fit to the observations. We discuss a heating mechanism capable of expanding the atmosphere in section 2.9.4.1, whereas in section 2.9.4.2 we consider collisional expansion by H_2O , which could accelerate the O_2 like a radial outflow. Of course, the corona could be a combination of the two mechanisms. Here, we discuss these two proposed mechanisms and their agreement with R15 and our EGM simulations.

2.9.4.1 Plasma-Driven Atmospheric Expansion

Europa's corona may be analogous to Io's escaping SO_2 corona [Summers et al., 1989]. The atmospheric escape at Io is thought to be primarily driven by atmospheric sputtering, a cascade of collisions triggered by momentum exchange between an incident ion and neutral below the exobase [Johnson, 1994]. These ion-neutral collisions were included in the 1-D temperature calculation of a 3-D MHD model for Europa by Saur et al. [1998]. The model predicted $T_x \sim 750 - 1000K$ and $H \sim 150 - 200km$. Here we fit the auroral profile to a scale height of $H \sim 300km$ (black dotted line) as in R15. Recent MHD simulations Rubin et al. [2015] including this heating also indicate that Europa's ionosphere may contribute to coronal expansion on orbital timescales.

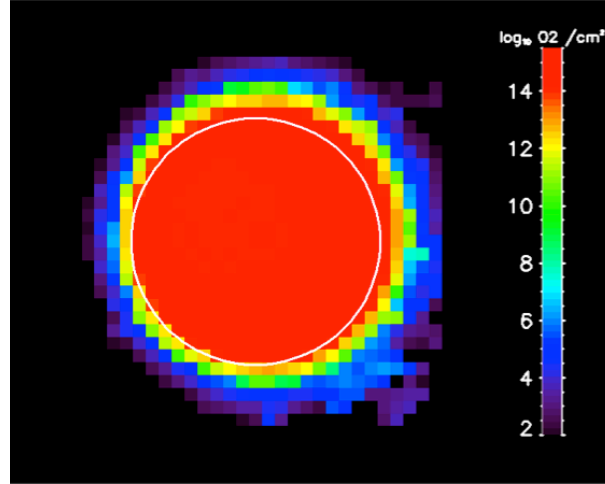
The models include dissociation, ionization, and various other loss processes which have been recently discussed in the literature to be dominated by charge-exchange (Dols et al., 2016; Lucchetti et al., 2016). Charge exchange here refers to the ion-neutral interactions between O_2 and O_2^+ resulting in O_2^* , an energetic neutral atom (ENA) with kinetic energies capable of escaping Europa's hill sphere $\sim 8.6r_{Eu}$. The recent loss rates discussed in the aforementioned papers report mass loss rates $\dot{M}_{O_2} \sim 160kg/s$ more than 30 times the O_2 production rates predicted by [Cassidy et al., 2013]: $\dot{M}_{O_{2,0}} \sim 5kg/s$. If the exosphere was isothermal at $\sim 1500K$ the corresponding Jeans escape yields $\dot{M}_{O_2} \sim 0.1kg/s$ of mass loss. On the other hand, charge-exchange rates with O_2^+ are larger by three orders of magnitude, leading to a far more energetic population than for an exosphere fit to an isothermal emission profile as in Fig. 2.13. Upon integrating the auroral emission over altitude, one can deduce the missing population of O_2 should the emission be directly proportional to

the LOS O_2 column as discussed previously. We find that HST observes ~ 2.5 times more O_2 than the production rates in our model. Simply increasing the production rate by 2.5 would result in average auroral intensities ~ 150 Rayleighs at the leading hemisphere which is far greater than what is observed, as shown in Fig. 2.12. Sourcing the calculated charge exchange escape rates in the literature would result in an average auroral intensity of ~ 1800 Rayleighs at the leading hemisphere. Thus, although these rates suggest a nonthermal expansion mechanism for the corona, the corresponding O_2 source presents a serious issue in the energy budget of the exosphere.

Given that charge exchange between O_2 and O_2^+ is equivalent to elastic scattering, as discussed in the context of Saturn's toroidal O_2 atmosphere sourced by water ice grain sputtering [Johnson et al., 2006a], the energy budget can be determined by first considering the energy of the ion, O_2^+ . For scattering, the thermal energy of the ion should be approximately equal to the pick-up ion energy $E_p \sim \frac{1}{2}m_{O_2^+}(v_{co} - v_o)^2$, where v_{co} is the corotation velocity of the Io- plasma torus near Europa's surface, and v_o is Europa's orbital speed. However, to accurately estimate this effect on the upper exosphere, one requires a knowledge of the plasma flow through the near-surface O_2 exosphere. Comparing our simulations with the latest observations turns out to still be insightful, in that we note that ion-neutral scattering would produce a more extended atmosphere, as suggested by the power law fit to the emission intensity in Fig. 2.13. For a radially dependent atmospheric density, $n_{O_2} \sim n_0 \left(\frac{rEu}{b}\right)^a$, the near-surface LOS column above the terminator will also have a rough power law dependence with exponent $\sim (a - 1)$. Assuming the auroral intensity is proportional to the LOS column, then based on our fit in Fig. 2.13, $a \sim 6$. Such an atmosphere is still steeply decaying but would have a somewhat larger escape rate than the Jeans rate, however not sufficient to explain the large escape rates discussed above.

2.9.4.2 Water-Driven Expansion

Water vapor is a significant component of Europa's exosphere. Today, there are three possible production mechanisms: sputtering, sublimation, and endogenic activity (Roth et al., 2014b ; Sparks et al., 2016b; Sparks et al., 2017). We consider only the first two in this work in the context of enhancing the oxygen exosphere as modeled in Figure 2.14. H_2O unlike O_2 does not migrate substantially due to its high sticking coefficients, and thus possible $O_2 + H_2O$ collisions are thought to occur at the region of ejection of H_2O . For sublimation this is generally the subsolar point, or noon, and for sputtering this is the anti-corotation direction, at the trailing hemisphere. In our simulations O_2 is ejected following a MB distribution whereas H_2O ejected by sputtering from the surface follows a $f(E) = \frac{2U}{(E+U)^3}$ distribution as was also described



(a) No Collisions. fMB

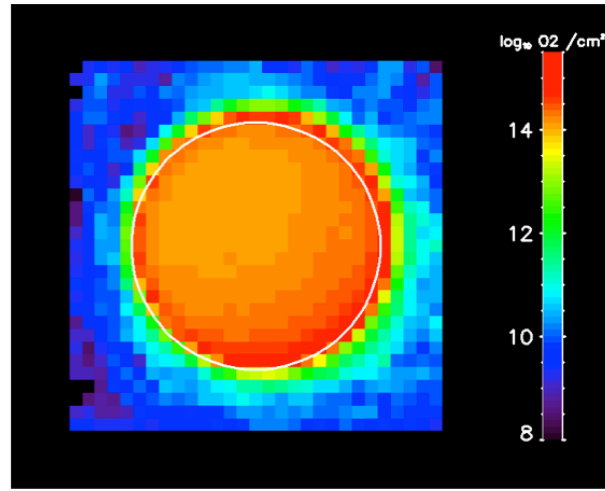
(b) O₂ + H₂O collisions. fMB

FIGURE 2.14: Simulated LOS column densities with and without O₂+H₂O collisions, at subobserver longitude of 20 degrees. O₂ collisions are thought to occur with H₂O near sublimation + sputtering sites where the column is largest.

by [Shematovich et al., 2005]. Consequently, H₂O sputtered from the surface is much more energetic than the radiolytically sputtered O₂ (§2.7.1). When ejected, H₂O might collide with the O₂ exosphere and populate the corona. We therefore simulate this interaction following an algorithm described in Leblanc et al. [2017a].

We simulate LOS column densities near $N_{H_2O} \sim 10^{14}$ H₂ O cm⁻² at the surface, and decreasing slowly to $N_{H_2O} \sim 10^{13}$ H₂ O cm⁻² at $1.25 r_{Eu}$. Using a collisional cross-section of $\sigma_{O_2+H_2O} \sim 2 \cdot 10^{-15}$ cm², Figure 2.14 shows simulated LOS column densities with and without collisions. One can see collisions are capable of extending the scale height of the O₂ exosphere. This radial extension is capable of expanding the exosphere to larger scale heights fit to observations. Beyond $1.4 R_{eu}$ however, there is

not a large enough LOS O₂ column, $N_{O_2} \ll 10^{13} \text{ O}_2 \text{ cm}^{-2}$, to reproduce the auroral intensities suggesting an alternate transport mechanism.

2.10 Conclusion/Summary

Guided by our EGM simulations of Europa's neutral exosphere as well as the HST auroral oxygen observations carried out by R15 throughout Europa's orbit we find, without exception, evidence of neutral O₂ accumulating at dusk-over-dawn by more than a factor of 1.5. This finding is consistent with the dusk-over-dawn brightening of HST oxygen aurorae, and strongly suggests that Europa's entire near-surface exosphere ($r \lesssim 1.25r_{Eu}$) experiences a diurnal cycle driven primarily by Europa's rotation. This exospheric oxygen cycle is best regarded in the point of view of the bulk O₂ source at Europa's plasma ram/trailing hemisphere:

1. **Plasma Ram Day:** The trailing hemisphere source is illuminated and rapidly builds an O₂ column rotating with Europa's surface, ejecting between $\sim 2.5 - 3.5 \cdot 10^8 \text{ O}_2 \text{ cm}^{-2} \text{ s}^{-1}$ throughout the day from $180^\circ \rightarrow 0^\circ$.
 - After half of an orbit, the rotating O₂ column has accumulated an atmospheric bulge of average density $\langle N \rangle_{O_2} \gtrsim 8 \cdot 10^{13} \text{ O}_2 \text{ cm}^{-2}$ spread across a quarter of a hemisphere from **dusk**, local time.
2. **Plasma Ram Night:** The trailing hemisphere source enters night, at which point the e⁻-impact dissociation begins to slowly overwhelm the O₂ production and acts to isotropically diminish the bulk O₂ exosphere from $0^\circ \rightarrow 180^\circ$.

A similar cycle appears to be present in Ganymede's atmosphere [Leblanc et al. \[2017a\]](#) and may have also been observed in Ganymede's FUV oxygen aurorae [\[McGrath et al., 2013\]](#). We note that these O₂ bulges maintained at dusk, hinge on the fortuitous timescales of these two icy Galilean satellite exospheres. The orbital timescale is comparable to the average exospheric lifetime of the O₂, so that $\tau_{orb} \sim \tau_{O_2}$. In other words, the O₂ exosphere survives long enough so that the rise and fall of the O₂ exosphere is linked with the solar cycle. If the O₂ exosphere survived for too long, for instance $\tau_{orb} \ll \tau_{O_2}$, the continued production would average out any bulges due to the diurnal cycle. If the O₂ exosphere was destroyed too quickly on the other hand, $\tau_{orb} \gg \tau_{O_2}$, the diurnal asymmetries would not have time to build a bulge. This near-resonance between the orbital time and the O₂ lifetime is remarkably unique in that a consistent, and predictable asymmetry can be observed with local time.

In this work we sought to model Europa's neutral O₂, with minimal plasma assumptions, when describing only the near-surface component, we find that the neutral dynamics are sufficient to act as the primary driver for the near-surface exosphere. Upon comparing with observations we are able to identify a couple principal, unresolved issues on Europa. While the near-surface O₂ can roughly reproduce the on-disk auroral intensities, and account for the global dusk-over-dawn asymmetry, the oxygen corona is rapidly expanded by an, as of yet, unknown mechanism likely linked to atmospheric collisions and/or Jovian plasma interactions with Europa's putative ionosphere. By simulating various heats of adsorptions (E_{ads}) for O₂, we confirm that the interaction between exospheric molecules with the surface is critically important. That is, the porosity, composition, and thermal properties affect the exospheric behavior, quenching the O₂ density over time.

When the atmospheric medium is a near-vacuum ($P_0 \leq 1nB$), and the volatiles experience relatively short hop times, the volatiles significantly interact with the surface.

While we believe the residence time of the O₂ adsorption to Europa's surface ice is small, in certain regions it may be significant. Although the dusk-over-dawn asymmetry in the column density occurs even for our simplest assumptions, it is overestimated by a factor of five when dusk, Europa local time, is closely aligned with the sub-Jovian hemisphere ($90^\circ < \phi_{obs} < 150^\circ$). This appears to indicate a process regulating O₂ density, either by surface ice adsorption (§2.9.2) or one or more of the exospheric loss processes discussed above (§2.9.4). In the Saturnian system, polar adsorption coupled with diffusion was also recently shown to influence the seasonal O₂ and CO₂ exospheric bulges of Rhea and Dione [Teolis and Waite, 2016]. Unlike the Saturnian system, where the Cassini-INMS directly detected O₂ at Rhea Teolis et al. [2010], oxygen aurorae are the only data we have with current instrumentation to infer the presence and distribution of O₂ exospheres in the Jovian system. Other tenuous species, such as Na & K have been probed by ground-based telescopes (Brown and Hill [1996] and Brown [2001] respectively). Simulating the behavior of these species could imply that there are further orbital asymmetries which can help in assessing the possibility of potential endogenic sources [Leblanc et al., 2002].

In this work we have provided strong evidence that Europa, hosts a dynamic neutral environment evolving over an orbital period. The exospheric dynamics which generate the apparent O₂ cycle evolving under rotation, are not only of particular interest in the context of future spacecraft trajectories at the icy Galilean satellites (e.g. NASA's Europa Clipper; ESA's JUICE) but also in assessing the environments of the numerous tidally-locked exoplanets known to have atmospheres.

2.11 Summary and Future Prospects of Chapter 2

In this chapter we find that the ability for satellite exospheres to generate observable atmospheric bulges is principally due to solar insolation acting on the satellite's surface while it rotates. In other words, the surface experiences a diurnal cycle which is coupled to the exosphere, should the species have a thermal dependence like O_2 . The species however must be heavy with a modest jeans parameter so that it is strongly gravitationally bound to the surface. H_2 is thought to be radiolytically produced in the same way as O_2 for example, yet one should not expect an atmospheric bulge.

Right-to-left hemispheric ratios vary from 0.93-0.97 throughout the orbit. H_2 is $16 \times$ lighter than O_2 , yielding speeds $v \propto m^{-1/2}$, $4 \times$ as fast. The greater kinetic energy results in larger ($16x$) and longer ballistic hop times ($4x$ longer ($t \sim 30$ minutes)). This implies a H_2 molecule travels half a European radii in one hop. When simulated H_2 turns out to hold the most symmetric exosphere of all water-products, which we will explore in detail in the next part of this thesis. Of course much of the molecular hydrogen also escapes along with many other water-products, possibly populating a torus of gas along the satellite's orbit, an exciting prospect we shall also consider in the next part of this thesis.

Part II

Perspectives on Ocean World

Exospheres

The prospect of abundant quantities of liquid water is perhaps one of the most exhilarating aspects in the study of icy satellite exospheres. Many icy satellites, in the far reaches of the outer Solar System are now thought to possess global oceans, recently referred to as 'ocean worlds': Europa, Ganymede, Callisto, Enceladus, Titan, Triton, Ceres, and Pluto [Hendrix et al. \[2017\]](#). Of these ocean worlds, certain bodies require the presence of liquid conductive material to explain measurements (e.g. Europa via Galileo magnetometer data [Khurana et al. \[1998\]](#), and Ganymede via HST observing damped oxygen auroral oscillations ([Saur et al., 2015](#))). Europa arguably holds the strongest evidence out of these ocean worlds of a global, liquid, saltwater ocean which may currently bear life today. Unlike Enceladus [Čuk et al. \[2016\]](#), it is almost certain that Europa was formed *in-situ*, in a disk of gas around Jupiter [Heller et al. \[2015\]](#). Thus, it is conceivable that the Laplace Resonance, responsible for the extreme gravitational tidal forces at Europa has been acting to heat the interior ocean for the last four billion years. This large span of time is critical for entropy to act and evolve molecules into a more complex state leading to the autonomous behavior expected of life [England \[2013\]](#). Following a similar logic as the conception of the first lifeforms on Earth, namely hydrothermal vents acting on the seafloor over an elongated period of time, Europa is therefore the most likely to host life [Russell et al. \[2014\]](#). In this part, given the momentous venting observations reported during this thesis ([Roth et al. \[2014b\]](#); [Sparks et al. \[2016a\]](#); [Sparks et al. \[2017\]](#)) I seek to discuss first, the exogenic behavior of water and its exospheric products over Europa and Ganymede's orbit, as to isolate this influence from the possible endogenic sources. As the endogenic sources are at best poorly known, I provide estimates based on our EGM model along with a tidal stress model, to predict the ability for a tidally-locked satellite to vent endogenic material to the surface today §3.4.2.

Exogenic & Endogenic

Water-Product Exospheres:

Examining Europa & Ganymede

Ensemble

A version of this section is in preparation for a presentation at the European Planetary Science Congress in September 2017.

Europa and Ganymede are thought to possess globally similar exospheres, in spite of the possibility that Europa is currently cryovolcanically active, and Ganymede's intrinsic magnetic field. Ions in Jupiter's magnetosphere bombard the icy surfaces, and produce an exosphere predominantly composed of O_2 , with slightly less H_2O and H_2 due to freezing and escape respectively. I investigate and compare the water-product exospheres of the two satellites under rotation, using our 3-D Exosphere Global Model (EGM). In previous works ([Oza et al. \[2017\]](#), [Leblanc et al. \[2017b\]](#)), I focused on the near-surface $z < 1.25r_s$, oxidized component of the exosphere, dominated by thermalized O_2 , which undergoes a dusk-over-dawn asymmetry due to diurnal solar insolation of the surface over the satellite's orbit. This was observed by asymmetries in oxygen aurorae. Here, I focus on characterizing the hydrogen-species: H , H_2 , and H_2O which have been far more elusive as Lyman- α emission has multiple production pathways.

3.1 Introduction to Water-Product Exospheres

Water-product exospheres surrounding ocean worlds are unique in that certain apparent components of their exospheres could also be vented from their subsurface oceans. Therefore a comprehensive understanding of the *exogenic* physics and *endogenic* physics is ultimately required to evaluate the satellite exosphere as a whole.

Water is produced exogenically on Europa and Ganymede by two mechanisms: solar insolation sublimation and magnetospheric ion sputtering. The former yields a thermal profile of water vapor which is quite similar to molecular oxygen. The latter is energetic as the water molecules are thought to leave the water ice lattice at high velocities. A portion of these bombarded water molecules undergo radiolysis in the regolith, leading to the population of exospheric molecular hydrogen and oxygen.

Smaller quantities of atomic hydrogen along with other trace species are also thought to be ejected into the exosphere. The sputtering production rates are difficult to constrain in the laboratory, due to uncertainties in surface ice concentration, grain sizes, and porosities. The trace water-product species (H, O, and OH) are also produced by photon and electron-impact dissociation of H₂O, H₂, and O₂. Only O₂ has been relatively well constrained on these worlds. At Europa, I have employed the globally-averaged sputtering rates by Cassidy et al. [2013] and find that these rates are able to reproduce the behavior and magnitude of the near-surface O₂ component reasonably well Oza et al. [2017]. However, auroral profiles by the HST seem to suggest the O₂ corona $z \gtrsim 1.25r_s$, is much more abundant than expected, suggesting energetic mechanisms that populate the corona. One mechanism could be O₂ collisions with the background H₂O atmosphere mentioned above. Additionally, the interaction with the Io-plasma torus could result in elastic, ion-neutral scattering or charge exchange of the near-surface component, enhancing escape rates which are uncertain at the present. At Ganymede, Leblanc et al. [2017b] showed that uncertainties in water vapor sublimation fluxes can produce vastly different behavior of the H₂O column density over the orbit §3.4.1.

In this chapter I first review the ground breaking water-product observations by HST and Herschel, and discuss their implications. As these observations display significant orbital asymmetries, I present recent EGM simulations of the line-of-sight column densities expected at Europa and Ganymede based on current sputtering and sublimation theory. To date, these observations have not yet been fully reconciled with neutral exosphere models, and thus I discuss the possible implications. Given the current uncertainties I scrutinize the well-known production mechanism of water vapor, water ice sublimation, and provide a perspective on the possibility that Europa's exospheric water vapor density may be influenced by tidal heating.

3.2 Water-Product Observations: Water Vapor and Atomic Hydrogen

Until three years ago, the icy, tidally-heated satellites, Europa and Ganymede, had no evidence regarding the presence of H_2O in their exospheres. These recent findings have reinvigorated the astronomical community to search for water on these worlds.

The 2014 observational evidence of water vapor was at Europa gathered from auroral inhomogeneities near Europa's leading hemisphere ($\phi_{orb} \sim 90^\circ$), observed over seven continuous hours [Roth et al., 2014b].

The UV auroral lines observed were hydrogen Lyman- α (1216) and the oxygen line at 1304, with auroral intensities of ~ 600 Rayleighs in Ly- α . The most likely explanation for the inhomogeneities are transient electron-impact dissociated water vapor plumes, which were not observed again at the same orbital longitudes (Roth et al. [2014a]). If this was indeed the source of the HI and OI auroral emissions, the water column would be $N_{H_2O} \sim 1 - 5 \cdot 10^{15} cm^{-2}$ roughly two orders of magnitude greater than the expected sputtered/sublimated water vapor exosphere (§3.4.1).

It was shown next year by Roth et al. [2015] that the tilt of the Io-plasma torus with magnetic latitude regulates the auroral inhomogeneities (c.f. Roth et al. [2015] Figures 10 A & B). Thus, an excess auroral inhomogeneity due to a large variance in plasma is unlikely during the windows of observation as the observed anomaly persisted over seven hours at the same hemisphere, much longer than the time expected for a plasma torus-driven anomaly $\sim 5hours$ where the moon is on either side of the plasma sheet. Most apparent is that the intensity of the Ly- α emission line $R \sim 600 Rayleighs$ is too large for resonant scattering on H atoms, sputtered or sublimated in Europa's exosphere from its surface.

3.2.1 Water Vapor Plumes

Roth et al. [2014b] (supplementary materials) constructed an ad-hoc atmospheric model based on their observations. Cross-sections from Hall et al. [1995] & Hall et al. [1998] were used, and e- impact excitation rates from various laboratory analyses. The electron density was chosen as $n_e = 40 cm^{-3}$. 2% of the electrons are assumed to be suprathermal with $T_e = 250eV$ while the rest are nominally $T_e = 20eV$ as in our simulations.

Roth et al. [2014b] modeled the plume density profile over altitude z , and angular size of the plume source θ , as a fit based on the inferred surface H_2O density, n_0 as:

$$n_{H_2O}(z, \theta) = n_0 \exp \left(-\left(\frac{z}{H_z}\right)^2 - \left(\frac{\theta}{H_\theta}\right)^2 \right) \quad (3.1)$$

where H_θ is a length scale of 10° and $H_z = 200$ km is the vertical scale height for the water plume. There are many unknowns that may deserve further investigation.

Firstly, it is unknown whether there were two plumes (Roth et al. [2014b]) or one plume (Teolis et al. [2017b]).

The upwards, endogenic mass loss can be written as:

$$\dot{M}_{H_2O} = A \rho u \quad (3.2)$$

where $A = lw$ is the plume area: l is the length of the fractures $\sim 1000 - 10,000$ km and w the width of a narrow fracture \sim cm (Goguen et al.). ρ is the inferred plume density equivalent to $\rho \sim 8.4 \cdot 10^{-8} \text{ g cm}^{-3}$. If one assumes that the observations correspond to two plumes, the upwards mass loss rate is quite high $\dot{M} = 7000 \text{ kg/s}$, with a moderate ejection velocity of $u_2 \sim 560 \text{ m/s}$, consistent with plumes heated to 230 K. On the other hand, it could be that there is only one plume Teolis et al. [2017b], with a much smaller mass loss rate $\dot{M} = 500 \text{ kg/s}$, with a corresponding larger velocity $u_1 \sim 1 \text{ km/s}$. Both of these plumes are of course consistent with the inferred H_2O column of $N_{H_2O} \sim 10^{16} \text{ cm}^{-2}$.

The water plume mechanism on Europa however, needs to be consistent with tidal heating of the core or an extreme enhancement of sublimation which we will explore in §3.4.2. Although, the orbital location of the water plumes was near apojove, it was not necessarily a sufficient condition to drive tidal activity Roth et al. [2014a] and thus alternative explanations invoking obliquity tides for example have been invoked since ([Rhoden et al., 2015]).

The consequences of plumes, or in general, a higher flux of H_2O , would contribute to a larger hydrogen column and more intense Lyman-alpha and oxygen emission via e-impact dissociation due to the following reactions Makarov [2004]:

- $H_2O + e^- \rightarrow H^* + H + O + e^-$
- $H_2O + e^- \rightarrow H^* + OH + e^-$
- $H_2O + e^- \rightarrow O^* + H_2 + e^-$

The efficiency of dissociation is dependent of course on the collisional cross sections. Figure 17 of [Itikawa and Mason \[2005\]](#) provides cross sections for the e^- impact dissociated emissions of water vapor at 1216 and 1304 .

Understanding the water plume mechanisms will rely on knowledge of the overall exospheric environment of Europa, which we believe our exospheric simulations can contribute to. The overall exosphere however, has not yet been observed §3.2.2, and its exospheric evolution §3.3 is still not understood. Besides the insight gained from our detailed work on the near-surface O_2 in the previous chapter, the only evidence left to understand the water species is Europa's hydrogen corona.

3.2.2 Europa Exospheric Hydrogen Observations

Evidence for Europa's hydrogen has been indirect until 2017. Recently, [Roth et al. \[2017\]](#) has helped constrain the atomic hydrogen column density at Europa, via HST transit observations. The Ly- α absorption at 1216 Å of Europa's exosphere when transiting Jupiter's solar reflectance Lyman alpha, appears to indicate a column of $N \sim 10^{12} \text{ H cm}^{-2}$ corresponding to ~ 80 Rayleighs of hydrogen auroral emission [Roth et al. \[2017\]](#). The derived number densities range from $n_E \sim 1.5 - 2.2 \cdot 10^3 \text{ H cm}^{-3}$.

At Ganymede the Lyman-alpha emission is even more mysterious as it is extremely large, when compared to models [Marconi \[2007\]](#); [Turc et al. \[2014\]](#). The Lyman-alpha intensity of $I \sim 560R$ was interpreted by [Barth et al. \[1997\]](#) to correspond to an atomic hydrogen density of $n_H = 1.5 \cdot 10^4 \text{ H cm}^{-3}$ with a scale height of 2634 km, yielding a column of $N_H \sim 4 \cdot 10^{12} \text{ H cm}^{-2}$ at Ganymede.

The sputtered atomic H, I simulate, leads to a line-of-sight density near $N_H \sim 10^{11} \text{ cm}^{-2}$ and is thus far less abundant than O_2 , H_2 , or H_2O . Furthermore there is a factor of 10 missing from the inferred maximum column of neutral H, from [Roth et al. \[2017\]](#). Thus, I simulate the 'background' exosphere to gain insight into the role of e^- impact, photo-dissociation of H_2O and H_2 in generating exospheric H at Europa.

3.3 Orbital Evolution of Exospheric Water Products

I simulate the orbital evolution of the dominant hydrogen species to gain an understanding of the range of column densities Europa and Ganymede experience throughout their orbit (Figure 3.1), some of which will be observed as Ly- α emission. These simulations represent nominal cases, where there are no enhancements due to

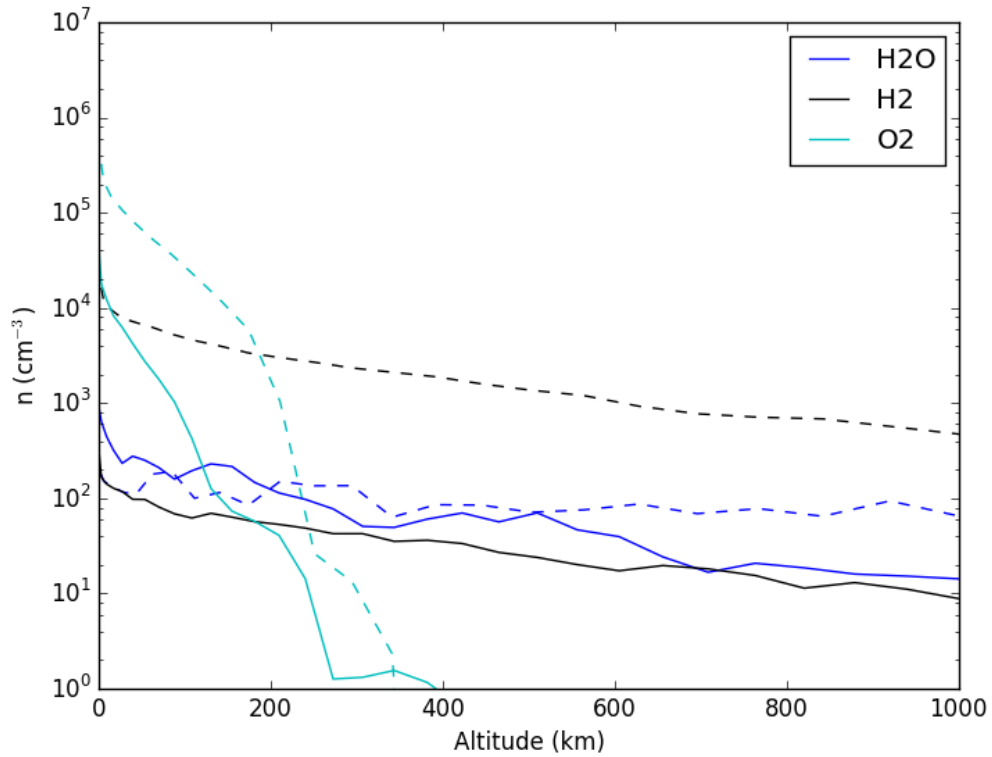


FIGURE 3.1: Simulated surface densities for the dominant species in Europa (solid) and Ganymede's (dashed) exospheres at the sunlit trailing hemisphere. The H_2O case represents a low-sublimation case[2].

ion interactions, nor are there endogenic water plumes contributing to the exospheres. This permits one to first assess the steady-state component of the exosphere, and its orbital variations.

3.3.1 H_2O Variability: Leading/Trailing Asymmetries

The leading hemisphere of the icy Galilean satellites is of particular interest due to a variety of reasons. Firstly, the only direct evidence of exospheric water vapor on a Galilean satellite has been at Ganymede [Hartogh \[2012\]](#). I seek to explain this leading/trailing dichotomy by discussing all exogenic parameters first, which can influence the observed leading-trailing asymmetry (bond albedo, sublimation, sputtering etc.)

Table [4.1](#) additionally reports simulated sputtering rates for each species as well as disk-averaged column densities at leading versus trailing. Values in parentheses are simulations ran for a higher water sublimation rate ([\[Fray and Schmitt, 2009\]](#)).

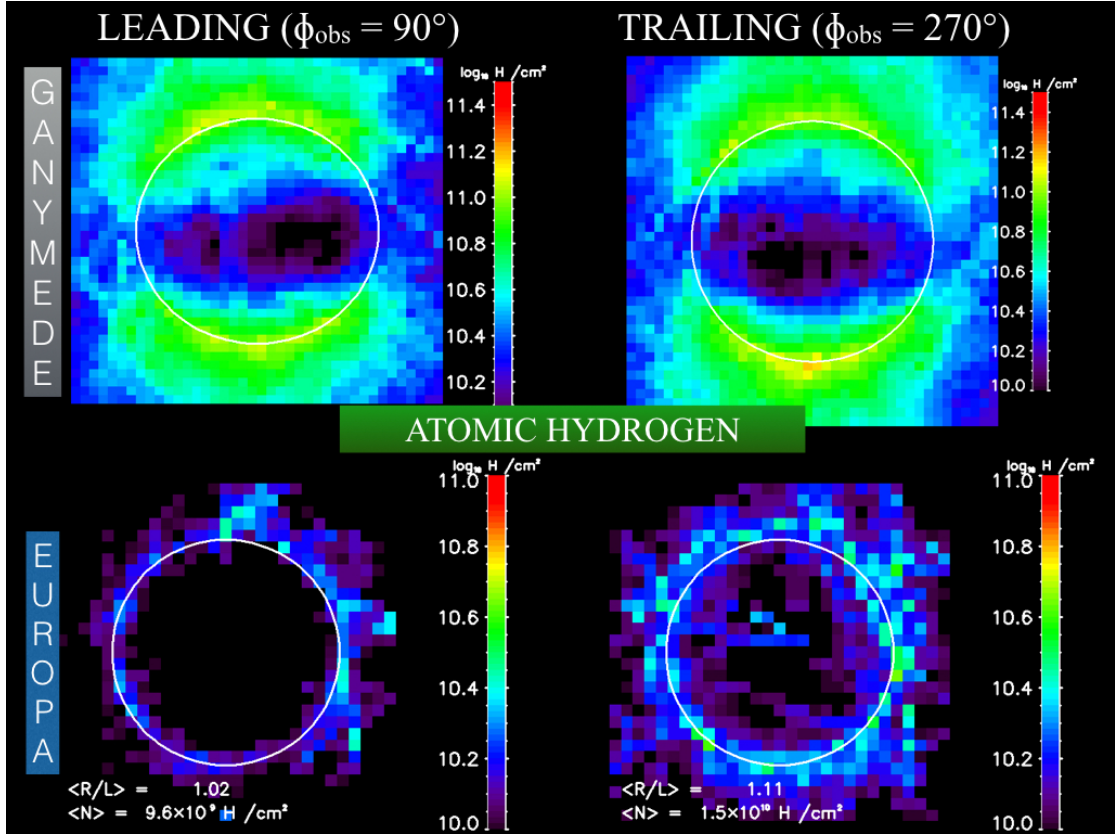


FIGURE 3.2: Line-of-sight column density maps for atomic hydrogen on Europa and Ganymede. The right hand side is the sunlit trailing hemisphere (T), and the left hand side is the sunlit leading hemisphere (L). The average line-of-sight columns for our nominal assumptions for Europa are: $\langle N_H \rangle \sim 1.2 \cdot 10^{10}$.

From sunlit trailing to leading, I calculate Europa's exosphere to decrease by $\sim 36\%$ in atomic hydrogen, 60% in H_2 , and 43% in H_2O . The atomic hydrogen column is $\sim 10^{10} H cm^{-2}$, whereas H_2 and H_2O are $\sim 10^{13} cm^{-2}$. Ganymede's atomic H ($N_H \sim 10^{11} cm^{-2}$) peaks at the poles and also decreases by $\sim 50\%$, whereas H_2 ($N_{H_2} \sim 10^{15} cm^{-2}$) and H_2O ($N_{H_2O} \sim 10^{14} cm^{-2}$) fall by an order of magnitude at sunlit leading.

Observed hydrogen column densities appear to be 1-2 orders of magnitude higher than our atomic H simulations, possibly suggesting more efficient atomic H sputtering rates, or more efficient exospheric H production via H_2 and H_2O . A similar phenomena may be present at Ganymede, in that the interpretation of the Galileo observations [Barth et al. \[1997\]](#) also imply an excess amount of atomic hydrogen than expected. The excess atomic hydrogen could be due to H_2O e- impact dissociation, which is then one of the main drivers for Ly- α emission. As H is also rapidly escaping from Europa, it is possible that it is also influencing Cassini's ENA observations far from Europa towards Ganymede in the so-called Europa-Ganymede neutral torus ([Mauk et al. \[2003\]](#)) which I will expand on in a later chapter.

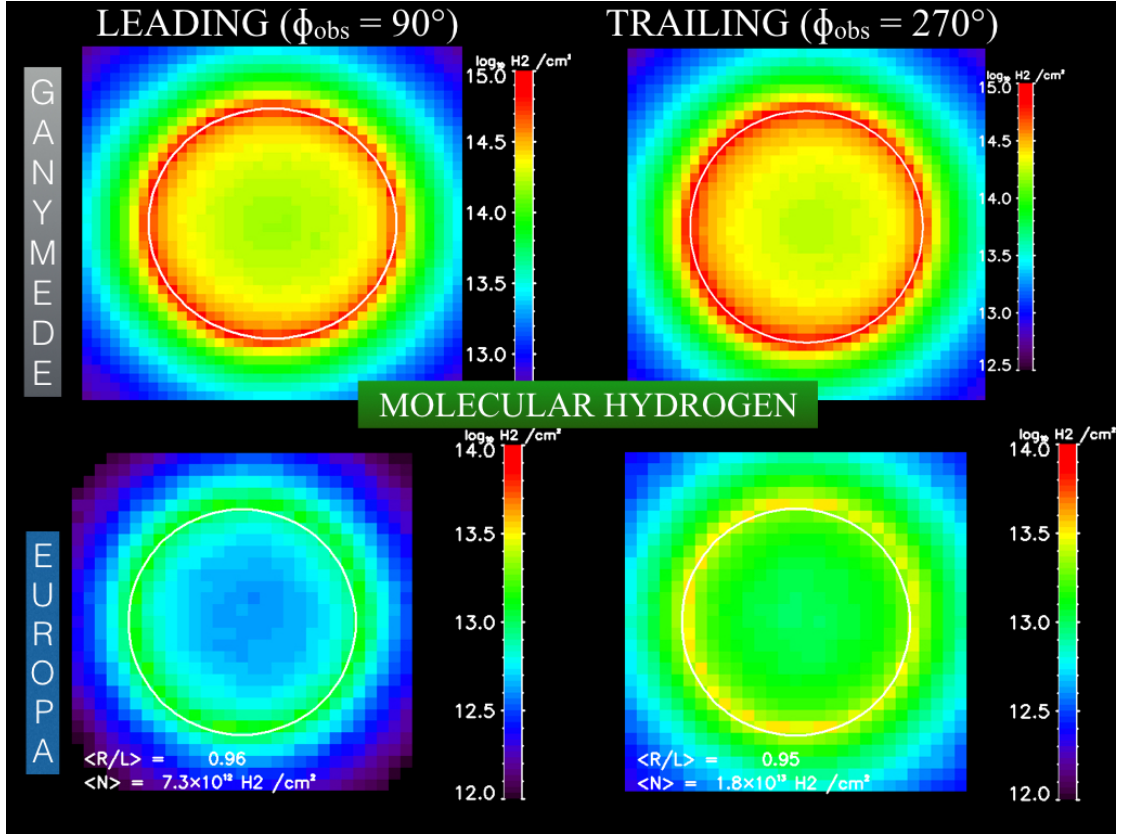


FIGURE 3.3: Line-of-sight column density maps for molecular hydrogen on Europa and Ganymede. The right hand side is the sunlit trailing hemisphere (T), and the left hand side is the sunlit leading hemisphere (L). The average line-of-sight columns for our nominal assumptions on Europa are: $\langle N_{H_2} \rangle 1.3 \cdot 10^{13}$.

3.4 Perspective on Water Vapor Production Mechanisms

Water vapor production mechanisms are poorly constrained on icy satellite exospheres. One of the reasons is a lack of direct observations, but another is a relatively poor understanding of the physics that govern sublimation (driven by radiation) and sputtering (sourced by magnetospheric ions) of H_2O , which I group into a category called: *surface-ice generated exospheric H_2O* §3.4.1. The second production mechanism is sourced from the subsurface liquid water, and thus I refer to it as *ocean-generated exospheric H_2O* in nature §3.4.2. Here it is the stretching and squeezing of the satellite's interior due to differential gravitation acting on the body which may result in significant heating, eventually pushing water reservoirs from the satellite interior to the surface, as observed on Enceladus Porco et al. [2006] and Io PC79. I seek to evaluate this so-called tidal heating mechanism for Europa as if this heating is significant, the resulting exospheric signatures should be observable by both ground-based and in-situ instruments in the near-future.

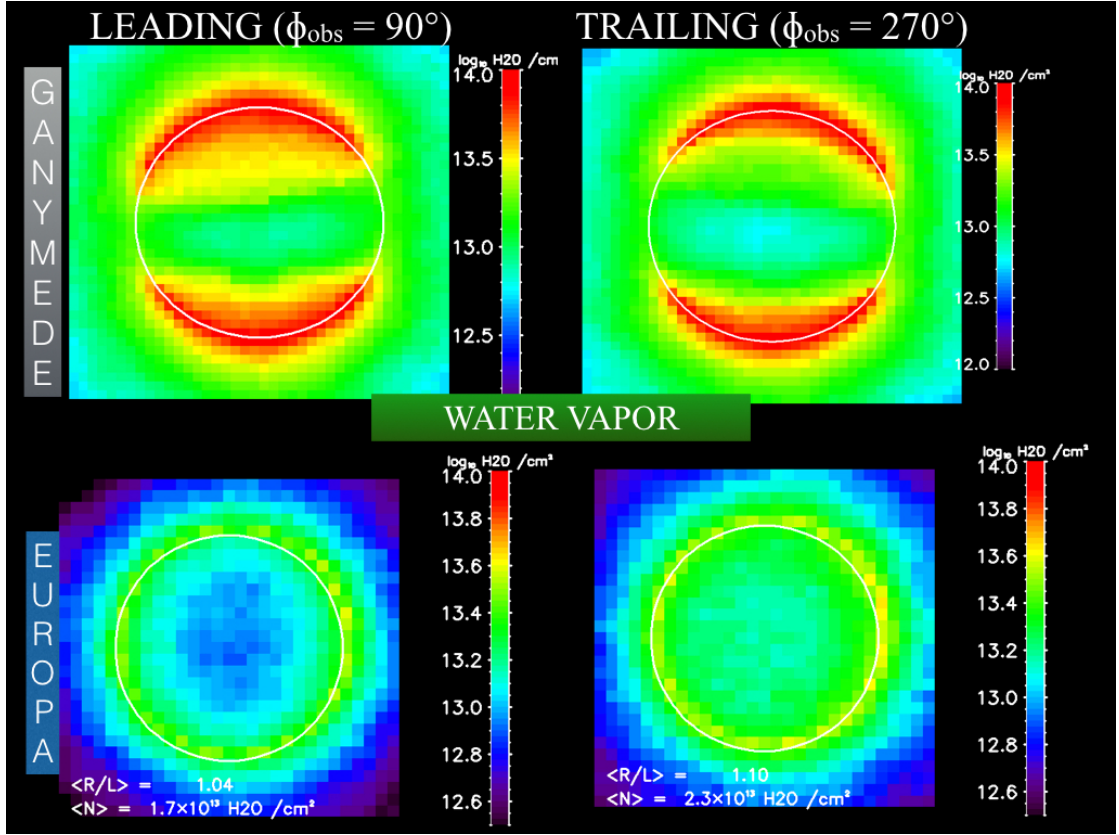


FIGURE 3.4: Line-of-sight column density maps for water vapor on Europa and Ganymede. The right hand side is the sunlit trailing hemisphere (T), and the left hand side is the sunlit leading hemisphere (L). First row: atomic hydrogen. Second row: molecular hydrogen. Third row: water vapor. The average line-of-sight columns for our nominal assumptions for Europa are: $\langle N_{H_2O} \rangle 2 \cdot 10^{13}$.

These perspectives on water vapor production are critical in our understanding of satellite exospheres, as many exospheric molecules are intertwined with H_2O molecules, often in caged molecular structures (clathrates) [Hand et al. \[2006\]](#). Thus, assessing and estimating the quantity of H_2O helps one assess the density and behavior of the exosphere. Lastly, our understanding of icy bodies in general such as comets and dwarf planets may be heightened by scrutinizing Europa and Ganymede. Recent observations by Herschel at the dwarf planet Ceres [Küppers et al. \[2014\]](#) have found that the laboratory constrained sublimation rates do not match what is occurring at Ceres. Thus, we are living in an era where the exogenic and endogenic H_2O degeneracy is present across many icy bodies.

3.4.1 Surface Ice-Generated Exospheric H_2O

We choose to scrutinize water ice sublimation in particular because there is evidence that it should behave very different than what has been tested in the laboratory. The

Species	$\Phi_{sputt} s^{-1}$	$\Phi_{net} cm^{-2} s^{-1}$	$\langle N \rangle_{trailing} cm^{-2}$	$\langle N \rangle_{leading} cm^{-2}$
H	$7.3 \cdot 10^{24}$	$3 \cdot 10^7$	$3 (3.2) \cdot 10^{10}$	$2.1 (1.9) \cdot 10^{10}$
H ₂	$2.4 \cdot 10^{27}$	$5.6 \cdot 10^8$	$1.8 \cdot 10^{13}$	$7.3 \cdot 10^{12}$
O	$7.29 \cdot 10^{24}$	$3 \cdot 10^7$	$2.1 (2.4) \cdot 10^{11}$	$1.8 (2.1) \cdot 10^{11}$
OH	$7.3 \cdot 10^{24}$	$3 \cdot 10^7$	$2.3 (5.8) \cdot 10^{11}$	$1.3 (0.94) \cdot 10^{11}$
O ₂	$1.2 \cdot 10^{26}$	$2.8 \cdot 10^8$	$2.5 \cdot 10^{14}$	$2.5 \cdot 10^{14}$
H ₂ O (high sub)	$2.2 \cdot 10^{27}$	$8.0 \cdot 10^9$	$1.1 \cdot 10^{14}$	$1.5 \cdot 10^{13}$
H ₂ O (low sub)	$7.3 \cdot 10^{24}$	$2.6 \cdot 10^7$	$2.2 \cdot 10^{13}$	$1.6 \cdot 10^{13}$
H ₂ O EGM U2	$2 \cdot 10^{27}$	$6.7 \cdot 10^9$	$1.7 \cdot 10^{13}$	$2.3 \cdot 10^{13}$

TABLE 3.1: Sputtering & sublimation Fluxes for water volatiles with corresponding column densities. Values in parentheses are for a simulation with a high sublimation rate. The relative sputtering yields are 0.01, 0.3, 0.01, 0.01, 0.15 for H, H₂, O, OH, and O₂. The sputtering rate is computed by multiplying the sputtering flux Φ_{sputt} by the surface area of Europa, $4\pi r_{eu}^2$. Φ_{net} is computed using an incident ion flux of 1.6e8, and yields reported in Cassidy et al. [2013], at a longitude in between the trailing and leading hemispheres. Water vapor production is considered only at the sub-solar hemisphere. $\langle N \rangle$ are the average line of sight column densities computed for the trailing hemisphere $\Psi = 90$ and leading $\Psi = 270$. The exospheric residence time of the sputtered species can be computed if desired as in Smyth and Marconi [2006]: $t_{res} \approx \langle N \rangle / \Phi_{net}$. **Reference:** EGM U2 10.2017 02; H₂O EGM U2 is a simulation run where the O₂ ejection flux is taken to be a U2 distribution as described in Ch.2.

motivation behind this scrutiny is a potential discovery by Herschel of H₂O vapor vastly larger at Ganymede's sunlit leading hemisphere Hartogh [2012]. The observation implies a column of $\sim 6 \cdot 10^{13} H_2O cm^{-2} \pm 60\%$. The sunlit trailing hemisphere on the other hand yields $\sim 3 \cdot 10^{12} H_2O cm^{-2} \pm 20\%$. When compared to vapor pressure models from Fray and Schmitt [2009], Johnson et al. [1981], as tested in Leblanc et al. [2017a] it would appear that the sublimation flux is orders of magnitude weaker than in the laboratory implying either a quenching mechanism or a very different crystalline ice surface than previously thought on Ganymede. I return to an analytical approach so that we can question the assumptions of water vapor production.

Johnson et al. [1981] provided one of the first estimations of H₂O vapor at Europa and Ganymede based on a balance between the sputtering flux (or equivalently the sublimation flux) and the escape flux $\Phi_{net} = \Phi_{sputt} - \Phi_{esc}$. The column density can be thus determined if the sticking coefficient is known s :

$$N_{H_2O} = \frac{2 (2\pi m k_b T)^{1/2}}{s mg} \Phi_{net} \quad (3.3)$$

We recall that the Jeans-escape parameter helps us easily determine the escape flux: $\Phi_{esc} = \Phi_{sputt}(1 + \lambda)e^{-\lambda}$. To treat the problem of escape in detail, I invite the reader to examine Appendix A for a full discussion on new analytical escape rates, for collisional and collisionless exospheres derived from detailed fluid and DSMC simulations for

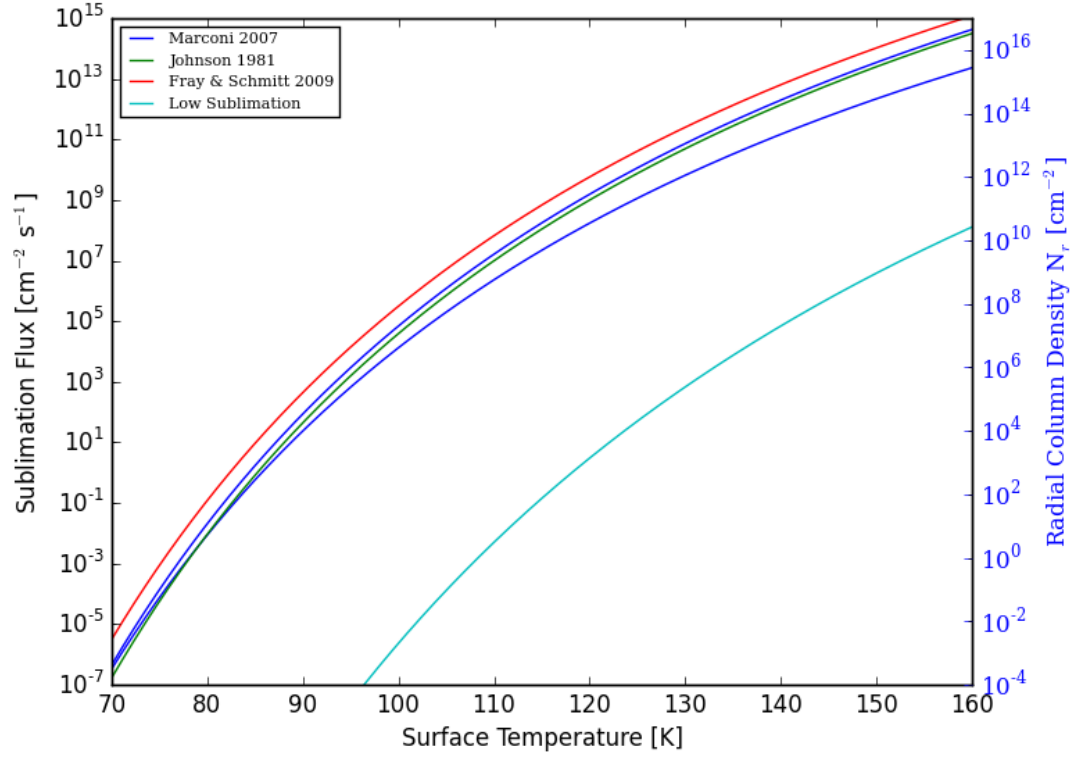


FIGURE 3.5: Water Vapor sublimation flux as calculated in [Leblanc et al. \[2017a\]](#) and corresponding column density taken for an atmospheric lifetime equivalent to Ganymede's orbit. The derived column densities for the low sublimation case are not representative as they have not yet reached steady state.

bodies with moderate Jeans parameters like these icy satellites ¹. Besides escape, the water vapor flux which sources this water vapor column is often uncertain and fit as well, following [Marconi \[2007\]](#):

$$\Phi_{sub} = aT^{1/2} \exp\left(\frac{-b}{T}\right) \quad (3.4)$$

We plot the water vapor flux in Figure 3.5 with a corresponding column density computed via Eqn. 3.3. The four sublimation cases which are plotted are those that are employed in [Leblanc et al. \[2017a\]](#) tabulated here:

This figure is especially curious because the low sublimation case, first presented in [Leblanc et al. \[2017a\]](#) orders of magnitude below the nominal cases, is the only case which accurately reproduces the column densities which have been potentially observed by Herschel [Hartogh \[2012\]](#).

¹ Appendix Equation 2b provides an expression for escape due to surface heating, fit to parameters depending on the Knudsen number. Appendix Equation 3a and equivalently Equation 4 provide expressions for escape due to upper atmospheric heating.

Model	a cm ⁻² s ⁻¹	b [K]
Johnson et al. 1981	1.9e32	6146
Marconi 2006	1.1e30	5737
Fray & Schmitt 2009	2.2e32	5950
Low Sublimation (Leblanc et al. 2017)	1.9e32	8500

When we simulate water vapor, we find that it behaves quite differently should the sublimation be high. The column density can increase by a factor of 2 and additionally it can be concentrated at the sub-solar point at the trailing hemisphere cases: Figure 3.6. It can be seen that once Europa leaves eclipse (orbital egress) the water vapor exosphere follows more of a sputtering dependency with respect to the plasma ram direction (incident plasma) and the surface temperature (solar insolation).

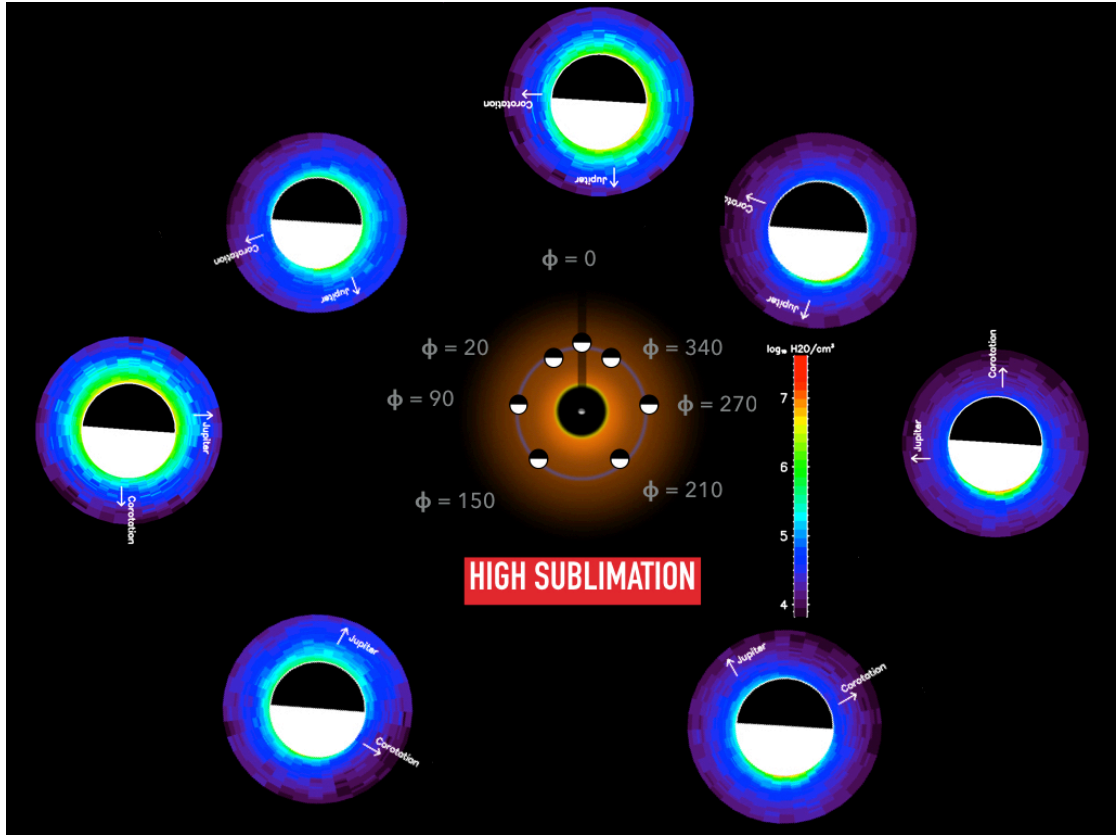


FIGURE 3.6: H₂O High Sublimation. The color gradient for this simulation peaks at $n \sim 10^{6.5} \text{ cm}^{-3}$

The lower sublimation rate produces a density map which is more consistent with atomic hydrogen which has no thermal dependence Fig. 3.7

From this analysis I converge on two conclusions:

If Europa's water is sputter dominated:

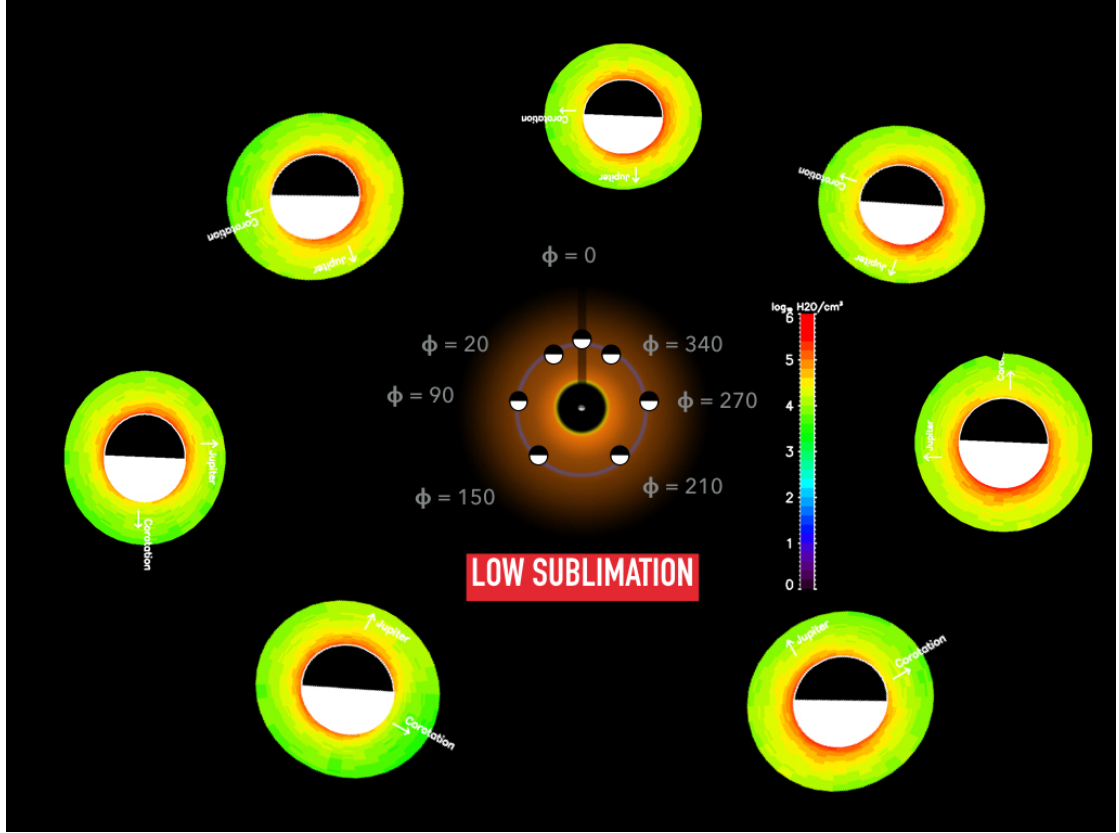


FIGURE 3.7: H₂O Low Sublimation; The color gradient for this simulation peaks at $n \sim 10^5 \text{ cm}^{-3}$

It is distinct from Ganymede due to two minor effects: (1) Europa's high albedo limits sublimation, (2) sputtering can occur in the ram direction (unlike Ganymede due to its intrinsic magnetic field).

If Europa's water is sublimation dominated:

It is more Ganymede-like and the possibility of observing its exosphere may be possible in the sub-mm wavelength. The water vapor exospheres thus rivals the sputtered-oxygen exosphere in thickness and may thus collide. H₂O - O₂ collisions however do not strongly affect the exosphere at Ganymede (Leblanc et al. [2017a]). When H₂O sublimation is high the oxygen column densities can increase by 15-20 % due to electron impact dissociation.

3.4.2 Subsurface: Ocean-Generated Exospheric H₂O

There remains the possibility of a powerful endogenic source driven by the gravitational tide, which could be testable with observations targeting specific species. Tidal heating, due to the gravitational tide is the mechanism responsible for the existence of most of the ocean worlds in the outer solar system. The forced eccentricities a satellite can experience results in vigorous stretching and squeezing of the interior resulting in tidal heat dissipation which propagates to the satellite's surface. This upwards surface pressure can crack the ice, venting volatiles from the subsurface to the exosphere, affecting the density of the background exosphere with a new source of volatiles, and in certain cases which we will explore in the next chapter: the exosphere's energetics via atmospheric sputtering and/or kinetic collisions with the ambient atmosphere. Here, I provide estimates for the ramifications of tidal heating on the surface and exosphere of a satellite, and in particular Europa.

3.4.2.1 Tidal Heating

The total tidal energy dissipated for a synchronous satellite orbiting a gas-giant of mass M_p as presented in [Peale et al. \[1979b\]](#) (hereafter PC79) is strongly dependent on the eccentricity e_s and rotation rate Ω of the satellite:

$$\dot{E} = \frac{42}{19} \frac{\pi e_s^2 \rho_s^2 \Omega^5 r_s^7}{\mu_s Q_s} \quad (3.5)$$

This is a gravitational energy dissipation (ergs s^{-1}) in a satellite's interior due to the differential gravity from the primary body. Therefore it is dependent on the rheology of the satellite: ρ_s , r_s , the density and radius of the satellite respectively, μ_s the rigidity in pressure units (dynes cm^{-2}), and Q_s the 'tidal Q' represents how responsive the satellite is to the stretching and squeezing of the satellite over an orbital time. In general rocky bodies have $Q \sim 100$, whereas gas-giants and stars $Q_* \sim 10$ [Barnes \[2011\]](#), corresponding to an order of magnitude more dissipation.

I estimate the tidal heating for satellites and estimate the cryovolcanism on these worlds. I find that PC79's analytic estimate are consistent with current, sophisticated viscoelastic tidal stress models. Below I tabulate the tidal dissipation for Io and Enceladus the two known cryovolcanically active and tidally-heated satellites in the solar system, and compare to Europa.

ΔT is the *local* change in surface temperature due to this tidal heat dissipation being spread over the surface. One can vary the source size Δr and derive different values,

SAT	$\dot{E}(Q = 100)$ [ergs s^{-1}]	P_{tidal} [kPa]	ΔT [K]
Io	$1.6 \cdot 10^{19}$	~ 1000	54
Europa	$3.0 \cdot 10^{20}$	~ 100	110
Enceladus	$2.7 \cdot 10^{15}$	~ 10	6

TABLE 3.2: Tidal stress parameters for Io (I), Europa (E), and Enceladus (E). The satellite's tidal energy dissipation, \dot{E} , is computed assuming a Tidal Q of 100. The energy dissipated in the satellite is equivalent to a 'tidal power'. At Io, the tidal power is of order one *sau-damini* an obsolete unit equivalent to 100 lightning bolts $\sim 10^{12}$ Watts [Dvorak \[2013\]](#). Tidal pressures P_{tidal} are directly computed from SATstress, a viscoelastic model also described in the next section. Local temperatures, near the cm-wide cracks are computed assuming the an average plume radius as determined by [Roth et al. \[2014b\]](#) for Europa: $\Delta r = 550\text{km}$ (Eqn. 3.6. Furthermore the temperature assumes all of the dissipated energy arrives at the surface via the diurnal fractures which open and close over a demi-orbit.

but to first order the surface temperature should follow the Stefan-Boltzmann law [Dobos and Turner \[2015\]](#):

$$\Delta T_T = \left(\frac{\dot{E}}{4\pi\sigma\Delta r^2} \right)^{1/4} \quad (3.6)$$

This increase in temperature will then result in an increase in water vapor flux, either due to venting, sublimation, and/or sputtering.

One implication from Table 3.2 when compared to a sophisticated viscoelastic model [Pappalardo et al. \[2016\]](#) is that one can discern the Tidal Q for the satellite. Io and Europa are rich in silicate content, whereas Enceladus with its much lower density $\rho \sim 1.6\text{gcm}^{-3}$ is vastly more comet-like [Catling and Kasting \[2017\]](#).

Perhaps the most interesting result is that Europa's tidal heating rivals Io's and surpasses that at Enceladus by an order of magnitude or two. If the conditions are right, as ultraviolet, visible/IR observations are beginning to suggest, Europa may be one of the most unique cryovolcanically active satellites in the solar system.

3.5 Final Perspectives

As I have outlined in this chapter, there are many unresolved questions regarding the water vapor content of the exosphere. Water vapor is split into two populations: **(1) Surface:** that which is produced from the surface ice, and **(2) Subsurface:** that which may be sourced internally from the tidally-heated ocean. The 1st population is interesting from a global point of view in that we may not understand the physical

mechanisms behind sublimation. For example, based on our current water ice sublimation assumptions (as well as those before us e.g. [Smyth and Marconi \[2006\]](#)) the atomic hydrogen column density discovered by [Roth et al. \[2017\]](#) is roughly an order of magnitude higher than expected. As an obvious atomic hydrogen source is not present, and observations are providing more and more evidence regarding the role of H₂O vapor, we conclude that the combined sublimation and sputtering flux of H₂O requires an additional source pointing to the subsurface population. Further comparisons with Lyman-alpha Galileo/HST and our EGM simulations may help resolve the surface-subsurface degeneracy. The subsurface population is of course tantalizing in that Europa may be currently cryovolcanic. With the aid of tidal force physics, we may be able to predict the magnitude of subsurface H₂O in the exosphere.

Part III

Detection of Exospheres

This thesis is coincidentally timed with a new era in planetary exploration, namely the exploration of ocean worlds and a focus on the Jupiter system. September 15, 2017 will mark the final day of the incredible Cassini-Huygens mission, which has truly advanced our knowledge of satellite exospheres embedded in a giant planet magnetosphere. Glimpses of these interactions are able to be discerned from the ground, or space observatories like Hubble. For example, global phenomena like the major dusk over dawn O_2 asymmetry on Europa and Ganymede discussed in Ch.2, can be probed via precise ultraviolet auroral observations. Exospheric atoms such as sodium which have large absorption and emission cross-sections can be observed from the ground, even in extrasolar giant planet atmospheres. Exospheric molecules which have favorable ro-vibrational transitions may be detectable in the sub-mm by the state-of-the-art ALMA array. Altogether, ground-based and space-based observatories have been indispensable in terms of observing the presence of new species in satellite exospheres and even discerning new exospheric phenomena. In these final two chapters I outline the various *Earth-based* detection methods available today §Chapter 4, and *In-situ* detection methods §Chapter 5 in the context of satellite exospheres.

Astronomical Observations of Exospheres

In this chapter I seek to begin my work on satellite exosphere detection by first reviewing the observational methods used to detect exospheres in general. Exoplanet exospheres orbiting around their primary star are, by definition, still characterized as satellite exospheres, and thus the dynamics described in the first part of this thesis, could be relevant to exoplanet exospheres and vice-versa. The ingenuity in exoplanet exosphere *observations* is perhaps the most relevant for the future, as new exoplanet observation techniques can be readily applied to Solar System satellite exosphere observations enabling discoveries (e.g. [Sparks et al. \[2016b\]](#); [Sparks et al. \[2017\]](#); c.f. Section 4.1.3). Ultimately this comparison between Solar System and extrasolar satellite exospheres brings our attention to the 'elephant in the room' : *extrasolar satellites*, also known as exomoons. Despite the 3630 exoplanets discovered in our galaxy (exoplanet.eu: July 11, 2017) not a single exomoon has been detected. Kepler, arguably the best exoplanet detector, cannot observe the small radii of moons. The smallest exoplanet observed being the planet Kepler-37b, with radius: $r_{Kepler-37b} = 0.3r_{\oplus}$. The transit photometry method therefore lacks the instrumentation to detect moons. Equivalently, radial velocity methods which rely on large satellite masses, require the ability to detect shifts smaller than $\Delta v < 10 \text{ cm/s}$. The satellite should be close to the parent star as well in the former case, which may be too close for comfort as a large exomoon should not be dynamically stable within a planetary orbital period of 2.4 days (thick atmosphere) or 6.6 days (tenuous

atmosphere) as was found by [Cassidy et al. \[2009b\]](#). Evidence via microlensing has also been scant. Exhausting the list of exoplanet detection methods, I believe the strongest evidence for a satellite will be best discerned via its exospheric signatures, spectrally as outlined below.

4.1 Detecting Exospheres Remotely

From Earth, there are three principal methods of detecting exospheres today. As is often the case in astronomy, certain species will be more favorable at certain wavelengths than others, due to different excitation mechanisms occurring at different frequencies. We provide a brief overview of these methods and comment on their ability to advance our knowledge of satellite exospheres.

1. Direct Imaging.
2. Direct Spectroscopy.
3. Transmission Photometry & Transmission Spectroscopy.

4.1.1 Direct Imaging of Exospheres

Direct imaging of exospheres is possible in the UV as many emission mechanisms, due to electron impact for instance, occur at these wavelengths. In the Solar System these detections often rely on space-based observatories. Direct imaging of extrasolar exospheres however is possible only with the largest telescopes on Earth equipped with a coronagraph capable of blocking out contaminating starlight, and mirrors equipped with adaptive optics. Since the star-planet intensity ratios are extremely large in the visible, it turns out the best wavelength to observe these types of planetary atmospheres are the mid-infrared (MIR) $\lambda = 3 - 5\mu m$. This is because the star-planet contrast is greatly reduced at these wavelengths, especially if one is observing young, $\tau \sim 10 Myr$ planets, which are still self-luminous in the IR due to their formation heat. Therefore these planetary atmospheres are unique and hold environments with temperatures $\sim 1000K$ (e.g. [Marois et al. 2008](#)). Several surveys using large telescopes are currently targeting such systems to better understand them. One such search is the LBTI Exozodi Exoplanet Common Hunt (LEECH) survey ([Skemer et al. \[2014\]](#); [Maire et al. \[2015\]](#)).

4.1.2 Direct Spectroscopy of Exospheres

4.1.2.1 Infrared Spectroscopy of Exospheres

LEECH additionally carried out *spectroscopic* infrared observations with LMIRcam a MIR spectrograph built at the University of Virginia to characterize the atmospheres of HR8799 b and c. These planets, along with several other self-luminous Jupiters have been observed to have atmospheres containing water vapor, methane, and carbon monoxide in the MIR. There are many other species thought to exist in these atmospheres, especially at high temperatures, but these species have not been targeted for high-sensitivity observations. Why this question is of relevance is that at such enormous distances when the planet is barely resolved, the exosphere of a planet is likely confounded with the exosphere of a satellite should it be present [Sengupta and Marley \[2016\]](#), and thus the spectrum one obtains even when directly imaged likely contains the signature of a satellite. How a satellite behaves around a self-luminous 1000 K gas-giant is unknown at the present and deserves future investigation. [Peters and Turner \[2013\]](#) for example assessed the possibility of directly imaging tidally heated exomoons, but not the contamination of metals or possible volatiles in the spectrum. Exogenic contamination in direct imaging has been postulated and for simplicity generalized as any high-dense object which can transport heavy volatiles to an otherwise light and inert planetary atmosphere. This has been explored for example by [Gao et al. \[2017\]](#); [Zahnle et al. \[2016\]](#).

Several other notable infrared spectroscopy measurements exist of exospheres. In the context of SO₂ (as we will discuss in detail in Section 4.2.2), [Lellouch et al. \[2015\]](#) recently employed VLT's CRIRES instrument at 4 μ m to characterize Io's SO₂ atmosphere. Recently at Europa, a brand-new, anomalous 3.78 μ m feature was observed at the trailing hemisphere. Since the stronger 4.07 μ m feature due to SO₂ frost was absent from the data, the new feature is not easily attributed to SO₂ and presents a new mystery at Europa [Trumbo et al. \[2017\]](#). Both of these observations rely on extremely large aperture size as VLT and Keck are 8.2-m and 10-m dishes respectively. Transitioning towards the radio spectrum, we recall that the aperture radius scales with the wavelength.

4.1.2.2 Sub-mm Spectroscopy of Exospheres

The sub-mm is perhaps one of the most powerful tools in Solar System planetary exosphere observations, as it has enabled the presence of molecular constituents which visible/IR cannot probe. The sub-mm relies on ro-vibrational transitions of exospheric

species that occur at precise frequencies. The transitions result in excitation and emission at low frequencies. A few of these species include SO₂ at Io [Lellouch et al. \[1990\]](#), NaCl at Io [Lellouch et al. \[2003\]](#), HCN at Pluto ([Lellouch et al. \[2017\]](#)). The Herschel space observatory, briefly mentioned in the last chapter has enabled several detections of water vapor due to ro-vibrational states occurring in the far-infrared, close to the sub-mm bands discussed.

The most powerful sub-mm instrument, and arguably most powerful astronomical telescope to date, is the ALMA observatory. ALMA hosts 64 dishes in the Atacama desert in Chile. A molecule undergoes several vibrational modes which are excited when sunlit emitting low-energy photons that can be detected at these excitation frequencies. The large collecting power of ALMA is not only advantageous for far-objects millions of light-years away but also for nearby objects with only trace amounts of gas present in them. I will describe two of these trace species: NaCl and SO₂ on Europa in Section §4.2.

4.1.3 Transmission Photometry/Spectroscopy Observations

Transmission data are very useful probes of tenuous atmospheres as they exploit the incident star light absorbing onto resonantly scattering species. If sodium for example, is present in an atmosphere *during transit*, its large cross-section at visible wavelengths $\lambda = 5890\&5896$ will readily absorb photons as to decrease the stellar radiation intensity. Subtracting then, the in-transit (IT) data from the out-of-transit (OOT) data results in an image or a spectrum solely of the absorbing species, in our case the atmosphere. In section §4.3, I briefly outline a probable pathway to detect the presence of an *extrasolar* satellite exosphere by observing volatiles in a transmission spectroscopy dataset. I have yet-to-be analyzed transmission spectroscopy data for one such candidate: the most eccentric transiting extrasolar planet, HD80606b, where potassium has already been found [Colón et al. \[2012\]](#). This planet may host a toroidal atmosphere, an atmosphere which is in the geometrical form of a torus due to its orbital speed. This type of atmosphere is thought to exist around Saturn due to O₂ + O₂⁺ charge exchange [Johnson et al. \[2006a\]](#). First, we return the Jupiter-system.

4.2 Searches for Volcanic Volatiles in Europa's Exosphere

in the age of ALMA

We target two specific molecules in Europa's exosphere which should be present in detectable quantities by a powerful sub-mm observatory if Europa is cryovolcanically active today: Sodium chloride (NaCl) and Sulfur Dioxide (SO₂). In the event that Europa is not cryovolcanically active, there is a possibility that past cryovolcanism thought to have sourced the NaCl and SO₂ observed on the surface can still sublime and/or sputter, thereby populating the exosphere.

4.2.1 NaCl Vapor at Europa

Europa hosts the most geologically young surface in our Solar System $\tau < 10\text{Myr}$ (Pappalardo et al. [1999a]; Zahnle et al. [2003]) hinting at an active surface. The Galilean satellites in general are of grand interest due to their tidally-heated, voluminous, salt-water oceans (Kivelson et al. [2000]; Saur et al. [2015]).

Due to the extremely tenuous pressures ($P < 1\text{nB}$), the atmosphere is quite sensitive to geologic activity. Therefore volatiles in the exosphere are indicative of surface interactions, or potential oceanic activity. Europa possesses a dynamic, water-product exosphere driven by Io's material propagating through the Jovian magnetosphere. Volcanic sulfur and oxygen become ionized in Jupiter's magnetic field to form the so-called Io plasma torus. The torus, at Europa's orbit, co-rotates at $v_{\text{plasma}} \sim 118$ km/s, constantly bombarding the icy surface with mostly S^{n+} & O^{n+} ions Bagenal et al. [2015]. This results in sputtering of Europa's water ice, ejecting $\sim 60\text{kg/s}$ of water vapor Cassidy et al. [2013].

Two other key volatiles have been observed at Europa: sodium and potassium (Brown and Hill [1996]; Brown [2001]). Several mechanisms exist to form these atomic alkalis.

(1): Iogenic contamination. It has long been thought Europa's observed sodium is influenced by neighboring Io. Dissociative recombination of NaCl^+ downstream of Io sends streams of fast Na atoms radially outward towards Europa. Recent ground-based imaging has observed Io's fast Na stream in Europa's environment near orbital resonance (c.f Fig. 4.1).

Despite this periodic alignment, it was found that Io's Na implantation rate is only $\sim 2\%$ of Europa's atmospheric Na loss rate Leblanc et al. [2005], suggesting Europa remains a net source of Na. Effectively ruling out Iogenic Na, the only other

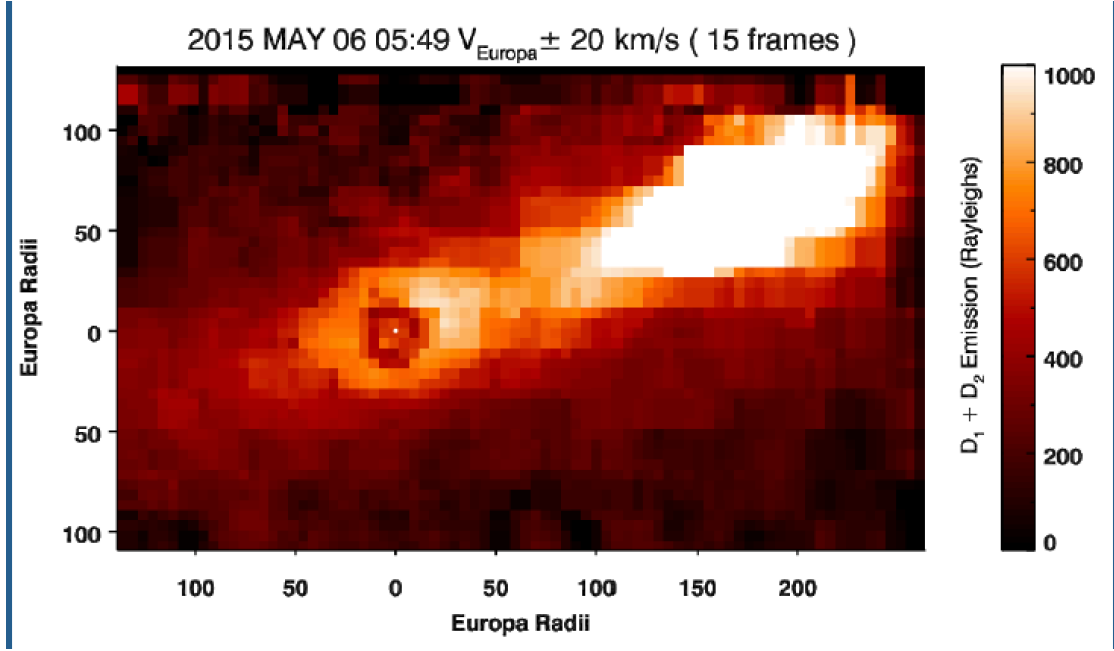


FIGURE 4.1: Iogenic sodium stream arriving at Europa at $v_{stream} \sim 30 - 50 \text{ km/s}$. Impact parameter for collision at Europa's surface is $b_{90} < 1.1 R_{EU}$. The derived Iogenic Na implana-tion rate from the observation is only 2% of the sputtered Europagenic Na loss rate [Leblanc et al. \[2002\]](#), indicating Europa is not strongly affected by Iogenic Na throughout its orbit.
Credit: [Schmidt et al. 2015](#)

Europagenic Na sources stem from molecules, with NaCl being the most likely candidate.

(2): Sodium sputtering. Analogous to the water products, atomic alkali products may be sputtered by incident Iogenic ions colliding with an unknown alkali-rich regolith: NaX & KY. The most likely candidate for parent molecules are salty oceanic brines. While it is thought the reddish-brown trailing hemisphere is dominated by sulfate salts ([Carlson et al. \[2005\]](#)), it was recently shown the yellowish leading hemisphere are chlorate salts NaCl and KCl [Brown and Hand \[2013\]](#). Heavy molecules, in this case NaCl, are thought to be sputtered at 10% the efficiency of atomic Na [Wiens et al. \[1997\]](#). The ejection velocity is not in local thermodynamic equilibrium (LTE) and is thus strongly non-thermal (rather, it is supra-thermal following a Thomson-Sigmund distribution). An attempt at determining the origin of Na & K has been done via Monte Carlo models and analyzing the sodium-to-potassium ratios ([Leblanc et al. \[2002\]](#); [Johnson et al. \[2002\]](#)). $\frac{Na}{K}_{EU} = 25 \pm 3$ (sputtered/oceanic.), $\frac{Na}{K}_{Io} = 10 \pm 3$ (direct volcanic input). These ratios also suggest the alkalis may be sourced from the ocean. [Zolotov and Shock \[2001\]](#) found that the 150% increase in the Na/K ratio is consistent with the upwelling of oceanic water vapor. From [Johnson et al. \[2002\]](#), $\frac{Na}{K}_{\oplus OCEAN} = 45 \pm 3$. Current computational chemistry model results are also supporting such an oceanic source [Ozgurel et al. \[2016\]](#).

(3): Water vapor venting. The NaCl (and KCl) column density can further increase if Europa is geologically active. With current observations (Roth et al. [2014b]) it has been difficult to discern whether Europa is actively venting or it is geologically inert (Shemansky et al. [2014]), offering a chance for ALMA to resolve the current ambiguities. If the HST did indeed observe transient oceanic water vapor, the stoichiometric ratios of NaCl would be preserved in Europa's exosphere. The exospheric temperatures would then be closer to LTE, $T_s \sim 100K$.

It is critical for future *in-situ* space missions (NASA's Europa Clipper, ESA's JUICE) to anticipate if Europa is an active body, effusing oceanic water like Enceladus (Spitale et al. [2015]) or not. If Europa is truly active, this can not only help guide instrument designs, and mission concepts, but also shed light on ambiguities in the exosphere, surface, and interior otherwise unresolved until orbit insertion in the 2030s.

Lellouch et al. [2003] directly observed volcanic NaCl at Io. At Europa, the NaCl may or may not be due to volcanic salts, but simply oceanic salts as thought to be present in non-sulfate form on the leading hemisphere (Brown and Hand [2013]). Furthermore, Europa being the most eccentric of the Galilean satellites may rival the tidal dissipation at Io. Europa's entire surface is fractured by diurnal tidal stresses generating cycloidal *lineae* up to 20-km across (Pappalardo et al. [1999a]) as well as *lenticulae* or cavities on the crust perhaps akin to magma chambers on Earth (Sotin et al. [2007]). These geological features offer direct pathways for saltwater to (A) effuse (as ocean brine) and (B) vent (as vapor).

The effusion of ocean brine and its subsequent exospheric population could in principle constrain the saltwater concentration in the subsurface ocean. The potential saltwater vapor could also place an upper limit on the venting rate from the ocean. Below we describe the implications and utility of these observations in detail.

Hand and Carlson [2015], used spectral measurements to show that Europa's leading hemisphere indicates significant amounts of saltwater, which has been effused to the surface. NaCl grains were irradiated in the laboratory for the equivalent of 100-years in ideal Jovian plasma conditions ($T \sim 100K$, $P \sim 1nB$, $E_i \sim 10keV$). Near-identical, yellow discoloration of the water ice was analyzed, as observed by Galileo on Europa's leading-hemisphere. It is believed that Europa's trailing hemisphere, being in the plasma-ram direction, receives a factor of three higher magnetospheric ion bombardment than the leading hemisphere on average (Cassidy et al. [2013]). Since sulfur and oxygen ions dominate the plasma it is believed the potentially effused saltwater would form hydrated sulfur salts (Carlson et al. [2005]), rather than chlorides like NaCl or KCl. Brown and Hand [2013] point out, based on ocean models run by Zolotov and Postberg [2014], that the most abundant oceanic anion is chlorine, Cl^- and not sulfates. Thus Europa's ocean brines should be chlorides.

If a maximum NaCl concentration, $\chi_{NaCl,max}$, is chosen, the resulting column density can rival Io's, ($N_{Io-NaCl} = 4 \cdot 10^{13} \text{ NaCl cm}^{-2}$, [Lellouch et al. \[2003\]](#)). It is generally assumed that the irradiated NaCl products behave as H₂O ($n_{H_2O} \sim 3 \cdot 10^{22} \text{ cm}^{-3}$), and thus the NaCl concentration can be derived from the irradiation density ratios: $\chi_{NaCl} = \frac{n_{NaCl}}{n_{H_2O}}$ (correspondance R.E. Johnson). For the maximum F-center yield ¹ from the laboratory experiments carried out by Hand & Carlson 2015, $n_{NaCl}(max) \sim 10^{19} \text{ cm}^{-3}$. To derive the column density one can observe, a sputter depth is required to predict the maximum column due to bombardment: $N \sim nr_{sputt}$. For an incoming keV ion, typical of the Jovian system, bombarding an NaCl brine, the depth is $r_{sputt} \sim 300$ yielding a column of $N_{Eu-NaCl}(max) \sim 3 \cdot 10^{-6} \text{ cm} \cdot 10^{19} \text{ cm}^{-3} \sim 3 \cdot 10^{13} \text{ NaCl cm}^{-2}$. However, it is not clear whether every NaCl molecule makes an F-center. A safer estimate of the brine evaporate is: $n_{NaCl} \sim 10^{17} \text{ cm}^{-3}$, yielding $N = 3 \cdot 10^{11} \text{ NaCl cm}^{-2}$. Given that only the leading hemisphere should be covered in chloride brines, one can reasonably expect $N \gtrsim 1.5 \cdot 10^{11} \text{ NaCl cm}^{-2}$. Another way to derive the expected NaCl column density at Europa is to scale it to the well-observed sodium columns at Io and Europa. Here it is assume that its production is volcanic and that the observed Na (e.g. Fig.7 [Burger et al. \[2001\]](#); Fig.1 [Johnson \[2000\]](#)) is a direct product of NaCl due to e- impact dissociation. Evaluating at a distance ~ 5 satellite radii away from the surfaces on both bodies then:

$$N_{NaCl,Eu} \sim N_{NaCl,Io} N_{Na,Eu} / N_{Na,Io} \sim 4 \cdot 10^{13} \times \frac{2 \cdot 10^9}{5 \cdot 10^{10}} \sim 1.6 \cdot 10^{12} \text{ NaCl cm}^{-2},$$

which falls in between the two oceanic brine sputtering estimates provided above, further validating our predictions.

For an exospheric temperature of 1000 K (given a non-thermal sputtering distribution), we find that ALMA for instance, should be able to detect a disk-averaged column density of $8 \cdot 10^{10} \text{ NaCl cm}^{-2}$ with a $\theta = 1''$ beam centered at Europa at the ro-vibrational transition occurring at $\nu_{NaCl} = 234.252 \text{ GHz}$.

Thus if the ocean brine is indeed chlorinated as observational evidence suggests we will be able to detect it.

Such a detection would enable one to predict the number density of NaCl in the ocean brine, and therefore the saltwater concentration of Europa's vast oceans, critical for assessing habitability. A useful ratio, is Io's dissociated atomic component to molecule ratio: $\frac{Na}{n_{NaCl}}$. This ratio was estimated by [Wiens et al. 1997](#) to be 10. That is to say, only 10% of the Na is sourced from sputtered NaCl. A direct measurement of this ratio would help constrain the origin of Europa's sodium (iogenic, sputtered, or vented). The

¹F-center yield is a crystallographic technique to determine the concentration of a salt crystal for example.

observed sodium was calculated to have a flux $\Phi \sim 5 - 10 \cdot 10^7 \text{ Na cm}^{-2} \text{ s}^{-1}$, alluding to a column of $N \sim 10^{10} \text{ cm}^{-2}$, based on $N_{\text{NaCl}} = \pi r_{\text{EU}}^2 \frac{\Phi_{\text{sputt}}}{v_{\text{esc}}} \frac{1}{b}$ from [Johnson \[2000\]](#). Lastly, it is conceivable that although Europa's sodium seems to be sputtered, it could also arise from direct venting from the ocean. This could be evidenced by the seasonal variation of sodium [Leblanc et al. \[2005\]](#). The leading hemisphere shows a 320% enhancement that may not be simple to explain due to sputtering alone. Thus a combination of effusive ocean brines, subsequently sputtered by ions, and light-venting may explain the sodium today. Physically, venting salt water would either be driven by tidal stresses or hydrothermal activities (like Enceladus, [Hsu et al. \[2015\]](#)). The venting rate, Φ_{vent} would then be proportional to the upward acceleration, helping identify the unknown pressure gradients fueling the activity. Venting would of course influence Europa's greater exosphere, as no observations of water vapor have yet to be made. Fig. 4.2 shows the disk-averaged column density of H_2O vapor, a result of a 3D Monte Carlo simulation taking into account the sputtering and sublimation of water ice. This is perhaps a reasonable tracer of sputtered NaCl, from ocean brines, as they are thought to behave similarly. We note a 50% increase in column density at the leading over the trailing hemisphere, likely due to dynamic effects, further improving odds of NaCl detection. The dynamic evolution of sodium, which may also trace NaCl is shown in Fig. 4.3. At the time of writing this dissertation, an ALMA observation has been taken to test for the presence of NaCl (and less abundant KCl $\nu_{\text{KCl}} = 253.271 \text{ GHz}$) in Europa's exosphere. The data is currently being processed. Meanwhile, we turn our attention to another volatile, perhaps even more telling of ongoing volcanism at Europa than NaCl.

4.2.2 SO_2 Vapor at Europa

Sulfur dioxide is a toxic trace gas which we believe should be present, like NaCl, in Europa's exosphere. SO_2 exists on other bodies, namely Venus, where it is the most abundant gas at 150 ppm, next to CO_2 and N_2 , originating most likely due to volcanism [Marcq et al. \[2013\]](#). Visible evidence of volcanism and SO_2 is already present on Europa's surface, namely the variety of colors at Europa's trailing hemisphere as viewed by Galileo. Below we describe how the observed SO_2 vapor can populate the exosphere by sputtering (§4.2.2.1) and venting (§4.2.2.2), as outlined above for NaCl.

4.2.2.1 Sputtered SO_2 Exosphere

Here I provide updated estimations of sputtered SO_2 as to populate Europa's global exosphere. The estimates I provide in this work provide a basis for future 3-D EGM

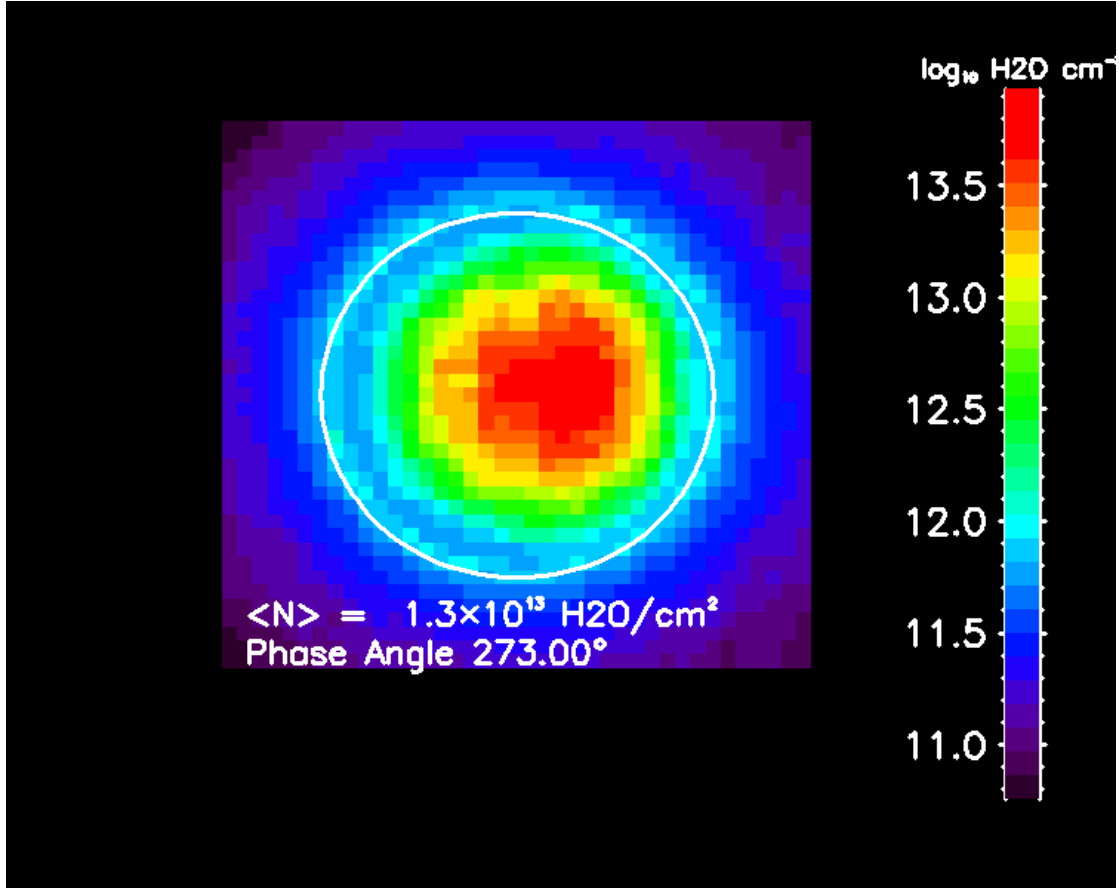


FIGURE 4.2: Europa's sublimated and sputtered water vapor, simulated at the sunlit leading hemisphere. The 3D Monte Carlo model was carried out with the LATMOS EGM (Exosphere General Model). Test particles are subject to gravitational fields, ionization, photolysis, as well as surface-interactions. The concentric pattern is due to peak columns at the center of the disk, due to solar insolation.

modeling of SO_2 . Europa's background atmosphere O_2 , H_2 , and H_2O is essential to deduce the spatial extent of the SO_2 exosphere. Since radiolysis is dependent on the surface temperature, hot spots due to explosive or effusive cryovolcanism would strongly affect the H_2 and O_2 source yields and hence the background atmosphere. Figures 4.6- 4.8 simulate the near-surface line-of-sight (LOS) column densities $\sim 10^{13} - 10^{14} \text{ cm}^{-2}$ for the sputtered H_2 , O_2 , and H_2O at the sunlit trailing hemisphere, where sputtering is maximal. The H_2O simulation (Fig. 4.8), also includes water vapor sublimation, resulting in a dense region of $N \gtrsim 2 \cdot 10^{14} \text{ H}_2\text{O cm}^{-2}$ covering $\sim 25\%$ of Europa's disk. This figure is also indicative of the approximate SO_2 source size, given that the trapped SO_2 peaks across $\sim 223 - 333^\circ$ longitude [Ockert et al. \[1987\]](#) with an average surface ice concentration near 0.3% [Hand et al. \[2006\]](#). Should the SO_2 be trapped in the water ice matrix, one can predict the SO_2 column density based on the previous SO_2 ice observations. Given an incident ion flux of $1.6 \cdot 10^8 \text{ ions cm}^{-2}$ impacting the trailing hemisphere, the ballistic lifetime of SO_2 before e- impact dissociation, and water ice sputtering yields consistent with Monte Carlo simulations

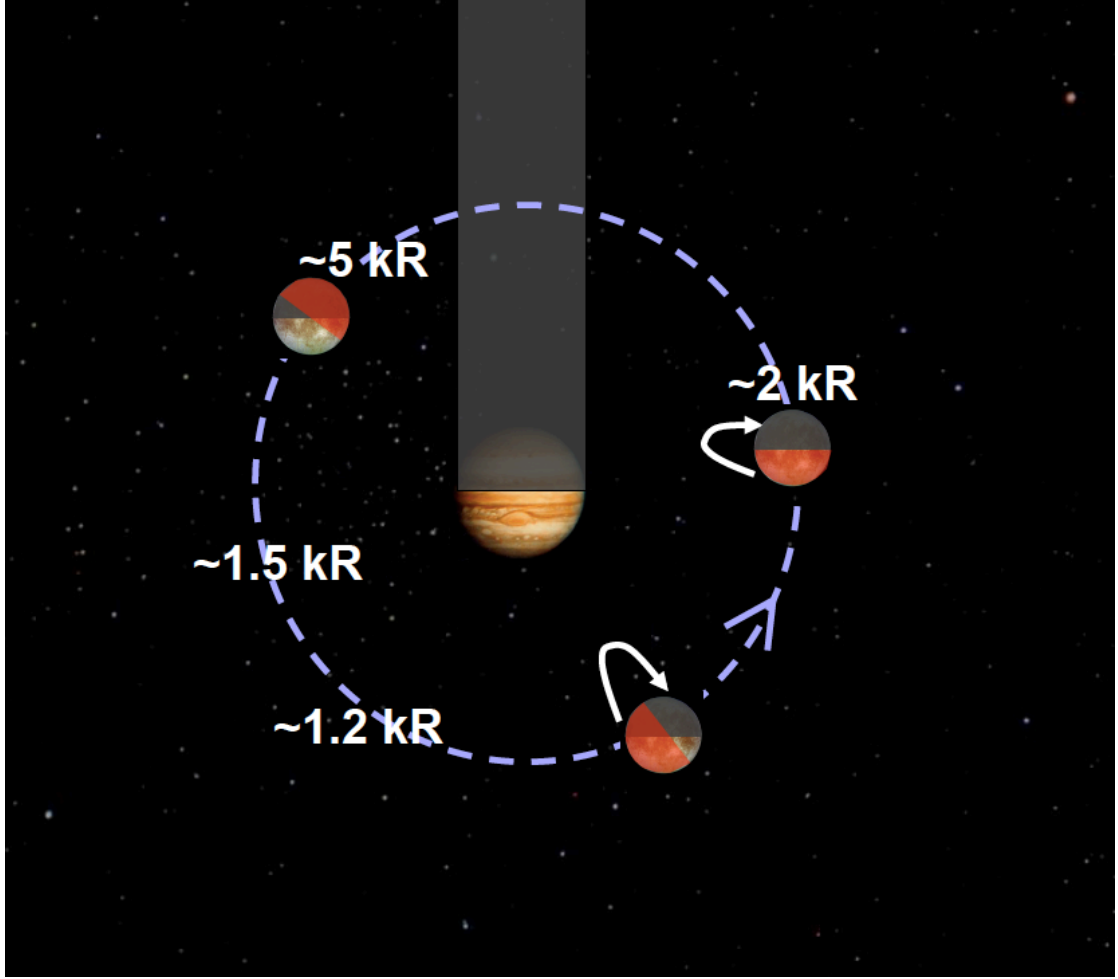


FIGURE 4.3: (Seasonal evolution of Europa's sodium. Europa's leading hemisphere as it arrives from eclipse shows the maximum sodium intensity. *Credit: F. Leblanc in Johnson et al. [2009]*

Cassidy et al. [2013], we estimate a sputtered line of sight column of $N \sim F_{\text{sputt}} t_x \sim 3 \cdot 10^{13} \text{SO}_2 \text{cm}^{-2}$. The larger column is highly sensitive to the ballistic lifetime of the SO_2 which is dependent on its interaction with Europa's surface ice. Below I outline how a column density is derived for SO_2 examining each parameter in detail, as the column will be strongly dependent on our assumptions. The net sputtering flux is defined as the product between the incident ion flux at a given planetary longitude $\mathcal{F}_{\text{eff}}(\phi')$, the effective porosity \mathcal{P}_{eff} of the regolith, the laboratory-constrained sputtering Yield, Y_i , for the species in question and the surface ice concentration χ_i :

$$\mathcal{F}_{\text{net}} = \mathcal{F}_{\text{eff}}(\phi') \mathcal{P}_{\text{eff}} Y_i(T_0) \chi_i \quad (4.1)$$

Incident Ion Flux: The incident ion flux is modeled as peaking at the trailing hemisphere/ plasma ram with null values at the leading hemisphere/plasma wake (e.g.

Species	$\mathcal{F}_{\text{sputt}}$ [$\text{cm}^{-2} \text{s}^{-1}$]	t_x [s] ; (τ_{orb})	N_r [cm^{-2}]	N_{LOS}
H ₂ O	$7 \cdot 10^9$	$2.8 \cdot 10^3$ ($9.1 \cdot 10^{-3}$)	$2.0 \cdot 10^{13}$	$2.3 \cdot 10^{14}$
H ₂ O plumes	$2 \cdot 10^{10}$	$2.8 \cdot 10^3$ ($9.1 \cdot 10^{-3}$)	$1.4 \cdot 10^{15}$	10^{16}
O ₂	$3.3 \cdot 10^8$	$3.3 \cdot 10^5$ (1.06)	$1.1 \cdot 10^{14}$	$2.03 \cdot 10^{15}$
H ₂	$6.6 \cdot 10^8$	$2.3 \cdot 10^4$ (0.074)	$1.5 \cdot 10^{13}$	$1.1 \cdot 10^{14}$
SO ₂ sputtered	$1.05 \cdot 10^7$	$4.8 \cdot 10^4$ (0.16)	$5.1 \cdot 10^{11}$	$1.3 \cdot 10^{13}$

TABLE 4.1: Maximum radial and line-of-sight (LOS) column densities at the sunlit trailing hemisphere at a surface temperature of $T_0 = 136\text{K}$. Calculated column densities are the product of the source flux (sputtering in most cases) and the atmospheric residence time, or ballistic lifetime of the species scaled to Europa's orbital time where $\tau_{Eu} = 3.06 \cdot 10^5 \text{s}$. Since H₂O and H₂ stick and escape we determine the atmospheric lifetimes via Monte Carlo simulations which treat these processes over the European orbit. For O₂ and SO₂ lifetimes we assume negligible interactions with the surface. The photodissociation lifetimes are found in Huebner et al. 1992, and the e- impact dissociation lifetimes for O₂ are given in Hall et al. [1995], whereas for SO₂ we use the values in Table 4.2.

Leblanc et al. [2002]). $\mathcal{F}_{\text{eff}}(\phi') = \frac{\mathcal{F}_i}{4\pi} \cos(\frac{1}{2}(\phi' - \pi))$ for incident flux $\mathcal{F}_i = 1.6 \cdot 10^8$ ions $\text{cm}^{-2} \text{s}^{-1}$ Cooper et al. [2001]

Porosity: Here we choose to neglect the estimated porosity values from albedo observations (Nimmo and Manga [2009] estimate an upper limit of $\mathcal{P} < 0.3$) and instead seek to include this consideration in the residence time of the molecular species on the grain as estimated for example by Cassidy and Johnson [2010]. This surface-exosphere interaction can also be described by considering the effective heat of adsorption T_{ads} (denoted as E_{ads} in Oza et al. [2017]). It is almost certain that the exosphere behaves differently between the leading and trailing hemispheres. Thus, future surface-exosphere interaction works may want to incorporate the increase in sputtering based on the increase in grain size from the leading $100 \mu\text{m}$ to trailing $1000 \mu\text{m}$ as shown by Cassidy et al. [2013].

Sputtering Yield: To determine Y_i we scale the sputtering fluxes for various species. For the dominant species H₂O and O₂ Cassidy et al. [2013] calculates globally averaged sputtering fluxes: $\mathcal{F}_{\text{H}_2\text{O}} = 7 \cdot 10^9 \text{cm}^{-2} \text{s}^{-1}$, $\mathcal{F}_{\text{O}_2} = 3.3 \cdot 10^8 \text{cm}^{-2} \text{s}^{-1}$ corresponding to production rates of: $\Phi_{\text{YH}_2\text{O}} = 2 \cdot 10^{27} \text{H}_2\text{O s}^{-1}$ and $\Phi_{\text{YO}_2} = 10^{26} \text{O}_2 \text{s}^{-1}$. The effective yield for these species is then: $Y_i(T_0) = Y_0(1 + q_i) \exp(-0.06/k_b T_0)$, where q_i is a constant depending on the species. Teolis et al. (2017B) (submitted) provides a detailed overview of these yields. Ice Concentrations: Finally the surface ice concentrations are critical for trace species such as Na, K, SO₂ (water products assume $\chi = 1$ and are scaled based on their yields:

$\chi_{\text{SO}_2} = 0.003$ (Hand et al. [2007]; Noll et al. [1995]; and Sack et al 1992).

Reaction	\mathcal{K} [cm ³ s ⁻¹]
$\text{SO}_2 + e \rightarrow \text{SO}^+ + 2e$	1E-7
$\text{SO}_2 + e \rightarrow \text{SO}^+ + \text{O} + e$	5e-8
$\text{SO}_2 + e \rightarrow \text{S}^+ + \text{O}_2 + e$	2e-8
$\text{SO}_2 + e \rightarrow \text{O}^+ + \text{SO} + e$	5e-9
$\text{SO}_2 + e \rightarrow \text{SO} + \text{O} + e$	1e-7
$\text{SO}_2 + e \rightarrow \text{S} + \text{O}_2 + e$	2e-8
$\text{O}_2 + e \rightarrow \text{O} + \text{O} + e$	1.3e-8
$\text{O}_2 + e \rightarrow \text{O}_2^+ + e + e$	2e-8
$\text{O}_2 + e \rightarrow \text{O} + \text{O}^+ + e + e$	1.1e-8

TABLE 4.2: SO₂ electron impact dissociation reactions used for Io's interaction with the plasma torus in (Dols et al. [2012]) and personal communication with Don Shemansky. The last three O₂ reactions are referenced: Marconi [2007] ; Ip [1996]; Smyth and Marconi [2006] respectively.

4.2.2.2 SO₂ Venting

Roth et al. [2014b] HST observations report a column of $N \sim 10^{16} \text{H}_2\text{O} / \text{cm}^2$, supersonic velocities of 700 m/s extending the plumes up to 200 km in height.

If we assume a radially expanding flux, $F = nu$, then the corresponding water flux from a plume is $\mathcal{F}_{plume} \sim 1.2 \cdot 10^{13} \text{H}_2\text{O} \text{ cm}^{-2} \text{s}^{-1}$. This flux assumes that one can derive the number density of H₂O by assuming the geyser's 'scale height' is 200 km, yielding $n_{plume} \sim 5 \cdot 10^8 \text{cm}^{-3}$.

Even if these plumes are transient, or if there is simply venting from the cracks one can possibly heighten the above SO₂ estimates considerably.

Ongoing [cryo]volcanism beyond Earth is so far only present on the satellites: Io, Triton, and Enceladus, all due to gravitational tidal heating from their gas giant (Peale et al. 1979b; Thomas et al. 2016; Jankowski et al. 1989). Tidally-driven *cryovolcanism*, by melting and invigorating the interiors of these bodies, provides an avenue for endogenic volatiles to enter an atmosphere where the volatiles would otherwise be frozen solid. In the last three years, increasing evidence surmounted by the Hubble Space Telescope (HST) has provided the tantalizing prospect that Europa's oxidized atmosphere and surface is currently influenced by *active* cryovolcanism (Fig. 4.4). Past cryovolcanism has been inferred based on the global resurfacing age of < 60 Myr based on impact crater dating Pappalardo et al. [1999b]. However, due to the nature of the two indirect observational methods (imaging and spectroscopy), the potential findings are limited to large, *explosive* cryovolcanic eruptions with a column > 10¹⁶ H₂O cm⁻², inferred via transient hydrogen Lyman- α and OI 1304 auroral anomaly that persisted for 7-hours near Europa's south pole Roth et al. [2014b].

The second, more recent method, via transmission images of Europa in transit, detected narrow, jet-like features at Europa's limb $\sim 10^{16} \text{H}_2\text{O} \text{ cm}^{-2}$ Sparks et al.

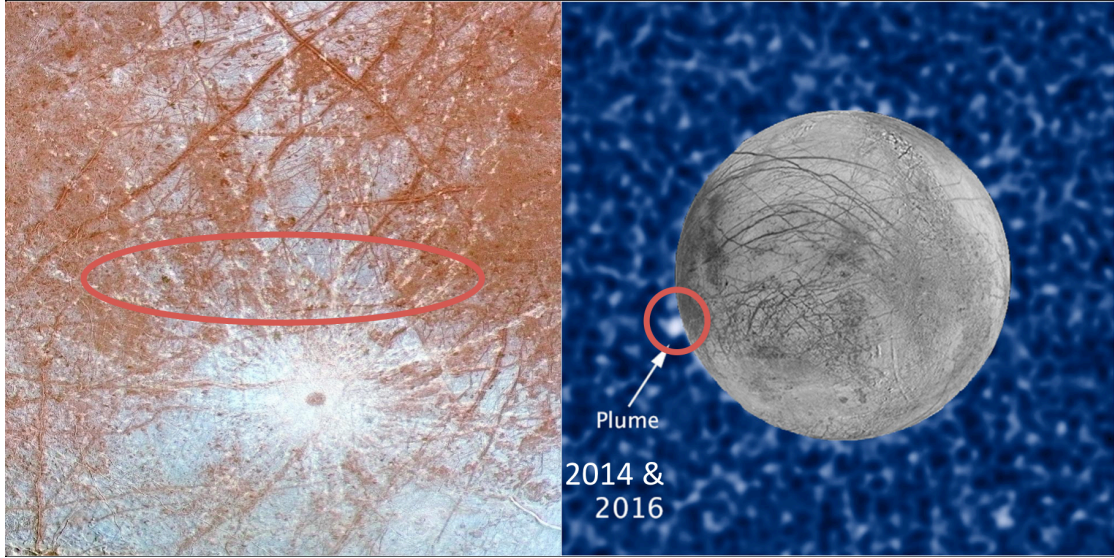


FIGURE 4.4: Possible cryovolcanically active region detected in 2014 and 2016 [6,13] near Pwyll crater (left panel), the mid-southern latitude region where our tidal stress estimates are carried out.

[2016a]. Both methods are at the limits of current instrumentation and are therefore unable to probe more modest venting as well as more *effusive* cryovolcanism as thought to be on Enceladus (Porco et al. 2016). The subsurface venting could also be more diffusive on the other hand, where the length of the emission region l_{crack} cm, is larger than the mean free path of the venting molecules: $l_{mfp} \gg l_{crack}$.

Perhaps the most critical piece of knowledge absent from the HST observations are the overall volatile content of the water plumes, a subsurface asset of great astrobiological importance Russell et al. [2014], as recently demonstrated with the detection of excess H_2 in Enceladus' plumes Waite et al. [2017].

SO_2 is the ideal candidate for discerning volcanism as hot spot terrestrial volcanoes emit $\sim 20\%$ SO_2 by volume, $\sim \frac{1}{3}$ of the predominant H_2O content (which will be very difficult to detect directly at Europa from the ground due to telluric absorption), and $\sim 6\times$ more than the next abundant volcanic volatile, CO_2 (Hoshyaripour et al. 2012). Interestingly, SO_2 at Europa was discovered trapped in ice, more than three decades ago with the IUE explorer (Lane et al. [1981]; Ockert et al. [1987]), for which an effective column of $\sim 2 \cdot 10^{16} SO_2 cm^{-2}$ volatiles were embedded into Europa's dark-red, trailing hemisphere, based on the ice absorption signatures in the ultraviolet. The origin of SO_2 , along with other volatiles trapped in Europa's ice, is thought to be due to the upwelling of oceanic material to the surface Hand et al. [2006], a process ultimately driven by tidal heating. It is also possible that S+ implantation from Io-plasma torus in the regolith could oxidize. On April 13, 2017 it was announced that an HST observation from 2016 Sparks et al. [2016a] had discerned a possible venting

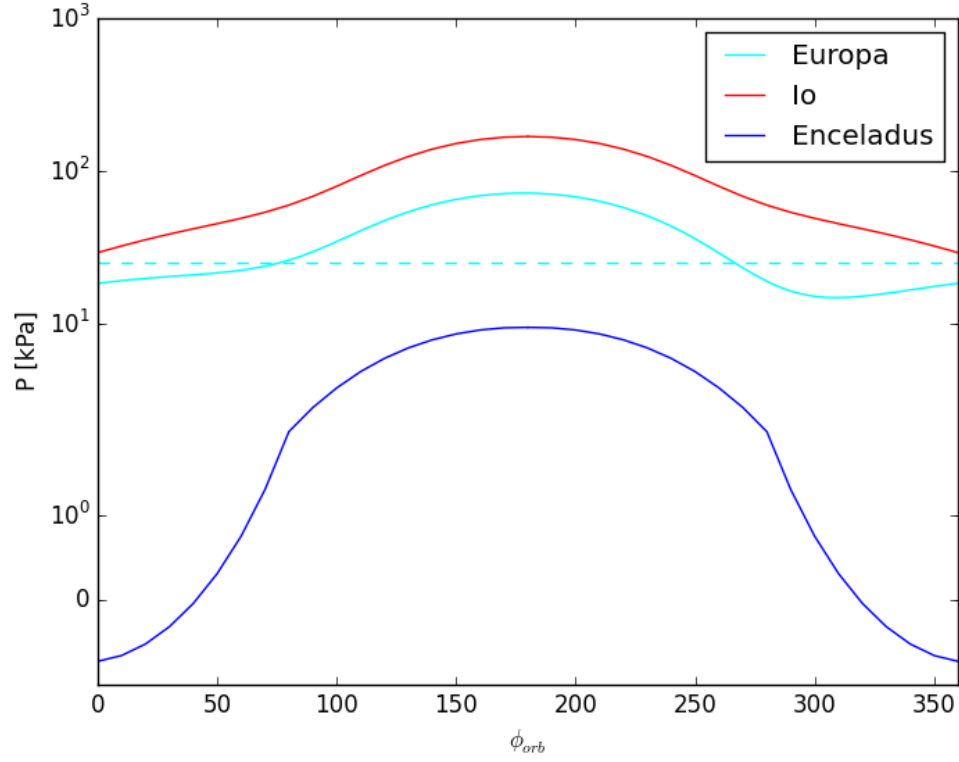


FIGURE 4.5: Results from a four-layer viscoelastic tidal stress model developed at JPL. Tidal stresses versus the true anomaly angle are plotted. 0 corresponds to perijove. Europa's average tidal stresses are roughly twice the crack initiation strength of 25kPa [Hoppa et al. \[1999\]](#) and furthermore, rival that of Enceladus ($\sim 14 - 85\text{kPa}$) whose four cracks are constantly venting.

Based on results from [Johnston et al. \[2016\]](#), and [Patthoff and Davies \[2017\]](#)

region near the Pwyll crater centered at $271^\circ W$, coinciding with thermal anomalies in Galileo data [Sparks et al. \[2017\]](#) (Fig 4.4).

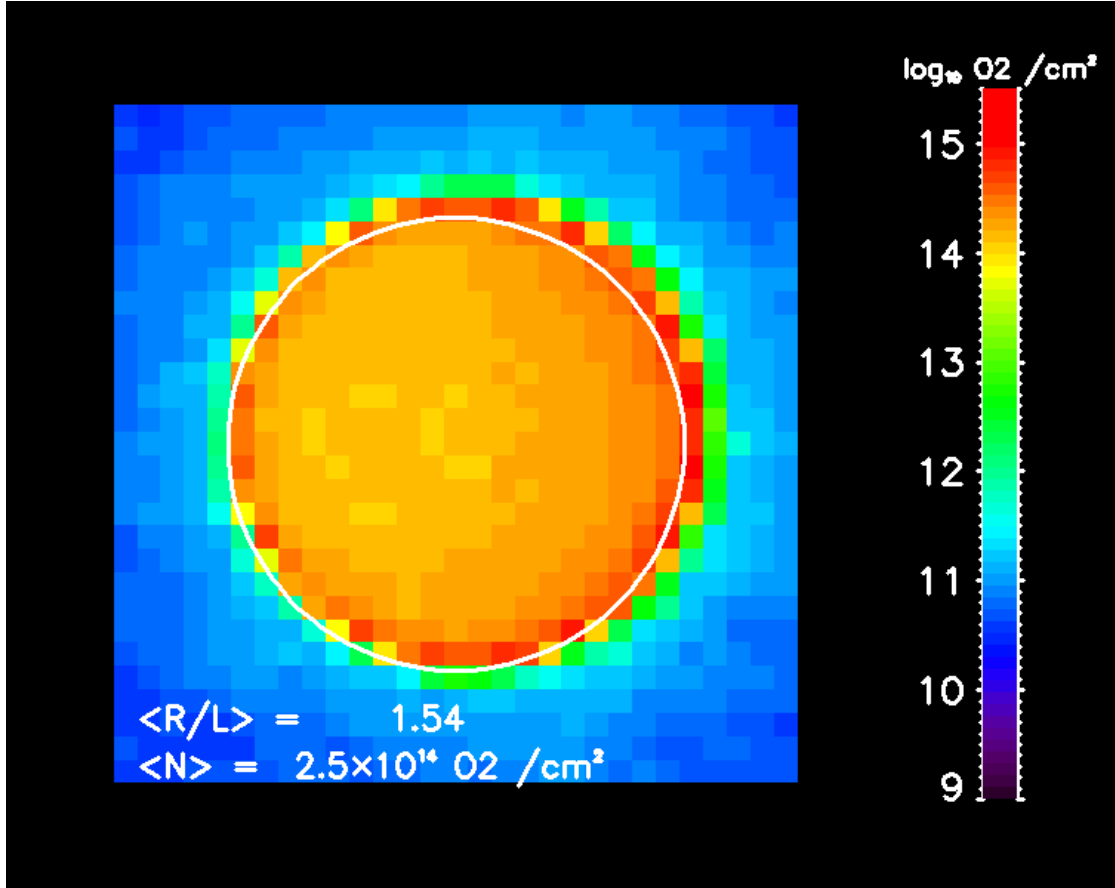


FIGURE 4.6: Next three figures: 3-D Monte Carlo simulations of line-of-sight column densities of Europa's background atmosphere at the sunlit trailing hemisphere. $N \sim 10^{14} \text{ H}_2\text{O}/\text{cm}^2$, $N \sim 3 \cdot 10^{14} \text{ O}_2/\text{cm}^2$, and $N \sim 10^{13} \text{ H}_2/\text{cm}^2$. Only O_2 has been confirmed indirectly through HST oxygen aurorae observations (Hall et al. [1995]). Roth et al. [2015] observation has also enabled us to understand the behavior of the near-surface O_2 throughout the European day, in that our recent 3D Monte Carlo simulations show that it builds preferentially at dusk local time (Figure based on Oza et al. 2017 in review).

As current venting estimations are limited to explosive events, we investigated the magnitude of the diurnal tides on mid-southern latitudes for all volcanic satellites by employing a [viscoelastic stress model](#) shown in Fig. 4.5. The estimations show that Europa's average tidal stresses are roughly twice the crack initiation strength of $\sim 25 \text{ kPa}$?, Enceladus' midsouthern latitude stresses are a factor of two less than that at the constantly venting south pole cracks, and finally the stresses at Io (where a $N \sim 10^{16} \text{ SO}_2$ atmosphere is present) are not substantially larger than at Europa, likely due to Europa having the largest eccentricity of the three bodies (0.0094). It is not surprising that tidally-driven cryovolcanic venting had evaded detection by the Galileo spacecraft, given that Cassini discerned Enceladus' plumes Porco et al. [2006] and later hydrothermal activity Hsu et al. [2015], only after near-surface $z < 150 \text{ km}$ flybys. Overall, these diurnal estimates seem to suggest that either Europa should be actively venting, or that Europa's interior rheology is drastically different than we think.

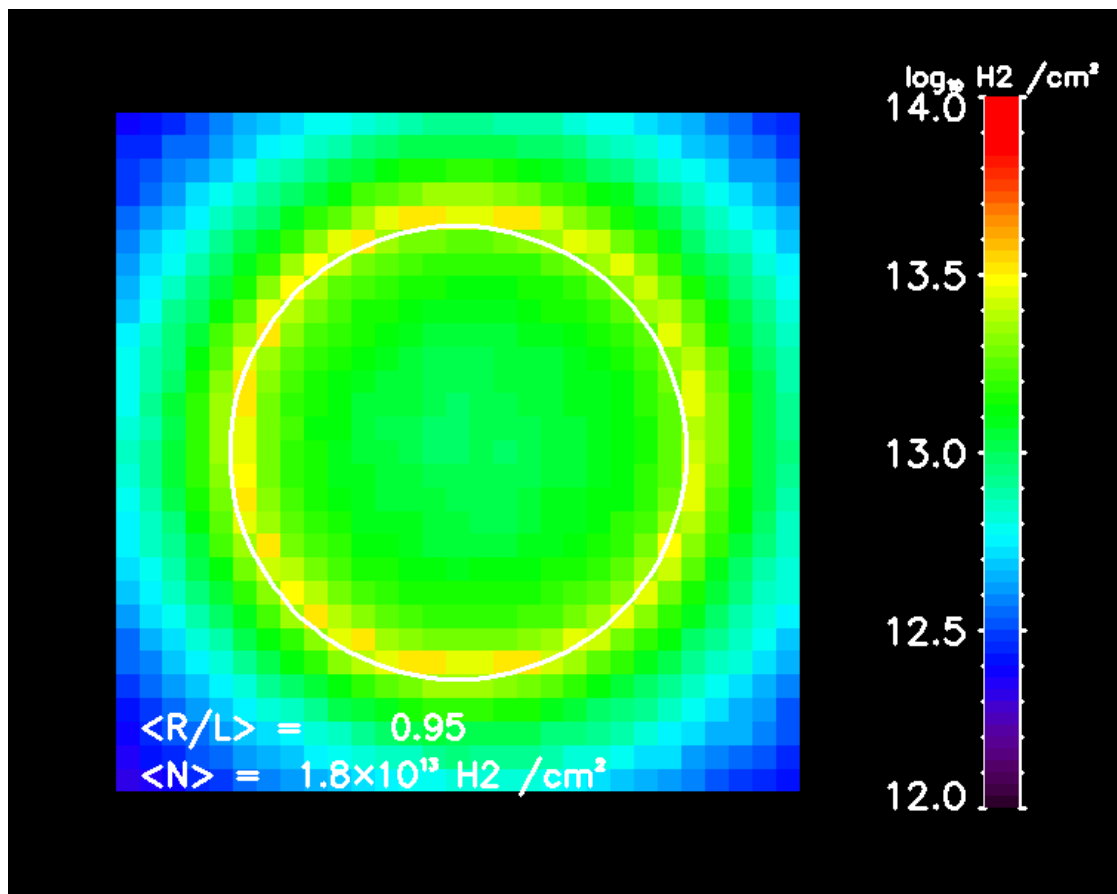


FIGURE 4.7: See previous figure.

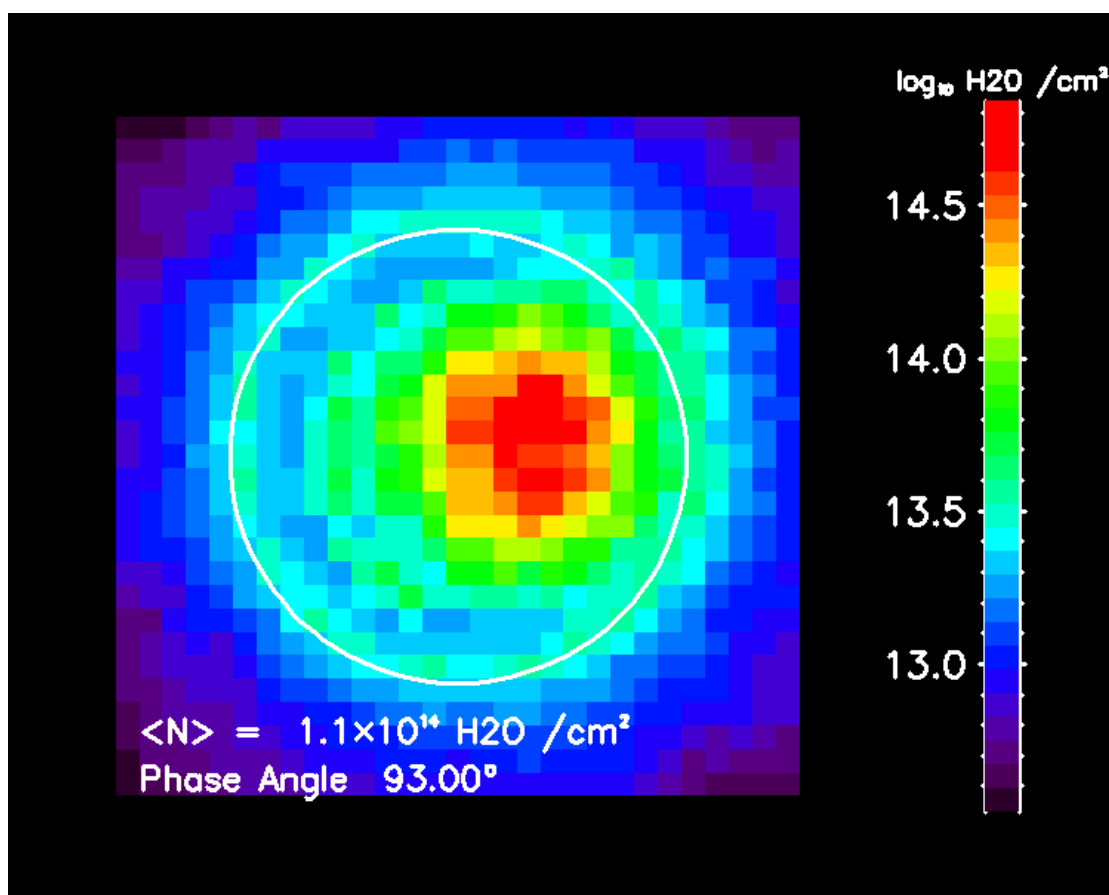
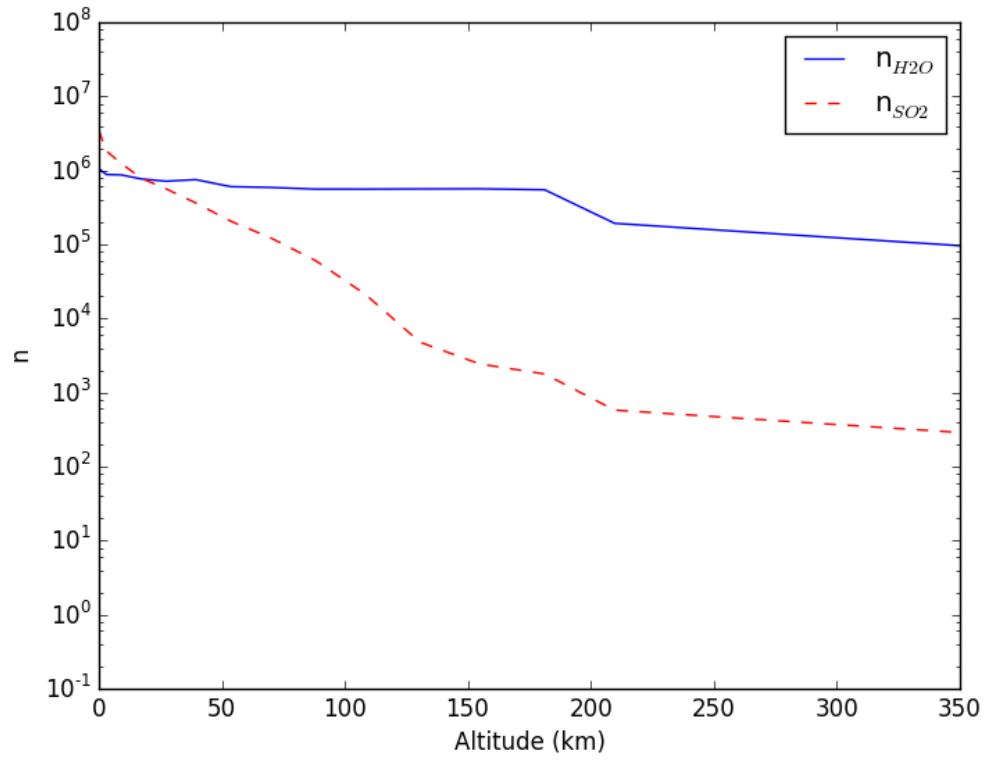
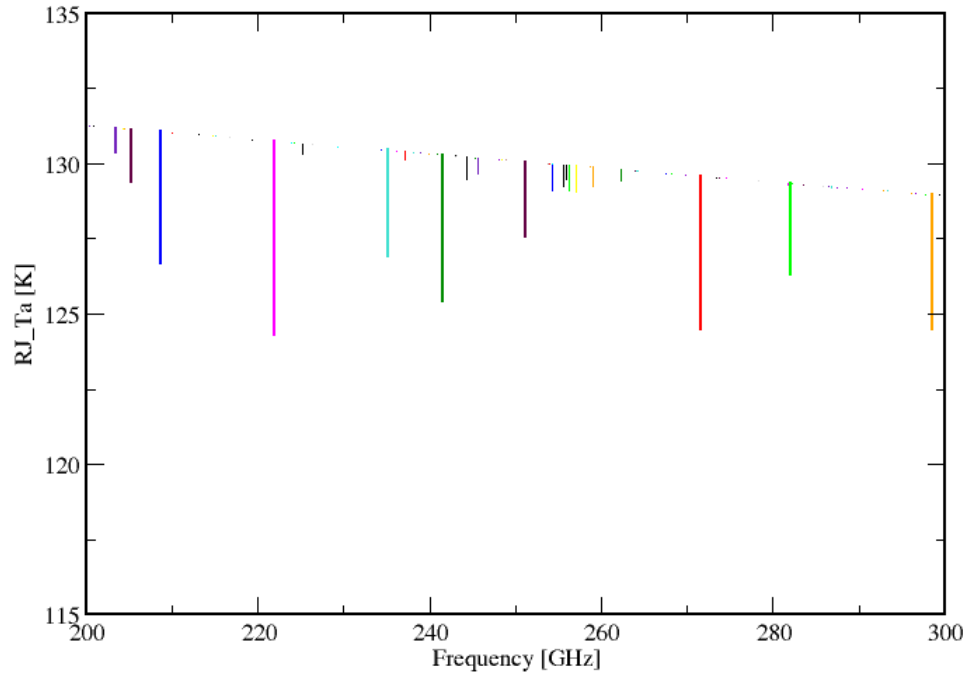


FIGURE 4.8: See previous figure.



.11

FIGURE 4.9



0.11

FIGURE 4.10

FIGURE 4.11: **A:** Density versus altitude profile for a moderate venting source of SO_2 . **B:** Simulated non-LTE spectrum for the former altitude profile. We anticipate local Rayleigh-Jeans contrasts of 5 K in regions where SO_2 is present.

4.2.2.3 Description & Consequences of Possible SO₂ Observations

Next Jupiter Opposition (May 9, 2018)

The relatively low atmospheric densities on Europa indicate that the rotational SO₂ populations quickly leave LTE. Therefore we have developed a rotational non-LTE model for SO₂ taking into account atmospheric collisions with the background atmosphere (Fig.2 a-c: H₂O, H₂, O₂) as well as SO₂ itself. The radiative transfer exchange among the atmospheric layers were ignored, due to the low optical depth of the SO₂ ($\tau < 0.03$) for the estimated SO₂ atmospheric profiles. The collisional rate coefficients were estimated from the SO₂-H₂ rates (available in the [LAMDA database](#)) using reduced mass scaling approximation for the other species. We present spectral line calculations for nominal collisional rate coefficients, 3-D Monte Carlo model results for the number density profile and the kinetic temperature profile, in Figure 4.10. Due to the unknown nature of Europa's exosphere, an increase or decrease in the above parameters can shift the absorption depth into lower/higher rotational quantum numbers, and/or increase/reduce the line amplitudes. Nonetheless, for the nominal value of these parameters, we anticipate local Rayleigh-Jeans line contrasts of 5 K in regions where SO₂ is present.

The non-LTE modeling indicates that ALMA will be sensitive to a SO₂ column of: $N \gtrsim 10^{13} \text{SO}_2 \text{ cm}^{-2}$, covering an area as small as 1/16th of Europa's disk. Thus the expected source size of 25% of the disk, is four times larger than this target's limit. The expected line contrast for the strongest line (*strongest line*: $\nu = 221.9652 \text{ GHz}$) is 8 mJy in absorption, which is detectable after 3.3 hrs on source (5.1 hrs of telescope time). A second SO₂ line (at 241.615 GHz), with expected contrast 70 % of the former, can be searched in parallel.

Even a non-detection of SO₂ by ALMA for example would:

- *Illuminate the physics of ion-water ice interactions at cold surface temperatures $T \sim 100 \text{ K}$:*

At $T \sim 136 \text{ K}$ magnetospheric ion sputtering should eject a column of $N \sim 10^{13} \text{SO}_2 \text{ cm}^{-2}$ even in the absence of venting. Cassidy et al. [2009a] showed that SO₂ on SO₂ ice at least thermally desorbs like O₂, populating the first $\sim 200 \text{ km}$. Above this near-surface component, the sputtered SO₂ expands radially like sputtered H₂O. Therefore, even if SO₂ is not detected we will be able to place constraints on the sputtering fluxes and sublimation fluxes of amorphous water ice containing trace amounts of SO₂, experiments which have not been done in the laboratory.

- *Test the efficiency of the radiolytic sulfur cycle.* : [Carlson et al. \[2005\]](#)
demonstrated that radiation processing fuels Europa's sulfur cycle, in which S^+ ions can form mostly sulfuric acid hydrates, and trace amounts of SO_2 trapped in the ice which are eventually thermally desorbed (also to be confirmed). A non-detection of SO_2 can place limits on the rate of SO_2 chemistry occurring at Europa's trailing hemisphere.

Our observation is time-dependent in that we target Europa's sunlit trailing hemisphere, which contains the maximum SO_2 concentration ([Lane et al. \[1981\]](#); [Ockert et al. \[1987\]](#); [Noll et al. \[1995\]](#)). The trailing hemisphere also possesses evidence of maculae or upwelled oceanic material which can increase the SO_2 content in the exosphere by an order of magnitude [Teolis and Waite \[2016\]](#). The 2017 cryovolcanism announcement [Sparks et al. \[2017\]](#) was centered at the trailing hemisphere. The observation was unable to observe the other half of the trailing hemisphere for venting, parts of which we will be able to probe during our observation. The observation should also be able to determine the venting source rate, and at the very least provide a useful upper limit for the entire trailing hemisphere.

4.3 Detecting the Presence of a Toroidal Atmosphere

If the exospheric source rates are high, and the ejection speeds permit entrance to the interplanetary medium beyond the satellite's hill sphere, volatiles can assemble around the satellite's orbit generating a donut shaped gas cloud: a toroidal atmosphere. The volatiles in this torus should last on the order of an orbital timescale to keep the torus structurally stable. At the same time, if the neutral volatiles are picked up, ionized, and dispersed along the orbit due to the magnetic field, they can form a plasma torus. Table 4.3 provides a list of possible candidates due to the detection of volatiles which have potentially ejected from a satellite and not necessarily from the planet.

4.3.1 Escaping Exosphere Mechanisms to Populate a Toroidal Atmosphere

There are several ways an exosphere can escape and populate a toroidal atmosphere. In this way, satellites are often regarded as plasma sources as is the case for Enceladus (e.g. [Johnson et al. \[2006b\]](#), [Cassidy and Johnson \[2010\]](#)). Our work in Ch.2 indicates that Europa like Enceladus may be populating a torus due to the possibility of

Planetary Body	Species	T_{eq} (K)	g (m/s ²)	R_p (R_J)	M_p (M_J)	P (day)
Escaping Exoplanet Exospheres						
WASP-17b	Na, K	1740	3.6	1.89	0.51	3.73 — 5.53
WASP-39b	Na, K	1120	4.1	1.27	0.28	4.06
HD209458*	Na, K	1450	9.4	1.36	0.69	3.52
WASP-19b	Na, K	2050	14.2	1.41	1.14	0.79
HAT-P-1b	Na, K	1320	7.5	1.32	0.53	4.46
WASP-31b	Na, K	1580	4.6	1.55	0.48	3.40
WASP-12b*	Na, K	2510	11.6	1.73	1.40	1.09
HAT-P-12b	Na, K	960	5.6	0.96	0.21	3.21
HD1897338b *	Na, K	1200	21.4	1.14	1.14	2.22
WASP-6b	1150 Na, K	8.7	1.22	0.50	3.36	
HD80606b [†]	Na, K	1500	9.6	0.921	4.3	111.4
Kepler-444	H, H ₂ O					

TABLE 4.3: **Atmospheric-bounded exoplanet exospheres** Exoplanet Exospheres: The listed physical parameters are based on data compiled from HST and Spitzer observations (Sing et al. [2015]).

* Recent asymmetric light curves also show evidence of potentially asymmetric exospheres in planets .

[†] unanalyzed transmission spectroscopy data on this planet exists from 2014, in which a fast K I wind was already detected Colón et al. [2012].

◊ Neutral atmospheric transport appears to generate photometri asymmetries in the light curve Turner et al. [2016].

plasma-driven expansion. The possibility of a neutral Europa torus was explored in detail by Smyth and Marconi [2006].

The major mechanisms for gas escape and eventual torus population should the timescales fit are:

1. Thermal Jeans escape (see Appendix A)
2. Upper atmospheric escape (Appendix A)
3. Plasma-Driven Expansion, i.e. charge-exchange induced escape
 $O_2 + O_2^+ \rightarrow O_2^* + O_2^+$
4. Tidally-driven volcanism

4.3.2 Detecting Neutral Tori

An O₂ toroidal atmosphere was discerned at Saturn (Johnson et al. 2006). The plasma-driven expansion described above at Europa could, in principle, produce the same at Jupiter. This would mean Jupiter has a large O₂ ring extending to 10s of km composed of molecular oxygen, H₂, H₂O.

Curiously, Cassini's ion-and-neutral camera (INCA) observed energetic-neutral-atoms at a rate of $\Phi_{ENA} \sim 8 \cdot 10^{23} s^{-1}$ [Mauk et al., 2003] with energies around $E = 50 - 80$ keV outside Europa's orbit in the direction of Ganymede. ENAs are thought to be a result of ion-neutral charge-exchange between ambient ions circulating in the Jovian magnetosphere and either H or H₂ [Mauk et al., 2003]. In this way INCA, an ENA imager, also functions as an exosphere detector as the images can indicate exosphere-magnetosphere interactions. We investigate the possibility that these neutrals are Europagenic atomic hydrogen or molecular hydrogen in section 2.9.1. The observation implied a population of $\mathcal{N} = 4.5 \cdot 10^{33} \pm 20\%$ molecules or atoms [Mauk et al., 2003].

Smyth and Marconi [2006] provided robust calculations of the expected content of Europa's neutral gas tori. We can then, in principle use updated values from our EGM simulations to check the expected content and compare again to the above values by [Mauk et al., 2003].

From [Johnson and Huggins, 2006], the total number of atoms or molecules in a neutral cloud is simply $\mathcal{N} = S\tau$. Where S is the source flux, and τ is the lifetime of the species in question. If, for example [Mauk et al., 2003] observations were actually charge-exchange from O₂ instead of hydrogen species then: $\mathcal{N} \sim 1e26 O_2/s * 3e5s \sim 3e31$ O₂ present in the torus. Thus O₂ based on Cassidy et al. 2013's source rates accounts for 1% of the observed ENAs. If [Dols et al., 2016] calculated escape rate for O₂ was accurate then $\dot{M} \sim 160$ kg/s corresponds to $\mathcal{N} \sim 10^{33}$, within a factor of 4-5 of the observed population. Furthermore there could be an added population of H₂O which could collisionally expand the O₂ or other atmospheric species in the same way Io does [Summers et al., 1989].

4.4 Conclusions on Ocean World Perspectives

Our estimations in this chapter acknowledge the large parameter space of unknowns regarding the endogenic and exogenic interactions on satellite exospheres. It is important to consider the consequences of the upper limits of a few of the unknown sources. The prodigious power a satellite exosphere can output into the interplanetary medium could even contaminate a transmission spectrum of an extrasolar planet. We note that in the case of HD 80606b, an escaping *potassium* atmosphere of $v \sim 200 km/s$ was inferred by [Colón et al., 2012], which appears to be far too fast questioning the interpretations. A more likely explanation may be a wider, less concentrated cloud of potassium due to -for instance- a satellite exosphere. Potassium is a key volatile in that its ratio with sodium can potentially indicate whether it has

been volcanically processed, or it emanates from the ocean as better evidenced on Europa. These links may deserve attention in the coming years as astronomical instrumentation advances. Future in-situ missions will resolve such questions once and for all, which is why we focus our attention now to the development of such technologies which may one day fly towards these satellite exospheres.

In-Situ Observations & Technology

As is the case in any field, theory cannot advance without new observations, and new observations cannot take place without new instruments. At this point, our attempts to deduce the actual satellite exosphere conditions based on observations and simulations may become instrumentation-limited. We thus focus our attention to the advancement of space instrumentation. We outline the interest of several in-situ instruments which are set to fly on the upcoming Europa Clipper and JUICE missions, below.

The exospheres we have studied in detail in this thesis are surface-bounded, and thus significant interaction with the regolith occurs, knowledge only *in-situ* observations can bring via low-altitude flybys (e.g. Europa Clipper $z < 100km$) or orbital observations (e.g. Ganymede (JUICE) $z \sim 500km$). Examples of observations to be made in the late 2020s by these missions include: visible (EIS) and thermal imaging (E-THEMIS, MISE), radar (REASON), and magnetic field characterization (ICEMAG, JMAG).

Direct *in-situ* observations of exospheres however are done chiefly by mass spectrometry (e.g. MASPEX, PEP). Mass spectrometry directly collects atoms or molecules present in the exosphere.

Questions are now raised, such as: how do mass spectrometers work in such tenuous environments? How can we improve them in the future of space exploration? In particular, how can we improve the efficiency of exosphere detection? The critical components regulating efficiency in space exploration are the power consumed and the mass.

	INMS/CASSINI	ROSINA/ROSETTA	NIMEIS/R&T CNES
Type	Quadrupole	Orbitrap	TOF Detector
M/dM	100	3000/500	30
Power consumption	23.3	19/24 W	7.3 W

TABLE 5.1: A few classic, neutral mass spectrometers and their essential properties: mass resolution and power consumption.

5.1 Mass Spectrometers

There are many mass spectrometers that have been developed over the decades. Table 1 demonstrates a few of these spectrometers and their properties. ROSINA is a mass spectrometer which was on the ROSETTA mission orbiting comet 67 P c/g. NIMEIS (Neutral and Ion Mass and Energy Imaging Spectrometer) is the mass spectrometer being developed at LATMOS equipped with a time-of-flight (TOF) detector. J. Becker (2013) describes these instruments in detail.

The CASSINI INMS is likely one of the most successful neutral mass spectrometers to date and provided the first direct detections of satellite exospheres with the detection of H₂O at Enceladus [Porco et al. \[2006\]](#), CO₂ and O₂ at Rhea and Dione ([Teolis et al. 2016](#)). Analysis of the ionized neutrals is performed by a quadrupole mass analyzer, which consists of four hyperbolic rods generating an electrostatic field which regulates the mass and mass/charge ratio of the ions reaching the detector. Figure 5.1 from [Waite et al. 2004](#), shows a schematic diagram. INMS has two chambers depending on the sensitivity needed for exospheric detection. The first chamber, the closed ion source, is for extremely tenuous gases which are permitted to accumulate in the antechamber before being ionized and accelerated down the collimation tube to the quadrupole mass analyzer. The second chamber, the open ion source, is for less tenuous gases, and minimizes issues related to chamber wall interactions.

We focus on a simple yet essential component of neutral mass spectrometers: the ionization source. In the case of ROSINA & INMS, neutral ionization was achieved by electron bombardment. When ionized, charged particles can then be analyzed by electrostatic analyzers leading to the measurement of their mass over charge ratio (ROSINA & INMS) and/or energy (NIMEIS). As we shall explore, advancing the state of electron guns is our principal goal of increasing the sensitivity for exosphere detection, essential to identify trace species. Furthermore, advancing the state of electron guns will give one the ability to reconstruct spatial and temporal variabilities in these extremely tenuous environments, as well as the ability to track the long term evolution of these exospheres.

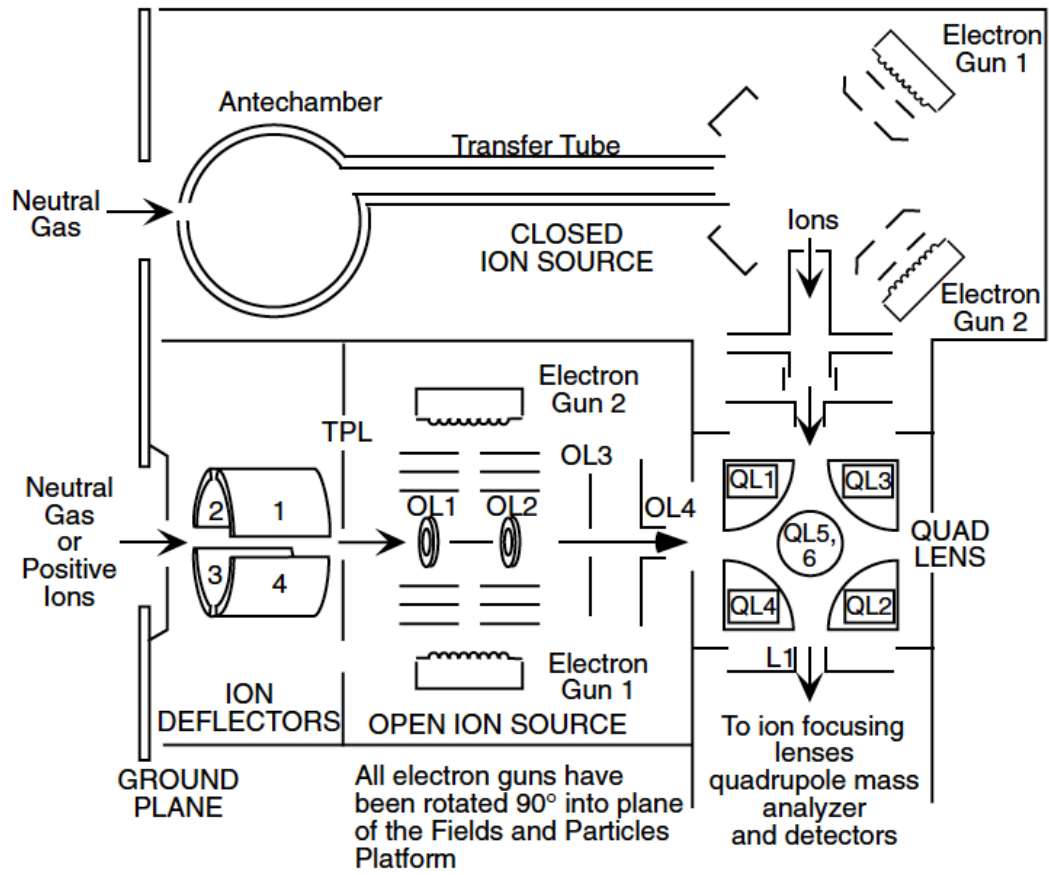


FIGURE 5.1: Schematic diagram of Ion Neutral Mass Spectrometer on board Cassini-Huygens. It shows the principle of the ion trap, where the neutral gas arrives along with the various electron guns. The closed ion source has a sensitivity to $n \gtrsim 10^4 \text{ cm}^{-3}$ and the open ion source has $n \gtrsim 10^5 \text{ cm}^{-3}$. From Waite et al. 2004.

5.2 Introduction: A Carbon Nanotube Electron Gun.

In this thesis we sought to demonstrate the efficiency and stability of Carbon Nanotube (CNT) field emission (FE) for spacecraft technologies, in particular mass spectrometry.

Currently, neutral mass spectrometers rely on thermionic emission of electrons from a heated cathode subject to a . The thermal electrons are then accelerated towards the ionization chamber at energies ranging from $\sim 50\text{-}100\text{ eV}$ (INMS & ROSINA). The classic element used is a Tungsten filament heated to $\gtrsim 2000\text{K}$, giving enough energy to free electrons in the conduction band to surpass the work function ϕ , potential barrier and allow electrons to escape from the metal (Murphy and Good [1956]). Such filaments utilize roughly $\sim 1 - 3\text{ Watts}$ of power.

CNT FE has been shown to be more efficient than their thermionic emission counterparts in several aspects. The most practical aspect is the power efficiency. Figure 5.2 demonstrates the $\sim \text{milliWatt}$ range of power required by the CNT for a standard emission current versus polarization voltage. Immediately this analysis alone demonstrates that the power efficiency of nanotechnology may be a factor of 100 greater than classic filament technology.

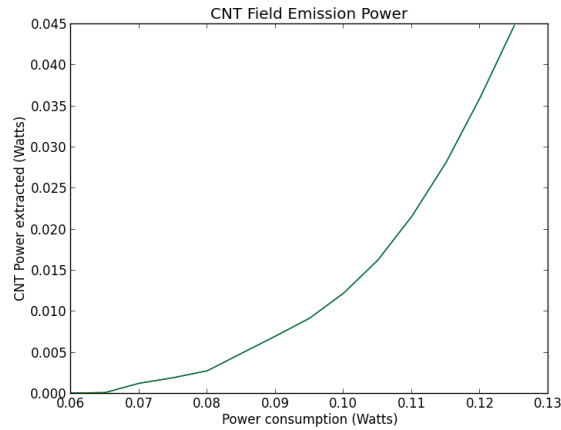


FIGURE 5.2: Power characterization of our CNT setup, which also serves as demonstration of FN emission. As we increase the extraction voltage, more power is consumed. If the CNTs are emitting nominally, the extracted power should grow exponentially versus consumed power. The extracted power is calculated simply via Ohm's law : $P_{\text{extracted}} = I_{\text{cnt}}V$, where the consumption of the source is $P_{\text{source}} = I_{\text{source}}V$. The voltage source was a Stanford Research systems high-voltage power supply. We can see that we are only using on the order of tens of milliwatts of power, which is about 10x better than nominal cathode ray tubes (CRTs).

Li et al. [2015] provided an excellent review of field electron emission principles and applications. Industrial examples include LCD technology, where electron impact of neutral phosphorous excites the atom, generating the emission necessary for color

displays. These FE displays (FED) have been shown to be 50% more power efficient (Li et al. [2015]). Medical applications where electron impact can serve as an X-ray source is also highly useful. Space applications for CNT FEs have been seldom discussed or demonstrated. Here, we identify and explore two direct applications which could contribute to the advancement of space exploration due to the power efficiency of CNTs. (1) Electron-impact ionization source for mass spectrometers, in the interest of detecting neutrals in planetary atmospheres and in the interplanetary medium. (2) Spacecraft charge regulators, in that electron emission sources can help neutralize a spacecraft if it is strongly charged (Matéo-Vélez et al. [2015]).

To realize these two applications, we have improved upon the CNT field emission apparatus from that described in Becker et al. [2013]. In Becker et al. [2013], a triode-type electron source was employed, whereas in this work we test and simulate more of a diode-type electron source since the anode is grounded and the electric field is restricted between two electrodes, the CNT chip and the G1 chip. The CNT chip, which is the basis of the Carbon NanoTube electron gun (CNTeg also known generally as FEGs) is a thin wafer of either silicon or iron, with a 15 mm^2 square of millions of vertically-aligned nanotubes (Hong et al. [2009]). A sample silicon CNT chip is shown through the lens of the G1 grid in Figure 5.4.

5.3 CNTegs

The Carbon NanoTube electron gun (CNTeg) is a stable electron source relying purely on cold cathode technology. The CNT wafers are fabricated in Ajou University, South Korea, using chemical vapor deposition techniques. Our most recent 2017 samples are fabricated by NAWA Technologies in France. Figure 5.3 shows a newly made CNT chip at the Edmund test bench.

5.3.1 Carbon Nanotube Field Emission

Field Electron Emission (FE), measured as a current I_{CNT} , directly depends on the local electric field (E_{loc}) at the cold cathode's surface which is in turn governed by the extraction potential, which we call V_{CNT} . The emission is quantum in nature, in that the emitted electrons surpass classical potential energy barriers in the metal due to Fowler-Nordheim tunneling effect Fowler and Nordheim [1928], and are then further accelerated due to the \vec{E} field.

The current can be calculated following Fowler and Nordheim:

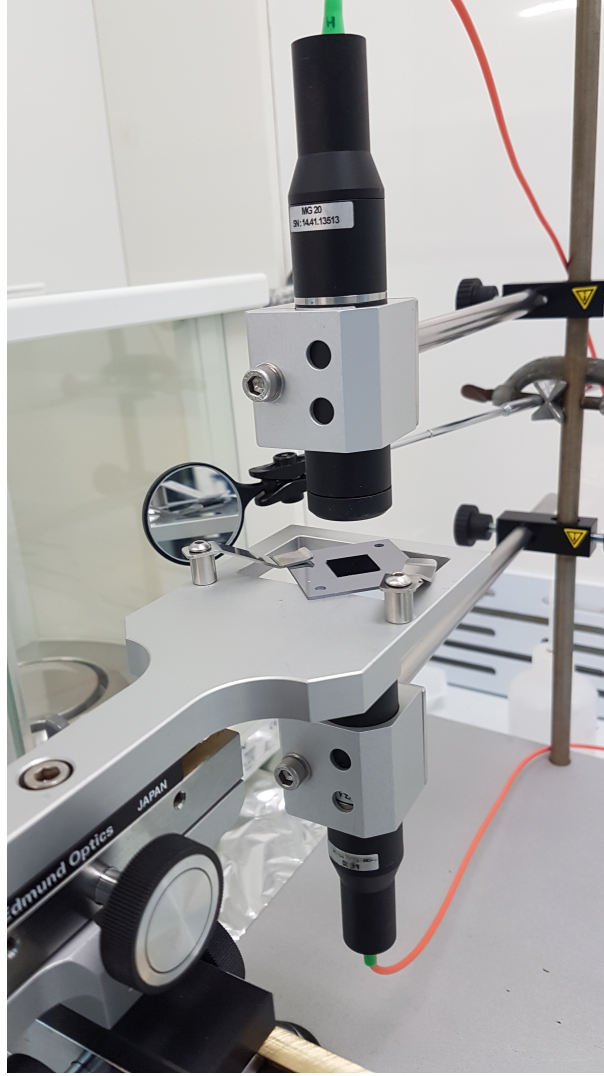


FIGURE 5.3: NAWA technologies CNT chip fabrication testbench, May 2017.

$$I(V, \phi) = A \frac{1.4 \cdot 10^{-8}}{\phi} \beta_e V^2 \exp\left(\frac{10.4}{\sqrt{\phi}}\right) \exp\left(\frac{-B\phi^{1.5}}{\beta_e V}\right) \quad (5.1)$$

Where A , in m^2 , is the effective emission area, β_e is the field factor measured in inverse microns, $\beta_e V = E_{loc}$, the local electric field. The local electric field was discussed in [Becker et al. \[2013\]](#) in regards to the CNT tips. $\phi(eV)$ is the work function, and $B = 6.44 \cdot 10^9 V/m/eV^{-1.5}$ is a constant.

FE has been studied heavily in experimental physics since the late 1990s ([Zhu et al. \[1999\]](#)) and has not, until recently, been tested for space technology in novel ways such as mass spectrometry.

The central CNT square emits currents on the order of $100 \mu A$, when subject to a voltage difference of $\sim -300V$, corresponding to an efficient power approaching $P \sim 10$ milliWatts. This power is sufficient for the aforementioned applications. Figures [5.6](#)

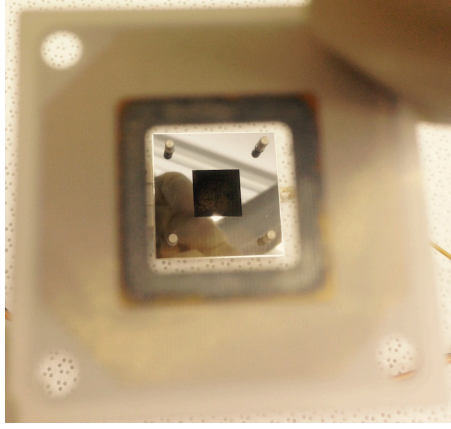


FIGURE 5.4: Birds eye view of the carbon nanotube chip through the lens of the G1 grill.

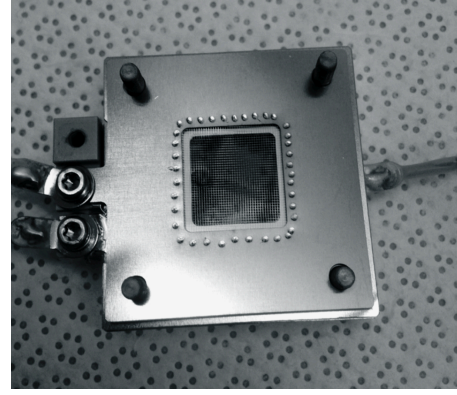


FIGURE 5.5: The CNTeg with the Anode facing up with a tungsten grill.

Figure	z_{CNT} [μm]	I_{max} [μA]	β	P [mW]
A	~ 350	209	73.3	52
B	150	21	76.2	9.5
C	200	152	77.4	76
D	200	46	66.8	23
E	600	48	95.4	19
F	340	25	72.0	8.2

TABLE 5.2: Six CNT samples tested at LATMOS from 2015-2017. Samples E & F use a different workbench setup at NAWA technologies than at Ajou University (Samples A- D).

and 5.9 are schematic diagrams showing the mechanics and electronic circuitry of our setup respectively. The primary electrons contributing to the $10^2 \mu A$ current traverse an extraction gate, (G1) with energies on the order of hundreds of eV ($\sim V_{CNT}$), which then travel through the final anode gate (A1) before reaching the collector. A top down view of the full CNTeg is shown, with the anode and its tungsten grid in Figure 5.5. Here we simulate these primary electrons and their secondary electron counterparts, rebounding off the tungsten wires ($r = 30 \mu m$), using the 3-D electromagnetic software suite SIMION. Lastly, experimental results are provided comparing Becker et al. [2013] emission and current characterization of the system, globally.

5.3.2 CNTeg emission runs

We have fully characterized nominal silicon substrate CNTegs. A more robust stainless steel substrate has been tested for emission for three samples emitting maximum currents of 3, 30, and $100 \mu A$. We summarize the silicon substrate CNTeg experiments performed at LATMOS from 2015-2017 and characterize their emission in Figures 5.10

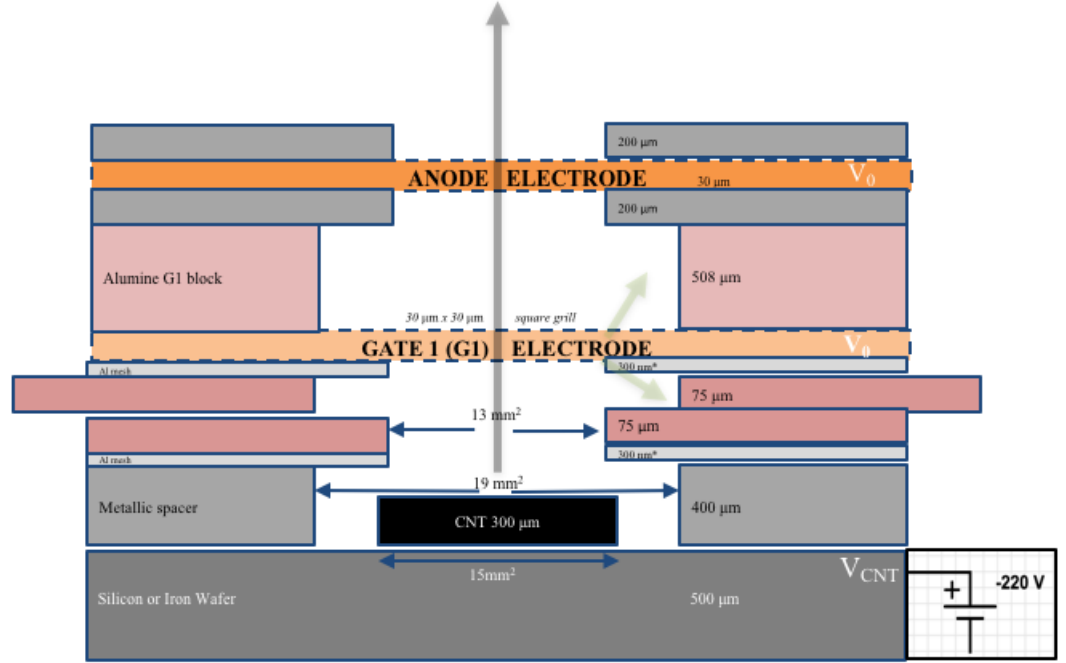


FIGURE 5.6: Schematic diagram of CNTeg. Electrodes and conductive elements are portrayed in gray tones, whereas insulators e.g. kaptons, coatings, are in pink. The two tungsten mesh-grills are in orange the Gate 1 electrode and the Anode electrode. The electric field which pushes the electrons upwards is between the CNT and G1, where the electric potential is applied at the CNT wafer. The two transparent green vectors emanating from G1 represent the secondary electrons we model.

The β_e factor, described above, is indicated in each figure which is a rough representation of the ability for the nanotubes to emit electrons when subjected to an electric field. Our maximum β_e value is ~ 100 , although this is not indicative of the most stable sample. In the next section, we simulate how this electron emission can be deflected due to the electric field present in the CNTeg, and specifically how it can characterize the energy distribution of the emitted electrons.

5.3.3 CNTeg energy characterization

The energy characterization of the CNTeg is critical in assessing its ability to ionize incoming neutrals for detection. For this purpose we utilized an electrostatic analyzer (EA) similar to the nominal tophat type as described in the literature (Victor et al. [2006]). The ionized molecules will arrive at the opening aperture of the EA, at energies corresponding to the exosphere generation process described in Chapter §1.

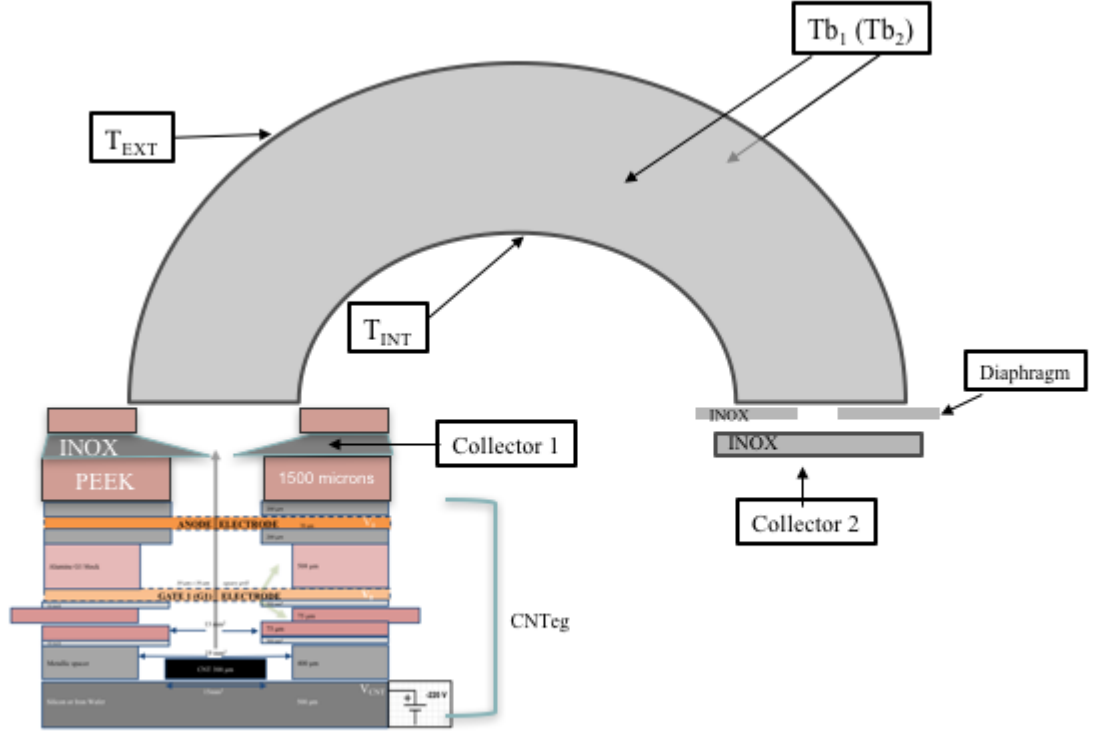


FIGURE 5.7: Schematic diagram of CNTeg + Electrostatic Analyzer. Electrodes are boxed. In our electronic setup we regulate the voltage of T_{ext} , which is connected via a voltage divider to T_{b1}, T_{b2} , T_{int} as indicated explicitly in Figure 5.9, in order to guide the incoming electron beam to Collector 2 the final electrode.

Figure 5.7 shows how electrons in our setup are deviated depending on their energy. The energy dependence is due to a simple force balance between the centrifugal force and electrostatic force: $F_c = F_e$, so that the radius of deflection is simply: $r = \frac{mv^2}{qE}$, where E is the electric field. In this way the EA can deflect the ion beam and thereby 'select' a given energy. To get the energy distribution, one performs *energy sweeps*, by varying the electrostatic field inside the EA while measuring the current on Collector 2. Figure 5.11 provides a picture of the experimental setup including the CNTeg & EA. The "T" electrodes correspond to the toroidal analyzer, which can be polarized to various electric potentials, enabling the measurement of the electron energy distribution of the electron beam we test. Simulating the entire device, to $100\mu m$ resolution, enables us to model the true energy distribution of the electron before entering the EA for the measurement. Below we describe a few of these simulations, leading up to a comparison between the simulated and experimental measurements.

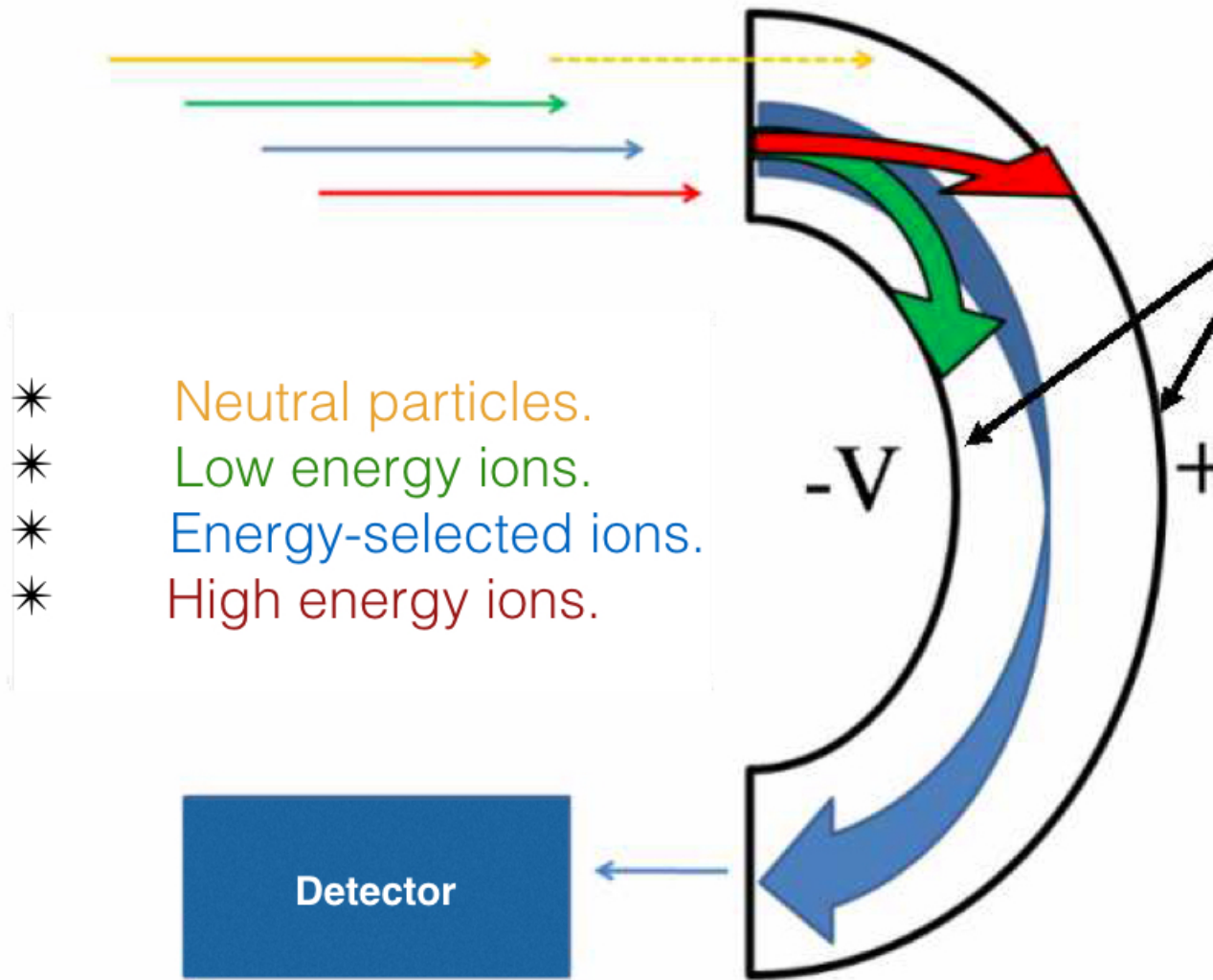


FIGURE 5.8: Illustration depicting the operation of the electrostatic analyzer, as adopted from J. Becker 2013. The utility of the analyzer is to select only a specific set of ions corresponding to the energy band-pass (blue). The rest of the ions will not be deflected to the detector along with the neutrals. The electric field guiding the circular trajectory of the electrons is generated by the difference in voltages across the EA analyzer. A demonstration of how the beam is deflected by the variable electric fields in our simulations is provided [here](http://oza.page.latmos.ipsl.fr/images/fast_emission.gif): <http://oza.page.latmos.ipsl.fr/images/fast_emission.gif>.

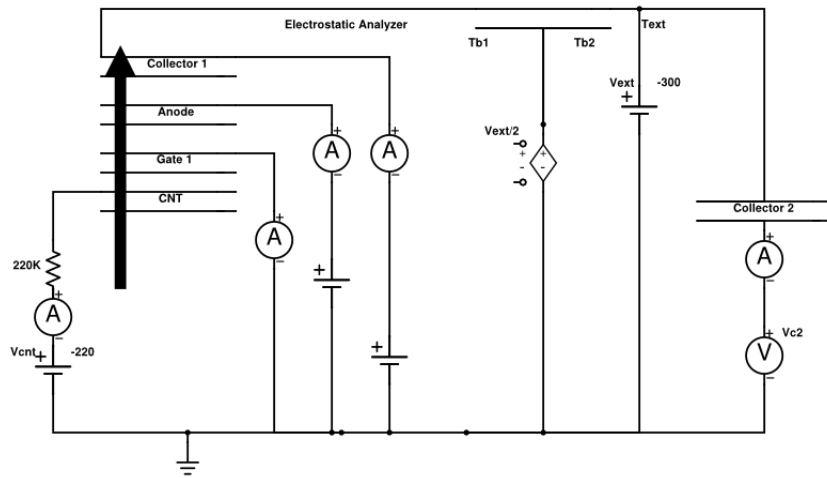


FIGURE 5.9: A simple electronic circuit diagram designed using the circuit simulator **Partsim**, which employs the engine **SPICE**. Only the principal electrodes are shown. The black arrow shows the direction of electron field emission. V_{CNT} is the negative cathode voltage of the CNT, V_{EXT} is the negative voltage of the external EA torus, and $V_{EXT}/2$ (via a voltage divider) is connected to Tb1 and Tb2 which are guiding electrodes places on the edge of the EA assembly. V_{C2} is a positive voltage applied to collector 2. Collector 1, Anode, and Gate 1 are all connected to ammeters for probing emission at each successive level above the CNT surface. Collector 2 is connected to a Keithley picoammeter in order to measure the electrons that reach the end of the analyzer. The anode and collector 1 are also connected to voltage sources.

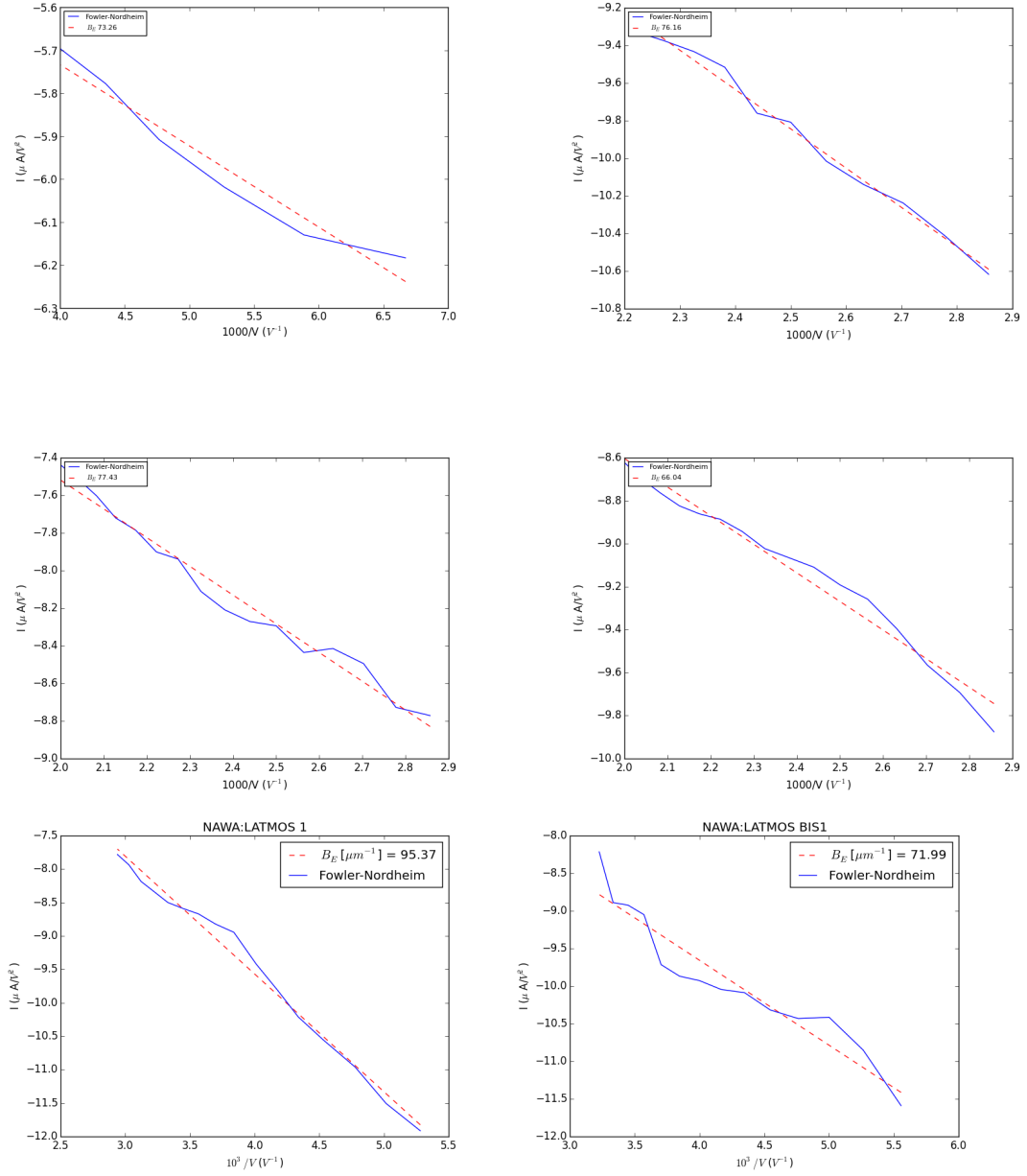


FIGURE 5.10: Silicon CNTs from 2015-2017 with corresponding Fowler Nordheim curves fit to the extracted CNT current versus voltage. For discussion: A is the top left figure, B the top right, continuing with C in the next row left, and so forth.

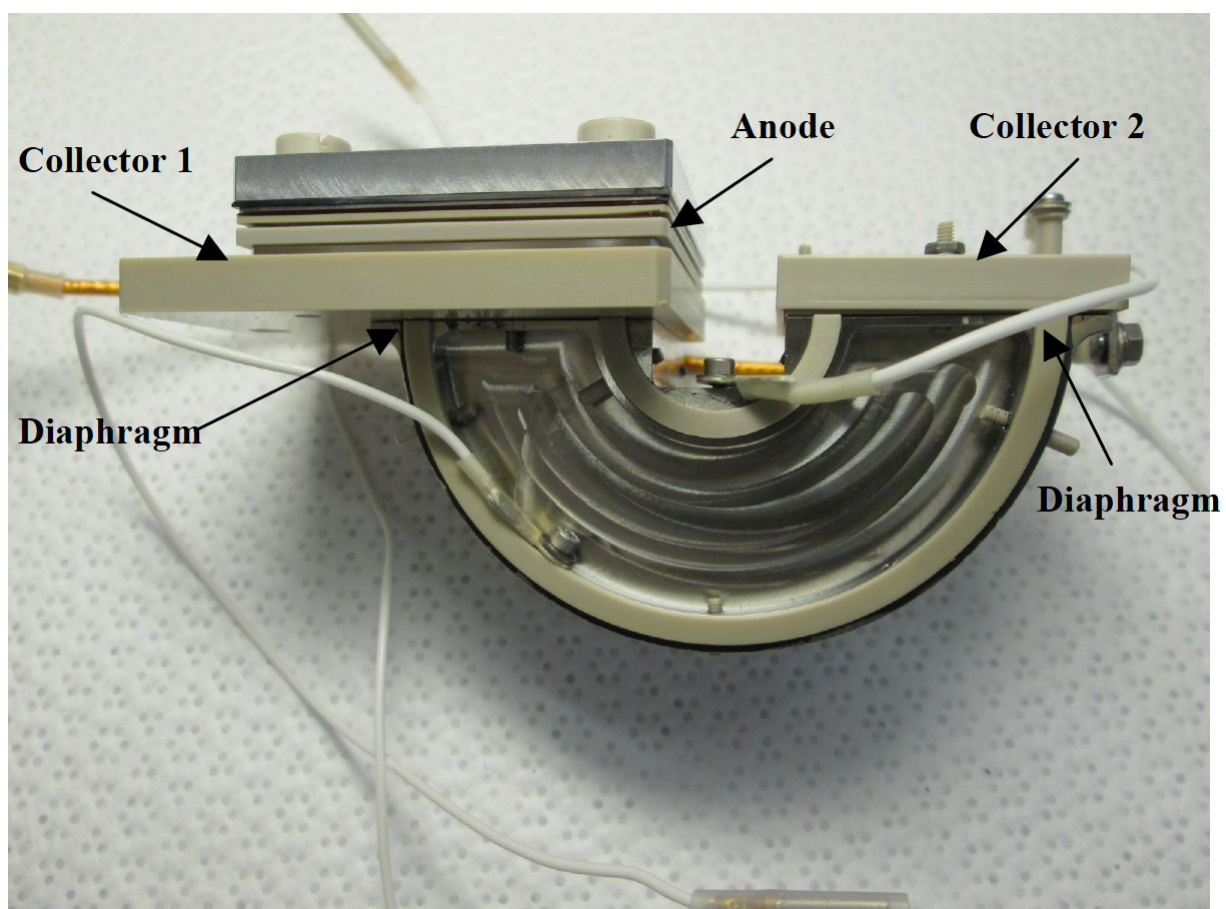


FIGURE 5.11: CNTeg + EA assembly.

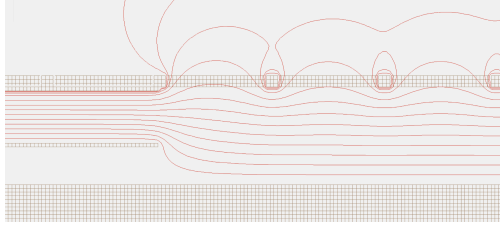


FIGURE 5.12: A zoom-in of the potential difference between the CNT cathode and the G1 electrode.

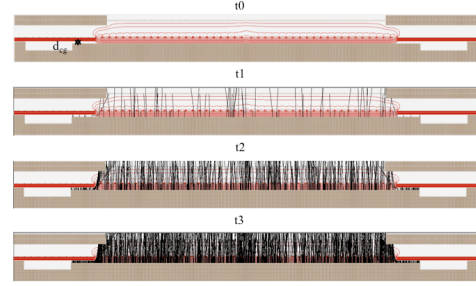


FIGURE 5.13: A simulation of the extraction device portraying how electrons are emitted in the presence of a sufficiently strong electric field.

5.4 Simulations of Primary Electron Emission Under Electric Fields

Numerical simulations of the ionization source aid in understanding how field electron emission works in practice. Here we employ the **SIMION** software suite to solve the 3-D Laplace equation using Dirichlet boundary conditions to solve for the electric field at each point at a resolution of 10

μm . *Figure 5.12 shows the electric field which is generated between the CNT and G1 electrodes (a distance we*

portraying a potential difference between the extraction potential V_{CNT} and the grounded electrode, $V_{G1} = 0$. Thus the resultant electric field is simply the electric potential gradient, $E = \nabla V$. The maximum electric field we employ is generally $V_{CNT} - V_{G1} = -250\text{V} / 250\mu\text{m} = 1 \text{ Megavolt/m}$. The figure shows this gradient via red [equipotential] lines of constant electric field in steps of 20 volts. The electrons will accelerate orthogonal to the equipotential lines in the +y direction to the analyzer.

One can also observe that the equipotentials bend gradually around the metallic spacer just above the CNT (distance denoted as d_{CM}). The transition region is sufficiently smooth such that significant edge-effect emission is very unlikely. Fig. 5.13 provides a demonstration of our extraction device. In this simulation primary electrons are released from the top of the CNT cathode and accelerated by the electric field between the G1 and the CNT cathode. After passing through G1, these electrons enter in a 'field free region' between G1 and the anode. In reality however, there is a possibility for secondary electrons emitted from the G1 grid contaminating this G1-Anode volume. The physics of secondary electrons is simply momentum-transfer, very similar to the interparticle physical processes that occur on planetary surfaces, such as sputtering [Johnson \[1990\]](#). In this case, it is an energetic primary electron ($N_{p,0}$) that collides

with an electrode, generating a new, secondary electron (N_{SE}). Both of these electron populations have a probability to backscatter. The population impacting the grid G1, is denoted as a prime, so that $N_{p,0} = N'_p + N_p$, with N_p the portion of the primaries moving through the grid.

The $30\ \mu m$ wires in the G1 mesh grid, whose dimensions are $13\ mm^2$, with $300\ \mu m^2$ squares, are made of tungsten. Given this geometry and an emission area of $dA_{CNT} = 15\ mm^2$, we can calculate the number of original primary electrons which are able to traverse the mesh. The transmission of the grid is found to be $\tau_p \sim 0.7$. Thus $N_p = \tau_p N_{p,0}$, and the part of the impacting primary ion primaries N'_p might lead to secondary electron emission.

A general expression for the yield is derived in [Lin and Joy \[2005\]](#), which we rewrite as:

$$\delta(E_{pe}) = \int \Phi(z, E_{PE}) P(z) dz \quad (5.2)$$

where $\Phi(z, E)$ is the generation rate of secondary electrons, $\Phi(z, E) = -\frac{1}{\epsilon} \frac{dE}{ds}$ given the effective energy required to produce a SE ϵ , and $\frac{dE}{ds}$ the stopping power of the primary electron. $P(z)$ is the probability that these secondaries get ejected from the surface.

We will use this formulation to derive an expression for our setup.

5.5 Secondary Electron Model

We begin with a simple Monte Carlo routine for the secondary electrons where we keep track of impacts on G1 in x, y, and z over a random series of counts. Typically, secondary electrons have energies below $20\ eV$, thus as a 1st approximation, their trajectories can be guided by equipotential lines as the electrons will follow the electric field perpendicular to the potential illustrated in [Fig. 5.13](#) (typically, the electric potential after the G1 electrode drops linearly from $-10V$ to about $-2V$ at the anode surface.) Then we eject $1-20\ eV$ secondary electrons from the surface assuming a uniform, random distribution. Furthermore, the altitude and azimuth of the SE are also tracked, which are then finally converted into SE velocities which we reinject into the SIMION simulation. In reality the ejection is non-random, where the probability distribution function (PDF) for a SE to return to the surface to be emitted, after production in the material, is:

$$P(z) = K e^{-z/\lambda} \quad (5.3)$$

where z points into the material, and λ is the secondary electron depth in cm. For tungsten, [Lin and Joy \[2005\]](#) finds the SE escape depth to be $\lambda_W = 0.2nm$. This is the effective depth at which the secondary electron can return or rise to the surface again. The actual penetration depth on the other hand R is useful in estimating the stopping power for a primary electron of energy E_{PE} on a material of density ρ and parameter $\beta = 76nm$ for keV E_{PE} :

$$(5.4) \quad \frac{dE}{ds} = -\frac{E_{PE}}{R}$$

Inserting the general expression for stopping power, Eqn. 5.5 into Equation 5.2, and integrating from 0 to the penetration depth, R one can solve for the secondary electron yield:

$$\delta(E_{pe}) = K \frac{E_{PE}}{\epsilon} \frac{\lambda}{R} (1 - e^{-R/\lambda}) \quad (5.5)$$

This is the general expression for secondary electron emission, however it is R the electron penetration depth which is difficult to determine as it is a function of energy.

$$R = \frac{\beta}{\rho} \cdot (E_{PE})^n \quad (5.6)$$

Where ρ is the material density (in our case Tungsten $\rho_W = 19.25gcm^{-3}$). The rest of the parameters are experimentally determined: $\beta = 76$ nm for a keV primary and $n = 1.67$ (Lane & Zaffarano 1954). Ultimately [Lin and Joy \[2005\]](#) present the *Universal law for SE yield* which we employ for our voltage dependent emission where $\mathcal{E} = \frac{E_{PE}}{E_{PE}^m}$. The constants $c_1 = 1.28$ and $c_2 = 1.614$ are found for $n = 1.67$.

$$\delta = \delta_m c_1 (\mathcal{E})^{-0.67} \left(1 - e^{-c_2 \mathcal{E}^{1.67}} \right) \quad (5.7)$$

For our parameters, $\delta \approx 1$ so we model the secondaries as 1:1 for each impacting primary. Thus we record the position of each primary impact on the Tungsten wires, and then re-emit.

5.6 Results

It is found empirically in Lin and Joy [2005] that $\delta_{SE} \sim 1$, for Tungsten. Thus the *total* number of secondary electrons generated will be $N_{SE,0} = \delta_{SE} N'_p$. To then calculate the transmitted secondaries, we perform numerous SIMION trials, and find that $N_{SE} = \delta'_{SE} N_{SE,0}$, where $\delta'_{SE} \sim 0.5$.

Figure 5.14 provides a zoom in on the secondary electron emission behavior on the Tungsten grid. It can be seen that the electric field modeled in Figure 5, generates a small arc which helps constrain δ'_{SE} and allows the secondary electrons to return to G1 or be lost into the bottom of the wire. The arcs show that the secondary electrons cannot escape the local G1 field. Thus secondary electron emission is localized at the generation site, and small compared to the primary electron emission. Figure 5.15 shows the secondary electron emission at high resolution ($N_e = 10^5 e^-$) in the CNTeg. We can see in Figure 5.16 that even in the high-resolution case the number of secondary electrons entering the electrostatic analyzer is negligible. Given these values, we estimate the current at each electrode in the CNTeg: I_{G1} , I_A , I_{C1} .

ELECTRODE	I_0 [microAmps]	I_{SIM} (μA)	i_{SE}
CNT	102	100.0	—
GATE 1	-23.4	-26.88	2.58
ANODE	-19	-30.99	2.96
COLLECTOR 1	-33.5	-43.03	3.20
ΔI	-26.1	+0.1	—

TABLE 5.3: Simulated and measured (for an arbitrary CNT) current at each electrode. It can be seen in this example the anode and collector seem to have a large discrepancy from simulations, which secondary electrons are unable to account for. ΔI is the missing current comparing before and after emission.

The second collector (C2) will be analyzed in the next section in order to characterize the energy of the ionization source.

5.6.1 Electron Energy Characterization

Besides the electrons in the G1-Anode volume, it is important to characterize the energy range of the primary electrons. Here we show numerous experiments where we measure the current after it passes through the energy analyzer subject to various external voltages. This exercise effectively characterizes the energy distribution of the electrons, as under normal conditions the peak in electrons should occur at the CNT extraction voltage.

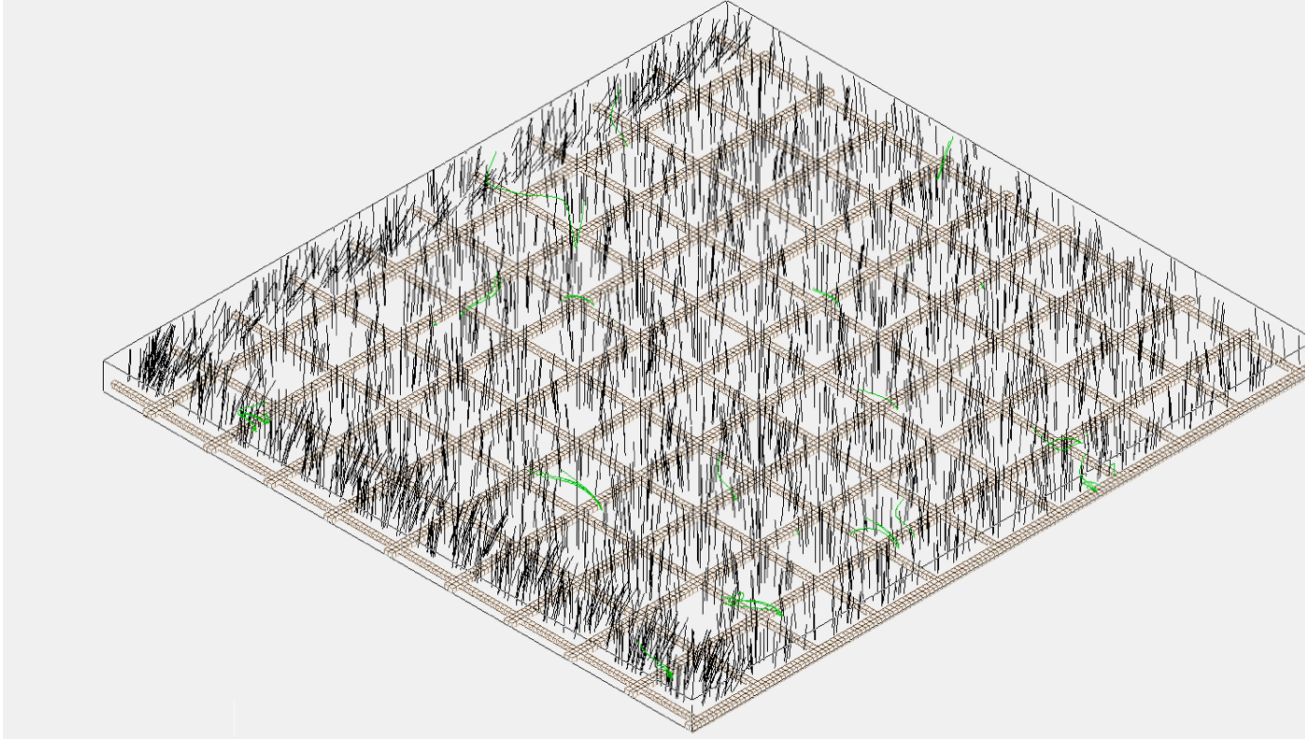


FIGURE 5.14: Primary electrons arriving through the G1 grid (black). Secondary electrons (green) are shown in the beginning of the simulation.

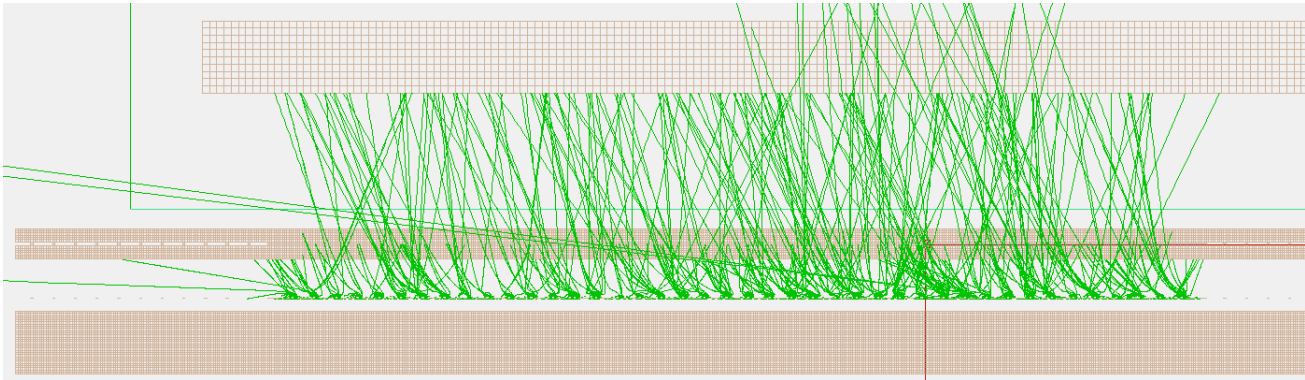


FIGURE 5.15: Simulated secondary electrons emitted from G1 continuing upwards to the anode grid. Only a small fraction of the secondary electrons arrive inside the electrostatic analyzer.

In Figure 5.17 we find that the peak is roughly $40 - 50V$ larger than the extraction voltage. This shift in peak is due to the entrance angle (FOV) of the electrostatic analyzer, which allows a much wider beam than desired based on far from nominal velocity distributions. As shown in Figure 5.17, the electrostatic simulation approximately reproduces the measured energy distribution.

We find that the peak in collected electron emission is consistent in energy with previous measurements performed in 2014, as well as multiple trials performed with the same CNT. The simulation peak is identical with the measurements near $-350V$, roughly 60 eV more energetic than the initial extraction energy of the electrons

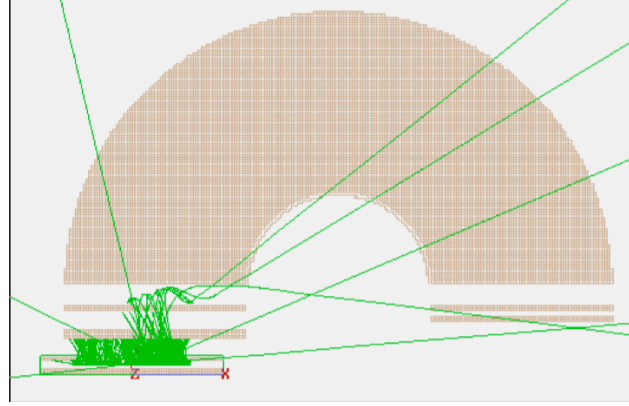


FIGURE 5.16: secondary electrons in the electrostatic analyzer

$E_0 = 290\text{eV}$. Since C2 electrode was at $+20\text{ V}$, the maximum energy of the primary electrons is thus $E = 310\text{eV}$. One explanation of the 'secondary electron' peak near 20 volts are backscattered primary electrons rebounding off of the EA torus. We find that no secondary electrons enter the EA torus, thus it is highly unlikely that they generate this emission.

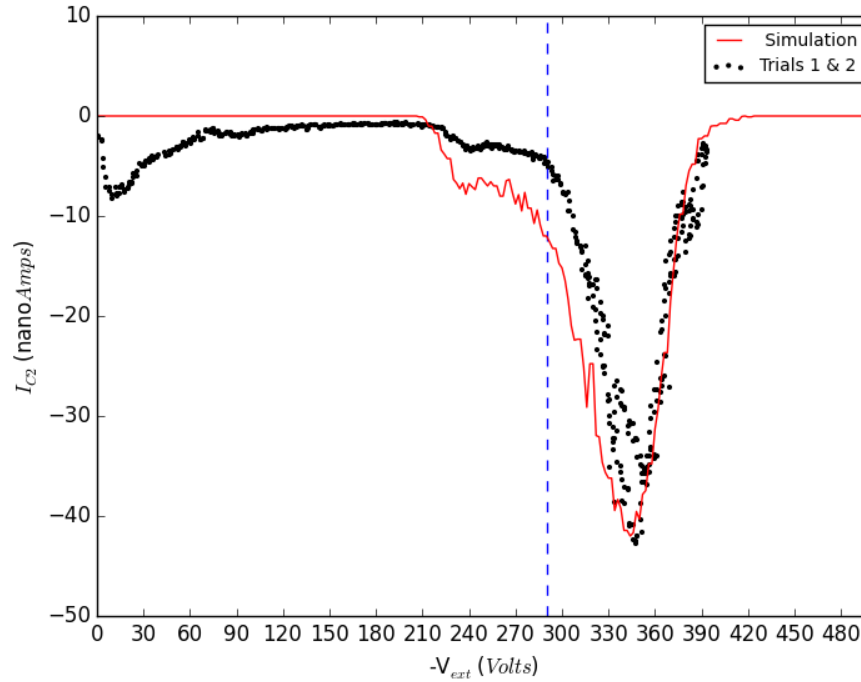


FIGURE 5.17: Energy characterization of Collector 2. Here it can be seen that the energy peaks at $\sim 340\text{V}$. A small secondary electron peak near $\sim 20\text{ volts}$ can be seen. The broader increase in energy beginning at $\sim 290\text{ volts}$ could be due to the choice of initial kinetic energy. Here the electrons were given $E = 0.1\text{ eV}$.

5.7 Conclusion

We have demonstrated with reproducible experiments and numerical simulations over the past three years that the carbon nanotube electron gun is fully functional and reliable as an electron source. The CNTeg can emit on average $\sim 100\mu A$, with a power of a few tens of milliWatts. The SIMION simulations match the energy-sweep experiments quite well. This consistency implies that our simulations reproduce the transparency of all of the grids (G1 , Anode), and the physical properties of the rest of the electrodes along with the non-conducting, supporting components. Above all the energy distribution of electrons can now be predicted using our simulations for any initial extraction potential, data which will be useful in estimating the e- impact ionization rates for the eventual coupling of this device to a neutral mass spectrometer. Lastly, we considered the 2nd order effect of secondary electrons, and found that they do not impact the electron energy distribution significantly, Overall this leads us to the conclusion that the ionization source is now fully characterized.

Conclusions & Summary

The past two decades have experienced an incredible surge of planetary exosphere discoveries, enabled most conspicuously by the Hubble Space Telescope Imaging Spectrograph (STIS), which has consistently pushed instrumentation limits to extract the faintest spectral lines thereby indicating the presence of unknown constituents of planetary atmospheres. In 2002, atomic sodium was detected as far out as ~ 150 light years, in the gas-giant exosphere of HD20458B ([Charbonneau et al. \[2002\]](#)), marking the first exoplanetary atmosphere discovery. The same year in our solar system, careful modeling of the sodium enshrouding Jupiter’s icy satellite Europa, provided strong evidence that Europa’s subsurface ocean may be the ultimate source of the observed sodium column $\sim 10^{10} \text{ cm}^{-2}$ [Leblanc et al. \[2002\]](#), highlighting the important consideration of past or present endogenic sources in the dynamics of satellite exospheres. The subsequent discoveries of volcanic NaCl and H₂O geysers at the satellites Io ([Lellouch et al. \[2003\]](#)) and Enceladus ([Porco et al. \[2006\]](#)) further elaborated the dynamics of satellite exospheres. Satellite exospheres are unique in that the tenuous gas closely interacts with their primary’s gravitational and/or magnetic fields while being subject to varying amounts of stellar insolation. What this dissertation sought to emphasize is that in order to fully understand the *behavior* of these atmospheric constituents, it is not sufficient to evaluate a ‘snapshot’ of the exosphere considering it to be at rest. Satellites by definition are *rotating* around a primary and this rotation drives several critical phenomena even when the atmosphere is collisionless.

In order to comprehend the physical mechanism behind the rotation, it is important to simplify the problem and carefully treat a well-observed case. Surface bounded exospheres (Table 1.1) are the simplest case in isolating how an atmosphere responds to rotation. Lastly, from the several surface bounded species, an atom or molecule which weakly interacts with the surface (simply bouncing along the surface) and is heavy enough so that it is not influenced by escape, is an ideal candidate. Therefore

the simplest and most easily understood surface-bounded exosphere under rotation is O_2 on Europa and Ganymede.

This setup should naturally result in several dynamic phenomena, but a consistent and periodically observed phenomena only appears if the exospheric timescales, are right. In this thesis we show how a satellite exosphere can undergo such periodicity, by focusing on the case of molecular oxygen on Europa and Ganymede. We found, consistent with the Hubble Space Telescope oxygen aurorae data indicative of near-surface O_2 , that Europa and Ganymede must undergo a diurnal O_2 cycle. The cycle, as far as we understand it, occurs due to the behavior of O_2 on icy satellites. The O_2 , to 1st order, weakly interacts with the ice and orbits with the satellite. The O_2 is also strongly sensitive to the solar insolation, due to its radiolytic production. The O_2 is also heavy, and survives the entire orbit and is thus 'locked into' a diurnal cycle. The cycle peaks at dusk, which is simply due to the geometrical setup of the planet-satellite system: the O_2 production occurs predominantly during plasma ram/trailing hemisphere day. Since the O_2 survives the entire day, it will peak at the end of the gradual accumulation occurring throughout *Ram Day*. During *Ram Night* the O_2 production will slow down due to the low temperatures and so at dawn, there will be a minimum amount of O_2 .

This cycle illustrates how the near-surface component of a satellite exosphere can behave. When one extends to higher altitudes where the atmosphere becomes vastly more tenuous and other species begin to dominate, plasma interactions as well as considerations of sub-surface, endogenic sources become relevant. Furthermore, when comparing the most recent observations and simulations at Europa and Ganymede, we highlighted the uncertainty of H_2O vapor sublimation in these two satellite exospheres. Higher sublimation rates than assumed would result in heightened H_2O column densities and their subsequent electron impact would result in larger exospheric signatures of $Ly-\alpha$, linked mostly to atomic hydrogen. On both bodies, Ganymede [Barth et al. \[1997\]](#) and Europa [Roth et al. \[2017\]](#) the hydrogen column density inferred from $Ly-\alpha$ is overestimated in comparison to current Monte Carlo test particle simulations. As H_2O sublimation is not the only avenue nor contributor, we also provided a perspective on how H_2O could emanate from Europa's subsurface ocean due to tidal forces, and potentially heat extremely narrow, centimeter-wide regions of length $\sim 10^3 km$ as modeled by [Roth et al. \[2014b\]](#). We calculate that other trace species indicative of potential cryovolcanism at Europa such as $NaCl$, and SO_2 could in principle be observed by ALMA, the largest telescopic array in the world. The most powerful characterization of these satellite exospheres will be done in a way similar to Cassini's INMS discovery of CO_2 & O_2 at Rhea and Dione ([Teolis and Waite \[2016\]](#)), namely using in-situ neutral mass spectrometry.

I have therefore tested and characterized a carbon nanotube electron gun for the past three years in the hope that it will be coupled to a highly sensitive mass spectrometer. The CNTeg as it is called works quite well and delivers $100\mu A$ of current stably and reliably. We also confirm that the simulated peak in electron energy corresponds to the experimentally verified peak in energy. The secondary electron population does not seem to be a significant contributor to the population entering the ionization volume. The CNTeg is extremely power efficient boasting only 10mWatts compared to the 1-2 watts of its tungsten filament counterpart. This technology could be used in a variety of ways besides the obvious e- impact ionizer. For example it could neutralize and regulate spacecraft which accumulate negative spacecharge, or also as an electron beam for studies of ionospheres.

This thesis was coincident with the first discovery of Europa's water vapor plumes as well as the ever-rising discoveries of atmospheres around extrasolar planets, some of which may be habitable. The former is an alluring future for the solar system due to the possibility that prodigious amounts of liquid water may be accessible at Europa, and the cryovolcanic activity may be actively shaping the observed exosphere. It presents an exciting challenge for high-risk technologies such as cubesatellites to dare to dive into a plume, or ultimately swim in an extraterrestrial ocean. All of these technologies will rely on efficient methods, one of which we have presented in this thesis. The latter discovery of new environments around other star system begs to ask why have we not yet seen a signature of an extrasolar satellite? The perspectives outlined in Section 4 of this manuscript demonstrated that should the tidal heating be sufficient certain volatiles should be evaporated off and be discerned, even by a ground-based observer. A possible ramification from connecting our two studies may enable one to target an exoplanetary system and discover an extrasolar satellite.

Bibliography

- O. Abramov and J. R. Spencer. Numerical modeling of endogenic thermal anomalies on Europa. , 195:378–385, May 2008. doi: 10.1016/j.icarus.2007.11.027.
- F. Bagenal, E. Sidrow, R. J. Wilson, T. A. Cassidy, V. Dols, F. J. Crary, A. J. Steffl, P. A. Delamere, W. S. Kurth, and W. R. Paterson. Plasma conditions at Europa’s orbit. , 261:1–13, November 2015. doi: 10.1016/j.icarus.2015.07.036.
- F. Bagenal, R. J. Wilson, S. Siler, W. R. Paterson, and W. S. Kurth. Survey of Galileo plasma observations in Jupiter’s plasma sheet. *Journal of Geophysical Research (Planets)*, 121:871–894, May 2016. doi: 10.1002/2016JE005009.
- D. D. Barbosa and M. G. Kivelson. Dawn-dusk electric field asymmetry of the Io plasma torus. , 10:210–213, March 1983. doi: 10.1029/GL010i003p00210.
- Rory Barnes. *Q (Tidal Quality Factor)*, pages 1395–1395. Springer Berlin Heidelberg, Berlin, Heidelberg, 2011. ISBN 978-3-642-11274-4. doi: 10.1007/978-3-642-11274-4_1319. URL http://dx.doi.org/10.1007/978-3-642-11274-4_1319.
- C. A. Barth, C. W. Hord, A. I. F. Stewart, W. R. Pryor, K. E. Simmons, W. E. McClintock, J. M. Ajello, K. L. Naviaux, and J. J. Aiello. Galileo ultraviolet spectrometer observations of atomic hydrogen in the atmosphere at Ganymede. , 24: 2147, September 1997. doi: 10.1029/97GL01927.
- Joel Becker, Nguyen Tuan Hong, Jean-Jacques Berthelier, Francois Leblanc, Soonil Lee, and Fabrice Cipriani. Multi-scale simulation of electron emission from a triode-type electron source with a carbon-nanotube column array cathode. *Nanotechnology*, 24(46):465303, 2013.
- G.A. Bird. *Molecular Gas Dynamics and the Direct Simulation of Gas Flows*. Oxford engineering science series. Clarendon Press, 1998. URL <https://books.google.fr/books?id=xd2knQEACAAJ>.

- M. E. Brown. Potassium in Europa's Atmosphere. , 151:190–195, June 2001. doi: 10.1006/icar.2001.6612.
- M. E. Brown and K. P. Hand. Salts and Radiation Products on the Surface of Europa. , 145:110, April 2013. doi: 10.1088/0004-6256/145/4/110.
- M. E. Brown and R. E. Hill. Discovery of an extended sodium atmosphere around Europa. , 380:229–231, March 1996. doi: 10.1038/380229a0.
- W. L. Brown, L. J. Lanzerotti, and R. E. Johnson. Fast Ion Bombardment of Ices and its Astrophysical Implications. *Science*, 218:525–531, November 1982. doi: 10.1126/science.218.4572.525.
- M. H. Burger, N. M. Schneider, I. de Pater, M. E. Brown, A. H. Bouchez, L. M. Trafton, Y. Sheffer, E. S. Barker, and A. Mallama. Mutual Event Observations of Io's Sodium Corona. , 563:1063–1074, December 2001. doi: 10.1086/323944.
- R. W. Carlson, R. E. Johnson, and M. S. Anderson. Sulfuric acid on Europa and the radiolytic sulfur cycle. *Science*, 286:97–99, October 1999. doi: 10.1126/science.286.5437.97.
- R. W. Carlson, M. S. Anderson, R. Mehlman, and R. E. Johnson. Distribution of hydrate on Europa: Further evidence for sulfuric acid hydrate. , 177:461–471, October 2005. doi: 10.1016/j.icarus.2005.03.026.
- T. A. Cassidy and R. E. Johnson. Collisional spreading of Enceladus neutral cloud. , 209:696–703, October 2010. doi: 10.1016/j.icarus.2010.04.010.
- T. A. Cassidy, R. E. Johnson, M. A. McGrath, M. C. Wong, and J. F. Cooper. The spatial morphology of Europa's near-surface O₂ atmosphere. , 191:755–764, November 2007. doi: 10.1016/j.icarus.2007.04.033.
- T. A. Cassidy, R. E. Johnson, and O. J. Tucker. Trace constituents of Europa's atmosphere. , 201:182–190, May 2009a. doi: 10.1016/j.icarus.2008.12.033.
- T. A. Cassidy, R. Mendez, P. Arras, R. E. Johnson, and M. F. Skrutskie. Massive Satellites of Close-In Gas Giant Exoplanets. , 704:1341–1348, October 2009b. doi: 10.1088/0004-637X/704/2/1341.
- T. A. Cassidy, C. P. Paranicas, J. H. Shirley, J. B. Dalton, III, B. D. Teolis, R. E. Johnson, L. Kamp, and A. R. Hendrix. Magnetospheric ion sputtering and water ice grain size at Europa. , 77:64–73, March 2013. doi: 10.1016/j.pss.2012.07.008.
- T. A. Cassidy, W. E. McClintock, R. M. Killen, M. Sarantos, A. W. Merkel, R. J. Vervack, and M. H. Burger. A cold-pole enhancement in Mercury's sodium exosphere. , 43:11, November 2016. doi: 10.1002/2016GL071071.

- David C. Catling and James F. Kasting. *Atmospheric Evolution on Inhabited and Lifeless Worlds*. Cambridge University Press, 2017. doi: 10.1017/9781139020558.
- Joseph W. Chamberlain. Planetary coronae and atmospheric evaporation. *Planetary and Space Science*, 11(8):901 – 960, 1963. ISSN 0032-0633. doi: [http://dx.doi.org/10.1016/0032-0633\(63\)90122-3](http://dx.doi.org/10.1016/0032-0633(63)90122-3). URL <http://www.sciencedirect.com/science/article/pii/0032063363901223>.
- D. Charbonneau, T. M. Brown, R. W. Noyes, and R. L. Gilliland. Detection of an Extrasolar Planet Atmosphere. , 568:377–384, March 2002. doi: 10.1086/338770.
- K. D. Colón, E. B. Ford, S. Redfield, J. J. Fortney, M. Shabram, H. J. Deeg, and S. Mahadevan. Probing potassium in the atmosphere of HD 80606b with tunable filter transit spectrophotometry from the Gran Telescopio Canarias. , 419: 2233–2250, January 2012. doi: 10.1111/j.1365-2966.2011.19878.x.
- J. F. Cooper, R. E. Johnson, B. H. Mauk, H. B. Garrett, and N. Gehrels. Energetic Ion and Electron Irradiation of the Icy Galilean Satellites. , 149:133–159, January 2001. doi: 10.1006/icar.2000.6498.
- M. Čuk, L. Dones, and D. Nesvorný. Dynamical Evidence for a Late Formation of Saturns Moons. , 820:97, April 2016. doi: 10.3847/0004-637X/820/2/97.
- V. Dobos and E. L. Turner. Viscoelastic Models of Tidally Heated Exomoons. , 804: 41, May 2015. doi: 10.1088/0004-637X/804/1/41.
- T. Doggett, R. Greeley, P. Figueredo, and K. Tanaka. *Geologic Stratigraphy and Evolution of Europa’s Surface*, page 137. 2009.
- V. Dols, P. A. Delamere, F. Bagenal, W. S. Kurth, and W. R. Paterson. Asymmetry of Io’s outer atmosphere: Constraints from five Galileo flybys. *Journal of Geophysical Research (Planets)*, 117:E10010, October 2012. doi: 10.1029/2012JE004076.
- V. J. Dols, F. Bagenal, T. A. Cassidy, F. J. Crary, and P. A. Delamere. Europa’s atmospheric neutral escape: Importance of symmetrical O₂ charge exchange. , 264: 387–397, January 2016. doi: 10.1016/j.icarus.2015.09.026.
- Paul Dvorak. How Much Power in a Bolt of Lightning. *Windpower*, 2013.
- Jeremy L. England. Statistical physics of self-replication. *The Journal of Chemical Physics*, 139(12):121923, sep 2013. doi: 10.1063/1.4818538. URL <https://doi.org/10.1063/1.4818538>.
- A. Eviatar, A. Bar-Nun, and M. Podolak. European surface phenomena. , 61:185–191, February 1985. doi: 10.1016/0019-1035(85)90100-9.

- M. Fama, J. Shi, and R.A. Baragiola. Sputtering of ice by low-energy ions. *Surface Science*, 602(1):156 – 161, 2008. ISSN 0039-6028. doi: <http://dx.doi.org/10.1016/j.susc.2007.10.002>. URL <http://www.sciencedirect.com/science/article/pii/S0039602807009879>.
- Ralph Howard Fowler and L Nordheim. Electron emission in intense electric fields. In *Proceedings of the Royal Society of London A: Mathematical, Physical and Engineering Sciences*, volume 119, pages 173–181. The Royal Society, 1928.
- N. Fray and B. Schmitt. Sublimation of ices of astrophysical interest: A bibliographic review. , 57:2053–2080, December 2009. doi: 10.1016/j.pss.2009.09.011.
- P. Gao, M. S. Marley, K. Zahnle, T. D. Robinson, and N. K. Lewis. Sulfur Hazes in Giant Exoplanet Atmospheres: Impacts on Reflected Light Spectra. , 153:139, March 2017. doi: 10.3847/1538-3881/aa5fab.
- R. Greenberg. Transport Rates of Radiolytic Substances into Europa’s Ocean: Implications for the Potential Origin and Maintenance of Life. *Astrobiology*, 10: 275–283, April 2010. doi: 10.1089/ast.2009.0386.
- D. T. Hall, D. F. Strobel, P. D. Feldman, M. A. McGrath, and H. A. Weaver. Detection of an oxygen atmosphere on Jupiter’s moon Europa. , 373:677–679, February 1995. doi: 10.1038/373677a0.
- D. T. Hall, P. D. Feldman, M. A. McGrath, and D. F. Strobel. The Far-Ultraviolet Oxygen Airglow of Europa and Ganymede. , 499:475–481, May 1998. doi: 10.1086/305604.
- D. P. Hand, C. F. Chyba, R. W. Carlson, and J. F. Cooper. Clathrate Hydrates of Oxidants in the Ice Shell of Europa. *Astrobiology*, 6:463–482, June 2006. doi: 10.1089/ast.2006.6.463.
- K. P. Hand and R. W. Carlson. Europa’s surface color suggests an ocean rich with sodium chloride. , 42:3174–3178, May 2015. doi: 10.1002/2015GL063559.
- K. P. Hand, R. W. Carlson, and C. F. Chyba. Energy, Chemical Disequilibrium, and Geological Constraints on Europa. *Astrobiology*, 7:1006–1022, December 2007. doi: 10.1089/ast.2007.0156.
- C. J. Hansen, L. Esposito, A. I. F. Stewart, J. Colwell, A. Hendrix, W. Pryor, D. Shemansky, and R. West. Enceladus’ Water Vapor Plume. *Science*, 311: 1422–1425, March 2006. doi: 10.1126/science.1121254.

- P. Hartogh. DDT_pharto01_6: First ever detection of Callisto's atmosphere and constraining the trailing side atmosphere of Ganymede. Herschel Space Observatory Proposal, id.2525, December 2012.
- R. Heller, G.-D. Marleau, and R. E. Pudritz. The formation of the Galilean moons and Titan in the Grand Tack scenario. , 579:L4, July 2015. doi: 10.1051/0004-6361/201526348.
- A. R. Hendrix, T. A. Hurford, and ROW Team. Roadmaps to Ocean Worlds. In *Planetary Science Vision 2050 Workshop*, volume 1989 of *LPI Contributions*, page 8171, February 2017.
- R. R. Hodges, Jr. and F. S. Johnson. Lateral transport in planetary exospheres. , 73: 7307, 1968. doi: 10.1029/JA073i023p07307.
- Nguyen Tuan Hong, Ken Ha Koh, Soonil Lee, Phan Ngoc Minh, Ngo Thi Thanh Tam, and Phan Hong Khoi. Comparison of field-electron emission from different carbon nanotube array structures. *Journal of Vacuum Science & Technology B: Microelectronics and Nanometer Structures Processing, Measurement, and Phenomena*, 27(2):749–752, 2009.
- G. V. Hoppa, B. R. Tufts, R. Greenberg, and P. E. Geissler. Formation of cycloidal features on Europa. *Science*, 285:1899–1902, September 1999. doi: 10.1126/science.285.5435.1899.
- H.-W. Hsu, F. Postberg, Y. Sekine, T. Shibuya, S. Kempf, M. Horányi, A. Juhász, N. Altobelli, K. Suzuki, Y. Masaki, T. Kuwatani, S. Tachibana, S.-I. Sirono, G. Moragas-Klostermeyer, and R. Srama. Ongoing hydrothermal activities within Enceladus. , 519:207–210, March 2015. doi: 10.1038/nature14262.
- D. M. Hunten, D. E. Shemansky, and T. H. Morgan. *The Mercury atmosphere*, pages 562–612. 1988.
- W.-H. Ip. Europa's Oxygen Exosphere and Its Magnetospheric Interaction. , 120: 317–325, April 1996. doi: 10.1006/icar.1996.0052.
- W.-H. Ip, D. J. Williams, R. W. McEntire, and B. H. Mauk. Ion sputtering and surface erosion at Europa. , 25:829–832, 1998. doi: 10.1029/98GL00472.
- Yukikazu Itikawa and Nigel Mason. Cross sections for electron collisions with water molecules. *Journal of Physical and Chemical Reference Data*, 34(1):1–22, mar 2005. doi: 10.1063/1.1799251. URL <https://doi.org/10.1063/1.1799251>.
- D. G. Jankowski, C. F. Chyba, and P. D. Nicholson. On the obliquity and tidal heating of Triton. , 80:211–219, July 1989. doi: 10.1016/0019-1035(89)90169-3.

- R. E. Johnson. *Energetic Charged-Particle Interactions with Atmospheres and Surfaces*. 1990.
- R. E. Johnson. Plasma-Induced Sputtering of an Atmosphere. , 69:215–253, August 1994. doi: 10.1007/BF02101697.
- R. E. Johnson. NOTE: Sodium at Europa. , 143:429–433, February 2000. doi: 10.1006/icar.1999.6327.
- R. E. Johnson and P. J. Huggins. Toroidal Atmospheres around Extrasolar Planets. , 118:1136–1143, August 2006. doi: 10.1086/506183.
- R. E. Johnson and W. A. Jesser. O₂/O₃ Microatmospheres in the Surface of Ganymede. , 480:L79–L82, May 1997. doi: 10.1086/310614.
- R. E. Johnson, L. J. Lanzerotti, W. L. Brown, and T. P. Armstrong. Erosion of Galilean satellite surfaces by Jovian magnetosphere particles. *Science*, 213: 1027–1030, 1981.
- R. E. Johnson, L. J. Lanzerotti, and W. L. Brown. Planetary applications of ion induced erosion of condensed-gas frosts. *Nuclear Instruments and Methods*, 198: 147–157, 1982. doi: 10.1016/0167-5087(82)90066-7.
- R. E. Johnson, F. Leblanc, B. V. Yakshinskiy, and T. E. Madey. Energy Distributions for Desorption of Sodium and Potassium from Ice: The Na/K Ratio at Europa. , 156:136–142, March 2002. doi: 10.1006/icar.2001.6763.
- R. E. Johnson, T. I. Quickenden, P. D. Cooper, A. J. McKinley, and C. G. Freeman. The Production of Oxidants in Europa’s Surface. *Astrobiology*, 3:823–850, December 2003. doi: 10.1089/153110703322736123.
- R. E. Johnson, J. G. Luhmann, R. L. Tokar, M. Bouhram, J. J. Berthelier, E. C. Sittler, J. F. Cooper, T. W. Hill, H. T. Smith, M. Michael, M. Liu, F. J. Crary, and D. T. Young. Production, ionization and redistribution of O₂ in Saturn’s ring atmosphere. , 180:393–402, February 2006a. doi: 10.1016/j.icarus.2005.08.021.
- R. E. Johnson, H. T. Smith, O. J. Tucker, M. Liu, M. H. Burger, E. C. Sittler, and R. L. Tokar. The Enceladus and OH Tori at Saturn. , 644:L137–L139, June 2006b. doi: 10.1086/505750.
- R. E. Johnson, M. Famá, M. Liu, R. A. Baragiola, E. C. Sittler, and H. T. Smith. Sputtering of ice grains and icy satellites in Saturn’s inner magnetosphere. , 56: 1238–1243, July 2008. doi: 10.1016/j.pss.2008.04.003.

- R. E. Johnson, M. H. Burger, T. A. Cassidy, F. Leblanc, M. Marconi, and W. H. Smyth. *Composition and Detection of Europa's Sputter-induced Atmosphere*, page 507. 2009.
- R. E. Johnson, R. W. Carlson, T. A. Cassidy, and M. Fama. Sputtering of Ices. In M. S. Gudipati and J. Castillo-Rogez, editors, *Astrophysics and Space Science Library*, volume 356 of *Astrophysics and Space Science Library*, page 551, 2013. doi: 10.1007/978-1-4614-3076-6_17.
- R. E. Johnson, A. Oza, L. A. Young, A. N. Volkov, and C. Schmidt. Volatile Loss and Classification of Kuiper Belt Objects. , 809:43, August 2015. doi: 10.1088/0004-637X/809/1/43.
- S. A. Johnston, D. A. Patthoff, and L. G. Montési. Combining Stresses from Diurnal Tides and a Pressurized Ocean on Enceladus. In *Lunar and Planetary Science Conference*, volume 47 of *Lunar and Planetary Science Conference*, page 2092, March 2016.
- K. K. Khurana, M. G. Kivelson, D. J. Stevenson, G. Schubert, C. T. Russell, R. J. Walker, and C. Polanskey. Induced magnetic fields as evidence for subsurface oceans in Europa and Callisto. , 395:777–780, October 1998. doi: 10.1038/27394.
- M. G. Kivelson, K. K. Khurana, C. T. Russell, M. Volwerk, R. J. Walker, and C. Zimmer. Galileo Magnetometer Measurements: A Stronger Case for a Subsurface Ocean at Europa. *Science*, 289:1340–1343, August 2000. doi: 10.1126/science.289.5483.1340.
- A. J. Kliore, A. Anabtawi, R. G. Herrera, S. W. Asmar, A. F. Nagy, D. P. Hinson, and F. M. Flasar. Ionosphere of Callisto from Galileo radio occultation observations. *Journal of Geophysical Research (Space Physics)*, 107:1407, November 2002. doi: 10.1029/2002JA009365.
- M. Küppers, L. O'Rourke, D. Bockelée-Morvan, V. Zakharov, S. Lee, P. von Allmen, B. Carry, D. Teyssier, A. Marston, T. Müller, J. Crovisier, M. A. Barucci, and R. Moreno. Localized sources of water vapour on the dwarf planet (1)Ceres. , 505: 525–527, January 2014. doi: 10.1038/nature12918.
- A. L. Lane, R. M. Nelson, and D. L. Matson. Evidence for sulphur implantation in Europa's UV absorption band. , 292:38, July 1981. doi: 10.1038/292038a0.
- F. Leblanc, R. E. Johnson, and M. E. Brown. Europa's Sodium Atmosphere: An Ocean Source? , 159:132–144, September 2002. doi: 10.1006/icar.2002.6934.

- F. Leblanc, A. E. Potter, R. M. Killen, and R. E. Johnson. Origins of Europa Na cloud and torus. , 178:367–385, November 2005. doi: 10.1016/j.icarus.2005.03.027.
- F. Leblanc, A. V. Oza, L. Leclercq, C. Schmidt, T. Cassidy, R. Modolo, J. Y. Chaufray, and R. E. Johnson. On the orbital variability of Ganymede’s atmosphere. , 293:185–198, September 2017a. doi: 10.1016/j.icarus.2017.04.025.
- F. Leblanc, A. V. Oza, L. Leclercq, C. Schmidt, T. Cassidy, R. Modolo, J. Y. Chaufray, and R. E. Johnson. On the orbital variability of Ganymede’s atmosphere. , 293:185–198, September 2017b. doi: 10.1016/j.icarus.2017.04.025.
- Ludivine Leclercq. *From exosphere to magnetosphere of planetary objects : optimization of parallelized modelisations for an application to Ganymede*. Theses, Université Paris-Saclay, October 2015. URL <https://hal-insu.archives-ouvertes.fr/tel-01256191>.
- E. Lellouch, T. Encrenaz, M. Belton, I. de Pater, and S. Gulkis. Io’s atmosphere from microwave detection SO₂. , 346:639–641, August 1990. doi: 10.1038/346639a0.
- E. Lellouch, G. Paubert, J. I. Moses, N. M. Schneider, and D. F. Strobel. Volcanically emitted sodium chloride as a source for Io’s neutral clouds and plasma torus. , 421:45–47, January 2003. doi: 10.1038/nature01292.
- E. Lellouch, M. Ali-Dib, K.-L. Jessup, A. Smette, H.-U. Käufl, and F. Marchis. Detection and characterization of Io’s atmosphere from high-resolution 4- μ m spectroscopy. , 253:99–114, June 2015. doi: 10.1016/j.icarus.2015.02.018.
- E. Lellouch, M. Gurwell, B. Butler, T. Fouchet, P. Lavvas, D. F. Strobel, B. Sicardy, A. Moullet, R. Moreno, D. Bockelée-Morvan, N. Biver, L. Young, D. Lis, J. Stansberry, A. Stern, H. Weaver, E. Young, X. Zhu, and J. Boissier. Detection of CO and HCN in Pluto’s atmosphere with ALMA. , 286:289–307, April 2017. doi: 10.1016/j.icarus.2016.10.013.
- N. R. Lewkow and V. Kharchenko. Precipitation of Energetic Neutral Atoms and Induced Non-thermal Escape Fluxes from the Martian Atmosphere. , 790:98, August 2014. doi: 10.1088/0004-637X/790/2/98.
- Yunhan Li, Yonghai Sun, and J T W Yeow. Nanotube field electron emission: principles, development, and applications. *Nanotechnology*, 26(24):242001, may 2015. doi: 10.1088/0957-4484/26/24/242001. URL <https://doi.org/10.1088%2F0957-4484%2F26%2F24%2F242001>.
- Yinghong Lin and David C Joy. A new examination of secondary electron yield data. *Surface and Interface Analysis*, 37(11):895–900, 2005.

- A. S. Lipatov, J. F. Cooper, W. R. Paterson, E. C. Sittler, R. E. Hartle, and D. G. Simpson. Jovian plasma torus interaction with Europa: 3D hybrid kinetic simulation. First results. , 58:1681–1691, November 2010. doi: 10.1016/j.pss.2010.06.015.
- A. Lucchetti, C. Plainaki, G. Cremonese, A. Milillo, T. Cassidy, X. Jia, and V. Shematovich. Loss rates of Europa’s tenuous atmosphere. , 130:14–23, October 2016. doi: 10.1016/j.pss.2016.01.009.
- A.-L. Maire, A. J. Skemer, P. M. Hinz, S. Desidera, S. Esposito, R. Gratton, F. Marzari, M. F. Skrutskie, B. A. Biller, D. Defrère, V. P. Bailey, J. M. Leisenring, D. Apai, M. Bonnefoy, W. Brandner, E. Buenzli, R. U. Claudi, L. M. Close, J. R. Crepp, R. J. De Rosa, J. A. Eisner, J. J. Fortney, T. Henning, K.-H. Hofmann, T. G. Kopytova, J. R. Males, D. Mesa, K. M. Morzinski, A. Oza, J. Patience, E. Pinna, A. Rajan, D. Schertl, J. E. Schlieder, K. Y. L. Su, A. Vaz, K. Ward-Duong, G. Weigelt, and C. E. Woodward. The LEECH Exoplanet Imaging Survey. Further constraints on the planet architecture of the HR 8799 system. , 576:A133, April 2015. doi: 10.1051/0004-6361/201425185.
- Oleg P. Makarov. Kinetic energy distributions and line profile measurements of dissociation products of water upon electron impact. *Journal of Geophysical Research*, 109(A9), 2004. doi: 10.1029/2002ja009353. URL <https://doi.org/10.1029/2002ja009353>.
- M. L. Marconi. A kinetic model of Ganymede’s atmosphere. , 190:155–174, September 2007. doi: 10.1016/j.icarus.2007.02.016.
- E. Marcq, J.-L. Bertaux, F. Montmessin, and D. Belyaev. Variations of sulphur dioxide at the cloud top of Venus’s dynamic atmosphere. *Nature Geoscience*, 6: 25–28, January 2013. doi: 10.1038/ngeo1650.
- C. Marois, B. Macintosh, T. Barman, B. Zuckerman, I. Song, J. Patience, D. Lafreniere, and R. Doyon. Direct imaging of multiple planets orbiting the star HR 8799. *Science*, 322(5906):1348–1352, nov 2008. doi: 10.1126/science.1166585. URL <https://doi.org/10.1126/science.1166585>.
- Jean-Charles Matéo-Vélez, M Belhaj, Jean-François Roussel, D Rodgers, and F Cipriani. Design and numerical assessment of a passive electron emitter for spacecraft charging alleviation. *IEEE Transactions on Plasma Science*, 43(9): 2839–2848, 2015.

- B. H. Mauk, D. G. Mitchell, S. M. Krimigis, E. C. Roelof, and C. P. Paranicas. Energetic neutral atoms from a trans-Europa gas torus at Jupiter. , 421:920–922, February 2003. doi: 10.1038/nature01431.
- W. E. McClintock, N. R. Izenberg, G. M. Holsclaw, D. T. Blewett, D. L. Domingue, J. W. Head, J. Helbert, T. J. McCoy, S. L. Murchie, M. S. Robinson, S. C. Solomon, A. L. Sprague, and F. Vilas. Spectroscopic Observations of Mercurys Surface Reflectance During MESSENGERs First Mercury Flyby. *Science*, 321:62, July 2008. doi: 10.1126/science.1159933.
- M. A. McGrath, E. Lellouch, D. F. Strobel, P. D. Feldman, and R. E. Johnson. *Satellite atmospheres*, pages 457–483. 2004.
- M. A. McGrath, C. J. Hansen, and A. R. Hendrix. *Observations of Europa’s Tenuous Atmosphere*, page 485. 2009.
- M. A. McGrath, X. Jia, K. Retherford, P. D. Feldman, D. F. Strobel, and J. Saur. Aurora on Ganymede. *Journal of Geophysical Research (Space Physics)*, 118: 2043–2054, May 2013. doi: 10.1002/jgra.50122.
- M. Mendillo, J. Baumgardner, B. Flynn, and W. J. Hughes. The extended sodium nebula of Jupiter. , 348:312–314, November 1990. doi: 10.1038/348312a0.
- A. Milillo, C. Plainaki, E. De Angelis, V. Mangano, S. Massetti, A. Mura, S. Orsini, and R. Rispoli. Analytical model of Europa’s O₂ exosphere. , 130:3–13, October 2016. doi: 10.1016/j.pss.2015.10.011.
- A. Moullet, E. Lellouch, R. Moreno, M. A. Gurwell, and C. Moore. First disk-resolved millimeter observations of Io’s surface and SO₂ atmosphere. , 482:279–292, April 2008. doi: 10.1051/0004-6361:20078699.
- E. L. Murphy and R. H. Good. Thermionic emission, field emission, and the transition region. *Phys. Rev.*, 102:1464–1473, Jun 1956. doi: 10.1103/PhysRev.102.1464. URL <https://link.aps.org/doi/10.1103/PhysRev.102.1464>.
- F. Nimmo and M. Manga. *Geodynamics of Europa’s Icy Shell*, page 381. 2009.
- K. S. Noll, H. A. Weaver, and A. M. Gonnella. The albedo spectrum of Europa from 2200 Å to 3300 Å. , 100:19057–19060, September 1995. doi: 10.1029/94JE03294.
- M. E. Ockert, R. M. Nelson, A. L. Lane, and D. L. Matson. Europa’s ultraviolet absorption band (260 to 320 nm) - Temporal and spatial evidence from IUE. , 70: 499–505, June 1987. doi: 10.1016/0019-1035(87)90091-1.

- A.V. Oza, F. Leblanc, R.E. Johnson, C. Schmidt, L. Leclercq, T.A Cassidy, and Chaufray J.-Y. Dusk over dawn molecular oxygen asymmetry in europa's exosphere. Submitted, 2017.
- O. Ozgurel, F. Pauzat, Y. Ellinger, A. Markovits, O. Mousis, and L. LCT. On the origin of alkali metals in Europa exosphere. In *AAS/Division for Planetary Sciences Meeting Abstracts*, volume 48 of *AAS/Division for Planetary Sciences Meeting Abstracts*, page 517.04, October 2016.
- R. T. Pappalardo, M. J. S. Belton, H. H. Breneman, M. H. Carr, C. R. Chapman, G. C. Collins, T. Denk, S. Fagents, P. E. Geissler, B. Giese, R. Greeley, R. Greenberg, J. W. Head, P. Helfenstein, G. Hoppa, S. D. Kadel, K. P. Klaasen, J. E. Klemaszewski, K. Magee, A. S. McEwen, J. M. Moore, W. B. Moore, G. Neukum, C. B. Phillips, L. M. Prockter, G. Schubert, D. A. Senske, R. J. Sullivan, B. R. Tufts, E. P. Turtle, R. Wagner, and K. K. Williams. Does Europa have a subsurface ocean? Evaluation of the geological evidence. , 104:24015–24056, October 1999a. doi: 10.1029/1998JE000628.
- R. T. Pappalardo, M. J. S. Belton, H. H. Breneman, M. H. Carr, C. R. Chapman, G. C. Collins, T. Denk, S. Fagents, P. E. Geissler, B. Giese, R. Greeley, R. Greenberg, J. W. Head, P. Helfenstein, G. Hoppa, S. D. Kadel, K. P. Klaasen, J. E. Klemaszewski, K. Magee, A. S. McEwen, J. M. Moore, W. B. Moore, G. Neukum, C. B. Phillips, L. M. Prockter, G. Schubert, D. A. Senske, R. J. Sullivan, B. R. Tufts, E. P. Turtle, R. Wagner, and K. K. Williams. Does Europa have a subsurface ocean? Evaluation of the geological evidence. , 104:24015–24056, October 1999b. doi: 10.1029/1998JE000628.
- R. T. Pappalardo, D. A. Patthoff, J. B. Li, B. J. Ayton, and D. Dubois. Cycloidal and Wavy Lineaments on Europa from Diurnal, Obliquity, and Nonsynchronous Rotation Stresses in a Visco-Elastic Ice Shell. In *Lunar and Planetary Science Conference*, volume 47 of *Lunar and Planetary Science Conference*, page 2712, March 2016.
- D. A. Patthoff and A. G. Davies. Tidal Stresses and Volcanism on Io. In *Lunar and Planetary Science Conference*, volume 48 of *Lunar and Planetary Science Conference*, page 1748, March 2017.
- S. J. Peale, P. Cassen, and R. T. Reynolds. Melting of Io by tidal dissipation. *Science*, 203:892–894, March 1979a. doi: 10.1126/science.203.4383.892.
- S. J. Peale, P. Cassen, and R. T. Reynolds. Melting of Io by tidal dissipation. *Science*, 203:892–894, March 1979b. doi: 10.1126/science.203.4383.892.

- M. A. Peters and E. L. Turner. On the Direct Imaging of Tidally Heated Exomoons. , 769:98, June 2013. doi: 10.1088/0004-637X/769/2/98.
- C. Plainaki, A. Milillo, A. Mura, S. Orsini, S. Massetti, and T. Cassidy. The role of sputtering and radiolysis in the generation of Europa exosphere. , 218:956–966, April 2012. doi: 10.1016/j.icarus.2012.01.023.
- C. Plainaki, A. Milillo, A. Mura, J. Saur, S. Orsini, and S. Massetti. Exospheric O₂ densities at Europa during different orbital phases. , 88:42–52, November 2013. doi: 10.1016/j.pss.2013.08.011.
- C. C. Porco, P. Helfenstein, P. C. Thomas, A. P. Ingersoll, J. Wisdom, R. West, G. Neukum, T. Denk, R. Wagner, T. Roatsch, S. Kieffer, E. Turtle, A. McEwen, T. V. Johnson, J. Rathbun, J. Veverka, D. Wilson, J. Perry, J. Spitale, A. Brahic, J. A. Burns, A. D. Del Genio, L. Dones, C. D. Murray, and S. Squyres. Cassini Observes the Active South Pole of Enceladus. *Science*, 311:1393–1401, March 2006. doi: 10.1126/science.1123013.
- J. A. Rathbun, N. J. Rodriguez, and J. R. Spencer. Galileo PPR observations of Europa: Hotspot detection limits and surface thermal properties. , 210:763–769, December 2010. doi: 10.1016/j.icarus.2010.07.017.
- J. A. Rathbun, J. R. Spencer, and C. J. A. Howett. Galileo PPR Observations of Europa: Correlations of Thermophysical Properties with Exogenic and Endogenic Processes. In *Workshop on the Habitability of Icy Worlds*, volume 1774 of *LPI Contributions*, page 4045, February 2014.
- F. Reif. *Fundamentals of Statistical and Thermal Physics*. Waveland Press, 1965.
- A. R. Rhoden, T. A. Hurford, L. Roth, and K. Retherford. Linking Europa’s plume activity to tides, tectonics, and liquid water. , 253:169–178, June 2015. doi: 10.1016/j.icarus.2015.02.023.
- L. Roth, J. Saur, K. D. Retherford, D. F. Strobel, and J. R. Spencer. Simulation of Io’s auroral emission: Constraints on the atmosphere in eclipse. , 214:495–509, August 2011. doi: 10.1016/j.icarus.2011.05.014.
- L. Roth, K. D. Retherford, J. Saur, D. F. Strobel, P. D. Feldman, M. A. McGrath, and F. Nimmo. Orbital apocenter is not a sufficient condition for HST/STIS detection of Europa’s water vapor aurora. *Proceedings of the National Academy of Science*, 111: E5123–E5132, December 2014a. doi: 10.1073/pnas.1416671111.
- L. Roth, J. Saur, K. D. Retherford, D. F. Strobel, P. D. Feldman, M. A. McGrath, and F. Nimmo. Transient Water Vapor at Europa’s South Pole. *Science*, 343:171–174, January 2014b. doi: 10.1126/science.1247051.

- L. Roth, J. Saur, K. D. Retherford, D. F. Strobel, P. D. Feldman, M. McGrath, J. R. Spencer, A. Blocker, and N. Ivchenko. Europa's far ultraviolet oxygen aurora from a comprehensive set of HST observations. *J. Geophys*, 261:1–13, November 2015. doi: 10.1016/j.icarus.2015.07.036.
- L. Roth, K. D. Retherford, N. Ivchenko, N. Schlatter, D. F. Strobel, T. M. Becker, and C. Grava. Detection of a Hydrogen Corona in HST Ly α Images of Europa in Transit of Jupiter. , 153:67, February 2017. doi: 10.3847/1538-3881/153/2/67.
- M. Rubin, X. Jia, K. Altwegg, M. R. Combi, L. K. S. Daldorff, T. I. Gombosi, K. Khurana, M. G. Kivelson, V. M. Tennishev, G. Tóth, B. Holst, and P. Wurz. Self-consistent multifluid MHD simulations of Europa's exospheric interaction with Jupiter's magnetosphere. *Journal of Geophysical Research (Space Physics)*, 120: 3503–3524, May 2015. doi: 10.1002/2015JA021149.
- M. J. Russell, L. M. Barge, R. Bhartia, D. Bocanegra, P. J. Bracher, E. Branscomb, R. Kidd, S. McGlynn, D. H. Meier, W. Nitschke, T. Shibuya, S. Vance, L. White, and I. Kanik. The Drive to Life on Wet and Icy Worlds. *Astrobiology*, 14:308–343, April 2014. doi: 10.1089/ast.2013.1110.
- J. Saur, D. F. Strobel, and F. M. Neubauer. Interaction of the Jovian magnetosphere with Europa: Constraints on the neutral atmosphere. , 103:19947–19962, September 1998. doi: 10.1029/97JE03556.
- J. Saur, P. D. Feldman, L. Roth, F. Nimmo, D. F. Strobel, K. D. Retherford, M. A. McGrath, N. Schilling, J.-C. Gérard, and D. Grodent. Hubble Space Telescope/Advanced Camera for Surveys Observations of Europa's Atmospheric Ultraviolet Emission at Eastern Elongation. , 738:153, September 2011. doi: 10.1088/0004-637X/738/2/153.
- J. Saur, S. Duling, L. Roth, X. Jia, D. F. Strobel, P. D. Feldman, U. R. Christensen, K. D. Retherford, M. A. McGrath, F. Musacchio, A. Wennmacher, F. M. Neubauer, S. Simon, and O. Hartkorn. The search for a subsurface ocean in Ganymede with Hubble Space Telescope observations of its auroral ovals. *Journal of Geophysical Research (Space Physics)*, 120:1715–1737, March 2015. doi: 10.1002/2014JA020778.
- N. M. Schneider and J. T. Trauger. The Structure of the Io Torus. , 450:450, September 1995. doi: 10.1086/176155.
- S. Sengupta and M. S. Marley. Detecting Exomoons around Self-luminous Giant Exoplanets through Polarization. , 824:76, June 2016. doi: 10.3847/0004-637X/824/2/76.

- D. E. Shemansky, Y. L. Yung, X. Liu, J. Yoshii, C. J. Hansen, A. R. Hendrix, and L. W. Esposito. A New Understanding of the Europa Atmosphere and Limits on Geophysical Activity. , 797:84, December 2014. doi: 10.1088/0004-637X/797/2/84.
- V. I. Shematovich, R. E. Johnson, J. F. Cooper, and M. C. Wong. Surface-bounded atmosphere of Europa. , 173:480–498, February 2005. doi: 10.1016/j.icarus.2004.08.013.
- M. Shi, R. A. Baragiola, D. E. Grosjean, R. E. Johnson, S. Jurac, and J. Schou. Sputtering of water ice surfaces and the production of extended neutral atmospheres. , 100:26387–26396, 1995. doi: 10.1029/95JE03099.
- D. K. Sing, H. R. Wakeford, A. P. Showman, N. Nikolov, J. J. Fortney, A. S. Burrows, G. E. Ballester, D. Deming, S. Aigrain, J.-M. Désert, N. P. Gibson, G. W. Henry, H. Knutson, A. Lecavelier des Etangs, F. Pont, A. Vidal-Madjar, M. W. Williamson, and P. A. Wilson. HST hot-Jupiter transmission spectral survey: detection of potassium in WASP-31b along with a cloud deck and Rayleigh scattering. , 446: 2428–2443, January 2015. doi: 10.1093/mnras/stu2279.
- A. J. Skemer, P. Hinz, S. Esposito, M. F. Skrutskie, D. Defrère, V. Bailey, J. Leisenring, D. Apai, B. Biller, M. Bonnefoy, W. Brandner, E. Buenzli, L. Close, J. Crepp, R. J. De Rosa, S. Desidera, J. Eisner, J. Fortney, T. Henning, K.-H. Hofmann, T. Kopytova, A.-L. Maire, J. R. Males, R. Millan-Gabet, K. Morzinski, A. Oza, J. Patience, A. Rajan, G. Rieke, D. Schertl, J. Schlieder, K. Su, A. Vaz, K. Ward-Duong, G. Weigelt, C. E. Woodward, and N. Zimmerman. High contrast imaging at the LBT: the LEECH exoplanet imaging survey. In *Adaptive Optics Systems IV*, volume 9148 of , page 91480L, July 2014. doi: 10.1117/12.2057277.
- W. H. Smyth and M. L. Marconi. Europa’s atmosphere, gas tori, and magnetospheric implications. , 181:510–526, April 2006. doi: 10.1016/j.icarus.2005.10.019.
- C. Sotin, O. Grasset, and A. Mocquet. Mass radius curve for extrasolar Earth-like planets and ocean planets. , 191:337–351, November 2007. doi: 10.1016/j.icarus.2007.04.006.
- W. B. Sparks, K. P. Hand, M. A. McGrath, E. Bergeron, M. Cracraft, and S. E. Deustua. Probing for Evidence of Plumes on Europa with HST/STIS. , 829:121, October 2016a. doi: 10.3847/0004-637X/829/2/121.
- W. B. Sparks, K. P. Hand, M. A. McGrath, E. Bergeron, M. Cracraft, and S. E. Deustua. Probing for Evidence of Plumes on Europa with HST/STIS. , 829:121, October 2016b. doi: 10.3847/0004-637X/829/2/121.

- W. B. Sparks, B. E. Schmidt, M. A. McGrath, K. P. Hand, J. R. Spencer, M. Cracraft, and S. E. Deustua. Active Cryovolcanism on Europa? , 839:L18, April 2017. doi: 10.3847/2041-8213/aa67f8.
- J. R. Spencer and W. M. Calvin. Condensed O₂ on Europa and Callisto. , 124: 3400–3403, December 2002. doi: 10.1086/344307.
- J. R. Spencer, L. A. Lebofsky, and M. V. Sykes. Systematic biases in radiometric diameter determinations. , 78:337–354, April 1989. doi: 10.1016/0019-1035(89)90182-6.
- J. R. Spencer, W. M. Calvin, and M. J. Person. CCD Spectra of the Galilean Satellites: Molecular Oxygen on Ganymede. , 100:19049–19056, September 1995. doi: 10.1029/95JE01503.
- J. R. Spencer, L. K. Tamppari, T. Z. Martin, and L. D. Travis. Nighttime Thermal Anomalies on Europa. In *Lunar and Planetary Science Conference*, volume 30 of *Lunar and Planetary Science Conference*, March 1999.
- J. N. Spitale, T. A. Hurford, A. R. Rhoden, E. E. Berkson, and S. S. Platts. Curtain eruptions from Enceladus’ south-polar terrain. , 521:57–60, May 2015. doi: 10.1038/nature14368.
- S. Alan Stern. The lunar atmosphere: History, status, current problems, and context. *Reviews of Geophysics*, 37(4):453–491, nov 1999. doi: 10.1029/1999rg900005. URL <https://doi.org/10.1029/1999rg900005>.
- M. E. Summers, D. F. Strobel, Y. L. Yung, J. T. Trauger, and F. Mills. The structure of Io’s thermal corona and implications for atmospheric escape. , 343:468–480, August 1989. doi: 10.1086/167720.
- V. Tennishev, D. C. S. Öztürk, M. R. Combi, M. Rubin, J. H. Waite, and M. Perry. Effect of the Tiger Stripes on the water vapor distribution in Enceladus’ exosphere. *Journal of Geophysical Research (Planets)*, 119:2658–2667, December 2014. doi: 10.1002/2014JE004700.
- B. Teolis, C. Plainaki, T. Cassidy, and U. Raut. Water Ice, O₂, H₂, and H₂O₂ Radiolysis and Sputtering Yields for any Projectile Species, Energy, or Temperature: A Model for Icy Astrophysical Bodies . 2017a.
- B. D. Teolis and J. H. Waite. Dione and Rhea seasonal exospheres revealed by Cassini CAPS and INMS. , 272:277–289, July 2016. doi: 10.1016/j.icarus.2016.02.031.

- B. D. Teolis, R. A. Vidal, J. Shi, and R. A. Baragiola. Mechanisms of O₂ sputtering from water ice by keV ions. , 72(24):245422, December 2005. doi: 10.1103/PhysRevB.72.245422.
- B. D. Teolis, G. H. Jones, P. F. Miles, R. L. Tokar, B. A. Magee, J. H. Waite, E. Roussos, D. T. Young, F. J. Crary, A. J. Coates, R. E. Johnson, W.-L. Tseng, and R. A. Baragiola. Cassini Finds an Oxygen-Carbon Dioxide Atmosphere at Saturns Icy Moon Rhea. *Science*, 330:1813, December 2010. doi: 10.1126/science.1198366.
- B. D. Teolis, D. Y. Wyrick, A. Bouquet, B. A. Magee, and J. H. Waite. Plume and surface feature structure and compositional effects on Europa’s global exosphere: Preliminary Europa mission predictions. , 284:18–29, March 2017b. doi: 10.1016/j.icarus.2016.10.027.
- P. C. Thomas, R. Tajeddine, M. S. Tiscareno, J. A. Burns, J. Joseph, T. J. Lored, P. Helfenstein, and C. Porco. Enceladus’s measured physical libration requires a global subsurface ocean. , 264:37–47, January 2016. doi: 10.1016/j.icarus.2015.08.037.
- S. K. Trumbo, M. E. Brown, P. D. Fischer, and K. P. Hand. A New Spectral Feature on the Trailing Hemisphere of Europa at 3.78 μm . , 153:250, June 2017. doi: 10.3847/1538-3881/aa6d80.
- C. C. C. Tsang, J. R. Spencer, E. Lellouch, M. A. Lopez-Valverde, and M. J. Richter. The collapse of Io’s primary atmosphere in Jupiter eclipse. *Journal of Geophysical Research (Planets)*, 121:1400–1410, August 2016. doi: 10.1002/2016JE005025.
- L. Turc, L. Leclercq, F. Leblanc, R. Modolo, and J.-Y. Chaufray. Modelling Ganymedes neutral environment: A 3D test-particle simulation. , 229:157–169, February 2014. doi: 10.1016/j.icarus.2013.11.005.
- J. D. Turner, D. Christie, P. Arras, R. E. Johnson, and C. Schmidt. Investigation of the environment around close-in transiting exoplanets using CLOUDY. , 458: 3880–3891, June 2016. doi: 10.1093/mnras/stw556.
- S. Vance and J. Goodman. *Oceanography of an Ice-Covered Moon*, page 459. 2009.
- S. D. Vance, K. P. Hand, and R. T. Pappalardo. Geophysical controls of chemical disequilibria in Europa. , 43:4871–4879, May 2016. doi: 10.1002/2016GL068547.
- Allen L. Victor, Thomas H. Zurbuchen, and Alec D. Gallimore. Top hat electrostatic analyzer for far-field electric propulsion plume diagnostics. *Review of Scientific Instruments*, 77(1):013505, 2006. doi: 10.1063/1.2165549. URL <https://doi.org/10.1063/1.2165549>.

- A. Vorburger, P. Wurz, H. Lammer, S. Barabash, and O. Mousis. Monte-Carlo simulation of Callisto's exosphere. , 262:14–29, December 2015. doi: 10.1016/j.icarus.2015.07.035.
- J. H. Waite, C. R. Glein, R. S. Perryman, B. D. Teolis, B. A. Magee, G. Miller, J. Grimes, M. E. Perry, K. E. Miller, A. Bouquet, J. I. Lunine, T. Brockwell, and S. J. Bolton. Cassini finds molecular hydrogen in the Enceladus plume: Evidence for hydrothermal processes. *Science*, 356:155–159, April 2017. doi: 10.1126/science.aai8703.
- R. C. Wiens, D. S. Burnett, W. F. Calaway, C. S. Hansen, K. R. Lykke, and M. J. Pellin. Sputtering Products of Sodium Sulfate: Implications for Io's Surface and for Sodium-Bearing Molecules in the Io Torus. , 128:386–397, August 1997. doi: 10.1006/icar.1997.5758.
- L. A. Young. Volatile transport on inhomogeneous surfaces: II. Numerical calculations (VT3D). , 284:443–476, March 2017. doi: 10.1016/j.icarus.2016.07.021.
- K. Zahnle, P. Schenk, H. Levison, and L. Dones. Cratering rates in the outer Solar System. , 163:263–289, June 2003. doi: 10.1016/S0019-1035(03)00048-4.
- K. Zahnle, M. S. Marley, C. V. Morley, and J. I. Moses. Photolytic Hazes in the Atmosphere of 51 Eri b. , 824:137, June 2016. doi: 10.3847/0004-637X/824/2/137.
- W. Zhu, C. Bower, O. Zhou, G. Kochanski, and S. Jin. Large current density from carbon nanotube field emitters. *Applied Physics Letters*, 75(6):873–875, 1999. doi: 10.1063/1.124541. URL <http://dx.doi.org/10.1063/1.124541>.
- M. Y. Zolotov and F. Postberg. Can Nano-Phase Silica Originate from Chondritic Fluids? The Application to Enceladus' SiO₂ Particles. In *Lunar and Planetary Science Conference*, volume 45 of *Lunar and Planetary Science Conference*, page 2496, March 2014.
- M. Y. Zolotov and E. L. Shock. Composition and stability of salts on the surface of Europa and their oceanic origin. , 106:32815–32828, December 2001. doi: 10.1029/2000JE001413.